Application of a Renal Proximal Tubule Microphysiological System for Drug Safety Assessment and Disease Modeling

Kevin A. Lidberg

A dissertation
submitted in partial fulfillment of the
requirements for the degree of

Doctor of Philosophy

University of Washington
2021

Reading Committee:
Edward J. Kelly, Chair
Yvonne Lin
Patrick L. Iversen

Program Authorized to Offer Degree:
Department of Pharmaceutics

University of Washington

Abstract

Application of a Renal Proximal Tubule Microphysiological System for Drug Safety Assessment and Disease Modeling

Kevin A. Lidberg

Chair of Supervisory Committee:
Edward J. Kelly
Department of Pharmaceutics

A combination of *in vitro* assays and animal models are used to evaluate the properties of novel drug molecules, including safety and efficacy, throughout the drug development process. The data produced by *in vitro* assays and animal models guide the selection of the optimal compounds to advance in the drug development process and form the basis for initiation of human clinical trials. This screening methodology combining *in vitro* assays and animal studies to gain a wholistic picture of a drugs' pharmacologic, toxicologic, and pharmacokinetic profile has enabled companies to bring molecules to market that successfully treat human disease and improve patient lives. However, the current drug development paradigm suffers from crucial limitations such as interspecies differences in animal models and poor cell phenotype of *in vitro* assays, which can cause the drug screening systems to fail to accurately imitate drug behavior in humans. As such, 85% of molecules that enter clinical trials do not make it to market because of a failure to demonstrate their safety and/or efficacy. In recognition of these shortcomings, the National Institutes of Health funded the development of tissue chips, which are 3-

dimensional microphysiological devices that emulate tissue-specific microenvironments that support drug safety assessment, disease modeling, and efficacy testing.

To that end, we previously developed a proximal tubule microphysiological system (PT-MPS) that recapitulates key metabolic, regulatory, and transport activities of renal proximal tubule cells *in vivo*. In this dissertation, we applied this PT-MPS to assess the safety of compounds with two antisense oligonucleotide backbone chemistries and to model the effect of glomerular dysfunction and subsequent proteinuria on the phenotype of the proximal tubule. We showed that compounds with phosphorodiamidate morpholino chemistry exhibited a more favorable safety profile while retaining pharmacodynamic activity compared to compounds with phosphorothioate chemistry. Together, these data support the choice of compounds with phosphorodiamidate morpholino chemistry for targeting renally-expressed genes such as cytochrome P450 3A5. We characterized the effect of proteinuria on proximal tubule cell phenotype and showed that human serum, but not albumin, causes a regenerative, secretory phenotype that is driven by a gain of nuclear factor kappa light chain enhancer of activated B cells (NF-κB) and activator protein 1 (AP-1) and loss of hepatocyte nuclear factor 4 alpha (HNF4α) and peroxisome proliferator activated receptor alpha (PPARα) epigenomic and transcriptional signatures. These findings are important because they largely reproduce the observations of other groups on the effect of proteinuria on proximal tubule epithelial cells (PTECs) and experimentally-derived animal models with glomerular dysfunction. Moreover, the response mirrors the changes observed from other insults suggesting that there is a conserved regulatory program that is activated by a variety of stressors and may represent a therapeutic target. Therefore, the PT-MPS can be used to evaluate novel strategies to prevent development of a secretory phenotype by PTECs during proteinuria, which is associated with fibrosis in progressive renal diseases. Taken together, the PT-MPS demonstrates utility in drug safety assessment and disease modeling, two areas where tissue chips could improve the drug development process.

Table of Contents

Abbreviations

1’-OH-MDZ: 1’-hydroxy-midazolam
1’-OH-MDZ-d_4: 1’-hydroxy-midazolam-d_4
1α,24R,25(OH)$_2$D$_3$: 1α,24R,25-trihydroxyvitamin D$_3$
1α,25(OH)$_2$D$_3$: 1α,25-dihydroxyvitamin D$_3$
1α,25(OH)$_2$D$_3$-d_6: 1α,25-dihydroxyvitamin D$_3$-d_6
2’-OMe-PSO: 2’-O-methyl-phosphorothioate oligonucleotide
24R,25(OH)$_2$D$_3$: 24R,25-dihydroxyvitamin D$_3$
24R,25(OH)$_2$D$_3$-d_6: 24R,25-dihydroxyvitamin D$_3$- d_6
25(OH)D$_3$-d_6: 25-hydroxyvitamin D$_3$-d_6
25OHD$_3$: 25-hydroxyvitamin D$_3$
4β,25(OH)$_2$D$_3$: 4β,25-dihydroxyvtitamin D$_3$
2D: two-dimensional
3D: three-dimensional
6βOH: 6β-hydroxycortisol
ABC: ATP-binding cassette
ACE2: Angiotensin I converting enzyme 2
AO: aldehyde oxidase
AP-1: activator protein 1
ASO: antisense oligonucleotide
ATP: adenosine triphosphate
BCRP: breast cancer resistance protein
BFC: 7-benzyloxy-4-[trifluoromethyl]-coumarin
CD28SA: superagonistic CD28 antibody
CKD: chronic kidney disease
c-MET: mesenchymal-epithelial transition factor
CORT: cortisol
CRS: cytokine release syndrome
CV-1: African green monkey kidney cells

CYP24A1: cytochrome P450 24A1

CYP27B1: cytochrome P450 27B1

CYP3A5: cytochrome P450 3A5

DAPTAD: 4-(4-(Dimethylamino)phenyl)-3H-1,2,4-triazole-3,5(4H)-dione

DBP: vitamin D binding protein

DDI: drug-drug interaction

DMSO: dimethylsulfoxide

DNA: deoxyribonucleic acid

dPBS: Dulbecco’s phosphate buffered saline

EpCAM: epithelial cell adhesion molecule

ESKD: end-stage kidney disease

FBS: fetal bovine serum

FOXM1: forkhead box M1

Ft: fraction of transport

G4: G-quadruplex

GR: glucocorticoid receptor

GRE: glucocorticoid response elements

HBP: high blood pressure

HEK293: human embryonic kidney 293 cells

HFC: 7-hydroxy-4-[trifluoromethyl]-coumarin

HNF4α: hepatocyte nuclear factor 4 alpha

HO-1: heme oxygenase 1

IFN-γ: interferon gamma

IgG: immunoglobulin G

IL-10: interleukin-10

IL-2: interleukin-2

IL-6: interleukin-6

IL-8: interleukin 8

IRI: ischemia reperfusion injury

Ki67: marker of proliferation Ki67

KIM-1: kidney injury molecule 1

LC MS/MS: liquid chromatography mass spectrometry mass spectrometry

LRP2: megalin

MATE1: multidrug and toxin extrusion protein 1

MATE2K: multidrug and toxin extrusion protein 2K

MHC: major histocompatibility complex

MPS: microphysiological system

MR: mineralocorticoid receptor

mRNA: messenger RNA

MRP2: multidrug resistance-associated protein 2

MRP4: multidrug resistance-associated protein 4

Na^+/K^+ATPase: sodium-potassium adenosine triphosphatase

NF-κB: nuclear factor kappa light chain enhancer of activated B cells

NMD: nonsense mediated decay

NOAEL: no-observed-adverse-effect-level

OAT1: organic anion transporters 1

OAT3: organic anion transporter 3

OATP4C1: organic anion transporting polypeptide 4C1

OCT2: organic cation transporter 2

OCTN1: organic cation transporter novel type 1

OCTN2: organic cation transporter novel type 2

PAH: para-aminohippurate

PBMC: peripheral blood mononuclear cell

PBS: phosphate buffered saline

PCT: proximal convoluted tubule

PDMS: polydimethylsiloxane

P-gp: P-glycoprotein

PMO: phosphorodiamidate morpholino oligonucleotide

PPARGC1A: peroxisome proliferator-activated receptor gamma coactivator 1-alpha

PPARα: peroxisome proliferator activated receptor alpha pre-mRNA: precursor messenger RNA

PSO: phosphorothioate oligonucleotide

PST: proximal straight tubule

PTEC: proximal tubule epithelial cell

PT-MPS: proximal tubule microphysiological system

RNA: ribonucleic acid

RNAseH: ribonuclease H

SGLT1: sodium-glucose cotransporter-1

SGLT2: sodium-glucose cotransporter-2

SLC: solute carrier

SMAD3: mothers against decapentaplegic homolog 3

SREBF2: sterol-regulatory element binding transcription factor 2

TCR: T-cell antigen receptor

$\mathrm{T_{EM}}$: effector memory T-cell

TGF-β: transforming growth factor beta

TNF-α: tumor necrosis factor alpha

$\mathrm{T_{REG}}$: regulatory T-cell

UUO: unilateral ureteral obstruction

List of Figures

List of Tables

Acknowledgements

I would like to thank my advisor, Dr. Edward J. Kelly, for his unparalleled passion for science, extraordinary patience, and thoughtful guidance. His support has fostered my personal and professional growth, for which I am truly grateful. I would also like to thank the members of my thesis committee: Yvonne Lin, Patrick Iversen, Rheem Totah, Kenneth Thummel, and Brian Werth for providing careful and constructive feedback during the course of my dissertation research. I would like to give a special thanks to Yvonne Lin and Patrick Iversen for their thorough and thoughtful review of my dissertation. I would like to thank former and present members of the Kelly lab who created an environment that was second-to-none. Lastly, I would like to thank my friends and family for their unwavering encouragement that motivated me throughout this long journey.

Dedication

To all those who donated their kidney tissue to science

1. Introduction

1.1 The drug development paradigm and clinical translation gap

The current drug development paradigm is inadequate. Spending on research and development by members of the Pharmaceutical Research and Manufacturers of America has skyrocketed, while the number of new drug approvals has remained relatively stable.[1] The inflation-adjusted average cost of a single approved drug increased from $179 million in the 1970s to $2.6 billion in the 2000s.[1] 85% of drug candidates that enter clinical trials fail to gain approval and the success rate is poor at each clinical phase (48-64% in Phase I; 29-32% in Phase II; 60-67% in Phase III).[1] A lack of efficacy or issues with safety are the primary drivers of drug attrition in the most costly stages of drug development, Phase II and Phase III trials.[2] Despite promising results on the safety and efficacy of candidate molecules in animals, there are a few reasons for the apparent disconnect in safety and efficacy between pre-clinical models and humans. First, to satisfy regulatory requirements to enable first-in-human trials, many *in vitro* assays and animal studies are required.[1] This regulatory stringency has undoubtedly improved patient safety by preventing unsafe molecules from entering clinical trials but at the cost of efficiency, so much so that it has led some to speculate that aspirin would be rejected by these standards.[3] Second, a core tenet of the drug development paradigm is a heavy reliance on animals to identify potential drug targets, characterize the efficacy and safety of new molecular entities, and predict the kinetics and metabolism of drug candidates in humans. However, the reliability of animal models to accurately reflect disease states and drug behavior in humans has been called into question.[4, 5] For example, the degree of agreement in drug efficacy between animals and humans is remarkably variable, differs by disease area, and can be inflated by publication bias.[6-8] In contrast, a toxicity signal in animals is generally predictive that a toxic event will occur in humans, but a compound that is shown to be safe in animals does not mean it will be safe in humans.[9] This gap in translation when progressing from the preclinical to clinical stage can be caused by interspecies differences in transporter, enzyme, or target expression, differing physiology and disease etiology in animal models, poor study design, and publication bias.[10-12].

1.1.1 Case Study: Species differences in target expression

As mentioned previously, target expression levels or expression patterns may differ between species, confounding the extrapolation of animal data to humans. The immune system is especially prone to species-specific differences, which is exemplified by the case of TGN1412.[13] TGN1412 was a superagonistic anti-CD28 monoclonal antibody in development for the treatment of inflammatory autoimmune diseases through activation and expansion of anti-inflammatory regulatory T lymphocytes (T_{REG}). However, in the first-in-human clinical trial, TGN1412 unexpectedly caused a sudden and pronounced elevation in plasma levels of inflammatory cytokines, a life-threatening response known as cytokine release syndrome (CRS), and led to systemic organ failure in all study participants.[14] This was surprising because preclinical testing provided few indications of a risk of CRS. So how did *in vitro* cultures of human peripheral blood mononuclear cells (PBMCs), an analogous rodent model, and a primate model all fail to predict that TGN1412 would cause CRS in humans?

T-cell activation, which promotes cell proliferation, cell survival, and effector functions, requires two signaling events: 1) interaction of the T-cell antigen receptor (TCR) with peptide-major histocompatibility complexes on a professional antigen-presenting cell, and 2) binding of a co-stimulatory receptor.[15] Ligand binding to TCR recruits and primes intracellular complexes for signal transduction while triggering of a co-stimulatory receptor, such as CD28, augments signaling cascades.[15] Stimulation of CD28 in $CD4^+$ T-cells *in vitro* in the absence of TCR engagement causes short-lived transcriptional changes and cytokine production but not proliferation, whereas ligand binding to the TCR without co-stimulation causes the T-cell to enter into a non-responsive state in which it will be refractory to stimulation.[16-18] However, superagonistic CD28 antibodies (CD28SA) appeared to be able to fully activate T-cells without strong, concurrent TCR activation.[19] At the time, this was attributed to their unique binding affinity for a laterally exposed epitope of amino acids in CD28 known as the C”D loop.[20] Conventional CD28 antibodies and natural ligands of CD28 bind instead near or at a MYPPPY epitope.[21]

CD4$^+$ T-cells are classified into subsets according to their cytokine secretion profile and biological role, two of which are CD4$^+$CD25$^+$CD28$^+$ regulatory T-cells (T_{REG}) and CD4$^+$CD45/RA/RC/RO$^+$CD28$^+$CCR7$^-$ effector memory T-cells (T_{EM}). T_{REG} have immunosuppressive properties as a result of secretion of transforming growth factor beta (TGF-β) and interleukin-10 (IL-10). In contrast, T_{EM} generate inflammatory responses primarily through production of tumor necrosis factor alpha (TNF-α), interferon gamma (IFN-γ), and interleukin-2 (IL-2).

TGN1412 failed to elicit an inflammatory response or cell proliferation in human PBMCs in an *in vitro* assay. The lack of response in this assay has largely been attributed to the non-physiological nature of the *in vitro* culture conditions. By culturing the PBMCs at a low density, there was an insufficient level of activation of TCR necessary to recruit and prime the intracellular complexes for CD28 signal transduction. Co-culture of PMBCs with endothelial cells or immobilization of TGN1412 on culture surfaces before treatment both allowed for replication of cytokine secretion and T-cell proliferation observed *in vivo* in the clinical trial.[22] Moreover, culturing of PMBCs at a high density prior to treatment with TGN1412 sensitized PBMCs to CD28 stimulation, presumably through TCR activation, and yielded a physiological response (i.e. T_{EM}-mediated production of TNF-α, IFN-γ, and IL-2).[23] The fact that the cell culture assay could be refined to produce a toxicologic response to TGN1412 highlights the importance of considering physiology when using *in vitro* cell cultures and demonstrates the utility of human *in vitro* cell cultures as an assay tool.

Rodent models failed to detect signs that TGN1412 could produce CRS. Treatment of rats with a CD28SA resulted in polyclonal expansion of all CD4$^+$ T-cells, but expansion of the T_{REG} compartment was most prominent.[19, 24] Based on these observations, it was hypothesized that a CD28SA could be used therapeutically to attenuate immune-based inflammatory diseases. Indeed, CD28SA administration effectively treated experimental models of autoimmune encephalomyelitis and adjuvant arthritis in rats without raising concerns for the potential of CRS.[25, 26] It was noted, when mice were first depleted of T_{REG} cells, CD28SA treatment increased plasma levels of inflammatory cytokines suggesting that a rapid expansion of the T_{REG} pool prevented a CRS-like response in rodents.[27] Moreover, the lack of an inflammatory response after CD28SA treatment in rodents can be explained by the housing of rodents in pathogen-free environments. In humans, the T_{EM} pool increases linearly with age as a result of recurrent exposure to pathogens and is accompanied by a decreased capability to replenish the pool of naïve T-cells.[28] Therefore, the ratio of T_{EM}/T_{REG} is higher in humans compared to rodents in pathogen-free environments, making humans more susceptible to the inflammatory effects of CD28-induced activation of T_{EM}.[29]

A separate mechanism is responsible for the lack an inflammatory response to TGN1412 in cynomolgus macaques. It was first speculated that the C”D loop epitope of CD28 lacked homology between macaques and humans. However, the amino acid sequence of those domains were identical and bound TGN1412 with similar affinity.[30] In fact, the disparate response was caused by a species-specific expression pattern of CD28 as macaque T_{EM} do not express CD28 while human T_{EM} express high levels of CD28.[31] Consequently, stimulation of CD28 by TGN1412 cannot activate T_{EM} in macaques, precluding the possibility of an acute inflammatory reaction.

The first-in-human dose of TGN1412 that resulted in CRS (i.e., 0.1 mg/kg) was based upon the no-observed-adverse-effect level (NOAEL) in primates and 500-fold lower than the dose administered to non-human primates. Retrospective analyses predicted that a dose of 0.1 mg/kg in humans could have resulted in a CD28 receptor occupancy of 86.2%-90.9% and 45%-80% based on *in silico* modeling and *in vitro* binding assays, respectively.[32] Thus, the TGN1412 dose administered is predicted to have caused a near maximal biological response and can explain the severity of the adverse events that were observed. Indeed, TGN1412 has been rebranded as TAB08 and been brought into clinical trials again but this time at doses ranging from 0.1 μg/kg to 7 μg/kg.[33] In line with data from preclinical species, the lower dose of TAB08 in humans led to a prominent increase in the anti-inflammatory cytokine IL-10 while the levels of the inflammatory cytokines (TNFα, IL-2, IFN-γ) were largely unchanged, supporting the ability of TAB08 to selectively activate T_{REG}.[33]

1.1.2 Species differences in drug metabolizing enzymes

Drug metabolizing enzyme activity, substrate specificity, and expression level and pattern can differ between species.[10, 11] This complicates the extrapolation of animal safety or efficacy data to humans as either the parent compound or its metabolites can be bioactive. Hence, metabolic profiling of lead compounds is performed with liver microsomes, liver S9 fractions, and/or hepatocytes from multiple species early in development to help choose the most appropriate animals for formal toxicological testing. While this method is accurate in many cases, there are examples in which species-specific metabolism-based outcomes were not captured. For example, liver microsomes from rat, dog, monkey, and human showed similar metabolism of the mesenchymal-epithelial transition factor (c-MET) inhibitor, SGX523.[34] *In vivo* toxicological studies were performed in rats and dogs with SGX523 demonstrating a favorable safety profile.[34] However in clinical studies, SGX523 caused acute renal failure, an adverse event not identified as a potential concern in rats or dogs.[35] Subsequently, it was shown in monkeys that SGX523 caused obstructive nephropathy with intratubular crystal formation and that this was likely the result of formation of a poorly water soluble metabolite, 2-quinolinone-SGX523, via aldehyde oxidase (AO).[34, 35] Importantly, rats and dogs have low AO activity and do not form appreciable levels of 2-quinolinone-SGX523. Furthermore, this metabolite was not identified in early metabolic profiling studies because AO is a cytosolic enzyme and is not present in microsomal preparations. Interestingly, a structurally-related c-MET inhibitor, JNJ-38877605, also caused obstructive nephropathy via AO-mediated formation of a less soluble metabolite, however in this case, the issue was detected as rabbits were used for toxicological testing.[36] Safety assessments using animals can also yield false-positive signals. For example, the formation of a nephrotoxic glutathione conjugate of efavirenz was observed in rats, but not other preclinical species or humans.[37] Of course, multiple species are used in evaluating new molecular entities which greatly improves accuracy of correctly categorizing a molecule as safe or toxic.[38] However, in a study looking at the concordance between human and animal data using a set of 182 compounds the positive predictive value, defined as the proportion of positive nonclinical findings that had positive clinical findings, of animals for detecting renal liabilities was poor. In fact, the positive predive value for rat, dog, and non-human primates at detecting renal liabilities was 19%, 33%, and 0%, respectively.[38] On the other hand, the negative predictive value, defined as the proportion of negative clinical findings that had negative clinical finding, of the rat, dog, and non-human primates was excellent at 96%, 95%, and 100%, respectively.

Altogether, the regulatory requirements to drug approval are higher than ever before, at increasing monetary and workforce costs, and the methods (i.e., animal models and conventional *in vitro* cell cultures) used to predict drug behavior in humans, particularly drug toxicity, are questionable. The glaring need for innovation to clear the translation gap was recognized when the National Institutes of Health (NIH) funded the development of novel human-relevant microphysiological models that are intended to supplement the use of animals and improve *in vitro* to *in vivo* extrapolation.[39, 40] During the 2012 and 2017/2018 award cycles, our group was funded by the NIH to develop and apply a microphysiological model of the human renal proximal tubule to drug safety assessment and disease modeling.

1.2 Kidney anatomy and physiology

The kidney is an essential organ that is crucial for the regulation of blood homeostasis. The kidney controls plasma volume, electrolyte and acid-base balance, synthesizes a number of hormones, and excretes xenobiotics and biological waste products.[41-43] Each kidney contains ~1 million nephrons, the individual structural and functional units of the kidney. The nephron consists of a renal corpuscle that includes the glomerulus and a segmented tubule unit that includes the proximal tubule, loop of Henle, distal tubule, connecting tubule, and collecting duct. The nephron segments carry out three basic functions: 1) filtration of blood; 2) reabsorption of electrolytes, solutes, and nutrients; and 3) secretion of waste products, xenobiotics, and excess electrolytes to ultimately produce a refined and concentrated filtrate (termed urine) that is excreted. Filtration occurs within the renal corpuscle at the glomerulus, a knot-like network of microvascular endothelial channels flanked on one side by the afferent arteriole (blood inflow) and on the other by the efferent arteriole (blood outflow) (Figure 1.1A).[43] The glomerular hydrostatic pressure is the driving force for movement of molecules from the blood into the tubular lumen which is controlled by the vascular tone of the afferent and efferent arterioles.[43] The glomerular microvascular endothelial cells are fenestrated (~60-70 nm pores) and are enwrapped by podocytes, epithelial cells that possess long foot processes that interdigitate and encapsulate the endothelium.[43] The basement membrane, a ~300 nm thick layer of extracellular matrix protein, separates the fenestrated endothelial cell and podocyte basal laminas.[43] The basement membrane core is comprised of collagen, laminin, and nidogen, while the outermost layers are negatively-charged heparan sulfate proteoglycans. Together, the endothelium, basement membrane, and podocytes make up the glomerular filtration barrier which restricts molecules from moving from the blood into the tubule system based on size (~70 kDa cutoff) and possibly charge (Figure 1.1B).[43] The solutes and low-molecular weight proteins that pass from the blood into the tubule system constitute the ultrafiltrate. The glomerular filtration barrier is essential for maintaining a normal ultrafiltrate (i.e., minimal protein >70 kDa) and proper kidney function, but can be disrupted in disease states such as chronic kidney disease or by insults (e.g., ischemia, toxicants) that cause acute kidney injury.[43] The consequences of disruption of glomerular filtration barrier function are discussed in Chapter 3.

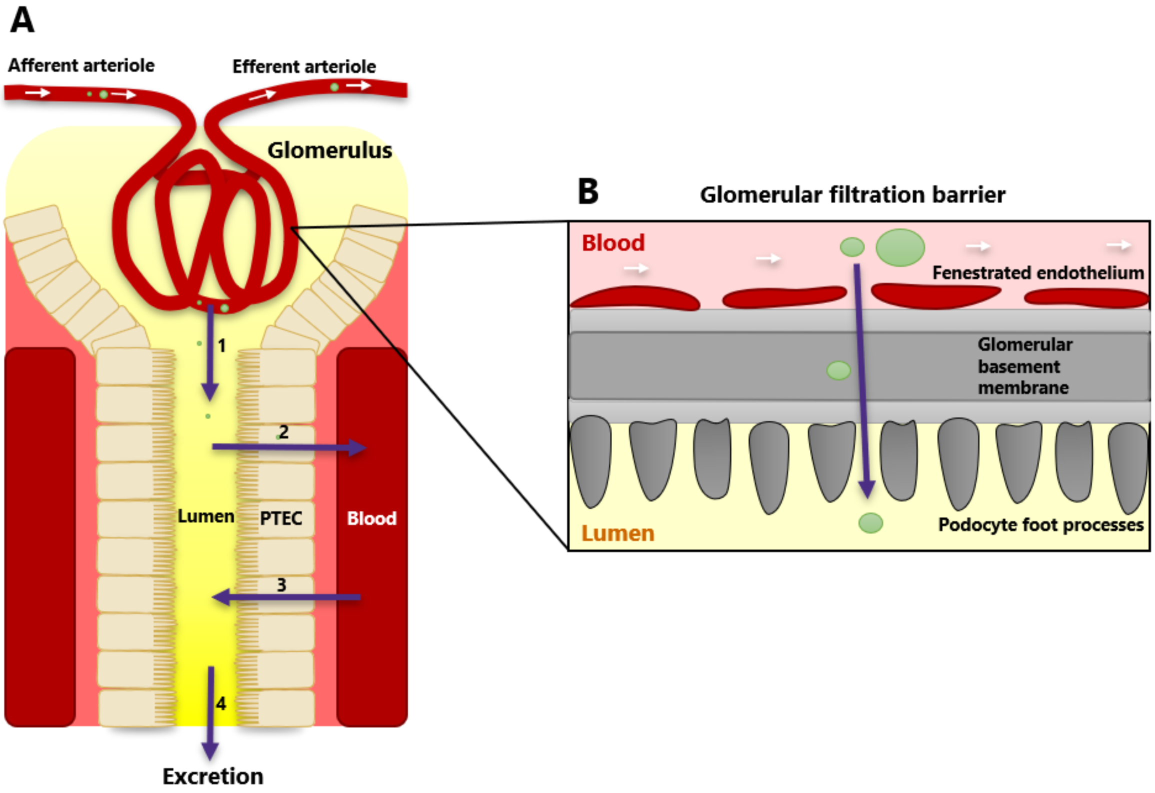

Figure 1.1. **Anatomy of the glomerulus and proximal tubule segment of the nephron**. A) The nephron performs four basic functions to regulate the composition of the blood: 1) filtration, 2) reabsorption, 3) secretion, and 4) excretion. 1) Filtration of the blood occurs in the glomerulus, a specialized microvasculature structure that restricts passage of molecules larger than ~70 kDa from entering the tubule system while allowing anything smaller to pass. Immediately following the glomerulus is the proximal tubule which possesses a brush border that expresses a wide repertoire of solute transporters and is active in both 2) reabsorption of molecules from the ultrafiltrate and 3) secretion from blood into the lumen. Other tubule segments in the nephron also perform reabsorption and secretion activities, though they primarily act on water and ions. 4) The concentrated and refined filtrate is eventually removed from the body by excretion. B) Cross section of the glomerular filtration barrier depicting the fenestrated microvascular endothelium, a thick extracellular basement membrane, and podocyte foot processes (pedicels), which function as the size exclusion filter of the glomerulus.

1.3 Proximal tubule

The proximal tubule is the first tubular nephron segment and can further be divided into three segments called S1, S2, and S3 based on morphology, topology, and location in kidney.[42] An alternative nomenclature system divides the proximal tubule into the proximal convoluted tubule (PCT) and proximal straight tubule (PST) based on the course of the tubule (convoluted vs. straight) and spatial localization within the kidney (i.e., cortical vs. medullary). The relationship between the two classification systems is the PCT contains S1 and S2 (late PCT), whereas the PST contains S2 (cortical PST) and S3 (medullary PST).[44] While there is a large degree of heterogeneity between the PT segments, in general, proximal tubule epithelial cells (PTECs) have a brush border (microvilli), a substantial endocytic system, numerous mitochondria, and basolateral interdigitations, with these features most prominent in the S1 segment. Aside from histological differences, the expression level of various transporters and enzymes also differs between the segments. For example, sodium-glucose cotransporter-2 (SGLT2) is expressed in the S1 and S2 segments, whereas sodium-glucose cotransporter-1 (SGLT1) is expressed in the S3 segment.[42] For the remainder of this thesis, the use of the terms proximal tubule and PTECs should be considered to encompass segments S1-S3 unless otherwise specified.

The proximal tubule performs several important physiological functions due to its prominent absorptive, metabolic, and secretory activities. The proximal tubule reabsorbs 65% of the ultrafiltrate load including nearly all filtered amino acids, glucose, organic solutes, and low molecular weight proteins.[45] The proximal tubule also reabsorbs most bicarbonate (~80%), phosphate (~80%), potassium (65%), and urea (50%). Despite reabsorbing 99% of filtered glucose, the proximal tubule is gluconeogenic and instead plays a role in glucose counter-regulation.[46] The proximal tubule contributes to renal metabolism and hormone production. The proximal tubule is the primary site for bioactivation of 25-hidroxy vitamin D_3 ($25OHD_3$) to its active form, $1\alpha,25$-dihydroxy vitamin D_3 ($1\alpha,25(OH)_2D_3$) via cytochrome P450 27B1 (CYP27B1). $1\alpha,25(OH)_2D_3$ is essential for bone homeostasis through regulation of uptake of calcium in the gut and modification of osteoclast activity.[47] Cytochrome P450 3A5 (CYP3A5) is expressed in the proximal tubule where the enzyme (in individuals with *CYP3A5*1* genotype) can play a role in intrarenal drug disposition.[48] Finally, renal clearance plays a major role in the elimination of 30% of the top 200 FDA approved drugs and the proximal tubule is primary nephron segment for active secretion.[49, 50]

The proximal tubule expresses a wide array of transporters with absorptive or secretory activity and broad substrate specificity. These transporters include members of the solute carrier (SLC) and ATP-binding cassette (ABC) families. Transporters localized to the basolateral membrane include: organic anion transporters 1 and 3 (OAT1/SLC22A6; OAT3/SLC22A8), organic cation transporter 2 (OCT2/SLC22A2), and organic anion transporting polypeptide 4C1 (OATP4C1).[49] Transporters localized to the apical membrane include: multidrug and toxin extrusion protein 1 and 2-K (MATE1/SCL47A1, MATE2/2-K/SLC47A2), multidrug resistance-associated protein 2 and 4 (MRP2/ABCC2, MRP4/ABCC4), P-glycoprotein (P-gp/ABCB1), breast cancer resistance protein (BCRP/ABCG2), and organic cation transporter novel type 1 and 2 (OCTN1/SLC22A4, OCTN2/SLC22A5).[49] In general, PTECs can execute a high vectorial or transcellular flux of molecules because the transporters expressed on the apical and basolateral membranes possess similar substrate specificity.[49] However, if the rate of transport into the cell is higher than transport out of the cell, or if the efflux process is inhibited, molecules can accumulate within PTECs (e.g. tenofovir).[51] Consequently, the proximal tubule is a site for drug-drug interactions (DDI) and drug-induced kidney injury.[49, 51, 52] The specific consequence of inhibiting an apical or basolateral transporter will depend on the magnitude of inhibition, the fraction of transport of the drug by the transporter (ft), the therapeutic index of the object drug, and whether or not the pharmacological target is expressed in PTECs. Inhibition of basolateral uptake transporters can decrease the renal clearance of the object drug and may lead to higher plasma concentrations or reduced proximal tubule cell concentrations.[53, 54] In some cases, these interactions can result in toxicities or even fatalities resulting from increased systemic exposure to the victim drug (e.g., methotrexate and ketoprofen).[55, 56] Similarly, inhibition of apical efflux transporters can result in accumulation of drug in PTECs, potentially increasing the risk for drug-induced injury.[57, 58] On the other hand, renal transporters have intentionally been targeted to produce DDI’s with therapeutic benefit. For example, penicillin has a short plasma half-life due to OAT1/3 mediated tubular secretion, but inhibition of OAT1/3 with probenecid drastically reduces the renal clearance, extending the time in which plasma concentrations of penicillin remain within an effective range.[59]

Evaluating the impact of renal transporters on the disposition of new molecular entities remains a challenge during drug development. Animal transporters can differ in their expression pattern (e.g., rat

Oct1 [rOct1] and mouse Oct1 [mOct1] vs. human OCT1 [hOCT1]) as rOct1 and mOct1 are expressed at high levels in the kidney whereas hOCT1 is very low.[60, 61] Animal transporters can also exhibit different substrate specificity (e.g., hOAT3 vs. rOat3).[62] For example, hOAT3 exhibits a lower K_m and higher V_{max} than rOAT3 for Famotidine.[62] Differences in expressed transporters can potentially affect the relative contribution of renal clearance to total drug elimination, or affect the fraction of transport of a drug by a particular transporter, which could change the magnitude of a drug-drug interaction. For example, renal clearance only accounts for 30% of the elimination of pemetrexed in mice, but can exceed 80% in humans (Woodland et al., 1997). Furthermore, species differences in kidney blood flow and plasma protein binding need to be accounted for in order to obtain an accurate prediction of human renal clearance.[63] Transporter-specific activities can be probed with gene-knockout animals, but the knockout itself can affect off-target gene activity and data should be interpreted with caution.[64] Immortalized proximal tubule cell lines are available and offer steady source of cells, however, their transcriptomes differ significantly from native tissue.[65] Primary human proximal tubule cells grown in monolayers have been successfully used to identify relevant transporters for particular drugs and retain expression of the entire complement of renal transporters. However, primary proximal tubule cells suffer from a limited availability of renal tissue, short duration in culture, poor phenotypic stability, and variability in cell phenotype from group to group because of differences in isolation protocols.[66-68] It is therefore important to develop a robust human cell-based system that can be used to evaluate transport kinetics, model the effects of DDIs, or discern the impact of disease on drug disposition.

Many of the secondary active and facilitative transporters that carry out the absorptive and secretory transport actions of the proximal tubule depend on the transcellular concentration gradient established by the sodium-potassium adenosine triphosphatase (Na^+/K^+ATPase), an electrogenic transmembrane ATPase localized to the basolateral membrane. Because the Na^+/K^+ATPase uses adenosine triphosphate (ATP) to fuel its transport, PTECs require a high ATP content to maintain their activity. PTECs are dense in mitochondria and generate most of their ATP from aerobic respiration and β-oxidation of fatty acids, rather than other less efficient mechanisms such as anaerobic glycolysis. In fact, the oxygen consumption rate and mitochondrial content of the proximal tubule are second to only the heart.[69] As the mitochondria transport of highly reactive electrons, and because accumulation of drugs or other small molecules in PTECs because of their high transport activities can disrupt mitochondrial function and integrity, Unlike most other organs, the kidney cannot alter blood flow (and thus oxygen supply) based on oxygen consumption rate because the blood flow is kept within tight limits to maintain glomerular filtration. Consequently, the proximal tubule is susceptible to hypoxia.[70] Moreover, the proximal tubule is particularly susceptible to drug-induced injury because drugs that target the mitochondria (e.g. gentamycin, cisplatin, polymyxin B) can accumulate within PTECs due to transporter-mediated uptake, resulting in ATP depletion and intolerable oxidative stress (because of mitochondrial generation of reactive oxygen species) that lead to cellular injury and death.[71]

Reabsorption of filtered protein by the proximal tubule is mainly accomplished by the activity of megalin (LRP2), a large endocytic receptor complex expressed on the apical membrane. Megalin is a member of the low-density lipoprotein receptor family, but has an incredibly broad substrate preference that includes lipoproteins, vitamin-binding proteins, albumin, hormones, enzymes, and even drugs such as aminoglycosides.[72] The lack of intact protein in urine indicates that the endocytic activity of the megalin apparatus is quite efficient. The presence of low molecular weight protein in urine (e.g., alpha-1-microglobulin or beta 2-microglobulin) has been postulated to be a marker of proximal tubule dysfunction.[73, 74]

1.4 Microphysiological systems

Microphysiological systems (MPSs) are bioengineered devices that strive to recapitulate certain functional aspects of a given tissue by incorporating tissue-relevant three-dimensional (3D) architecture and biomechanical forces (such as fluid flow). As previously discussed, animal models may have species-specific differences that can hinder accurate extrapolation to humans. Likewise, inaccuracies from the *in vitro* to *in vivo* extrapolation of data produced by conventional 2-dimensional (2D) cell culture may due to issues inherent with 2D cell culture (e.g., a loss or change in transporter or enzyme expression, differing degrees of tight junction formation and replication, loss of polarity, and altered interactions with extracellular environment).[75] These phenotypic changes seen in 2D cells *in vitro* resemble those of dedifferentiated cells *in vivo* after injury.[76] After injury, mature adult cells can contribute to organ repair through dedifferentiation to a proliferation-competent state followed by redifferentiation at the resolution of wound healing.[77-79] As demonstrated above, there are two key concepts about the dedifferentiation of adult cells: 1) it is a normal process that likely aids in tissue resiliency; and 2) it is transient and reversible.[76-79]

Differentiation of pluripotent stem cells and induced pluripotent stem cells has provided the proof-of-concept that the microenvironment can have a major effect on cell status, as stem cells can be directed toward a differentiated state simply by adding growth factors to cell culture medium in a specific order and for specific durations.[80, 81] To promote and maintain a differentiated cell phenotype, MPSs attempt to mimic various microenvironment factors that are present in native tissue environments such as cell-cell and cell-matrix interactions, chemical stimuli, and mechanical and shear stress as described in the next section.

1.4.1 Proximal tubule microphysiological system

The choice of culture environment or culture protocol significantly influences *in vitro* cell phenotype (e.g. hepatic spheroids vs. plated hepatocytes), and that is also true for PTECs.[67] Our group previously developed a proximal tubule microphysiological system (PT-MPS), which is comprised of a Nortis microfluidic chip populated with primary human PTECs. The key components of the Nortis microfluidic device and general scheme for generation of the PT-MPS are depicted in Figure 1.2. The microfluidic device is constructed from polydimethylsiloxane (PDMS) and is encapsulated in a polycarbonate shell. Use of PDMS is advantageous because it is gas permeable, so no special handling of media is required for proper oxygenation. However, care must be taken when working with lipophilic molecules as extensive binding to PDMS could occur. To generate the PT-MPS, the culture chamber is filled with rat tail collagen type I extracellular matrix to generate a scaffold upon which PTECs are seeded.

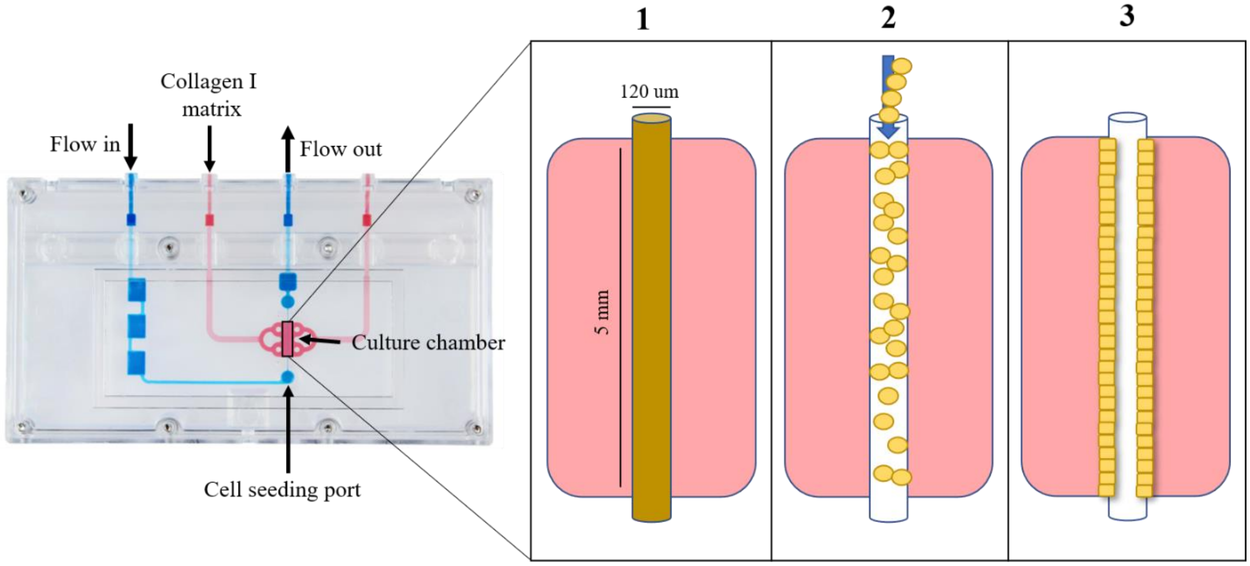

Figure 1.2. Generation of PT-MPS. The Nortis microfluidic device is comprised of a PDMS mold that enables creation of a flow path (blue) through which media and treatments are continuously perfused. The first step is to fill the culture chamber with rat tail type collagen type 1 (pink) to create the matrix scaffold upon which cells will adhere. 1) After the collagen I has polymerized, a glass mandrel that traverses the culture chamber is removed, creating a hollow tubular cavity into which the PTECs are seeded (2). The PTECs adhere within a few hours, then flow is initiated. The PTECs self-assemble into a confluent tubule within a few days (3).

Once the PTECs establish a tubule (Figure 1.3A), the PTECs are polarized and express various proximal marker proteins such as Na^+K^+ATPase (Figure 1.3B). Their low mitotic activity can be inferred from the low expression of Ki67, a proliferation marker (Figure 1.3C). DAPI, or 4’,6-diamidino-2-phenylindole, is a fluorescent molecule that binds strongly to deoxyribonucleic acid (DNA). As such, DAPI is commonly used to label cellular nuclei. While epithelial cell adhesion molecule (EpCAM) is normally localized to distal tubule segments in healthy kidneys *in vivo*, it is upregulated in proximal tubule cells after injury and during hypoxia and is thought to be associated with tubule regeneration.[82] Recently, in a single-cell RNAseq analysis from human kidney samples, EpCAM was found co-expressed with angiotensin I converting enzyme 2 (ACE2), which is specific to the proximal tubule.[83] Nevertheless, the distribution pattern of EpCAM appears to be localized to a membrane, supporting the notion that the cells in the PT-MPS are well polarized (Figure 1.3C).

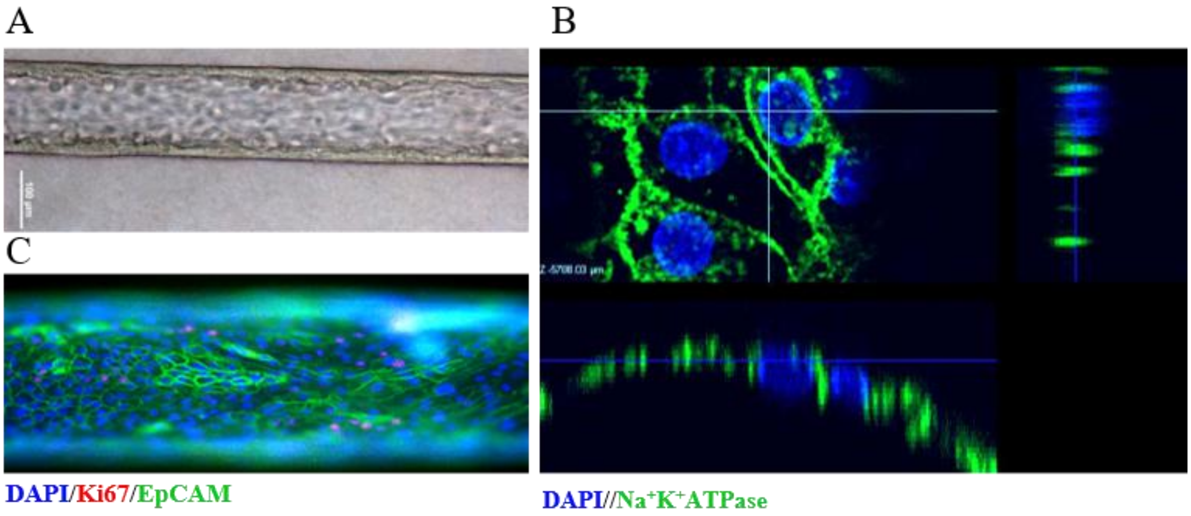

Figure 1.3. Cells in the PT-MPS polarize and express proximal tubule marker proteins. A) Phase contrast image of a tubule 10 days post-seeding shows a confluent tubule. B) Immunocytochemical staining of a PT-MPS tubule for Na$^+$K$^+$ATPase demonstrates high expression and preferential lateral localization. C) Immunocytochemical staining of PT-MPS tubule for Ki67 (red) and EpCAM (green). Few cells express the proliferation marker Ki67, whereas EpCAM appears to be strongly localized to a membrane. Nuclei in B and C were labeled with DAPI (blue). Images in panels A-C were generated from different donors.

In previous work, we demonstrated the ability of cells in the PT-MPS to recapitulate a variety of *in vivo* functions of the proximal tubule including: glutathione reclamation, ammoniagenesis, glucose reabsorption, generation of ATP via oxidative phosphorylation, expression of the proximal marker protein aquaporin-1, and vitamin D bioactivation, and feedback regulation.[84] In addition, PT-MPS tubules displayed transepithelial transport of the OAT substrates, para-aminohippurate (PAH) and indoxyl sulfate, and transport was inhibited by probenecid, an OAT inhibitor.[84] Subsequently, the PT-MPS was used to investigate polymyxin B toxicity, study the interplay between liver metabolism and kidney transport in aristolochic acid nephrotoxicity, explore the mechanisms of ochratoxin bioactivation and nephrotoxicity, model tubular secretion of morphine and its glucuronide, and probe the role of megalin in regulating vitamin D uptake and metabolism.[85-88] As described below, the PT-MPS was used as a tool for drug safety assessment and disease modeling in this dissertation.

1.5 Antisense oligonucleotides

Antisense oligonucleotides (ASOs) are short (12-30 base), single-stranded nucleic acid analogues of ribonucleic acid (RNA) that interact with RNA via Watson-Crick base pairing to modulate target protein expression.[89] Because ASOs target RNA rather than protein, rational design of the base sequence alone can offer a high affinity, specific interaction which expands the number of potential targets. Accordingly, ASOs are being investigated for the treatment of a wide range of indications including: viral infections, cancer, diabetes, high cholesterol, and various rare genetic diseases and use of ASOs in humans is likely to increase in the near future.[89, 90] ASOs are comprised of three core components: the nucleobase, sugar ring, and nucleotide linkage (Figure 1.4). Two of the most common therapeutic ASO chemistries are the phosphorothioate oligonucleotides (PSOs) and phosphorodiamidate morpholino oligonucleotides (PMOs). ASOs require chemical modification because unmodified oligonucleotides such as RNA and DNA are rapidly degraded by endonucleases and exonucleases in serum and tissue.

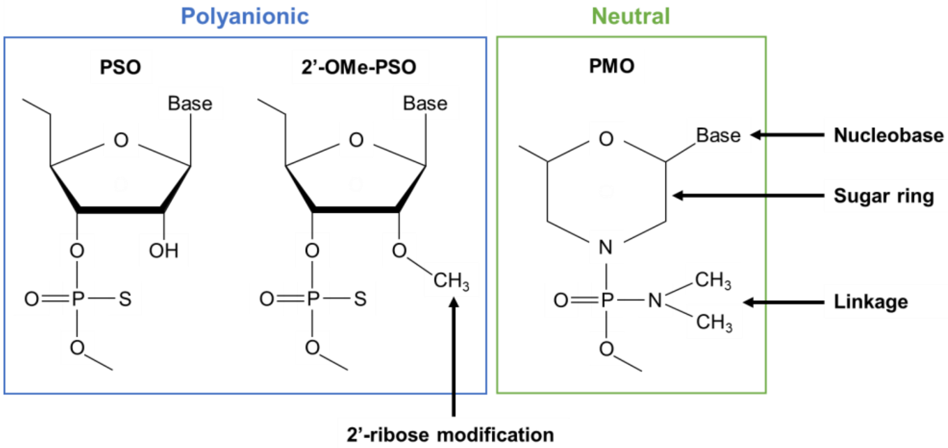

Figure 1.4. Chemical structure of ASOs. Arrows denote the three core components of an ASO and site of 2'-ribose modification (*O*-methyl modification). Phosphorothioate oligonucleotides (PSO) are polyanionic due to the phosphorothioate linkage whereas the phosphorodiamidate morpholino (PMO) is uncharged.

PSOs have sulfur substituted for one of the non-bridging oxygens in the nucleotide linkage and include modifications to some or all of the ribose sugars at the 2' position (e.g., *O*-methyl [OMe], Figure 1.4). Phosphorothioate linkages increase binding to plasma proteins and render the oligonucleotide resistant to degradation by endonucleases, while the 2’-ribose moieties confer resistance to exonucleases and improve binding affinity to RNA.[91, 92] PSOs accumulate extensively in the liver and kidney, but exhibit a broad tissue distribution with sufficient uptake into non-hepatic and non-renal tissue for pharmacologic activity.[93] PMOs contain morpholine rings in place of ribose sugars and a dimethyl amine replaces one of the non-bridging oxygens in the nucleotide linkages (Figure 1.4). PMOs have greater affinity for RNA than unmodified oligonucleotides and are not subject to nuclease-mediated degradation.[94] However, PMOs do not extensively bind to plasma proteins and are rapidly cleared from plasma by renal excretion.[94] The pharmacokinetic parameters of three splice-switching ASOs with different chemistries are summarized in Table 1.1. Drisapersen and nusinersen are fully 2’ modified PSOs. As such they do not possess the ability to recruit ribonuclease H (RNAseH) for cleavage of target RNA, which requires a central unmodified 2’ region for catalytic activity (termed gapmers). Instead, they function as splice-switching oligonucleotides that bind target pre-mRNA near intron-exon boundaries to cause skipping or inclusion of exons. Likewise, PMOs (sometimes referred to as morpholinos) cannot recruit RNAseH and only function as modulators of pre-mRNA splicing or mRNA translation.[89]

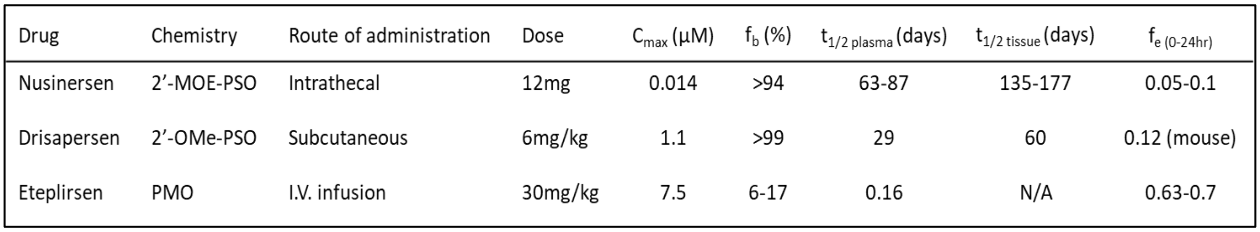

Drug	Chemistry	Route of administration	Dose	C_{max} (µM)	f_b (%)	$t_{1/2\ plasma}$ (days)	$t_{1/2\ tissue}$ (days)	$f_{e\ (0\text{-}24hr)}$
Nusinersen	2’-MOE-PSO	Intrathecal	12mg	0.014	>94	63-87	135-177	0.05-0.1
Drisapersen	2’-OMe-PSO	Subcutaneous	6mg/kg	1.1	>99	29	60	0.12 (mouse)
Eteplirsen	PMO	I.V. infusion	30mg/kg	7.5	6-17	0.16	N/A	0.63-0.7

Table 1.1. Pharmacokinetic parameters from clinical trials of three ASOs. Polyanionic PSOs exhibit drastically different protein binding properties than uncharged PMOs, which explains the difference in apparent plasma half-life and renal excretion in the first 24 hours. The discordance between plasma and tissue half-life is likely due to limits of detection of the quantification assay. Abbreviations: 2’-MOE-PSO, 2’-O-methoxyethyl-PSO; C_{max}, maximal plasma concentration; f_b, fraction of drug bound to protein in plasma; $t_{1/2\ plasma}$, plasma half-life; $t_{1/2\ tissue}$, tissue half-life; $f_{e\ (0\text{-}24hr)}$, fraction of dose excreted in urine in first 24 hours.

PSOs and PMOs display contrasting safety profiles. Oligonucleotides with phosphorothioate backbones can cause dose-limiting toxicities, such as thrombocytopenia, complement activation, and liver and kidney injury.[95-101] Of these adverse events, nephrotoxicity has been the most difficult to model and the mechanism by which these molecules produce renal dysfunction remains unknown. ISIS 388626, a 12-base 2’-O-methoxyethyl-PSO (2’-MOE-PSO) gapmer, and SPC5001, a 14-base 3’-locked nucleic acid-PSO gapmer, had minimal safety concerns in multiple preclinical species, including non-human primates, but caused acute kidney injury in Phase I clinical trials.[97, 101] More recently, two splice-switching PSOs (nusinersen and drisapersen) caused proteinuria in patients enrolled in the clinical trials (Figure 1.5). Nusinersen also caused low serum bicarbonate, which is characteristic of proximal tubular acidosis (NDA209531). Drisapersen also caused increased renal excretion of α_1-microglobulin and kidney injury molecule 1 (KIM-1).[102, 103] α_1-microglobulin is a low molecular weight protein (26 kDa) that freely crosses the glomerulus into the ultrafiltrate then is endocytosed by megalin and cubilin at the proximal tubule. KIM-1 is a transmembrane glycoprotein absent from non-proliferative PTECs but is highly upregulated during acute kidney injury (AKI) and is cleaved proteolytically from the plasma membrane to produce a soluble form that is detectable in urine.[104, 105] Thus, increased renal excretion of α_1-microglobulin and KIM-1, along with low serum bicarbonate, are suggestive of PSO-induced proximal tubular dysfunction.

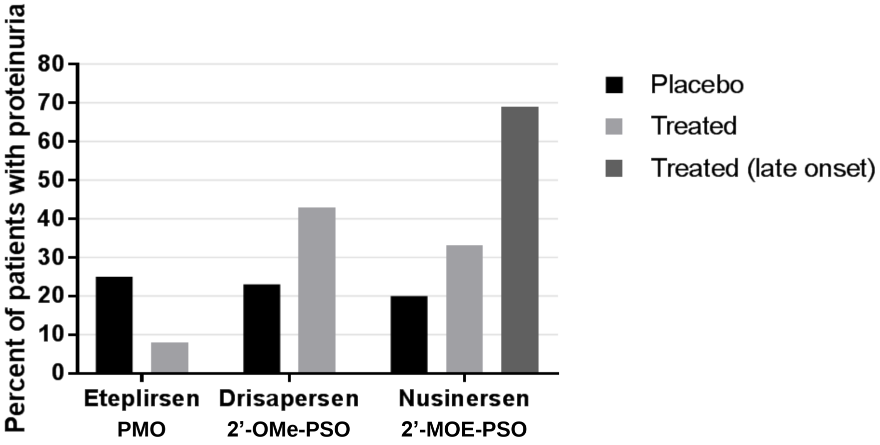

Figure 1.5. Incidence of proteinuria from clinical trials of three ASOs. Eteplirsen placebo (black, n=4), eteplirsen treated 30 mg/kg (light grey, n=114); Drisapersen placebo (black, n=95), drisapersen treated 6 mg/kg (light grey, n=161); nusinersen placebo (black, n=25), nusinersen treated 12mg (light grey, n=51), nusinersen treated late-onset 1-12mg (dark grey, n=52). Data compiled from: Eteplirsen NDA206488. Drisapersen NDA206031. Nusinersen NDA209531.

In contrast to PSOs, PMOs do not exhibit any significant organ toxicities even when administered at high weekly doses (320 mg/kg) to non-human primates for up to 39 weeks.[106] The only notable changes were the formation of basophilic granules and mild cytoplasmic vacuolation in PTECs, which were reversible within 4-8 weeks after cessation of dosing and are thought to reflect accumulation of oligonucleotide rather than an adverse event.[106] Renal tubular basophilia was also observed with administration of PSOs in non-human primates, but at much lower doses (6 mg/kg).[106] Twelve patients were treated weekly (30 mg/kg) with the PMO eteplirsen for 4 years without any apparent treatment-related adverse effects.[107] Together, these data suggest that the chemistry of the oligonucleotide backbone is at least in part responsible for the development of renal injury. We proposed to compare the safety of drisapersen (2'-OMe-PSO) to a PMO using primary human PTECs cultured in a 3-dimensional microfluidic device. Our goals were to better understand the impact of PSO treatment on PTEC function and to identify novel biomarkers of ASO-induced tubular injury.

1.5 Role of proteinuria in kidney disease progression

Chronic kidney disease (CKD) describes a broad range of conditions characterized by a sometimes progressive and irreversible loss of renal function that can result in end-stage kidney disease (ESKD). CKD and ESKD are major health concerns because they decrease quality of life, increase morbidity and mortality, and place a considerable economic burden on the US healthcare system.[108-110] While diabetes and hypertension are the primary risk factors for developing CKD, episodes of acute kidney injury (AKI), especially if severe or recurrent, can increase risk and worsen disease.[111] Vascular rarefaction, tubular atrophy, and interstitial inflammation and fibrosis are the histological hallmarks associated with loss of kidney function in CKD.[112] However, these histological changes occur regardless of the underlying cause of CKD, suggesting that processes independent of the initiating disorder can drive disease progression.[112]

Proteinuria, the appearance of serum proteins into the urine due to a loss of glomerular barrier selectivity, occurs in most forms of CKD and is associated with disease pathogenesis.[112] Proteinuria is a prognostic biomarker for CKD progression and reduction of protein in the urine is associated with favorable clinical outcomes, particularly when baseline proteinuria was >1 gram per day.[113-115] In both humans with glomerular disease (e.g., lupus glomerulonephritis) and animals with experimentally-derived glomerular dysfunction, the degree of proteinuria correlates with the severity of tubular lesions.[116-118] However, rather than being simply correlated, several lines of evidence support a role for a direct action of proteinuria on the pathophysiologcal changes to the proximal tubule. First, when treated *in vitro* with serum proteins such as albumin, transferrin, and immunoglobulin G (IgG), PTECs induce and secrete vasoactive and pro-inflammatory factors.[119-121] Second, the proximal tubules from proteinuric patients exhibit a pro-inflammatory phenotype.[122-124] Lastly, PTECs reabsorb nearly all protein from the glomerular ultrafiltrate via receptor mediated endocytosis (e.g., megalin-cubilin complex). In animal models with experimental proteinuria, knockout of megalin and cubilin protects proximal tubule cells from cellular injury and blunts a pro-inflammatory response.[125, 126] As such, proteinuria is thought to play an important role in the formation of tubular lesions, in part through its action on the proximal tubule.[112]

The proximal tubule is the most active, vascularized, and energy-demanding segment of the nephron.[45] This aspect makes it a vulnerable target for ischemic, obstructive, drug-induced, and immune-mediated injury. After injury, PTECs mount a repair response wherein the cells dedifferentiate to a proliferation-competent state, replicate, then differentiate to regenerate the epithelium.[76, 127, 128] However, during this process a subset of the PTEC pool exhibits certain attributes such as defective fatty acid metabolism, enhanced pro-inflammatory signaling, and aberrant cell cycle arrest, which are maladaptive if the normal epithelium is not restored.[129-131] Importantly, injury to the proximal tubule is sufficient to cause renal inflammation and fibrosis.[132] The signaling pathways and transcription factors that control PTEC phenotype during injury or in states of disease (e.g., proteinuria) are therefore of considerable interest as they represent potential therapeutic targets for slowing CKD progression.

1.6 Vitamin D metabolism and microgravity

The bounds of human physiology are tested aboard the International Space Station (ISS), a modular spacecraft that orbits Earth above its protective atmosphere. Astronauts aboard the ISS face superterrestrial levels of ionizing radiation (IR), disruption of circadian rhythm, and encephalic fluid redistribution.[133, 134] For example, astronaut Scott Kelly received a radiation dose equivalent to 54 years of background exposure on Earth during a 340 day spaceflight on the ISS.[135] IR is particularly dangerous because it creates reactive oxygen species and alters antioxidant-oxidant balance which can promotes cellular and genetic damage.[136] Astronauts commonly exhibit reduced muscle mass, changes to serum chemistry, and bone loss.[137-140] Because many of these physiological changes mirror what happens in age-related disease states on Earth, the microgravity environment has been proposed as a unique stressor that can be harnessed to delineate the cellular and molecular drivers of pathological changes in astronauts to advance the development of strategies to 1) enable long-term spaceflight and 2) better treat disease on Earth.[141-143]

Plasma levels of 1α,25-dihydroxy vitamin D_3 (1α,25$(OH)_2D_3$), the most biologically active form of vitamin D_3, decrease over time in astronauts in space. Astronauts also exhibit impaired intestinal absorption of calcium.[144] As 1α,25$(OH)D_3$ is important for bone homeostasis by promoting calcium absorption in the gut and modulating osteoclast number and activity, and because the kidney is the primary organ responsible for generation of plasma 1α,25$(OH)D_3$ through bioactivation of 25-hidyroxy vitamin D_3 (25$(OH)D_3$) via cytochrome P450 27B1 (CYP27B1), microgravity may promote bone loss in astronauts by decreasing renal production of 1α,25$(OH)D_3$.[47] The kidney also eliminates 25$(OH)D_3$ via cytochrome P450 24A1 (CYP24A1) to 24R,25-dihdroxy vitamin D_3 (24R,25$(OH)_2D_3$) and CYP3A5 to 4β,25-dihydroxy vitamin D_3 (4β,25$(OH)_2D_3$), while 1α,25$(OH)_2D_3$ is eliminated via CYP24A1 to 1α,24, 25-trihydroxy vitamin D_3 (1α,24R,25$(OH)_3D_3$).[47] Furthermore, 1α,25$(OH)_2D_3$ self-regulates vitamin D_3 metabolism through an autocrine mechanism whereby 1α,25$(OH)_2D_3$ activates the vitamin D receptor (VDR) leading to induction of *CYP24A1*, which in turn can increase the clearance of 25$(OH)D_3$ and 1α,25$(OH)_2D_3$. Therefore, microgravity could decrease plasma levels of 1α,25$(OH)_2D_3$ in astronauts by 1) decreasing renal CYP27B1 expression or activity, 2) increasing renal CYP24A1 expression or activity, or 3) increasing renal CYP3A5 expression or activity.

$25(OH)D_3$ is bound almost exclusively to vitamin D binding protein (DBP) in plasma.[47] Delivery of $25(OH)_2D_3$ to the proximal tubule, its site of bioactivation within the kidney, occurs through filtration of $25(OH)_2D_3$ bound to DBP followed by endocytosis via megalin.[145] Therefore, another mechanism by which microgravity could reduce renal formation of $1\alpha,25(OH)_2D_3$ is by altering megalin localization or activity.

To test whether microgravity affects the transcript expression or activity of CYP27B1, CYP24A1, and CYP3A5, we treated cells in the PT-MPS with $25(OH)D_3$ and monitored metabolite formation as well as conducted global transcriptomics via RNAseq. As megalin modulates proteinuria induced tubular injury in animal models, an altered response of PTECs to serum challenge could implicate differential activity or localization of megalin in microgravity.[125, 126] To probe whether megalin and cubilin activity was impacted by microgravity, PTECs were challenged with serum treatment as a model of tubular injury (see Chapter 3 for proteinuria-induced tubular injury).

1.7 Research directions

The main objective of this dissertation was to apply the PT-MPS to drug safety assessment and disease modeling. Novel *in vitro* culture systems are needed to improve *in vitro* to *in vivo* extrapolation, particularly in the context of drug development. Adoption of these new technologies by the pharmaceutical industry will require proof-of-principle examples of their use in those contexts. In Chapter 2, I tested the hypothesis that phosphorothioate chemistry is a major determinant of ASO-induced proximal tubular injury by conducting a safety comparison in PT-MPS of two antisense oligonucleotide backbone chemistries, which have historically lacked a suitable *in vitro* assay for safety assessment. A novel post-transcriptional mechanism driving regulation of CYP3A5 expression is also explored and the potential of antisense oligonucleotides as a therapeutic modality is discussed. In Chapter 3, I addressed the ability of the PT-MPS to model disease, specifically proteinuria-induced tubular injury. The molecular response of PTECs to serum was differentiated from that of albumin, and key transcriptional and epigenomic factors were identified along with a novel potential pathogenic mediator, matrix metalloproteinase 1. Finally, in Chapter 4, I explored the ability of microgravity to act as an accelerator of disease-associated processes. The metabolism of $25(OH)D_3$ in microgravity by PTECs was investigated and demonstrated that the activities and transcript expression of CYP27B1, CYP3A5, and CYP24A1 were unchanged by microgravity. Furthermore, the inducibility of *CYP24A1* was equivalent between normogravity and microgravity. Therefore, the intrinsic ability of PTECs to regulate vitamin D_3 levels was unimpaired by microgravity. Overall, this dissertation supports the use of the PT-MPS as a novel *in vitro* tool that can screen new molecular entities for renal liabilities and investigate the molecular mechanisms driving pathophysiological changes of the proximal tubule during renal disease.

1.7.1 First hypothesis

Phosphorothioate chemistry is a major determinant of ASO-induced proximal tubular injury.

Specific Aim 1a: Compare the toxicity of 2’-OMe-phosphorothioate and phosphorodiamidate morpholino oligonucleotide chemistries toward PTECs by quantifying cell-associated protein, secreted protein, and secreted microRNA biomarkers using immunocytochemistry, ELISA, and qPCR, respectively.

Specific Aim 1b: Identify global transcriptomic changes in cells in PT-MPS by RNAseq after exposure to a 2’-OMe-phosphorothioate oligonucleotide or a phosphorodiamidate morpholino oligonucleotide.

1.7.2 Second hypothesis

Serum will induce a secretory phenotype in PTECs.

Specific Aim 2a: Measure cell-associated and secreted markers of proliferation, injury, and inflammation from cells in PT-MPS treated with serum and albumin.

Specific Aim2b: Conduct RNAseq on serum and albumin treated cells in PT-MPS to identify affected transcriptional programs.

Specific Aim2c: Perform ATAQseq on native and cultured PTECs to identify serum-induced epigenomic signatures.

1.7.3 Third hypothesis

A microgravity environment will modulate PTEC response to serum and $25OHD_{3.}$

Specific Aim3a: Measure secreted markers of proliferation, injury, and inflammation in from cells in PT-MPS treated with serum or $25OHD_3$ in microgravity and normogravity.

Specific Aim3b: Assess the effect of microgravity on metabolism of $25OHD_3$ in PT-MPS by quantifying $25OHD_{3,}$ $1\alpha,25(OH)_2D_3$, $4\beta,25(OH)_2D_3$, and $24R,25(OH)_2D_3$ from device effluents.

Specific Aim3c: Characterize the effects of serum and $25OHD_3$ on PTEC transcriptome in microgravity and normogravity using RNAseq.

2. Antisense Oligonucleotide Development for the Selective Modulation of CYP3A5 in Renal Disease

Portions of this chapter were accepted for publication in Scientific Reports in February 2021

Co-first authorship was shared with Andrew J. Annalora

2.1 Abstract

Cytochrome P450 3A5 (CYP3A5) is the primary CYP3A subfamily enzyme expressed in the human kidney and its expression may contribute to a broad spectrum of renal disorders. Pharmacogenetic studies have reported inconsistent linkages between *CYP3A5* genotype and hypertension, however, most investigators have considered *CYP3A5*1* as active and *CYP3A5*3* as nonfunctional. Observations of gender specific differences in CYP3A5 expression in *CYP3A5*3/*3* carriers suggests additional complexity in gene regulation that may underpin an environmentally responsive role for CYP3A5 in renal function. The focus of this work is to reconcile the molecular mechanism driving conditional restoration of functional CYP3A5 from alternatively spliced *CYP3A5*3* transcripts, and validate an antisense oligonucleotide-based approach for selectively suppressing renal CYP3A5 expression. Phosphorodiamidate morpholino oligonucleotides (morpholinos) targeting a cryptic splice acceptor created by the *CYP3A5*3* variant in intron 3 rescued functional CYP3A5 expression *in vitro*, and salt-sensitive cellular mechanisms regulating splicing and conditional expression of *CYP3A5*3* transcripts are reported. The potential for a G-quadruplex (G4) in intron 3 to mediate restored splicing to exon 4 in CYP3A5*3 transcripts was also investigated. Finally, a proximal tubule microphysiological system (PT-MPS) was used to evaluate the safety profile of morpholinos in proximal tubule epithelial cells, highlighting the potential of morpholinos as a therapeutic platform for the treatment of renal disease.

2.2 Introduction

Cytochrome P450 3A5 (CYP3A5) is a heme-thiolate monooxygenase that oxidizes a variety of xenobiotics such as cyclosporine A and tracrolimus and steroid hormones including cortisol and corticosterone.[146, 147] CYP3A5 is the only CYP3A isoform expressed in the human kidney but genetic variants can affect its expression level and activity.[147-149] Specifically, the *CYP3A5*1* allele encodes a full-length, functional enzyme, while the *CYP3A5*3* allele contains a single nucleotide polymorphism (6896G>A) in intron 3, generating a cryptic splice acceptor and nonsense mediated decay (NMD) of the aberrant messenger RNA (mRNA).[150, 151] Genetic variation in CYP3A5 expression contributes to interindividual differences in intrarenal disposition of drugs like cyclosporine and is postulated to modulate blood pressure, due to the ability of CYP3A5 to form and eliminate glucocorticoid receptor (GR) and mineralocorticoid receptor (MR) substrates that influence sodium retention.[48, 152-154] Cyp3A expression and activity are consistently correlated with blood pressure in animal models of hypertension.[152, 155-157] However, attempts to establish a link between *CYP3A5* genotype and hypertension in humans have yielded inconsistent results.[158-163] The allele linkage may be complicated by the fact that *CYP3A5*3/*3* individuals can sometimes express functional CYP3A5, albeit at levels 5.6 fold lower than heterozygotes at the mRNA level.[149, 151] While it has been shown that a certain portion of *CYP3A5*3* pre-mRNA transcripts are properly spliced to wild-type, the cellular mechanisms and environmental factors regulating *CYP3A5*3* pre-mRNA splicing remain unclear.[164]

Alternative pre-mRNA splicing occurs in all multi-exon human genes and provides functional expansion of the proteome.[165, 166] For the human cytochrome P450 (CYP) family of 57 genes, alternative splicing results in nearly 1000 unique mRNA transcripts, and may represent an adaptive mechanism to chemical exposure.[167] Recently, it was reported that polyguanine sequences are overrepresented in RNA near splice sites where they can form G-quadruplex (G4)-RNA structures capable of altering pre-mRNA splicing patterns.[168] G4 structures observed in both intronic and exonic regions can act as either splice enhancers or splice silencers.[169-175] G4 RNA formation is strongly influenced by flanking nucleic acid sequence, and the local concentrations of RNA binding proteins and both monovalent and divalent cations.[176] Potassium (K^+) is maintained at levels above 100 mM in many cell types, and it is assumed to be the primary driver of G4 assembly *in vivo*.[177, 178] Alternative cations, including sodium (Na^+), are known to stabilize different G4 structures *in vitro*, while lithium (Li^+) can be a G4 destabilizing agent.[176-179] Cations could also impact *CYP3A5* expression via altering tonicity, as a tonicity-responsive enhancer element located in intron 2 of the *CYP3A7* is known to regulate CYP3A family gene expression.[180] We hypothesize that functional CYP3A5 expression is restored by cation-dependent alternative splicing of *CYP3A5*3* pre-mRNA.

Because some MR ligands generated by CYP3A5 promote sodium retention, renal CYP3A5 inhibition strategies may be appropriate for treating hypertension. However, most small molecule inhibitors of CYP3A5 also tend to inhibit CYP3A4, creating the potential for drug-drug interactions.[181, 182] Alternatively, CYP3A5 expression could be modulated using ASOs, which are molecules that interact with target RNA via Watson-Crick base pairing to modify target protein expression through a variety of mechanisms, including splice-switching.[89, 183]

Therapeutic ASOs are analogues of RNA, with phosphorodiamidate morpholino oligomers (PMOs) and phosphorothioate oligomers (PSOs) the two ASO chemistries most used for splice-switching applications. PSOs have phosphorothioate nucleic acid linkages with fully or partially (in the case of gapmers) substituted ribose rings at the 2’ position of various chemistry (e.g. O-methyl, OMe; O-methoxyethyl, MOE), while PMOs have phosphorodiamidate linkages and morpholine rings. These chemical modifications affect several properties including protein binding, affinity for RNA, metabolic and renal clearance, and are required to achieve a pharmacologically-relevant resident time in target tissue.[91, 93, 94] PMOs and PSOs of various 2’-ribose chemistries are primarily eliminated by renal excretion, but they also accumulate in PTECs, which can cause tubular degeneration and regeneration once the ASO surpasses a molecule-specific concentration threshold.[184, 185] Tubular degeneration and regeneration is observed at lower doses for PSOs than PMOs and can be accompanied by increases in biomarkers of acute kidney injury (AKI) such as serum creatinine and urinary kidney injury molecule 1 (KIM-1). In addition, proteinuria is observed more often in humans after treatment with PSOs than

PMOs, though PSO-mediated proteinuria may represent competitive inhibition of an uptake process rather than overt tubular injury.[102, 186-190] Therefore, targeting renal *CYP3A5* transcripts with ASOs is not without risk as nephrotoxicity is a safety liability for this class of molecules in humans, although it may be chemistry-dependent and is usually mild and reversible.[106, 191, 192]

Screening strategies to select candidate ASOs with favorable safety profiles include *in silico* optimization of base sequence to maximize specificity and reduce off-target hybridization events as well as conventional toxicology studies in animals. However, ASO-induced toxicity can be sequence-dependent, making safety characterization of candidate molecules difficult.[193, 194] Several phosphorothioate-containing ASOs were well-tolerated in preclinical species but caused AKI in first-in-human trials.[97, 101, 195, 196] The mechanism by which ASOs cause renal injury remains largely unknown. Consequently, human-relevant *in vitro* cell culture models that can discriminate between safe and toxic ASOs as well as better describe and identify the molecular mechanisms of ASO-induced toxicity are needed. We developed a fluidic microphysiological system (MPS) populated with primary human PTECs that demonstrates many of the biochemical, synthetic, and transport activities of the proximal tubule.[84, 197] PTECs within this MPS (PT-MPS) have promise in safety screening applications because they manifest physiological injury responses that discriminate between structurally similar compounds of differing toxicity.[86, 198] Culture of PTECs within the MPS enables biologically relevant cell-cell and cell-matrix interactions as well as application of shear stress, all of which are microenvironment factors that improve cell phenotypes over conventional 2D cultures.[86, 199-202]

We leverage this MPS technology to compare the safety profile of a PMO to a 2’-OMe-PSO by quantifying cell-associated and secreted biomarkers as well as performing global transcriptomic analyses with RNAseq. Hemeoxygenase-1 (HO-1) was chosen as a cell-associated biomarker because it is strongly induced in PTECs after exposure to nephrotoxic compounds, including those that promote generation of reactive oxygen species.[198] KIM-1 was chosen as a secreted biomarker because it is a widely-accepted urinary biomarker of PTEC injury.[104] KIM-1 outperforms traditional markers of renal function such as serum creatinine and blood urea nitrogen in early detection of injury.[203] A panel of miRNAs that are associated with various renal disease pathologies or injury were also screened as potential biomarkers of ASO induced injury.[204, 205]

Here, we tested the hypothesis that a dynamic G4-motif located near the *CYP3A5*3* SNP site regulates the cryptic, mutant splice acceptor in intron 3, conditionally shifting spliceosome recognition back to the wild-type exon 4 splice acceptor. These studies were performed using *CYP3A5*3/*3* genotyped HEK293 cell line, and ASOs targeting the cryptic splice acceptor site (*6986A>G*; *rs776746*) or a putative G4 motif in intron 3. We previously showed the utility of using ASO interference to alter spliceosome function by targeting an exon splice-acceptor site in the *c-myc* transcript.[206] This strategy has been used to restore the reading frame in mutant forms of *dystrophin*, create a ligand independent *CTLA-4* splice variant, and modulate immune responses to Ebolavirus.[207-212] The current studies utilized synthetic oligomers to confirm the role of the *CYP3A5*3* SNP and a putative, intron 3 G-quadruplex in enhancing the exon 4 splice-acceptor in *CYP3A5*3/*3*, which leads to restoration of functional enzyme expression under high salt conditions.

2.3 Materials and Methods

2.3.1 Reagents

DMEM (Dulbecco's Modified Eagle Medium) and additives were obtained from Sigma (St. Louis, MO). Fetal Bovine Serum was obtained from Atlanta Biologics (Flowery Branch, GA). TMPyP4 (sc-204346) was obtained from Santa Cruz Biotech (Dallas, TX). Gentest™ 7-benzyloxy-4-[trifluoromethyl]-coumarin (BFC; #451730) and 7-hydroxy-4-[trifluoromethyl]-coumarin (HFC; #451731) were obtained from Corning (Corning, NY). Cortisol (H-0888) and 6β-hydroxycortisol (H-6904) were obtained from Sigma (St. Louis, MO). Human embryonic kidney proximal tubule epithelial cells (HEK293), and African green monkey kidney cells (CV-1), were purchased from ATCC.org (Manassas, VA). Molecular Weight Marker was obtained from Wester Sure (LI-COR #926-98000).

2.3.2 Cell Culture

HEK293 and CV-1 cells were grown DMEM media plus 10% fetal bovine serum and 2 mM L-Glutamine (Corning; #25-005-CI) supplemented with 1X Pen-Strep (Gibco; #15140-122). Sanger DNA sequencing was used to validate the proper sequence of *CYP3A5* gene in both cell lines (CGRB services, Oregon State University). Experimental and Scrambled Control PMOs used in cell culture experiments (0.1 – 5 mM) were prepared in maintenance media and administered using passive uptake.

Primary human PTECs were sourced from kidney tissue obtained from patient nephrectomies at the University of Washington Medical Center in collaboration with Northwest BioTrust, as described previously.[84] Human PTECs were isolated in accordance with a protocol approved by the University of Washington Human Subjects Institutional Review Board (IRB STUDY00001297).[84] Cells were maintained as described previously with the exception of donor 2, which was maintained in DMEM/F12 no glucose (US Biological, D9807-02) supplemented with 5 mM glucose (Sigma, G7528), 14.3 mM sodium bicarbonate (Sigma, S6297), insulin-transferrin-selenium (ITS; Sigma, I-1884-1VL), 25 ng/mL prostaglandin E1 (Sigma, P5515), 25 ng/mL hydrocortisone (Sigma, H-0135), 3.5 ug/mL ascorbic acid (Sigma, A-4544), 3.652 ng/mL sodium selenite (Sigma, S-9133), 5 pM triiodo thyronine (Sigma, T-5516), 10 ng/mL rhEGF (R&D Systems, 236-EG-200), and antibiotic-antimycotic (Gibco, 15240062). See Supplemental Table 2.1 for donor demographics.

2.3.3 Nucleic Acid and Antisense Oligomer Synthesis

The eight antisense oligomers used in this study and their targets are listed in **Table 2.1** along with their anticipated biological significance. The oligomers were synthesized as phosphorodiamidate morpholino oligomers (PMOs or morpholinos) by Gene-Tools, LLC (http://www.gene-tools.com/history_production_and _properties#preparation) as described by Summerton and Weller.[109] Every PMO generated by Gene-Tools was accompanied by an oligomer properties specification sheet and a spectral analysis of the product to demonstrate removal of impurities (synthesis resin, ammonia, cleaved base-protective groups, and minor amounts of short truncation fragments) by selective precipitation. The five DNA oligomer sequences used in gel mobility studies are listed in **Table 2.2**. DNA and RNA oligomers were purchased from Integrated DNA Technologies.

2.3.4 Nucleic Acid Gel Mobility Shift Assay

Nucleic acid mobility shift assays were performed using the method of Nambiar et al.[213] Oligomers, including HOX11 C strand were incubated in 10 to 100 mM KCl in Tris-EDTA buffer pH 8.0 at 37°C for 1 hour. The different G4 structures were resolved on 12% native polyacrylamide gels in the presence of 10 mM KCl in both gel and the running buffer, at 150V at 4°C. The gels were stained with ethidium bromide and photographed on a UV-transilluminator.

2.3.5 RNA Isolation and PCR Analysis

Total RNA was isolated from HEK293 or CV-1 cells using the QIAshredder (Qiagen; #79654) and RNeasy Mini Kit (Qiagen; #74104). RNA was treated with Dnase I (New England Biolabs; 1 U/ µg RNA; 30 minutes at 37°C; 5 minutes at 75°C) to remove genomic DNA prior to reverse transcription of mRNA to cDNA using the iScript cDNA synthesis kit (Bio Rad; #170-8890). Endpoint PCR was performed using the Platinum Taq High Fidelity DNA Polymerase kit (Invitrogen; #11304-011) using the manufacturer's recommended protocol with minor modifications. Optimal annealing temperatures for the *CYP3A5* primer sets were determined empirically, between 50-55°C for 30 seconds. PCR products were visualized on 1% UltraPure Agarose gels (Invitrogen; #15510-027) prepared in 1X tris/borate/EDTA (TBE) buffer and stained with Ethidium Bromide Solution (Calbiochem; #4410). Exon 4 inclusion in *CYP3A5* mRNA transcripts was monitored using the following primer sets: hCYP3A5_dex4_FP1: 5'-GGA AAC CTG GCT TCT CCT G-3' and hCYP3A5_dex4_RP1: 5'-TGA CAG GCT TGC CTT TCT CT-3'. All primers were purchased from IDTDNA.com (Coralville, IA).

qRT-PCR analysis was performed using the iQ SYBR Green Supermix (BioRad; #170-8880) using the ABI PRISM® 7500 FAST Sequence Detection System (Applied Biosystems; 2-hour run protocol; 96-well plate) using the manufacturer's recommended settings for SYBR Green qPCR analysis. Assays were performed in technical quadruplicates using pre-validated, Primetime™ qPCR primer set assays from for human target genes: *CYP3A4* (Hs.PT.58.19392980); *CYP3A5* (Hs.PT.58.41063109), *18S RNA* (Hs.PT.39a.22214856.g) and beta-actin (*ACTB*)(Hs.PT.39a.22214847), obtained from Integrated DNA Technologies (Coralville, IA). Template (10-25 ng) and primer concentrations (0.5-1X Primetime mix) were optimized for each primer set to eliminate primer dimer formation in final experimental conditions. Results of four replicate biological samples were quantified using the $2^{-\Delta\Delta CT}$ method and relative fold-changes were normalized to the relative expression of 18S RNA in each sample.[214] Standard deviation (SD) was calculated using replicate delta CT values as described.[180]

2.3.6 Western Immunoblotting

Total protein was extracted from HEK293 and CV-1 cell lines using the RIPA Buffer Lysis System (Santa Cruz Biotech; #sc-24948). Fresh RIPA buffer was prepared just prior to extraction and supplemented with protease inhibitors (Complete Mini; Roche; #11777500; 1 tablet/10 mL RIPA buffer). After removing cell culture media, cells were washed with 1x PBS and removed from plates with a rubber policeman in 1 mL of cold 1X PBS. Cells were pelleted at 1500 x g for 5 minutes. Pellets were re-suspended in 0.75 mL of fresh RIPA buffer and incubated on ice for 30 minutes with intermittent vortexing. Supernatant was separated from cell debris via centrifugation at 14,000 x g for 15 minutes at 4°C. Samples were frozen at -80°C or prepared for Western Blot analysis immediately via suspension into 4X Laemmli Sample Buffer (BioRad; #161-0747) supplemented with 400 mM β-mercaptoethanol (Sigma; #M6250). Western blot analysis was completed using the BioRad Mini-PROTEAN Electrophoresis System (Hercules, CA). Standard manufacturer settings and protocols were used for blotting with a minor modification to sample preparation procedures that included the storage of proteins in fresh 1X Laemmli Sample buffer at 4°C overnight prior to boiling to facilitate denaturation of hydrophobic target proteins. Monoclonal antibodies for human CYP3A5 (F18 P3 B6) were obtained from ThermoFisher Scientific (Waltham, MA; Cat# MA3-033; RRID:AB_2090513)[215] and used at 1-2 µg/mL. Monoclonal antibodies for CYP3A4 (HL3) were obtained from Santa Cruz Biotechnology, Inc. (Dallas, TX; Cat# sc-53850; RRID:AB_782375)[216] and used at dilutions between 1:100 and 1:200. Monoclonal antibodies for the housekeeping gene GAPDH (G-9) were obtained from Santa Cruz Biotechnology, Inc. (Dallas, TX; Cat# sc-365062; RRID:AB_10847862) and were used at a dilution of 1:100. Total and variant CYP3A5 protein expression was determined semi-quantitatively using grayscale, densiometric analysis in ImageJ.[111] Original uncropped images for blots shown in Figure 2.4a are presented in Supplemental Fig. 2.4. The blot membrane was first probed with monoclonal antibodies for GAPDH, and then stripped with Restore Plus Western Blot Stripping Buffer; ThermoScientific #46430 before labeling CYP3A5.

2.3.7 CYP3A5 Enzyme Activity Assays

CYP3A activity was evaluated by a fluorometric assay that monitors the conversion of BFC to HFC as previously described with slight modification.[217, 218] Briefly, HEK293 cells were grown in 35 mm dishes in media supplemented with 1 nM cortisol. HEK293 cells were incubated with 100 µM BFC for 3 hours at 37°C. Conversion of BFC into HFC was monitored using an excitation wavelength of 409 nm and emission wavelength of 530 nm. Fluorescent signal was normalized to total protein measured by a BCA assay (ThermoFisher, 23227).

An LC-MS/MS method was developed for simultaneous evaluation of cortisol (CORT) and 6β-hydroxycortisol (6βOH) levels on an MDS Sciex 4000 Q TRAP LC-MS/MS System (Applied Biosystems). CORT (*m/z* 363 → 121) and 6βOH (*m/z* 379.3 → 343.1) fragments were monitored and standard curves were prepared for each fragment. 2 mL of control and 12 mM KCl-treated cell culture supertants (N=4) were extracted in 4 mL methylene chloride, dried under nitrogen gas, then resuspended in 10% methanol for LC/MS analysis. Targeted LC-MS/MS analysis was conducted using a Poroshell

120 EC-C18 column (Agilent; 2.1x50 mm, 2.7 µm) and a standard water:ethanol gradient (10-95%) containing 5% formic acid. Standard curves (n=3) for quantifying fragment ion peaks are shown in Supplemental Fig. 2.5.

2.3.8 Mineralocorticoid Receptor Activity

The hypothesis that CYP3A5 activity will transform glucocorticoids, cortisol, and corticosterone, into 6β-hydroxy metabolites gaining mineralocorticoid activity was evaluated using the Human MR Reporter Assay System (#IB00501-32) from Indigo Biosciences (State Park, PA). The media from cells incubated in control media and media supplemented with 12 mM KCl (24 hrs; N=4) were added to the Human MR Reporter Assay System and MR transactivation was detected via quantification of luminescence from a luciferase reporter as described in the manufacturer's protocol.

2.3.9 CYP3A5 Oligonucleotide Treatment in PTEC Cells

PTECs (passage number: 2-4) were seeded into uncoated 24-well plates at 50,000 cells/well and allowed to recover for 24 hours before treatment with 1 µM PMO in maintenance media for 6 days. Fresh treatment media was added after 72 hours. On the 7th day, the cells were co-treated with 1 µM PMO and 1 µM midazolam (Sigma, M-908) for 24 hours. Biological triplicates were used for all donors and treatments, except for treatment of Donor 3 with 10 µM 3A5*3 PMO, in which case biological duplicates were used.

2.3.10 Midazolam Extraction and Quantification

At the end of treatment, the supernatant was collected, and the wells were washed with 500 µL methanol containing 40 ng/mL 1'-hydroxy-midazolam-d4 (1'-OH-MDZ-d4) (Sigma, H-921) followed by another 500 µL methanol wash and addition of 1 mL methanol to each supernatant tube. The supernatant samples were stored at -80°C until extraction. Standard calibration curves were prepared fresh daily by spiking 1’-OH-midazolam (0.025-3.2 ng; Sigma, H-902) and 1’-OH-MDZ-d4 (20 ng) into PTEC maintenance media. The amount of 1’-OH-MDZ produced by PTECs was quantified by LC/MS-MS as described previously with minor modifications.[219] Briefly, the extracts were reconstituted in a 50:50 mixture of water:methanol and analytes were separated using the following gradient: solvent A (0.1% formic acid in water) and solvent B (100% methanol) starting at 50% for the first minute, solvent B increasing linearly to 90% from 1-3 min, held at 90% until 6 min, then returning to 50% from 6.1-10 min at a flow rate of 0.25 mL/min.

2.3.11 Generation and Treatment of PT-MPS

Microfluidic devices were purchased from Nortis Biotechnology (Woodinville, WA) and PTEC tubules were generated as reported previously.[84, 86] All tubules were allowed to culture for 5-7 days before initiating treatment. Oligonucleotide stocks were prepared at 1 mM in water and stored at room temperature. Working solutions were prepared in PTEC maintenance media. All treatments were administered to devices via syringe-pump-driven perfusion (KD Scientific Inc., model KDS220) at a flow rate of 0.5 µL/min.

2.3.12 HO-1 Immunocytochemistry and Quantification

Procedures were performed at room temperature and solutions were perfused through the devices at a flow rate of 10 µL/min. The tubules were fixed with 10% phosphate buffered formalin (Fisher, SF100-4) for 30 minutes, followed by a wash with DPBS (ThermoFisher, 14040133) for 60 minutes. The devices were stored at 4°C until further processing. To label HO-1, the tubules were blocked and permeabilized with DPBS containing 5% bovine serum albumin (BSA) and 0.1% Triton X-100 for 2 hours. Rabbit monoclonal anti HO-1 primary antibody (Abcam, ab52947) was diluted 1:100 in DPBS containing 5% BSA and the device was perfused for 1 hour, followed by a wash with DPBS containing 0.05% Tween-20 for 2 hours. Goat anti rabbit secondary (Fisher, A11037) was diluted 1:1000 in DPBS with 5%BSA and the device was perfused for 1 hour followed by a 2-hour wash with DPBS with 0.05% Tween-20. Nuclei were labeled with DAPI and imaged on a Nikon Eclipse Ti-S microscope. The fluorescence intensity of HO-1 labeling was quantified using ImageJ software.

2.3.13 KIM-1 ELISA and Chemiluminescent Assay

Levels of KIM-1 protein were quantified from 50 µL or 100 µL of device effluent according to the manufacturer's instructions using a chemiluminescent assay (Meso Scale Discovery, K151JHD-2) or ELISA (R&D Systems, DY1750B). Each sample was assayed in technical duplicates and every treatment was performed in at least biological triplicates.

2.3.14 miRNA Analysis

Effluent was collected over 44 hours and 200 µL was used for qPCR analysis as previously described.[86] Samples were assayed in technical duplicates and each treatment had at least biological triplicates.

2.3.15 RNA Extraction and Sequencing

PTECs were harvested from devices by injecting 100 µL of detergent (Abcam, part 8206000) into the injection port using a 1mL slip-tip syringe (BD, 309659) equipped with a 22-gauge needle (BD, 305142). Cell lysate was collected into 900 µL Trizol and frozen at -80°C until extraction. RNA was isolated using a RNeasy Micro Kit (Qiagen, 74004) and the RNA library was prepared and sequenced as described previously.[86] Aligned data were read into R and summarized as counts per gene using the Bioconductor TxDb.Hsapiens.UCSC.hg38.knownGene package in concert with the GenomicAlignments package (version 3.4.0).

2.3.16 Statistical Analysis

Data are expressed as mean and standard deviation for replicate samples (at least three per treatment group). Statistical analyses were performed using GraphPad Student's two-tailed t-test and ANOVA with Tukey-Kramer multiple comparisons test. Differences were considered significant at $p < 0.05$. Statistical analyses for HO-1, KIM-1 and miRNA were carried out in R (version 4.0.0) using the lm function, and the ANOVA function from the car package was used to perform a two-way or three-way ANOVA (Type-III sums of squares). The glht function from the multcomp (version 1.4) package was used for the Tukey's multiple testing comparisons.

Statistical analysis for global transcriptomics was carried out using R (version 3.4.0). Before fitting any models, we excluded any genes that were expressed at consistently low levels across all samples. Prior to filtering, we had 25,221 genes and after filtering, we had 13,779 genes. We performed a trimmed mean of M-values (TMM) normalization.[220] To test the treatment difference, we used a GLM framework with quasi-likelihood method in edgeR package (v3.18.1).[221] Rather than using a post-hoc fold change filtering criterion, we used the glmTreat function from edgeR, which is analogous to the t-tests relative to a threshold (TREAT) approach.[222] We selected genes based on a threshold of 1.1-fold change and a false discovery rate of 10%.

Microsoft Excel and GraphPad Prism were used for statistical evaluation of PCR data, and statistical comparisons were made using the Student's t-test between individual delta CT replicates. Statistical significance was considered at p-values < 0.05.

2.4 Results

2.4.1 Role of *CYP3A5*3* SNP in transcript splicing and rescue of CYP3A5 protein activity with a phosphorodiamidate morpholino oligonucleotide

The *CYP3A5*3* variant (rs776746) is found within intron 3 of the human gene (Fig. 2.1a). The adenine nucleobase (*6986A>G*) altered by this mutation is highly conserved in non-human primates

(Supplemental Figure. 2.1a), and the resulting polymorphism (*3-SNP) creates a pseudo-exon with a splice acceptor site in intron 3, with an intron/exon sequence (CAG/TA), that can compete with the reference sequence (CAG/AA) at the authentic exon 4 splice acceptor site (Fig. 2.1a). In addition, a U2 snRNP branch point sequence (AAAGAG) found upstream from the *3-SNP, resembles the reference branch point (AATCAG) near the exon 4 splice acceptor. Incorrect splicing of exon 4 at the *3-SNP site creates a pseudo-exon with a termination codon, located upstream of the exon 4 splice acceptor site, capable of triggering NMD and loss of the *CYP3A5* mRNA. To validate the role of the 6896A>G polymorphism in creating the cryptic splice acceptor site in intron 3, an antisense oligonucleotide designed to bind to the SNP site was prepared, 3A5*3 PMO (Table 2.1). To clarify the role of the *3-SNP in promoting NMD of mature transcripts, we explored splicing of *CYP3A5* pre-mRNA in the HEK293 cell line, which was verified to be homozygous *CYP3A5*3/*3* by DNA sequencing (Supplemental Figure. 2.1b). Incubation of HEK293 cells with the 3A5*3 PMO (1 µM; 48 hours), which masks the cryptic splice acceptor, led to increased levels of *CYP3A5* mRNA as revealed by both endpoint PCR (Fig. 2.1b) and quantitative (qRT) PCR (Fig. 2.1c). Functional restoration of CYP3A5 protein activity with the 3A5*3 PMO but not the (AUG) start site inhibitor, a PMO designed to block translation of all genotypes (Table 2.1), was confirmed in *CYP3A5*3/*3 primary human PTECs using a midazolam metabolism assay (Fig. 2.1d). Efficiency of restoration of CYP3A5 activity by the 3A5*3 PMO was donor-dependent (Donor 3; See Supplemental Table 2.1), and was not related to cellular toxicity, as PMO treatments did not alter normal PTEC morphology (see Supplemental Figure. 2.6).

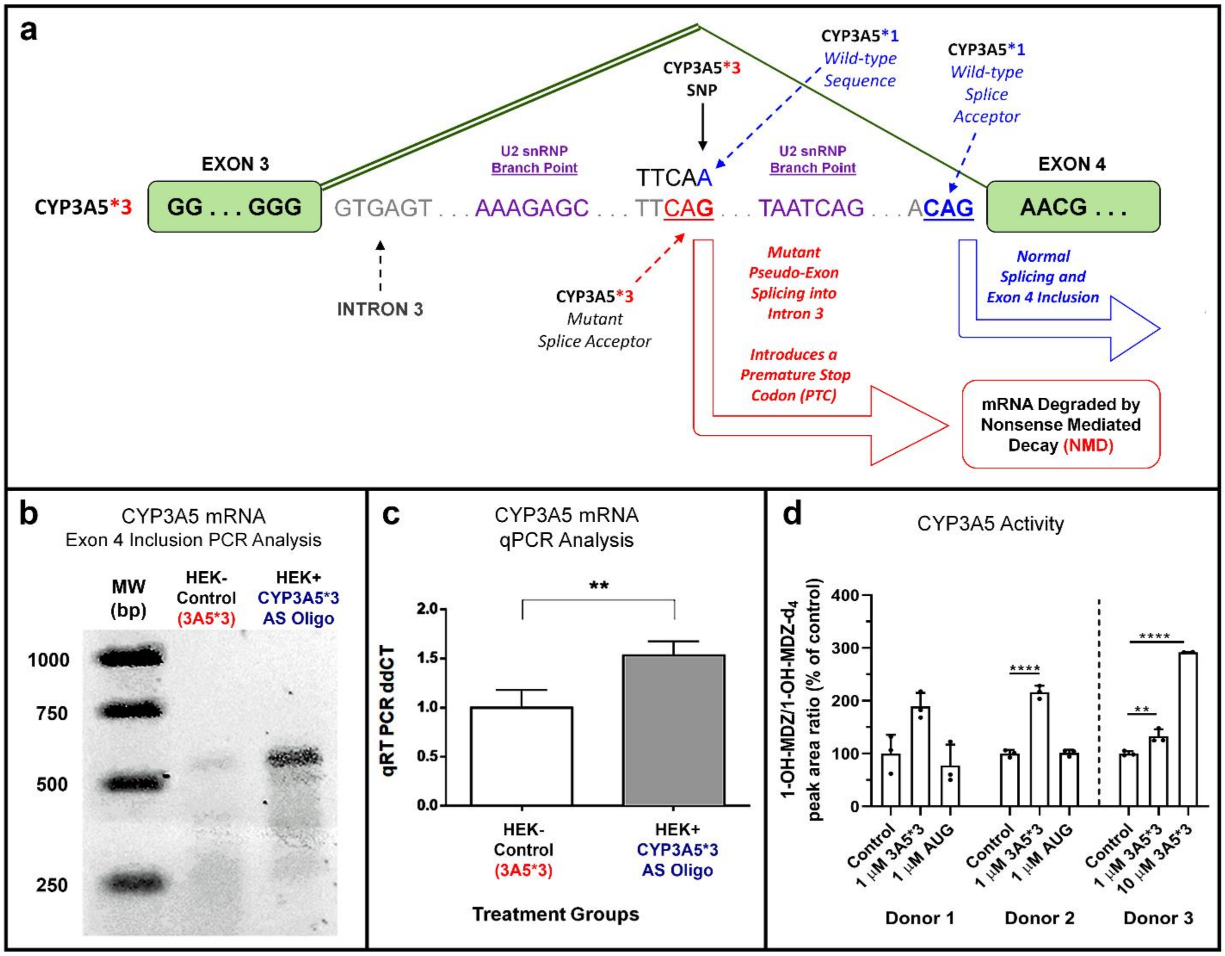

Figure 2.1. The *CYP3A5*3* SNP regulates gene splicing and can be modulated with ASO in renal cell culture models. a) Schematic for the *CYP3A5*3/*3* polymorphism found in HEK293 cells. The *CYP3A5*3*-SNP creates a cryptic splice acceptor within intron 3 that results in the aberrant splicing of a pseudo-exon containing a premature termination codon (PTC) that targets the mRNA transcript for degradation by nonsense mediated decay (NMD). Both the cryptic splice acceptor (CAG/TA) and the exon 4 splice acceptor (CAG/AA) are preceded by canonical U2 snRNP branch point cis-acting elements. b) Endpoint PCR results monitoring exon 4 inclusion in mature *CYP3A5* mRNA transcripts demonstrate the role of the **3*-SNP in altering splicing and transcript stability. Wild-type *CYP3A5* mRNA transcripts encoding exon 4 are virtually undetectable (no band) in HEK293 cell lysates under normal conditions, however when the **3*-SNP site is masked by interactions with an antisense oligomer (3A5*3 PMO; 3 µM; 48 hours), transcript stability is restored, leading to enhanced detection of exon 4 inclusion via endpoint PCR. c) Quantitative PCR (qRT-PCR; SYBR green) results demonstrating a 1.5-fold increase in total *CYP3A5* mRNA when HEK293 cells were treated with the 3A5*3 PMO (1 µM; 48 hours). d) Quantification of the formation of 1’-OH-midazolam from midazolam by LC/MS/MS after treatment with either 3A5*3 PMO or AUG PMO for 6 days in primary human PTECs. CYP3A5 activity was increased in PTECs treated with 3A5*3 PMO but not AUG PMO (** $p<0.01$).

2.4.2 Cation-dependent formation of a putative G4 structure in *CYP3A5*3* transcripts

While the mechanism by which *CYP3A5*3/*3* individuals produce functional CYP3A5 remains unknown, our results with the 3A5*3 PMO showed that blocking the *3-SNP site can correct splicing and restore CYP3A5 activity in HEK293 cells. We hypothesized that a salt-sensitive, G4 structure located in proximity to the *3-SNP site might play a similar "*trans*-acting" role in driving alternative splicing of the pre-mRNA transcript. Computational analysis of the human *CYP3A5* intron 3 gene structure identified multiple G4 targets in a repeating triplet G sequence spanning 151 bases located between the *3-SNP and the exon 4 splice acceptor. A quadruplex forming G-rich sequences (QGRS) computational search of this region identified the signature of two conserved G4 structures at the 3' end of intron 3 (see Supplemental Figure. 2.2).[223] To validate the hypothesis that a G4 structure participates in *CYP3A5* splicing and NMD suppression in *CYP3A5*3* carriers, we tested the effect of G4-stabilizing, Na+ cations on pre-mRNA splicing in cultured HEK293 cells. RNA extracted from HEK293 cells grown in standard media failed to produce a visible band indicative of normal exon 4 inclusion (Fig. 2.2a), while a visible band of expected size (500 bp) was present in RNA extracted from cells grown in hyperosmolar media (supplemented with 100 mM NaCl). Two minor bands at 350 and 600 bp were also present in the PCR reaction but were not considered diagnostic for exon 4 inclusion. It is possible that these bands indicate additional complexity in exon 4 splicing under high salt conditions, but further analysis is required to rule out off-target PCR artifacts (Fig. 2.2a). To discriminate the role of the cis-acting tonicity-responsive enhancer element in *CYP3A7* from the putative G4 element in intron 3 of *CYP3A5*, we supplemented HEK293 media with G4-destabilizing, Li+ cations (LiCl; 100 mM) to raise osmolarity while destabilizing any G4 structures in the pre-mRNA transcript. Exon 4 inclusion bands were not observed in HEK293 cells treated with LiCl, indicating that splice correction in *CYP3A5*3/*3* mRNA transcripts was cation-specific, and not simply a function of tonicity, further supporting a G4 element in proximity to *3-SNP of *CYP3A5* (Fig. 2.2a). To further establish the discrete role of the *3-SNP in mediating, cation-specific modulation of *CYP3A5* expression in HEK293 cells, we utilized qPCR to compare the effects of hyperosmolarity on a related mammalian cell type (CV-1 cells; African Green Monkey Kidney

Fibroblasts) expressing the *CYP3A5*1* genotype (Fig. 2.2b); genomic sequencing has confirmed the green monkey does not express the human (*6986A>G*) SNP, similar to other non-human primates (Supplemental Figure 2.1c). The relative fold-change in wild-type *CYP3A5* mRNA expression was monitored in both HEK293 and CV-1 cells using the $2^{-\Delta\Delta CT}$ method.[214] KCl supplementation of 1, 3 and 10 mM to DMEM media containing 4 mM KCl had minimal influence on *CYP3A5* mRNA expression in CV-1 cells, but significantly induced *CYP3A5* mRNA transcript levels in HEK293 cells in a dose-dependent manner that supports the participation of a G4 structure (Fig. 2.2b).

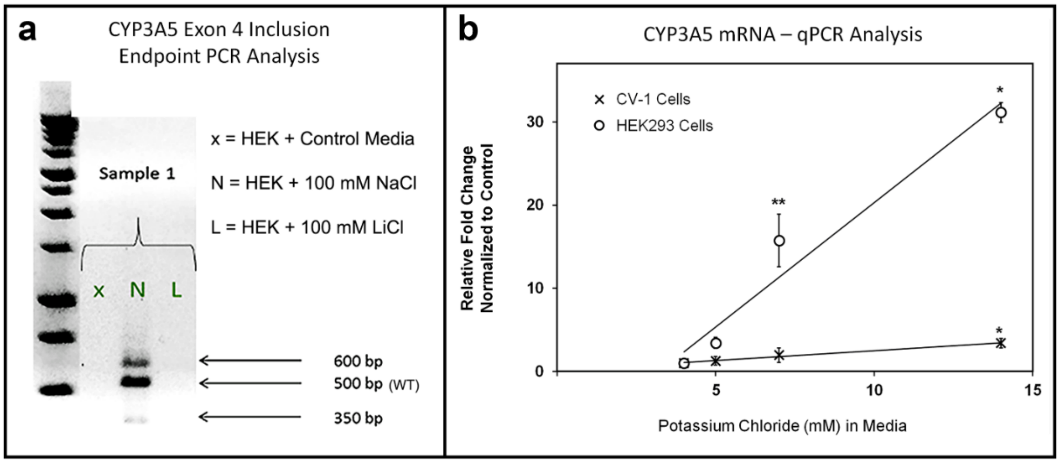

Figure 2.2. Cation-specific restoration of *CYP3A5*3/*3* mRNA in HEK293 cells, but not CYP3A5*1/*1 CV-1 cells. a) Endpoint PCR monitoring *CYP3A5* mRNA in HEK293 cells exposed to: X (normal), N (NaCl enriched), and L (LiCl enriched) media revealed cation-specific induction. b) SYBR Green qPCR Analysis of *CYP3A5* mRNA from HEK293 (*CYP3A5*3*) and CV-1 (*CYP3A5*1*) cells incubated with media supplemented with increasing amounts of (0, 1, 3, and 10mM) of KCl. * $p<0.05$; ** $p<0.01$.

A model depicting G4 structures in *CYP3A5* intron 3 that modulate exon 4 splicing events is shown in Fig. 2.3a. Cation-specific G4 stabilization of *3-SNP transcripts may shift the splice acceptor back to the reference exon 4 splice acceptor creating viable mRNA that bypasses pseudo-exon splicing and PTC incorporation that leads to altered translation of wild-type *CYP3A5* or NMD of mRNA transcripts. We predicted ASOs targeting the G4 motif (called G4 Disrupt; Table 2.1) could prevent NMD escape and limit the cation-specific restoration of *CYP3A5*3/*3* transcripts in HEK293 cells. To test whether the proposed G-rich motifs in intron 3 could fold into G4-like structures *in vitro*, oligomeric DNA and RNA spanning the 151-base G-rich region of intron 3 was prepared (Table 2.2). Equal length oligomers containing the complementary C-rich sequences were used as controls. The DNA oligomers were incubated in the presence of 100 mM KCl and resolved on a native PAGE gel (Fig. 2.3b, Lanes 1-5). Multiple, differentially migrating bands were observed in lanes with the "G strand" DNA oligomer from intron 3 (Fig. 2.3b, Lanes 3-5); these bands were absent in matched "C-strand" experiments (Fig. 2.3b, Lanes 1-2). The G4 Disrupt PMO, with sequence complementary to the G-rich motifs identified by QGRS, had no effect on the C-strand mobility, but at high concentrations (5-fold molar excess) ablated the faster migrating bands in the G-strand (Fig. 2.3b, Lane 5). An RNA oligomer with sequence equivalent to the intronic DNA oligomer was used to establish G4 characteristics in the related RNA structure. Nearly all the intronic RNA formed faster migrating intra-strand G4 structures in the presence of KCl (Fig. 2.3c, Lane 1). Incubation with 1:1, 3:1, and 5:1 G4 Disrupt PMO to RNA ratios led to an increasing shift from fast migrating G4-like structures to the slower migrating linear form (Fig. 2.3c, Lanes 2-4).

Next, we tested the ability of the G4 Disrupt PMO to suppress cationic rescue of *CYP3A5*3/*3* transcripts in HEK293 cells incubated with KCl (Fig. 2.3d). Incubation with the G4 Disrupt PMO significantly blocked salt induction of viable *CYP3A5* transcripts in HEK293 cells (48 hrs, 1 µM; as compared to the scrambled (Scr) PMO control (Table 2.1); $p<0.01$) (Fig. 2.3d). Interestingly, CYP3A5 exon 4 skipping PMOs (Table 2.1) designed to target the *CYP3A5* intron 3/exon 4 border may also alter the assembly of the exon junctional complex (EJC), as canonical eIF4AIII binding sites have been identified near their target site, ~10-40 bp upstream of the splice junction, with a conserved EJC target site at 20-24 bp upstream.[224, 225] Dex4 oligomers that bind downstream of the EJC, but not exclusively within exon 4 (Exon 4 Splice Acceptor PMOs (E4SA) -3 and -9, but not -17 and +94; see Table 2.1), were able to induce both wild-type and delta exon 4 (Dex4) *CYP3A5* mRNA expression in HEK293 cells, without NaCl supplementation to the cell culture media (Fig. 2.3e). High salt levels appear to alter the interaction of E4SA PMOs with target sequences near the EJC assembly zone, reducing the cationic-specific suppression of pseudo-exon inclusion and NMD, while enhancing the targeted skipping of exon 4 (Fig. 2.3e). These results highlight the dynamic splice sensitivity of *CYP3A5*3* transcripts, that we attribute in part to a newly identified G4 element in intron 3 and identify sites amenable to ASO targeting.

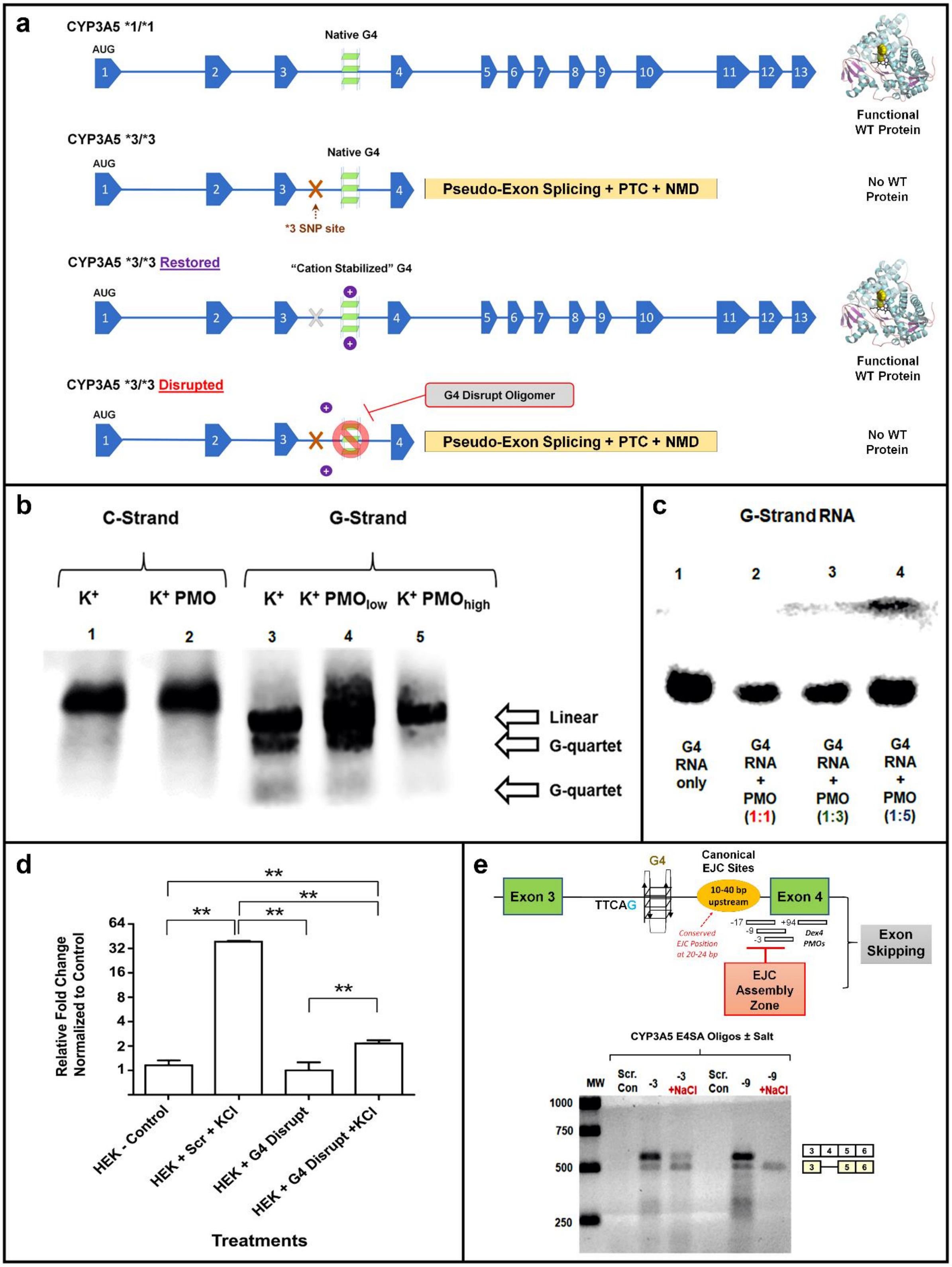

Figure 2.3. G4 Structures Regulate *CYP3A5* Expression and Represent Novel Targets for ASO Modulation. a) Schematic diagram of the *CYP3A5* gene showing the location of a putative G4 motif in intron 3. Cation-specific stabilization of native G4 structure shifts the splice acceptor back to the reference exon 4 splice acceptor, creating an in frame *CYP3A5*3/*3* transcript that bypasses pseudo-exon introduction and suppression of wild-type protein translation via PTC or NMD-related mechanisms. Salt-sensitive splice correction of *CYP3A5*3* transcripts (shown in Fig. 2a) can be abrogated using the G4 disrupting PMO (Table 2.1). b) Computational analysis of the *CYP3A5* gene (see Supplemental Fig. 2) and RNA/DNA gel shift assays (shown here), confirmed the existence of a G4-like structure in the *CYP3A5* intron 3 region. Control lanes 1 and 2 depict the mobility of the 151 nucleobase, *CYP3A5* intron 3 "C-strand" DNA, in KCl-enriched running buffer [100 mM KCl]. The C-strand does not display faster migration typical of a G4 structure in the presence of KCl, and a G4 disrupting PMO does not alter C-strand mobility (lane 2). In contrast, the 151 nucleobase "G-strand" DNA demonstrated enhanced mobility bands reflecting both inter- and intra-strand G4 formation in KCl-enriched running buffer (lane 3). Addition of the G4 disrupting PMO diminishes the enhanced mobility bands at low concentration (1:1 molar ratio; lane 4) and ablates the enhanced mobility bands at high concentration (5:1 molar ratio; lane 5). c) A 151 nucleobase RNA strand forms a putative G4-structure in KCl-enriched running buffer (Lane 1). Addition of increasing amounts of G4 disrupting PMO to the G4 RNA (Lane 2 – 1:1 PMO:RNA ratio, Lane 3 – 3:1 PMO:RNA ratio, and Lane 4 – 5:1 PMO:RNA ratio) shifts the RNA structure to the slower mobility form. d) qPCR analysis of *CYP3A5* mRNA from HEK293 cells exposed to no PMO and normal media (HEK control), scramble PMO (1 µM, 48 hrs) and KCl (12 mM) (HEK+Scr+KCl), G4 disrupting PMO only (1 µM, 48 hrs) (HEK + G4 Disrupt), and G4 disrupting PMO (1 µM, 48 hrs) and KCl (12 mM) (HEK+G4 Disrupt+KCl). Statistical differences were assessed by ANOVA; p-value < 0.01. Post-hoc test **: p<0.01. e) (Top) A schematic illustrating the location of the exon junctional complex (EJC) in relation to the cryptic splice acceptor in intron 3 and the G4 structure. PMOs designed to skip exon 4 in *CYP3A5* at various sites (+/- base position relative to EJC) are also shown (-17= E4SA-17, -9=E4SA-9, -3=E4SA-3, and +94= E4SA+94). (Bottom) Endpoint PCR results for RNA expression in HEK293 cells treated with three PMOs (E4SA-3, E4SA-9, or a scramble control (Scr); 1 µM; 48 hrs) and 100 mM NaCl are shown. The Scr oligomer did not induce stable transcripts, while exon 4 skipping PMOs (E4SA-3 and -9) induced transcripts that both include and exclude exon 4. The addition of high salt media diminished the cell's ability to express transcripts including exon 4. Cationic-specific stabilization of the transcript may have improved the ability of exon skipping PMOs to properly bind the transcript near the EJC assembly zone and promote targeted exon 4 exclusion.

2.4.3 Salt-induced rescue of CYP3A5 protein expression, enzyme activity, and mineralocorticoid receptor signaling in *CYP3A5*3*3* HEK293 cells

Western blot analysis was used to confirm that in-frame *CYP3A5*3* transcripts, rescued from NMD by NaCl or KCl, can be translated into viable protein in HEK293 cells (Fig. 2.4a). We observed two CYP3A5 protein bands in our Western blots, corresponding to the ~56 KDa reference protein, and a shortened, ~30 KDa splice variant. Total CYP3A5 protein expression increased when HEK293 cells were treated with increasing KCl (10-100 mM) or 100 mM NaCl (Fig. 2.4a and 2.4b, Lanes A-E), however the ratio of wild type to variant protein was reduced in all salt treatments compared to the HEK control (Fig.

2.4b, Lanes B-E). The salt-induced expression of both reference and variant CYP3A5 protein in HEK293 cells further supports the hypothesis that a G4 structure can mask the cryptic splice acceptor formed by the *3-SNP and alter the structure of the EJC at the *CYP3A5* intron3/exon 4 border. Two models to explain this alternative splicing, where the G4 motif serves as either an internal ribosomal entry site (IRES) or an exonic splicing enhancer (ESE) element that can influence the availability of translational initiation start sites, are proposed in Supplemental Figure 2.3.

The functional activity of salt-induced CYP3A5 expression was confirmed by observing CYP3A-specific metabolic activity in HEK293 cells based on the conversion of 7-benzyloxy-4-[trifluoromethyl]-coumarin (BFC) to 7-hydroxy-4-[trifluoromethyl]-coumarin (HFC). As shown in Fig. 2.4c, HEK293 cells treated with KCl (12 mM; 48 hrs) showed a significant increase in CYP3A enzyme activity that was not suppressed when cells were co-treated with a scramble control (Scr) PMO ($p<0.01$). In contrast, co-treatment with either the G4 Disrupt PMO or the start-site targeting (AUG) PMO (Table 2.1) significantly reduced CYP3A enzyme activity to levels observed for untreated HEK293 cells. CYP3A5 is also known to catalyze the endogenous conversion of glucocorticoids, including cortisol and corticosterone, to 6β-hydroxylated products that stimulate MR activity. LC/MS/MS analysis was used to confirm the HEK293 cell-based conversion of parent cortisol to 6β-hydroxycortisol (6βOH) metabolites. As shown in Fig. 2.4d, HEK293 cells incubated in normal media supplemented with cortisol (1 nM; 24 hrs) produced 6-fold less 6β-hydroxycortisol metabolite (AUC=$1.93\text{x}10^{-3} \pm 0.05 \text{ x}10^{-3}$) compared to HEK293 cells cultured in KCl-enriched media (12 mM; AUC=$1.19 \text{ x}10^{-2} \pm 0.48 \text{ x}10^{-2}$; $p=0.031$). Enhanced 6β-hydroxycorticosteroid production was subsequently confirmed to significantly increase MR signaling activity (more than 2-fold) in a luciferase-based cell reporter system ($p < 0.01$) (Fig 2.4e).

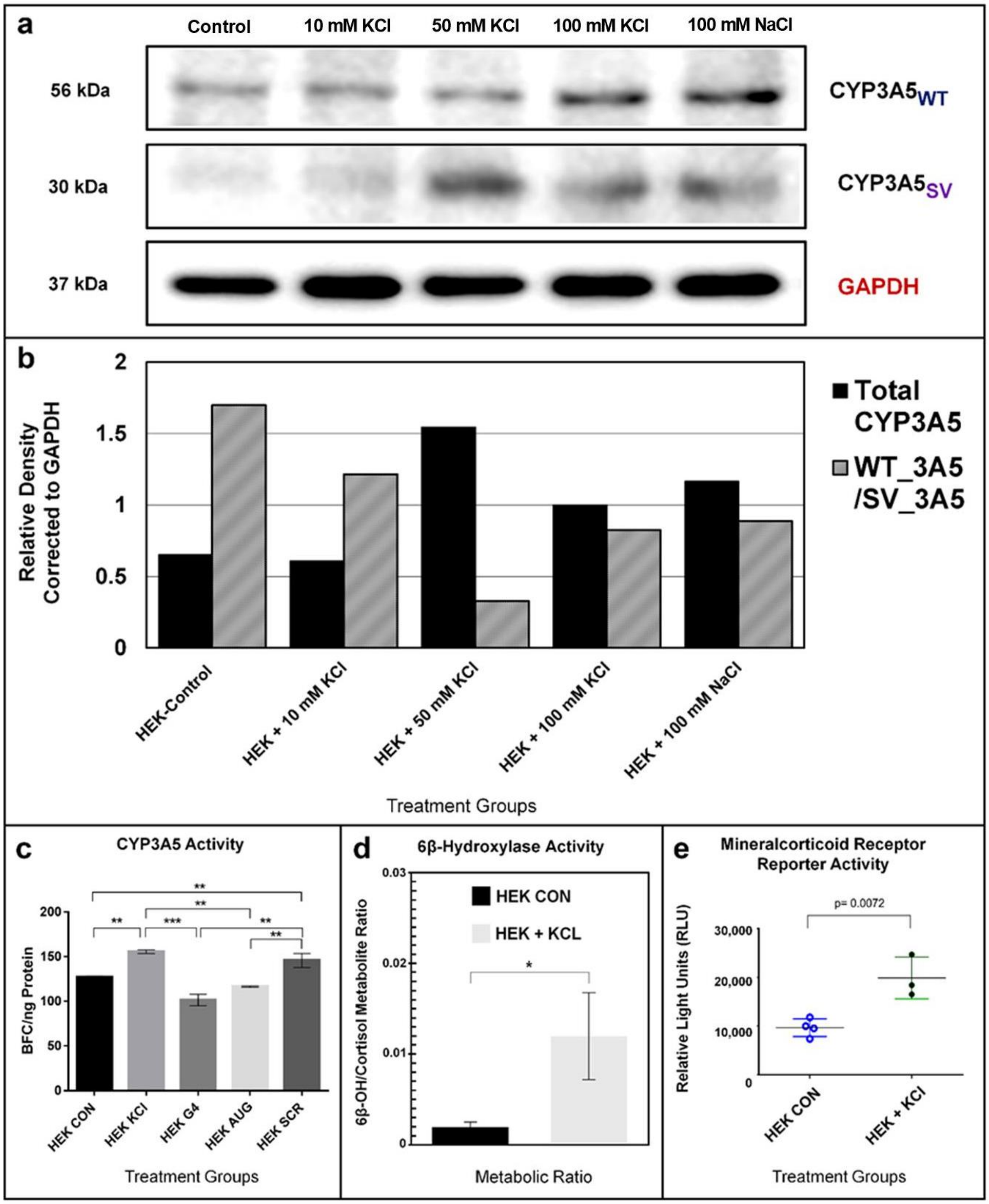

Figure 2.4. Salt-induced *CYP3A5*3* protein expression, enzyme activity and mineralocorticoid receptor signaling in HEK293 Cells. a) Confluent HEK293 cells were exposed for 48 hours to control media or media supplemented with 10 mM KCl, 50 mM KCl, 100 mM KCl, or 100 mM NaCl. Two protein bands attributed to CYP3A5 were detected via western blot, including the full-length reference protein (*CYP3A5*$_{WT}$) at 56 kilodaltons (kDa) and a truncated 30 kDa splice variant form (*CYP3A5*$_{sv}$). The housekeeping gene *GAPDH*, detected at 37 kDa, was used to normalize sample loading. b) Total CYP3A5 protein and the ratio of CYP3A5$_{WT}$ to CYP3A5$_{SV}$ protein normalized to GAPDH expression was determined using densiometric analysis in ImageJ**.** c) CYP3A enzyme activity was monitored in HEK293 cells under normal conditions and with elevated KCl (12 mM; 48 hrs) and PMOs (1 µM; 48

hrs), as measured fluorometrically by BFC metabolism (see Methods). KCl supplementation significantly induced enzyme activity ($p<0.01$) in HEK293 cells (KCl) compared to control cells (CON). The G4 disrupting PMO (G4) and the *CYP3A5* start-site inhibitor (AUG) PMO both significantly prevented KCl induction of BFC metabolism ($p<0.01$ compared to KCl treated control) and were not different from control cells. The scrambled (SCR) PMO control did not inhibit KCl induction of CYP3A activity ($p< 0.01$. Post-hoc test **: $p< 0.01$, and ***: $p< 0.005$). d) LC MS/MS analysis of HEK293 cell media demonstrated KCl enrichment (12 mM, 24 hours) stimulated the conversion of cortisol to 6β-hydroxycortisol. An ~6-fold change in the metabolic ratio was observed for HEK293 cells grown in normal media ($1.93\text{x}10^{-3}$, solid black) compared to 12 mM KCL-supplemented media ($1.19\text{x}10^{-2}$, solid gray). e) Conditioned media from HEK293 cells (+/- KCl (12 mM); 48 hrs) was added to a luciferase-based cell reporter system for MR transactivation. MR activity was significantly elevated more than two-fold ($p < 0.01$) in HEK293 media containing 12 mM KCl. The ligand-specific sensitivity of the MR activity assay was validated using a standard curve for aldosterone (1 nM sensitivity = ~ 100,000 RLU).

2.4.4 Impact of ASO chemistry on safety toward PTECs

Given that CYP3A5 activity may exacerbate high blood pressure (HBP) in both fast metabolizing *CYP3A5*1/*1* and slow metabolizing (or conditional) *CYP3A5*1/*3* and **3/*3* genotypes, and CYP3A5 activity can be modulated with ASO *in vitro*, developing CYP3A5-directed therapeutics targeting renal disorders is worth consideration. To advance *in vivo* development of a CYP3A5-specific antisense inhibitor, we utilized our human kidney PT-MPS to evaluate whether ASO safety towards target PTECs would depend on the charge of the antisense backbone chemistry (e.g., neutral PMO or (-) charged PSO) (Fig 2.5a). We assessed whether HO-1 expression in the human kidney PT-MPS was affected by treatment with either a model PSO (Drisapersen, DSP) or model PMO targeting the human papillomavirus (HPV) (5 days; 1 µM) (Table 2.1). Staining for HO-1 by immunocytochemistry showed an expected perinuclear and cytoplasmic localization that was unchanged by either treatment (Fig. 2.5b). Neither the DSP PSO nor HPV PMO significantly affected the expression of HO-1 while controlling for donor effect (Fig. 2.5c), indicating there was no change in intracellular redox environment. KIM-1 secretion was significantly lower in the PMO group (Fig. 2.5d) compared to control while controlling for time and donor effect ($p=0.043$) and lower compared to PSO while controlling for time and donor effect ($p=0.01$). However, the reduction of KIM-1 to levels ~87% of control was quite modest, suggesting that both ASO chemistries were well tolerated in the PT-MPS when dosed at 1 µM for 5 days. However, secretion of miR-30e-5p was significantly increased by the DSP PSO ($p=0.024$), but not HPV PMO when treated at 10 µM for 44 hours (Fig. 2.5e). RNAseq of total RNA from this experiment (HPV PMO and DSP PSO; 10 µM, 44 hrs) revealed the DSP PSO significantly affected the expression of 18 genes relative to control (Table 2.3), while the HPV PMO did not significantly affect the expression of any genes. DSP PSO treatment mainly affected genes associated with ribosome biogenesis, transcript splicing, and inflammatory response. Several members of the small nucleolar RNA C/D box 3 (SNORD3 or U3) family, which direct post-transcriptional cleavage of ribosomal precursor RNA and are required for proper biogenesis of the small ribosomal subunit, were increased. Other genes that were induced include WD repeat domain 74 (WDR74) and RNA 5S ribosomal 9 (RNA5S9), which function in assembly of the large ribosomal subunit while RNA variant U1 small nuclear 7 (RNVU1-7), RNA variant U1 small nuclear 18 (RNVU1-18), and dual specificity protein kinase (CLK1) regulate transcript splicing. Next, we tested whether a KIM-1 response could be observed in base sequence-matched ASOs (HPV PMO and HPV PSO) when dosed at 10 µM. No treatment related change in KIM-1 secretion was observed while controlling for time and donor effect (Figure 2.5f).

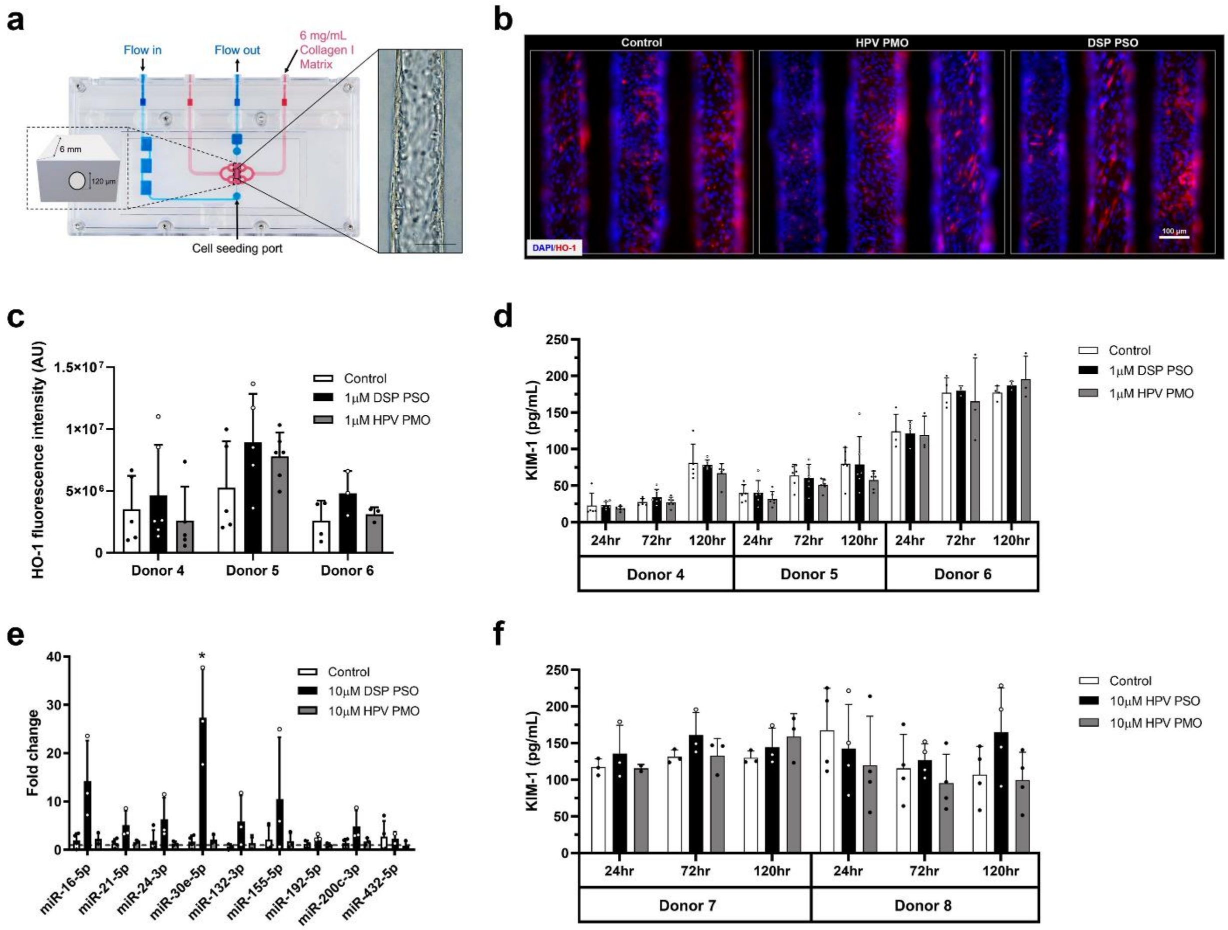

Figure 2.5. Safety evaluation of ASO chemistry in PT-MPS. a) Schematic of the PT-MPS with a phase contrast image of a confluent PTEC tubule. b) Representative images of tubules stained for HO-1 (red) by immunocytochemistry after 5 days of treatment with 1 µM HPV PMO or 1 µM DSP PSO (scale=100 µm). Cells display a predominately perinuclear and cytoplasmic HO-1 signal. c) Quantification of HO-1 fluorescence intensity from tubules depicted in B. Expression and localization of HO-1 was not significantly affected by HPV PMO or DSP PSO treatment. d) Quantification of levels of KIM-1 in device effluent over time by mesoscale chemiluminescent assay after treatment with 1 µM HPV PMO or 1 µM DSP PSO. There was a significant reduction in KIM-1 secretion with PMO treatment compared to control (p=0.043) and PSO groups (p=0.01). e) Quantification of levels of renal disease- and injury-associated miRNAs by qPCR after treatment with 10 µM HPV PMO or 10 µM DSP PSO for 44 hours. Data are presented as the $2^{-\Delta\Delta CT}$ fold change in miRNA levels relative to control. Secretion of miR-30e-5p (p=0.024) was significantly increased by DSP PSO treatment. f) Quantification of levels of KIM-1 in device effluent over time by ELISA after treatment with 10 µM HPV PMO or 10 µM HPV PSO. There was no time- or dose- dependent effect of HPV PMO, DSP PSO, or HPV PSO treatment on the secretion of KIM-1. For all quantitative panels (C-F), data are presented as mean ± s.d. with black or white circles representing the value for each individual tubule tested.

2.5 Discussion

Polymorphisms in both coding and non-coding RNA can cause unpredictable effects on gene expression, and the impact of polymorphisms on gene splicing is increasingly recognized as a primary driver of multiple diseases (e.g., spinal muscular atrophy and β-globin thalassemia).[166, 167] In this regard, SNPs in the *CYP3A5* gene have been extensively studied, due to their tendency to suppress gene expression and promote renal disorders.[48, 147-164, 226] However, *CYP3A5*3/*3* individuals harboring a nonfunctional variant (*6986A>G*) are reported to unpredictably express wild-type CYP3A5 activity, presumably due to conditional correct intron 3 splicing.[164] While the mechanisms driving interindividual variability in CYP3A5 expression in *CYP3A5*3* homozygotes remain unclear, particularly in renal tissues, gender specific differences in sex or dietary hormones, like estrogen, vitamin A or the vitamin D hormone, have been postulated.[164, 227] We investigated the possibility that sodium and potassium could also regulate the alternative splicing of *CYP3A5*3/*3* transcripts and help explain conflicting reports that *CYP3A5* genotype is associated with hypertension.[154, 162, 163, 180] We also explored the mechanistic basis of alternative splicing in *CYP3A5*, using antisense oligonucleotides targeting the **3*-SNP site and other secondary structural elements (i.e., G4) in close proximity that may act in cis or trans to alter the splicing and expression of *CYP3A5*3* transcripts.

When a termination codon (UAA, UAG, or UGA) is positioned at the ribosomal A site, translation termination occurs; when termination precedes an EJC, NMD is initiated.[228] The cryptic splice acceptor in intron 3 created by the *6986A>G* mutation leads to a premature termination codon upstream of the exon 4 EJC, which explains why *CYP3A5* mRNA is diminished in **3/*3* variants (Figures 2.1b, 2.1c and 2.2a). However, a PMO (3A5*3) targeting the **3 SNP* site in *CYP3A5*'s intron 3 can mask the mutant splice acceptor site and promote normal pre-mRNA processing (Figures 2.1b and 2.1c). PMO-mediated correction of *CYP3A5*3* transcript splicing led to production of a functional protein, as confirmed by a midazolam metabolism assay (Figure 2.1d). Strikingly, supplementation of cell culture media with Na+ or K+, but not Li+, promoted correct alternative splicing of the *CYP3A5*3* transcript (Figures 2.2a and 2.2b), greater CYP3A5 content (Figure 2.4a and 2.4b) and higher CYP3A5 activity (Figure 2.4c-e). To explain the observation of cation-mediated restoration of CYP3A5, we investigated the possibility that a G4 structure located near the*3-SNP site could play a salt-sensitive role in shifting spliceosome activity from the mutant splice acceptor site in intron 3 to the canonical exon 4 splice acceptor.

Two conserved G4 candidates were identified in intron 3 leading to our confirmation of G4-structural character in a 151-base-region between the *CYP3A5*3* SNP site and the exon 4 splice acceptor. G4 assembly was facilitated by Na+ and K+ cations, but not Li+ cations, consistent with previously reported G4-structural behavior.[176-179, 229, 230] The G4-like structure in intron 3 appears to efficiently recruit *trans*-acting splicing factors, including hnRNPs and SR proteins, because the splicing shift from the *6986A>G* site to exon 4 splice acceptor is mediated by a relatively small number of bases. The action of G4 motifs in modulating pre-mRNA splicing is well-established, therefore it is not surprising to observe a G4-mediated splicing shift in *CYP3A5*3/*3* pre-mRNA transcripts to a mature mRNA, which is translated into a functional protein.[169-175] While more advanced biophysical methods (e.g., circular dichroism or nuclear magnetic resonance) are needed to fully characterize this theoretical G4 secondary structural element, our data strongly support the existence of a conserved G4 element in intron 3 that alters the phenotypic presentation of *CYP3A5*3* genotypes via salt-sensitive, alternative splicing and NMD suppression. These studies investigated the behavior of the putative G4-structure when exposed to biologically relevant monovalent cation concentrations. However, the mechanisms regulating the transport of cations into the nucleus where splicing occurs, particularly in cultured PTECs, remains unresolved. Additional experiments are also needed to determine the efficiency of the cation-sensitive “switch” and better define its ability to impact CYP3A5 activity *in vivo*.

The finding of salt-sensitive restoration of CYP3A5 from *CYP3A5*3* transcripts are significant, because alterations in CYP3A5 expression levels can promote disease by disturbing the local concentrations of endogenous metabolites such as glucocorticoids, steroid hormones, and retinoids.[148] CYP3A5, unlike CYP3A4, is expressed in steroidogenic organs including the prostate, adrenals, and kidney, making it a major mediator of pleiotropic, hormone signaling events.[148] The renal localization of CYP3A5, within the proximal tubule and collecting duct, allow for the local conversion of glucocorticoids including corticosterone to metabolic products like 6β-hydroxycorticosterone, which promote paracrine signaling and a metabolic switch from glucocorticoid to mineralocorticoid activity. Prolonged MR signaling leads to enhanced salt retention, which in turn, can promote hypertension (see Fig. 2.6).

Induction of *CYP3A5* transcription in response to glucocorticoids requires dual activation of two, glucocorticoid response elements (GRE) in the promoter.[231] As mentioned above, a tonicity-responsive enhancer located in intron 2 of *CYP3A7* also acts as an enhancer for neighboring *CYP3A4* and *CYP3A5* expression.[180] Transcriptional *CYP3A5* amplification from stress-induced release of glucocorticoids and salt intake, combined with salt retention, and vitamin D hormone insufficiency, may contribute to hypertension via modulation of the renin-angiotensin-aldosterone-system (RAAS) (Fig. 2.6).

A high Na+/low K+ diet also promotes hypertension and K+ supplements can reduce blood pressure in hypertensive patients.[232, 233] In contrast, aldosterone is normally secreted in response to hyperkalemia, and therefore the shunting of glucocorticoids to the MR pathway by CYP3A5 during elevated stress could potentially disrupt innate K+ feedback loops required to prevent hypokalemia. Human migration from equatorial regions increased vitamin D insufficiency, and an increasingly high salt diet, may have reduced the fitness of the sodium sparing *CYP3A5*1* genotype in some populations.[234, 235] Today, the *CYP3A5*3* allele is most commonly found in people of European ancestry, with allele frequencies ranging from 0.14 among sub-Saharan Africans to >0.95 in European populations.[235] *CYP3A5*3* carriers may have acquired an advantageous mutation in *CYP3A5* intron 3, that slowed renal metabolism of key hormones, and alleviated the tendency to excrete K+ and retain Na+ during stress. However, because the SNP regulating *CYP3A5*3* variant expression is located near a putative G4 structure that responds to fluctuations in intracellular K+ levels, it appears to represent a conditional mutation, rather than an obligate null mutation.

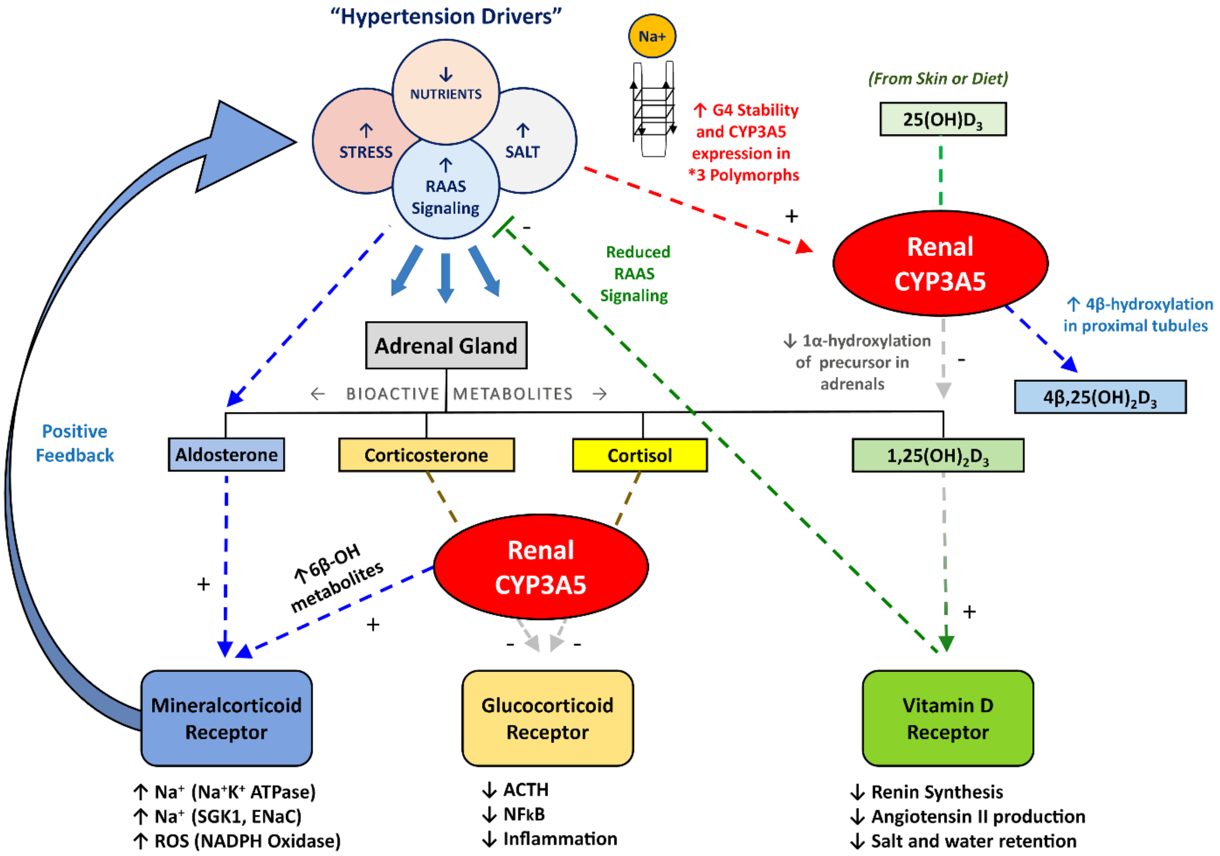

Figure 2.6. Schematic Diagram of CYP3A5's Dual Role in the Regulation of Hypertension. Renal CYP3A5 activity plays a dual role in modulating vitamin D- and glucocorticoid-hormone signaling cascades that may drive HBP pathology. First, CYP3A5 activity can convert stress-related glucocorticoids (corticosterone and cortisol) to mineralocorticoids via 6β-hydroxylation that enhances MR signaling and triggers sodium retention (via several transporter related mechanisms) and increased ROS production. A CYP3A5-mediated glucocorticoid to mineralocorticoid shift also silences glucocorticoid signaling (via ACTH and NF-kB) and increases inflammation. Second, CYP3A5 can hijack endogenous vitamin D hormone signaling cascades by shunting 25-hydroxyvitamin D_3 metabolism from CYP27B1 (1α-hydroxylase) towards a 4β-hydroxylation pathway that limits 1,25-dihydroxyvitamin D_3 signaling via the VDR, reducing renin production that suppresses systemic RAAS activity. Thus, CYP3A5 appears to play a role in regulating positive feedback loops that drive the accumulation of stress hormones and sodium in the renal proximal tubule cells. Sodium cationic-stabilization of G4-like elements in *CYP3A5* intron 3 may exacerbate this hypertensive signaling arc in *CYP3A5*1/*3* and *CYP3A5*3/*3* polymorphs, who may conditionally express CYP3A5.

While our results suggests that gene-directed approaches targeting *CYP3A5* for the treatment of HBP are viable and deserve greater consideration, ASO-induced nephrotoxicity is a hard-to-predict adverse event that may only be discovered once the molecule enters clinical trials. Consequently, new models and biomarkers need to be tested for their ability to screen for renal liabilities earlier in drug discovery to facilitate the development of safer ASOs. As backbone chemistry may be a core determinant of the safety of ASOs toward renal cells, we utilized a PT-MPS to characterize the safety of a PMO and two 2'-OMe-PSOs. KIM-1 secretion was not affected by treatment with HPV PSO or DSP PSO while being slightly reduced by HPV PMO. A previous report showed KIM-1 secretion by renal tubule cells *in vitro* in response to toxic locked-nucleic acid modified PSO gapmers was sequence-dependent and variable.[100] Additional compounds, particularly those with sequences known to be toxic, should be tested to fully evaluate the value of KIM-1 secretion as a marker of ASO-induced injury in the PT-MPS. Likewise, a larger matrix of 2'-OMe-PSO sequences should be tested to better determine the relationship between miR-30e-5p secretion and ASO-induced cell injury.

We also observed increased expression of genes involved in nucleoprotein activity as a response to ASO linkage chemistry, validating the role of linkage chemistry as a key driver of the intracellular distribution kinetics and protein binding properties of oligonucleotides. PSOs are known to associate with various RNA binding proteins to form nucleoprotein complexes.[236-238] Interaction of PSOs with ribonucleoproteins can result in displacement of endogenous RNA molecules (e.g., nuclear paraspeckle assembly transcript 1[NEAT1] from paraspeckles).[236] Among the proteins known to bind PSOs are nucleolin (NCL1) and nucleophosmin (NPM1), both of which have roles in regulating ribosome biogenesis and function.[239-242] NCL1 forms a complex with the U3 small nucleolar ribonucleoprotein (which contains SNORD3 RNAs) during the initial steps of small subunit processome formation.[243] Taken together, we postulate that the transcriptional response in DSP PSO-treated cells may be driven by competition with endogenous molecules for nucleoprotein binding. Toxic phosphorothioate gapmers have been shown to delocalize RNA binding proteins from the nucleolus in an RNAse H1-dependent manner, resulting in nucleolar stress and cell death.[244] While we did not observe overt cellular injury with DSP PSO treatment, the induction of genes involved in ribosome biogenesis warrants further investigation as it is an energetically demanding process.

Unlike the DSP PSO treatment, we observed no changes in miRNA secretion or transcriptional signature with HPV PMO treatment, which strongly supports the safety of PMOs in PTECs. A limitation is that the metabolic stability of the PSOs tested was not evaluated, so some of the biological effects may be due to chain-shortened metabolites and not solely the intact parent compound. On the other hand, metabolic stability is not a concern for PMOs because they are not metabolized.[94, 245] The inert nature of the HPV PMO is unlikely to be due to a lack of cellular entry, as activity was demonstrated in monolayer PTECs with gymnotic delivery of the 3A5*3 PMO (Figure. 1d).

In summary, we conclude that a G4-like structure within intron 3 of *CYP3A5* forms a cation-sensitive “switch” that can suppress NMD in *CYP3A5*3* polymorphs. This is the first report of a transient restoration of *CYP3A5*3/*3* expression *in vitro,* potentially mediated by a G4 pre-mRNA element. CYP3A5 may therefore represent a novel druggable target for treatment of HBP, even in *CYP3A5*3* carriers. Using a novel *in vitro* PT-MPS platform, the safety of the PMO chemistry in PTECs was demonstrated. PMO treatment did not increase cell-associated (HO-1) or secreted biomarkers (KIM-1, miRNAs) of injury and did not affect the expression of any transcript relative to media control. Therefore, the PMO chemistry appears to be an optimal choice for selectively targeting renal *CYP3A5*.

Table 2.1 PMO oligomer sequences

Name	Sequence (5’-3’)	Target	Purpose
AUG	TTTCCCATGAGGTCCATCGCCAC	Translation start	Inhibit CYP3A5 synthesis
3A5*3	CAGGGAAGAGATATTGAAAGAC	*6986A>G* SNP	Shift splicing to exon 3
G4 Disrupt	CCGATTCTGCAGCTGGAGCCACAC	G4 structure in intron 3	Prevent G4 structure
E4SA-3	GAGTTGACCTTCATACGTTTCTG	Exon 4 splice acceptor	Skip exon 4; E4 EJC site
E4SA-9	TTGACCTTCATACGTTCTGTGTGGG	Exon 4 splice acceptor	Skip exon 4; E4 EJC site
E4SA-17	ACGTTCTGTGTGGGGACAACGG	Exon 4 splice acceptor	Skip exon 4; E4 EJC site
E4SA+94	CAAAAAATGGATGCTTACCCTTCGA	Exon 4 splice acceptor	Skip exon 4
Scr	ACTCCATCGTTCAGCTCTGA	Scramble control	Negative control
HPV PMO	CCTTTAGGGTAACAAGTCTTC	Human papillomavirus	Morpholino
HPV PSO	CCTTTAGGGTAACAAGTCTTC	Human papillomavirus	2’-OMe-PSO
DSP PSO	UCAAGGAAGAUGGCAUUUCU	Dystrophin Exon 51	2’-OMe-PSO

Table 2.2 DNA and RNA oligomers used in gel shift mobility assays

Name	Sequence
HOX11 G-strand - DNA oligomer sequence:	5’-GCG CGA GGG AGG GGA GGG GAG GGG GAG AGG-3’
HOX11 C-strand - DNA oligomer sequence:	5’-CCT CTC CCC CTC CCC TCC CCT CCC TCG CGC-3’
*CYP3A5_intron3_*G-strand - DNA oligomer sequence:	5’-GGG TGG CTC CTG TGT GAG ACT CTT GCT GTG TGT CAC ACC CTA ATG AAC TAG AAC CTA AGG TTG CTG TGT GTC GTA CAA CTA GGG TCG TAT GGA TTA CAT AAC ATA ATG ATC AAA GTC TGG CTT CCT GGG TGT GGC TCC AGC TGC AGA ATC GGG-3’
*CYP3A5_intron3_*C-strand - DNA oligomer sequence:	5’- CCC GAT TCT GCA G CT GGA GCC ACA CCC AGG AAG CCA GAC TTT GAT CAT TAT GTT ATG TAA TCC ATA CCC CTA GTT GTA CGA CAC ACA GCA ACC TTA GGT TCT AGT TCA TTA GGG TGT GAC ACA CAG CAA GAG TCT CAC ACA GGA GCC ACC C-3’
*CYP3A5_intron3_*G-strand - RNA oligomer sequence:	5’-GGG UGG CUC CUG UGU GAG ACU CUU GCU GUG UGU CAC ACC CUA AUG AAC UAG AAC CUA AGG UUG CUG UGU GUC GUA CAA CUA GGG UCG UAU GGA UUA CAU AAC AUA AUG AUC AAA GUC UGG CUU CCU GGG UGU GGC UCC AGC UGC AGA AUC GGG-3’

Table 2.3 Transcriptional response of PTECs in PT-MPS to DSP PSO treatment

Gene Symbol	Description/function	Fold change	logCPM	P-value	FDR
WDR74	Ribosome assembly, large subunit	1.72	8.07	1.27E-07	0.002
RNA5S9	Ribosomal RNA, large subunit	16.19*	3.87	2.84E-06	0.017
DUSP5	Negative regulator of MAPK pathway	1.60	5.85	4E-06	0.017
RNVU1-18	Pseudogene of U1 small nuclear spliceosomal RNA	1.54	11.12	5.05E-06	0.017
RNVU1-7	Pseudogene of U1 small nuclear spliceosomal RNA	1.53	8.09	7.18E-06	0.020
SNORD3B-1	Guides cleavage of pre-rRNA, small subunit	1.48	9.56	9.69E-06	0.022
SNORD3D	Guides cleavage of pre-rRNA, small subunit	1.47	8.37	1.13E-05	0.022
RGS4	Negative regulator of G protein signaling	1.79	4.75	1.43E-05	0.025
MIR663AHG	Long non-coding RNA	1.42	8.35	2.1E-05	0.032
SNORD3A	Guides cleavage of pre-rRNA, small subunit	1.47	9.13	2.32E-05	0.032
FN1	Extracellular matrix protein	1.51	11.19	3.27E-05	0.037
SNORD3C	Guides cleavage of pre-rRNA, small subunit	1.50	8.49	3.34E-05	0.037
LIF	Cytokine	1.36	6.77	3.53E-05	0.037
ICAM1	Adhesion molecule	1.56	5.97	4.05E-05	0.040
PLAUR	Tissue reorganization	1.82	5.00	4.47E-05	0.041
TNFAIP3	Deubiquitinating protein; negative regulator of NF-kB pathway	1.64	6.10	6.06E-05	0.052
ADAMTS9	Metalloprotease; protein transport from ER to Golgi	1.36	8.79	6.42E-05	0.052
CLK1	Phosphorylates spliceosomal complex proteins	0.69	6.11	0.000117	0.090

Table 2.3. Shaded rows depict genes that have functions related to nucleoprotein activity; LogCPM: log counts per million reads is the average expression level for each gene across all samples; FDR: false discovery rate.

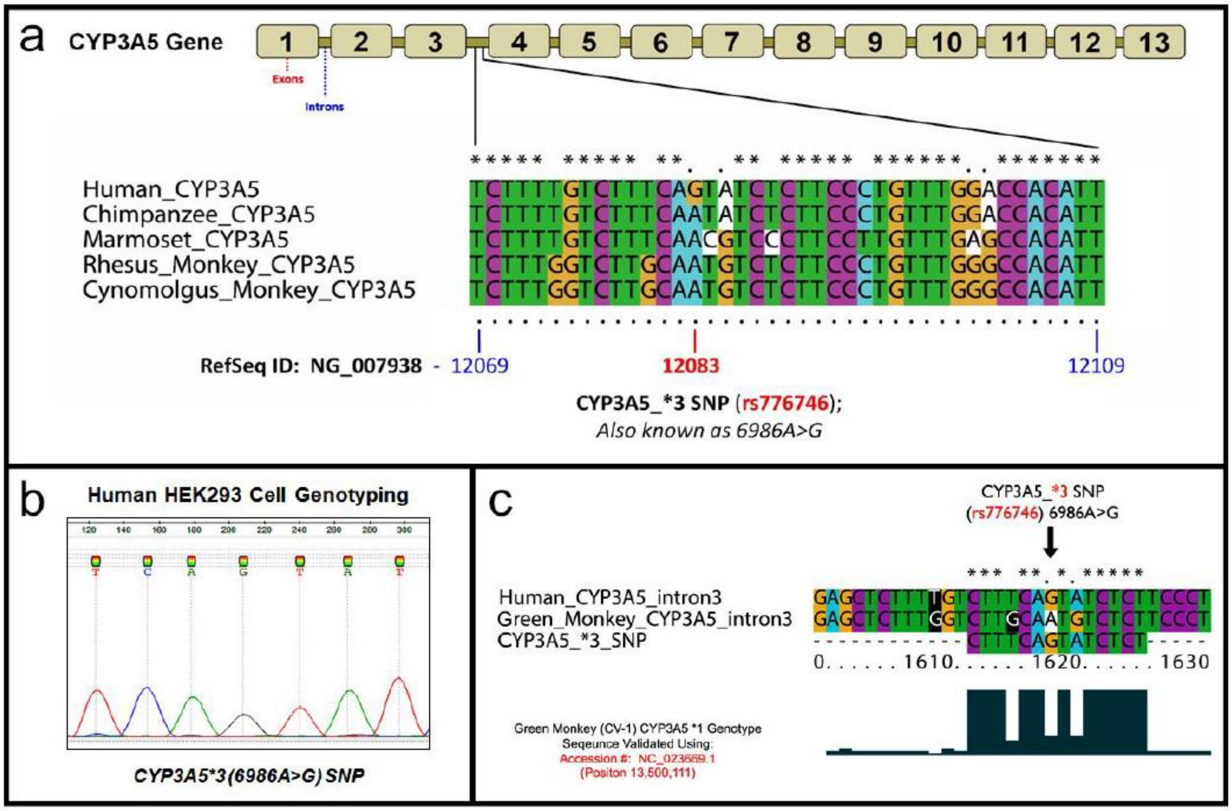

Supplemental Figure 2.1. Multiple Sequence Alignment of the Intron 3 region of *CYP3A5* and Genomic Sequencing of the *CYP3A5* gene in HEK293 and CV-1 cell lines. a) DNA sequence alignment comparisons among human and various nonhuman primate DNA sequences reveal consensus within human intron 3 region near the *CYP3A5*3* (*6986A>G; rs776746*) SNP site. The reference human sequence (*NG_007938.1*) reveals the presence of the *CYP3A5*3* SNP at position 12083. All other primate sequences, including chimpanzee (*NC_006474.4*), marmoset (*NC_013897.1*), rhesus monkey (*NC_027895.1*) and cynomolgus monkey (*NC_022274.1*) express the *CYP3A5*1* SNP at this site. b) The *CYP3A5* intron 3 sequence region from HEK293 cells indicates they are **3/*3* genotype (left). c) Genomic Sequencing (Accession #: NC_023669.1) confirms that CV-1 cells are CYP3A5*1 carriers like other non-human primates shown in panel a.

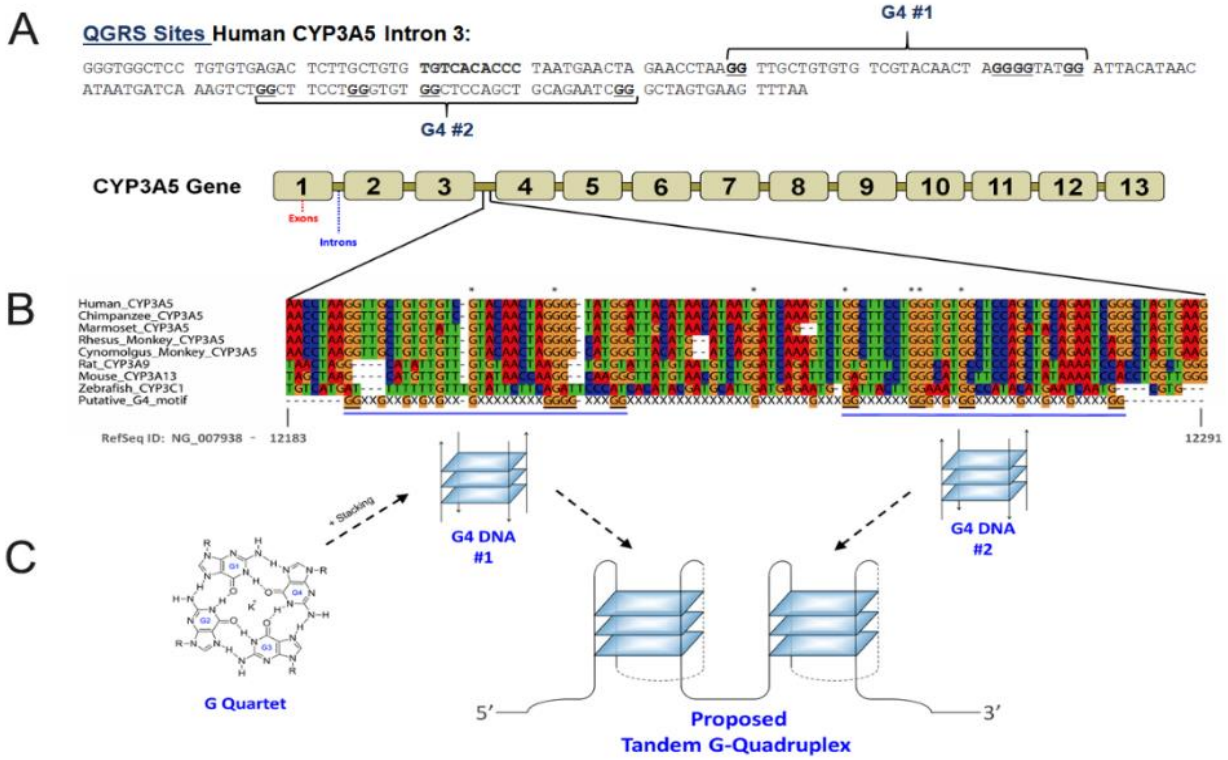

Supplemental Figure 2.2. Computational Analysis of *CYP3A5* Intron 3 Reveals a Putative G Quadruplex Structure in Proximity to the *CYP3A5*3* SNP site. A) The program QGRS-Conserve was used to identify two putative G quadruplex (G4) sequences in the intron 3 region of the human *CYP3A5* gene; the two putative G quartet (G4) motifs are shown. B) DNA sequence alignment analysis of the intron 3 region of the *CYP3A5* gene (or the species-specific ortholog) among humans (*NG_007938.1*), various nonhuman primates (chimpanzee (*NC_006474.4*), marmoset (*NC_013897.1*), rhesus monkey (*NC_027895.1*), cynomolgus monkey (*NC_022274.1*), rat (*NC_005111.4*), mouse (*NC_000071.6*) and fish (zebrafish *NC_007114.7*)) reveal strong consensus in the intron 3 region located between the *CYP3A5*3* (*6986A>G; rs776746*) SNP site and intron 3/exon 4 splice junction. A larger G quartet structure (151 base pairs) overlapping the two smaller G4 motifs, not identified by the program, was identified visually (not shown). C) Schematic representation of the G quartet and G4 structure; four guanine Hoogstein base pairing, fundamental to G4 structures is shown with an internal, stabilizing potassium ion (K+). The proposed assembly of a tandem G quadruplex structure in the region adjacent to *CYP3A5*'s intron 3/exon 4 splice junction is also depicted.

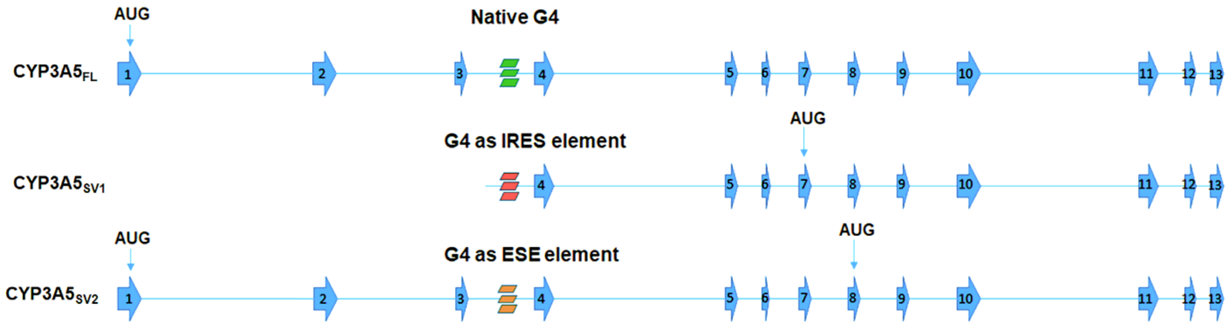

Supplemental Figure 2.3. Models for G4-mediated-induction of *CYP3A5* splice variant proteins in *CYP3A5*3/*3* HEK293 cells. We detected a prominent 30 kDa splice variant of *CYP3A5* in HEK293 cells treated with potassium or sodium cations. We propose the 151 bp G4 motif in intron 3 serves as either an internal ribosomal entry site (IRES) or an exonic splicing enhancer (ESE) element redirecting translational initiation to start sites in exons 7 or 8, or the skipping of multiple internal exons, which remain uncharacterized.

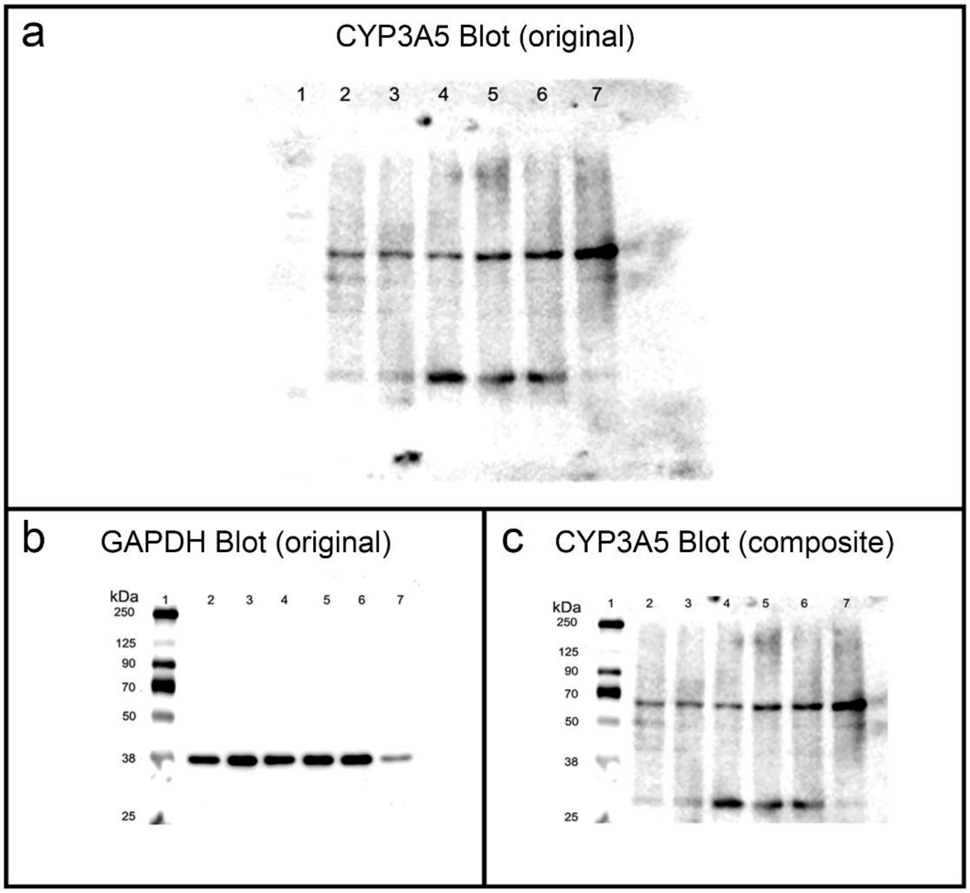

Supplemental Figure 2.4. Uncropped Western Blots for CYP3A5 and GAPDH expression in HEK293 cells. a) The Western blot data shown in Fig 4 was cropped from the original CYP3A5 blot shown in panel a. b) The blot membrane was initially probed with monoclonal antibodies for GAPDH, and then stripped prior to re-probing with the CYP3A5 antibody. After stripping the GAPDH antibody, the molecular weight marker was poorly resolved when re-probing with the CYP3A5 antibody. However, the CYP3A5 blot could still be oriented using weakly visible bands at 90, 70 and 25 kilodaltons (kDa). c) To aid in interpretation, a composite version of the CYP3A5 blot was developed with the molecular weight marker from the GAPDH blot superimposed onto the weak marker bands of the original CYP3A5 blot. Samples 1-7 correspond to the following total protein extracts: (1) Molecular Weight Marker; (2) HEK293 Control; (3) HEK293 + 10 mM KCl (48 hours); (4) HEK293 + 50 mM KCl (48 hours); (5) HEK293 + 100 mM KCl (48 hours); (6) HEK293 + 100 mM NaCl (48 hours); (7) HEK293 + 100 mM NH_4Cl (48 hours); Note: The results from lane 7 were not discussed in the main manuscript, due to lack of complimentary data for NH_4Cl in related assays. However, NH_4Cl was also a potent inducer of NMD read-through for *CYP3A5*3* transcripts expressed in HEK293 cells.

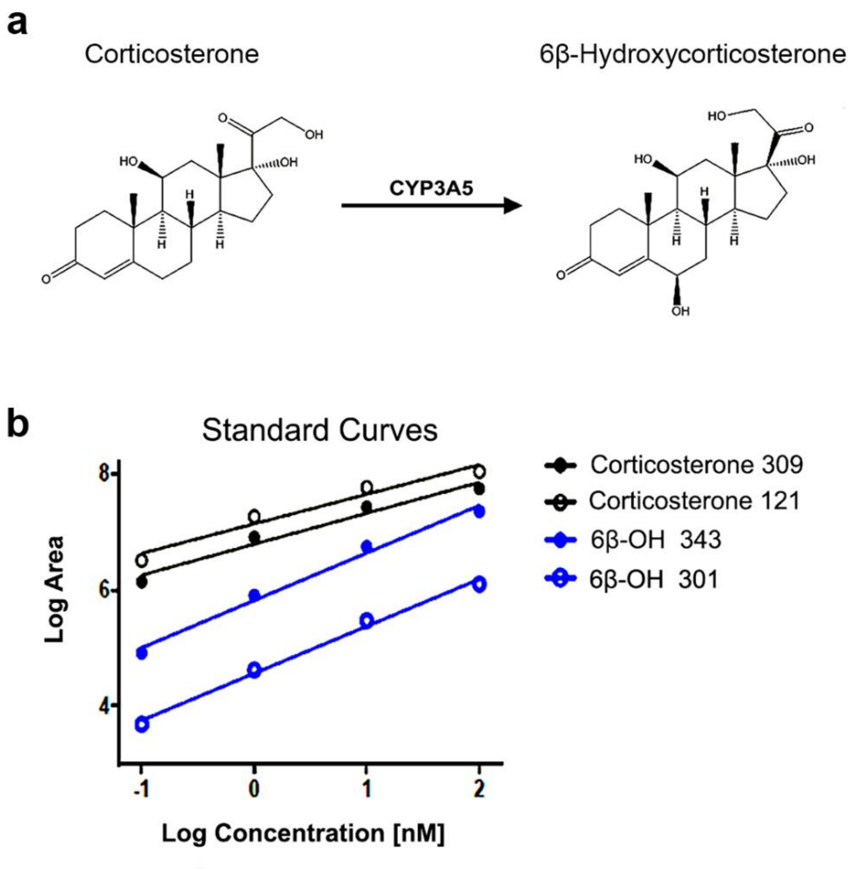

Supplemental Figure 2.5. LC/MS Standard Curves for Detecting the Conversion of Cortisol to 6β-hydroxycortisol in KCl-treated HEK293 cells. a) Chemical structures of cortisol and the CYP3A5 metabolite, 6β-hydroxycortisol. b) LC/MS standard curves for diagnostic fragment ions of cortisol and 6β-hydroxycortisol.

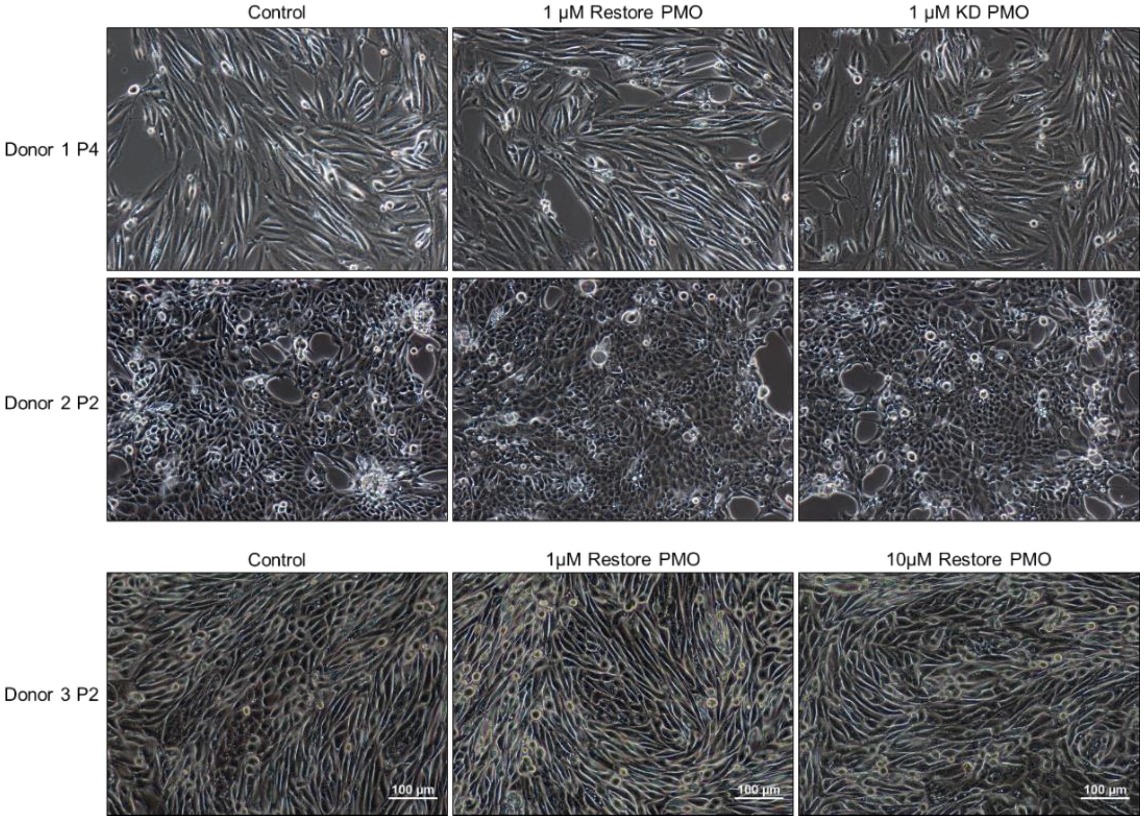

Supplemental Figure 2.6. PTEC morphology is unaffected by treatment with 3A5*3 or AUG PMOs. Phase contrast images of PTECs at the end of treatment with the restore (3A5*3) or knock down (KD) or AUG PMO shows no change in cell morphology. At higher passage, the cells take on an elongated morphology.

Donor no.	Age	Sex	Ethnicity	Pre-existing conditions	Reason for nephrectomy
1	69	Male	White	N/A	Renal Cell Carcinoma
2	55	Male	White	Polyuria, Hyperkalemia, Polymyalgia Rheumatica	Renal Cell Carcinoma
3	62	Male	White	Gross hematuria, Hypertension, Obstructive Sleep Apnea, Depression	Clear Cell Renal Cell Carcinoma
4	63	Female	White	N/A	Unclassified Renal Cell Carcinoma
5	63	Male	White	Horseshoe Kidney	Oncocytoma
6	62	Male	White	Hypertension	Clear Cell Renal Cell Carcinoma
7	57	Male	White	N/A	Clear Cell Renal Cell Carcinoma
8	64	Male	White	Diverticulosis, Hyperlipidemia, Hypothyroid	Chromophobe Renal Cell Carcinoma

Supplemental Table 2.1. Kidney Tissue Donor Demographics for PT-MPS Study.

3. Serum protein exposure activates a core regulatory program driving human proximal tubule injury

Portions of this chapter have been submitted to JCI in May 2021.

3.1 Abstract

The kidneys efficiently filter waste products while retaining serum proteins in the circulation. However, in numerous diseases, this barrier function is compromised resulting in spillage of serum proteins into the urine (proteinuria). It remains controversial if specific serum components can directly injure the downstream tubular portions of the kidney which in turn can lead to inflammation and fibrosis. Since this question cannot be directly answered in animal models, we tested the effects of serum protein exposure in a human kidney tubule microphysiological system (MPS). Serum, but not its major protein component albumin, induced tubular injury and secretion of pro-inflammatory cytokines and matrix modifying enzymes. Concordant transcriptional changes in pro-inflammatory cytokines and matrix modifying enzymes were observed in an independent cohort of patients with proteinuric kidney disease. Epigenomic comparison of serum-injured tubular cells and intact kidney tissue revealed the injury induced genes were regulated by canonical stress-inducible transcription factors. Our results demonstrate a causal role for serum proteins in tubular injury and identify regulatory mechanisms and novel pathways for intervention.

3.2 Introduction

The kidneys play an essential homeostatic function by filtering out waste products of metabolism. While small waste molecules are freely filtered, larger serum proteins such as albumin and immunoglobulins are efficiently retained within the circulation. However, the selectivity of the kidney filtration barrier is disrupted in several common diseases, resulting in the spillage of serum proteins into the urine (proteinuria). It is estimated that 10% of adults in the United States have elevated levels of serum-derived albumin detectable in their urine.[246] A low protein diet reduces proteinuria and slows the progression of chronic kidney disease.[247, 248] Even the benefits of widely used anti-hypertensive medications, angiotensin converting enzyme inhibitors (ACEi), in slowing chronic kidney disease progression are in part due to their proteinuria-lowering effect and independent of blood pressure control.[118, 249, 250]

Whether proteinuria can directly activate injury programs in kidney tubules still remains controversial.[120] In fact, some studies propose that tubules downstream of the kidney filter may be exposed to high concentrations of serum proteins even under normal physiologic conditions.[251, 252] Serum represents a complex mixture of major proteins such as albumin, immunoglobulins, fibrinogen, transferrin, a2-macroglobulin, complement C3 as well as numerous other proteins, sugars, lipids and small molecules. Even if serum can cause tubular injury, it is not known which protein component(s) are responsible. This question cannot be studied in animal models since it is not possible to expose tubules *in vivo* to protein mixtures of defined composition. Traditional *in vitro* 2D culture systems do not faithfully recapitulate the complex transcriptional programs of intact tubules in native kidney cortex.[253] In multiple systems, injured kidney tubules acquire a pro-inflammatory state and express extracellular matrix (ECM) remodeling enzymes which can lead to progressive kidney injury, fibrosis and chronic kidney disease.[76, 127-130, 132] Therefore understanding whether serum proteins can directly injury kidney tubules and dissecting the underlying mechanisms is a pressing human health need.

To address this, we used transcriptional and epigenomic profiling to study the human tubular epithelial cell response to serum protein exposure. First, we studied serum induced injury using a microphysiological system (MPS) that creates a three dimensional *in vivo*-like microenvironment. The MPS enables primary human proximal tubule epithelial cells (PTECs) to recapitulate the metabolic, regulatory, and transport activities of the kidney proximal tubule as shown by our group [84-88] as well as others [199, 201, 202]. These studies revealed that whole human serum, but not albumin alone induced an injury-associated transcriptional response. Second, we compared the transcriptional and epigenomic landscapes of fetal bovine serum-injured tubular cells to those of intact kidney tissue. This elucidated the regulatory programs driving the tubular injury response. Finally, we validated our transcriptional findings at the protein level and identified matrix metalloproteinase 1 (MMP1) and matrix metalloproteinase 7 (MMP7) as potential mediators of serum-induced injury in proteinuric human kidney disease.

3.3 Materials and Methods

3.3.1 Human kidney tissues and primary cell cultures

Deidentified kidney samples were collected through Northwest Biotrust at the University of Washington (UW) Medical Center with UW IRB approval (Study 00001297). Donor demographics are listed in Supplemental Table 3.1. Both intact renal tissue and primary tubular cell cultures were derived from tumor-adjacent normal tissue in nephrectomy specimens. For intact tissues, macrodissected portions (~100-200mg) of renal cortex and medulla were snap-frozen in liquid nitrogen and stored at -80°C until experiments were performed. In addition, tissue sections were stabilized in RNALater (Invitrogen) overnight at 4°C before long term storage at -80°C. Isolation and culture of primary tubular epithelial cells in the presence of 10% FBS has been described earlier.[254] In brief, after protease digestion, cortex fragments were placed in tissue culture-treated flasks enabling outgrowth of cortical tubular epithelial cells. Cells were grown in RPMI supplemented with 10% FBS and insulin-transferrin-selenite+ (ITS+, Corning, 354352) supplement. Isolation and culture of PTECs in serum-free media has also been previously described.[88, 255] PTEC cultures were maintained in serum-free medium comprised of DMEM/F12 (Gibco, 11330-032) supplemented with 1x insulin-transferrin-selenium-sodium pyruvate

(ITS-A, Gibco, 51300044), 50 nM hydrocortisone (Sigma, H6909), and 1x Antibiotic-Antimycotic (Gibco, 15240062). For passaging, the cells were subjected trypsin digestion using 0.05% trypsin EDTA (Gibco, 25200056) and manual cell scraping upon reaching 70-80% confluence. The single-cell suspension solution was neutralized with defined trypsin inhibitor (Gibco, R007100), centrifuged at 200 x g for 5 mins, and resuspended in serum-free maintenance media. The cells were replated into tissue culture-treated flasks at >30% confluence. All experiments were performed with cells passage 2-4.

3.3.2 Generation of proximal tubule microphysiological system (PT-MPS)

Triplex™ microfluidic devices were purchased from Nortis, Inc. (Woodinville, WA) and prepared as previously described with slight modifications [84, 255]. Briefly, device chambers were filled with 6 mg/mL rat tail type I collagen (Corning, 354236) and the matrix was allowed to polymerize overnight at room temperature. Microfiber inserts were removed, and the resultant channel was coated by injecting 2 µL of 0.1 mg/mL collagen IV (Corning, 354233) using a 5 µL syringe (Hamilton, 7634-01) outfitted with a 22-gauge small hub needle (Hamilton, 7804-01). Devices were incubated for 30 min at 37°C before initiating flow at 1 µL/min and equilibrating the system with serum-free maintenance media for 2 hours. PTECs were harvested from culture vessels and resuspended at a concentration of ~20 X 10^6 cells/mL, and ~2.5 µL was injected into each channel. The cells were allowed to adhere for 2-4 hours before initiating flow at 1 µL/min. During treatment, effluent was collected from outflow collection reservoirs at specified timepoints and transferred to microcentrifuge tubes for storage at -80°C until analysis.

3.3.3 Treatment of PT-MPS

PT-MPS were maintained in serum-free medium for 7-10 days prior to treatment with serum-free medium (control), 2% normal human serum, or albumin. To prepare 2% human serum treatment medium, normal human serum (Valley Biomedical, HS1021) was diluted in serum-free medium to a final volume/volume ratio of 2%. To prepare albumin treatment medium, albumin powder (GeminiBio, 800-126P) was solubilized in serum-free medium to 720 µg/mL, the concentration of albumin present in the 2% human serum treatment medium. A flow rate of 1 µL/min was used for all treatments and cell-conditioned effluent was collected for measurements. PT-MPS were treated for 48 hours with serum-free medium (control) or 2% normal human serum for Ki67 labeling (Figure 3.1B-C) and RNAseq (Figure 3.2, Supplemental Figures 3.2 and 3.3). PT-MPS were treated for 7 days with serum-free medium, 2% normal human serum, or albumin (720 µg/mL) for RNAseq (Figure 3.6) and analysis of cell-conditioned effluent by ELISA (Figure 3.7B).

3.3.4 Immunofluorescence microscopy

All procedures were performed at room temperature with a flow rate of 10 µL/min for all solutions. At the end of treatment, the cells were fixed by perfusing 10% phosphate-buffered formalin (Fisher, SF100-4) for 30 min followed by a 60-min wash with phosphate-buffered saline (PBS, ThermoFisher, 14040133). The devices were stored at 4°C for not more than 2 weeks before further processing. To prepare the tubules for labeling of marker of proliferation Ki-67 (Ki-67), the channels were blocked and permeabilized with PBS containing 5% bovine serum albumin (BSA; Sigma, A2153) and 0.1% Triton X-100 for 2 hours. Rabbit monoclonal anti-Ki67 (Abcam, ab16667) was diluted 1:10 in PBS with 5% BSA and 10 µL was injected into each channel and allowed to incubate for 1 hour. The channels were washed with PBS with 0.05% Tween-20 for 2 hours followed by a 1-hour perfusion of a fluorescently tagged goat anti-rabbit secondary antibody (Fisher, A11037) diluted 1:1000 in PBS with 5% BSA. The channel was washed once more with PBS with 0.05% Tween-20 for 2 hours before the nuclei were labeled by perfusion of 1 ug/mL Hoechst 33342 in PBS for 30 min followed by a 30-min PBS wash. The cells were imaged on a Nikon Eclipse Ti-S microscope (Melville, NY) equipped with a Nikon DS-Fi3 camera (Melville, NY). The total number of nuclei and Ki67-positive nuclei in each 10x image were determined by manual count with the multi-point tool in ImageJ (Laboratory for Optical and

Computational Instrumentation, University of Wisconsin, v.151). The percentage of nuclei positive for Ki67 was calculated as the ratio of the number of Ki67 positive nuclei over the total number of nuclei.

3.3.5 ELISA

Protein levels of IL-6, IL-8, KIM-1 (HAVCR1), total MMP1, and total MMP7 were quantified from device effluents using the DuoSet® line of ELISAs from R&D Systems according to the manufacturer's instructions. For quantification of MMP7, all samples were diluted 1:12 in reagent diluent (R&D systems, DY995). To adjust for baseline MMP1 levels in human serum, the baseline value determine in 2% human serum (50 pg/mL) was subtracted from all serum-treated samples. The levels of IL-6, IL-8, KIM-1, and MMP7 in 2% human serum were below the limit of detection.

3.3.6 RNA-seq data generation and analysis

For MPS cultures treated for 48-hours with either serum-free medium or 2% human serum, the cells were harvested from devices by injecting 100 µL of detergent (Abcam, part 8206000) into the injection port using a 1mL slip-tip syringe (BD, 309659) equipped with a 22-gauge needle (BD, 305142). Cell lysate was collected into 900 µL Trizol and frozen at -80 degrees Celsius until extraction. RNA was isolated using a RNeasy Micro Kit (Qiagen, 74004) and the RNA library was prepared with the SMARTer Stranded Total RNA Sample Prep Kit - Low Input Mammalian (Takara Bio, 634861) and sequenced as described previously [86].

RNA-seq data for primary cultures of human tubular epithelial cells grown in 10% FBS were previously generated [254] and downloaded from the Gene Expression Omnibus (GSE115961). For intact human kidney cortex and medulla, RNA extraction and RNA-seq was performed by GeneWiz (South Plainfield, New Jersey). For both sets of RNA-seq data, the paired end fastq files were trimmed and then aligned to human reference genome sequence hg38 using STAR 2.7.5b (doi:10.1093/bioinformatics/bts635) with parameters --outFilterIntronMotifs RemoveNoncanonical --

outFilterMismatchNoverReadLmax 0.04 using annotation file Homo_sapiens.GRCh38.100.gtf downloaded from Ensembl database. The number of reads aligned to each exon (feature) was counted using *featureCounts* from subread package (doi:10.1093/bioinformatics/btt656). Multimapped reads were excluded. Differential expression of genes and read count normalization was performed using DESeq2 (doi:10.1186/s13059-014-0550-8) with the design formula "~ condition".

Slight variations of the above protocol and analysis were used for the MPS treated for 7 days with 2% human serum, albumin (720 µg/mL), and serum-free medium (control). Cells were isolated by injecting 100 µL of the lysis buffer RLT (Qiagen, 79216) and the lysate was collected at the outflow port into an additional 900 µL of buffer RLT and frozen at -80°C until total RNA extraction using a Qiagen RNeasy Micro Kit. Total RNA was normalized to 2 ng in a total volume of 9 µl and then transcribed to cDNA in a dedicated PCR clean workstation using the SMART-Seq v4 Ultra Low Input RNA Kit (Takara Bio). Sequencing libraries were constructed from cDNA using the SMARTer ThruPLEX DNA-Seq kit (Takara Bio). Final libraries were quantified, and library insert size distribution was checked using the Bioanalyzer (Agilent Technologies, Santa Clara, CA). Base calls generated in real-time on the NovaSeq 6000 instrument (RTA 3.1.5); demultiplexed, unaligned BAM files produced by Picard ExtractIlluminaBarcodes and IlluminaBasecallsToSam are converted to FASTQ format using SamTools bam2fq (v1.4).

Resulting sequences were aligned to the reference genome GENCODE human release 30 using STAR (v2.6.1d). Aligned data were read into R (version 3.6.1) and summarized as counts per gene using the Bioconductor GenomicAlignments package [256]. Before fitting any models, we first excluded any genes that were expressed at consistently low levels across all samples. Prior to filtering, we had data for 58,870 genes and after filtering we had data for 15,336 genes. We then performed a trimmed mean of M-values (TMM) normalization [220]. We used the voom method from the Bioconductor limma package, which estimates the mean-variance relationship of the log2-counts per million (logCPM) and generates a precision weight for each observation and enters these into the limma analysis pipeline. We used a linear mixed model approach, fitting the treatment as the fixed effect and the donor as the random effect by estimating the within-donor correlation. We fit a linear model with treatment and incorporating the within-donor correlation. Since not all donors received all the treatments at each condition, the mixed model approach provides more statistical power for the unbalanced design. Rather than using a post-hoc fold-change filtering criterion, we used a t-tests relative to a threshold (TREAT) approach [222], which incorporates the fold-change into the statistic, meaning that instead of testing for genes which have fold-changes different from zero, we tested whether the fold-change is greater than 1.1-fold in absolute value. We selected genes based on a threshold of 1.1-fold-change and a false discovery rate of 5%.

Identification of pathway perturbation and key upstream regulators was performed using Advaita iPathwayGuide (https://advaitabio.com/ipathwayguide/). Gene ontology and known transcription factor target enrichments using ENRICHR were both performed using the BioJupies web tool (https://doi.org/10.1016/j.cels.2018.10.007).

3.3.7 Chromatin accessibility data

DNase-seq data for primary cultures of human tubular epithelial cells grown in 10% FBS were previously generated [254] and downloaded from the Gene Expression Omnibus (GSE115961). ATAC-seq was performed on snap-frozen samples of human kidney cortex by ActiveMotif (Carlsbad, California) and aligned to the GRCh38 (hg38) reference genome using BWA and default settings. Read depth was normalized by random downsampling to the level of the sample with lowest coverage (29,795,703 tags). Total peaks were called using MACS 2.1.0 at a cutoff of p-value = 10^{-7}, without a control file and with the -nomodel option. Peak filtering was performed by removing false ChIP-Seq peaks as defined within the ENCODE blacklist. The resulting intervals were merged into a non-overlapping ATAC-seq masterlist. We merged this with our previously reported masterlist (primary cultures of human kidney tubules, glomerular outgrowths and ENCODE tubule culture datasets RPTEC, HRE and HRCE) using a bedops -u command. Overlaps between lists of regulatory elements were determined using the bedops -e (element of) and bedmap set operations. To identify regulatory elements with significantly different accessibility between intact renal cortex and cultured tubular cells, we counted reads mapping to every master list element in each sample. We utilized the DESeq2 software package in R to identify regulatory elements with significantly different accessibility between replicate cortex and tubule culture samples, analyzing each sample separately. Sites that met an adjusted p-value < 0.001 were considered to be differentially accessible regulatory elements. The distance of regulatory elements to the nearest gene transcription start site (TSS) and the associated biologic ontologies were computed using the Stanford GREAT analysis tool. An adjusted p-value < 0.0001 was used for determination of differentially accessible regulatory elements within 2.5kb of the TSS of differentially expressed genes (also determined using an adjusted p-value<0.0001). Transcription factor motif enrichment analysis was performed using HOMER using the list of non-significantly changed regulatory elements as the background set and default settings. The 733-cell regulatory element index and UCSC custom track of transcription factor archetypes and DNaseI footprints were obtained from recent publications.

3.3.8 Data availability

RNA-seq data from MPS cultures were submitted to GEO (GSE159554; reviewer token mhybqguqdtihtgn). RNA-seq and ATAC-seq data from intact renal cortex is also available on GEO (GSE152302; reviewer token gfmfesyorbunfon).

3.4. Results

3.4.1 Serum exposure induces a consistent injury response in kidney tubular epithelial cells

Seeding of primary human proximal tubular epithelial cells into the central lumen of a collagen I matrix within a microphysiological system (MPS) reproducibly produced a polarized monolayer of cells with a central lumen (hereafter referred to as PT-MPS; Figure 3.1A). Once established, the tubular epithelial monolayer was maintained under continuous flow without evidence of tubular epithelial turnover or proliferation as measured by Ki-67 immunofluorescence. In contrast, exposure of cells to 2%

human serum in the perfusate resulted in an increase in Ki-67 immunofluorescence, a marker of mitotic activity (Figure 3.1B, C).

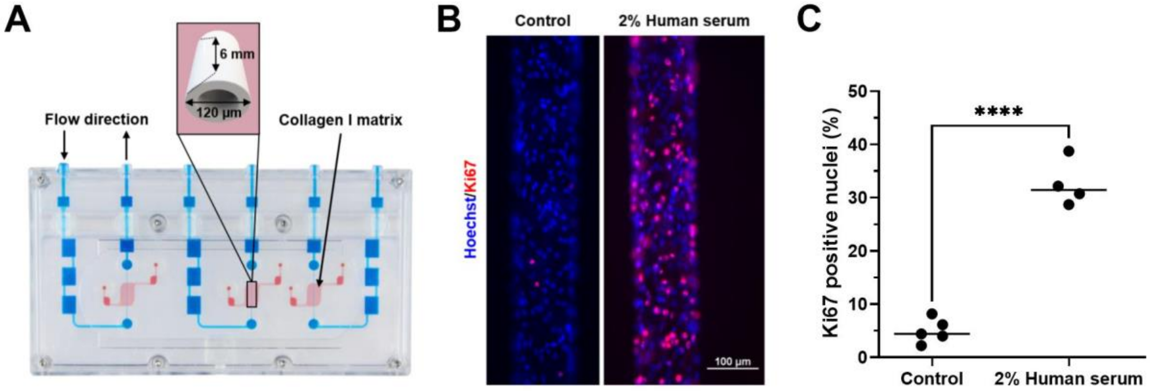

Figure 3.1. Human kidney tubules in 3D microphysiologic devices proliferate in response to serum exposure. A) Schematic of 3-channel Nortis microphysiologic system (MPS). The red areas represent a 3D chamber filled with collagen I extracellular matrix in which a central channel seeded with proximal tubular epithelial cells can be perfused with medium (blue). B) Compared to control, PT-MPS treated with 2% human serum for 48 hours have a higher proportion of nuclei (blue) that are positive for the proliferative marker Ki-67 (red). C) Percent of Ki-67 positive nuclei in control (n=5) and serum-treated PT-MPS (n=4) from Donors 1 and 2; **** p <0.0001 by two-tailed t-test.

To further characterize the changes induced by acute 48-hour 2% human serum exposure, we extracted RNA from replicates of control or serum-treated tubular MPS, and measured gene expression by RNA-seq. Exposure of PT-MPS to 2% human serum induced upregulation of 533 genes and downregulation of 406 genes with a fold-change > 1.5 and Benjamini & Hochberg adjusted p-value < 0.05 (Figure 3.2a). Gene ontology enrichment analysis of the differentially expressed genes showed significant upregulation of biological processes related with cytokine-mediated signaling pathways (GO:0019221), extracellular matrix organization (GO:0030198) and negative regulation of apoptotic processes (GO:0043066) in 2% human serum-treated PT-MPS. Conversely, biological processes associated with regulation of cholesterol metabolic process (GO:0090181) and regulation of alcohol biosynthetic process (GO:1902930) were significantly downregulated (Figure 3.2b). Overall, the gene ontology terms identified in 2% human serum treated PT-MPS were similar to a standard model of kidney injury and fibrosis, the murine unilateral ureteral obstruction model (Supplemental Figure 3.1).[257] Advaita iPathwayGuide analysis identified TNF, EGF, FOXM1 and IL1A/B as key upstream regulators based on differential expression of their known target genes (data not shown). Advaita Pathway analysis also identified that cytokine/chemokine- (FDR =3.383x10-6), TNF- (FDR =3.371x10-4) and NF-κB- (FDR =3.371x10-4) signaling pathways were prominent points of regulation in 2% human serum-treated MPS (Figure 3.2c).

Next, we sought to confirm our findings in an orthogonal and supraphysiologic system by comparing the transcriptional and epigenomic response of primary human tubular epithelial cells cultured in 10% FBS to intact renal cortex. Comparison of the transcriptome of human tubular epithelial cells cultured in 10% FBS to intact renal cortex revealed 21,092 genes were differentially expressed, of which 939 were also differentially expressed in the PT-MPS (Figure 3.2A). Of these 939 genes, 661 (70.4%) showed significant differential expression with the same directionality i.e., up- or down-regulated as the MPS system (Figure 3.2A). In Advaita iPathwayGuide analysis, significantly enriched pathways include: metabolic pathways (FDR = 7.117x10-19), cell cycle pathways (FDR = 8.819x10-5), and cytokine/chemokine-mediated signaling pathways (FDR = 1.304x10-5), similar to that seen with serum-treated PT-MPS (Figure 3.2B). Taken together, these findings demonstrated that upon exposure to serum, human kidney tubular epithelial cells activate an injury response program involving production of pro-inflammatory cytokines, extracellular matrix (ECM) remodeling components, alteration of metabolism and induction of proliferation which is similar to the transcriptional changes in a mouse model of unilateral ureteral obstruction induced injury (Supplemental Figure 3.2).

To gain insight into the regulatory processes driving the tubular epithelial cell injury response, we generated chromatin accessibility profiles from intact renal cortex from 3 donors using ATAC-seq. We compared these profiles to previously generated DNase-seq data from primary tubular epithelial cells cultured in 10% FBS. We generated a master list of 555,884 regulatory elements that incorporated accessible chromatin regions from adult kidney derived primary cultures, cell lines and intact kidney cortex. Within this, 44,756 elements (8.1%) showed significantly higher accessibility in tubular epithelial cells cultured in 10% FBS compared to intact renal cortex (Figure 3.3C). Conversely, 37,053 elements (6.7%) showed higher accessibility in intact renal cortex compared to cultured tubular epithelial cells.

Differentially accessible regulatory elements likely represented the portion of the epigenome that was driving gene expression differences between intact renal cortex and culture tubular epithelial cells. In support of this idea, differentially-accessible regulatory elements were more likely to be located near genes exhibiting significantly different expression levels between cultured tubular epithelial cells and intact cortex. For example, 2,941/11,633 (25.3%) of differentially-expressed genes had a differentially accessible regulatory element within 2.5kb of their TSS. In contrast 5,828/49,017 (11.9%) of non-changing genes had at least one differentially accessible regulatory element near their TSS (Chi-squared with Yates Correction $p<0.0001$). Stanford GREAT analysis of the regulatory elements with higher chromatin accessibility in serum-injured tubular epithelial cell cultures showed enrichment for molecular functions related to cytokine activity, extracellular matrix binding, and TGFβ and TNF receptor binding (Figure 3.3C), which correlated well with the transcriptional analysis of serum-injured tubular epithelial cells in both 2D and 3D contexts.

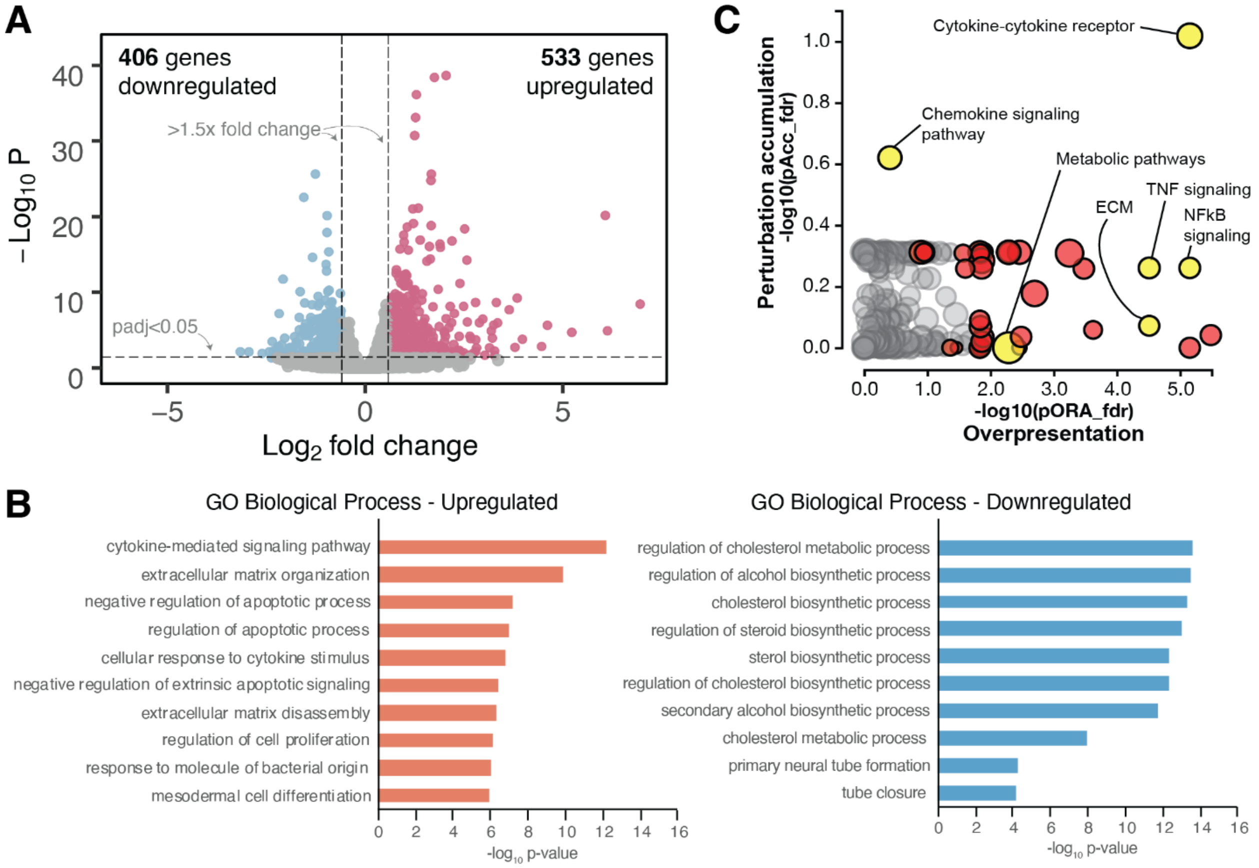

Figure 3.2. Serum exposure induces cytokine production and metabolic reprogramming in kidney tubule cells. A) Volcano plot of differentially expressed genes in MPS exposed for 48hrs to 2% human serum (n=6) vs. untreated control (n=5). Upregulated = higher expression in serum treated MPS. B) Gene ontology enrichments for top 10 up- and down-regulated biological process in the differentially expressed gene set. C) Advaita pathway analysis demonstrates significant perturbation of cytokine, chemokine, TNF and NF-κB signaling pathway components in serum-exposed tubule cells. Dots representing pathways are positioned by their p-value from an impact analysis measuring total perturbation accumulation (pAcc) vs. a classic over-representation analysis (pORA). Pathways with FDR < 0.05 by both analyses are shown in red. Selected pathways are highlighted in yellow.

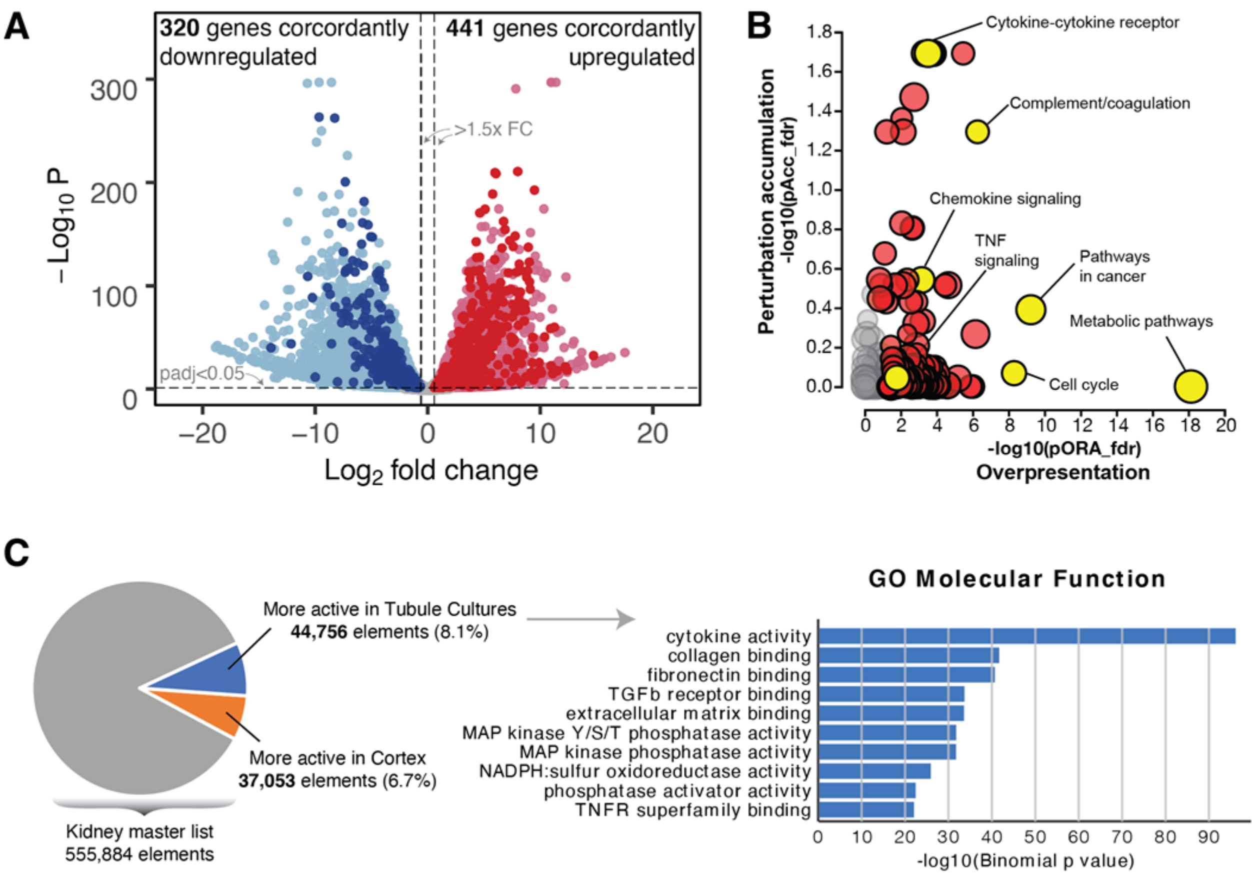

Figure 3.3. Global transcriptional changes induced in primary tubules cultures in 10% FBS. A) Volcano plot of differentially expressed genes between intact renal cortex and kidney tubular epithelial cells cultured in 10% FBS (lighter dots). Upregulated = higher expression in cultured tubules. The darker dots represent genes that exhibit the same directionality of significant gene expression change in the PT-MPS serum exposure experiment (Figure 3.2A). B) Advaita pathway analysis demonstrates significant perturbation of metabolic, cytokine/chemokine, and cell cycle pathway components in 10% FBS-exposed tubular epithelial cells. Dots representing pathways are positioned by their p-values from an impact analysis measuring total perturbation accumulation (pAcc) vs. a classic over-representation analysis (pORA). Pathways with FDR < 0.05 by both analyses are shown in red. Selected pathways are highlighted in yellow. C) The molecular function of genes located close to regulatory elements with greater accessibility in serum-injured tubular epithelial cells are shown.

3.4.2 Transcription factor drivers of serum-induced tubular transcriptional response

Next, we used two complementary approaches to understand the influence of transcription factors on gene regulation. First, we used ENRICHR-ChEA which utilizes a database of transcription factor target genes annotated by ChIP-seq (i.e., ChEA database) and analyzes whether groups of genes within a gene set (i.e., control vs serum-treated PT-MPS) are enriched under a particular transcription factor.

ENRICHR-ChEA implicated NF-κB, SMAD3, AP-1 and FOXM1 transcription factors in orchestrating the tubular response to serum exposure in both the PT-MPS and tubular epithelial cell vs intact cortex systems (Figure 3.4A and B). The transcript expressions of many of these transcription factors were increased in serum-exposed tubular epithelial cells in both of our model systems (Figure 3.4A and B). The lack of significant induction of *JUN*, an AP-1 component is consistent with its known regulation at the post-transcriptional level. In a complementary approach, we leveraged our chromatin accessibility datasets to ask which transcription factor binding motifs were enriched in regulatory elements with greater accessibility in intact renal cortex vs. tubular epithelial cells cultured in 10% FBS. Using HOMER, we found that regulatory elements more accessible in renal cortex compared to tubular epithelial cells in 10% FBS were highly enriched in binding motifs for HNF4A, PPARA, PPARG, RARA, ESRRA and RXR transcription factor families (Figure 3.4C). Conversely, the regulatory elements with greater accessibility in cultured tubular epithelial cells compared to intact renal cortex exhibited a strong enrichment for AP-1, NF-κB and FOXM1 transcription factor binding motifs (Fig. 3.4D), some of which also exhibit increased transcript expression in serum-exposed tubular epithelial cells (Supplemental Figure 3.3). Taken together, the complementary and orthogonal analyses (GREAT, ENRICHR, HOMER) depicted in Figure 3.3 and 3.4 demonstrate that serum-exposed tubules exhibit a strong stress-response signature coordinated by AP-1, NF-κB and FOXM1 transcription factors.

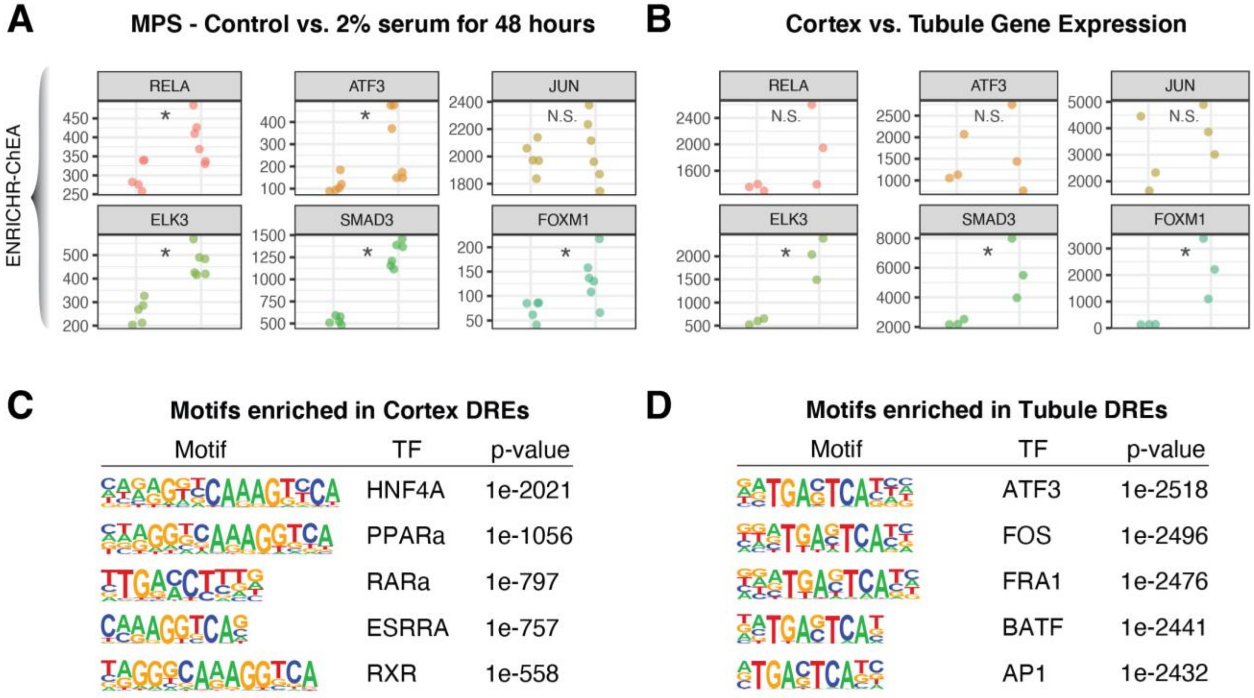

Motifs enriched in Cortex DREs

Motif	TF	p-value
	HNF4A	1e-2021
	PPARa	1e-1056
	RARa	1e-797
	ESRRA	1e-757
	RXR	1e-558

Motifs enriched in Tubule DREs

Motif	TF	p-value
	ATF3	1e-2518
	FOS	1e-2496
	FRA1	1e-2476
	BATF	1e-2441
	AP1	1e-2432

Figure 3.4. Transcription factor drivers of the transcriptional landscape of serum-exposed tubules. Gene expression dot plots of transcription factors implicated by ENRICHR-ChEA as having significant changes in expression of their known target genes in A) PT-MPS and B) tubular epithelial cells cultured in 10% FBS. Transcription factor binding motif enrichments in regulatory elements with higher accessibility in C) intact renal cortex and D) tubules cultured in 10% FBS.

3.4.3 Integrative analysis of the canonical kidney injury gene loci

Regulatory elements can exhibit cell type and state-dependent patterns of accessibility. We therefore hypothesized that serum induced gene loci would exhibit kidney-specific patterns of regulatory activity. In testing this, we were aided by the recent publication of the ENCODE regulatory element index derived from 733 diverse cell types.[258] This index permitted identification of elements restricted to particular cell types or lineages and included kidney tubular epithelial cells cultured in 10% FBS. First, we examined the genomic region around the classic kidney injury biomarker gene *HAVCR1* (KIM-1). The *HAVCR1* gene is expressed at 23-fold higher levels in cultured tubular epithelial cells compared to intact renal cortex. This increased expression corresponded to distinct regions of open chromatin, with at least 5 regulatory elements in cultured tubular epithelial cells (vertical orange bars) that were not accessible in intact renal cortex (Figure 3.5A). In the 733-cell index, these regulatory elements exhibit an activity profile restricted to renal epithelial cells suggesting a kidney-specific role in *HAVCR1* gene regulation. Compared to intact renal cortex, other kidney injury marker gene loci showed distinct regulatory elements that were more accessible in tubular epithelial cells cultured in 10% FBS including *LCN2* (increased 64-fold), *HMOX1* (increased 4.3-fold), *QPRT* (decreased 3.4-fold), *IL6* (increased 2,435-fold) and *CXCL8* (increased 194-fold), though not all of these differentially accessible regulatory elements showed kidney-restricted patterns in the 733-cell regulatory index (Supplemental Figure 3.4).

Using deeply sequenced chromatin accessibility profiling data, the nucleotide sequence bound by a transcription factor appears as a region of protection (a footprint) in the broader region of open chromatin associated with that regulatory element. By reading the underlying DNA sequence and matching it against transcription factor motif archetypes, it is possible to infer transcription factor binding at a particular genomic location (at least at the level of transcription factor family with shared binding motifs). Recently, a large-scale effort to map transcription factor motif archetypes and actual footprints in multiple cell types/states has been described.[259] High-resolution examination of the regulatory elements around *HAVCR1* revealed overlap of predicted transcription factor motif archetypes with actual footprints in kidney tubule cells even at increasingly stringent FDRs (Figure 3.5B). This analysis implicated KLF, AP1 and nuclear receptor (NR) transcription factor families in the regulation of *HAVCR1* gene expression. Using our maps, similar analysis is possible at any locus within the genome. In this way, we were able to integrate gene expression, epigenomics and transcription factor binding to define the circuitry of the serum-induced tubular injury response at high-resolution.

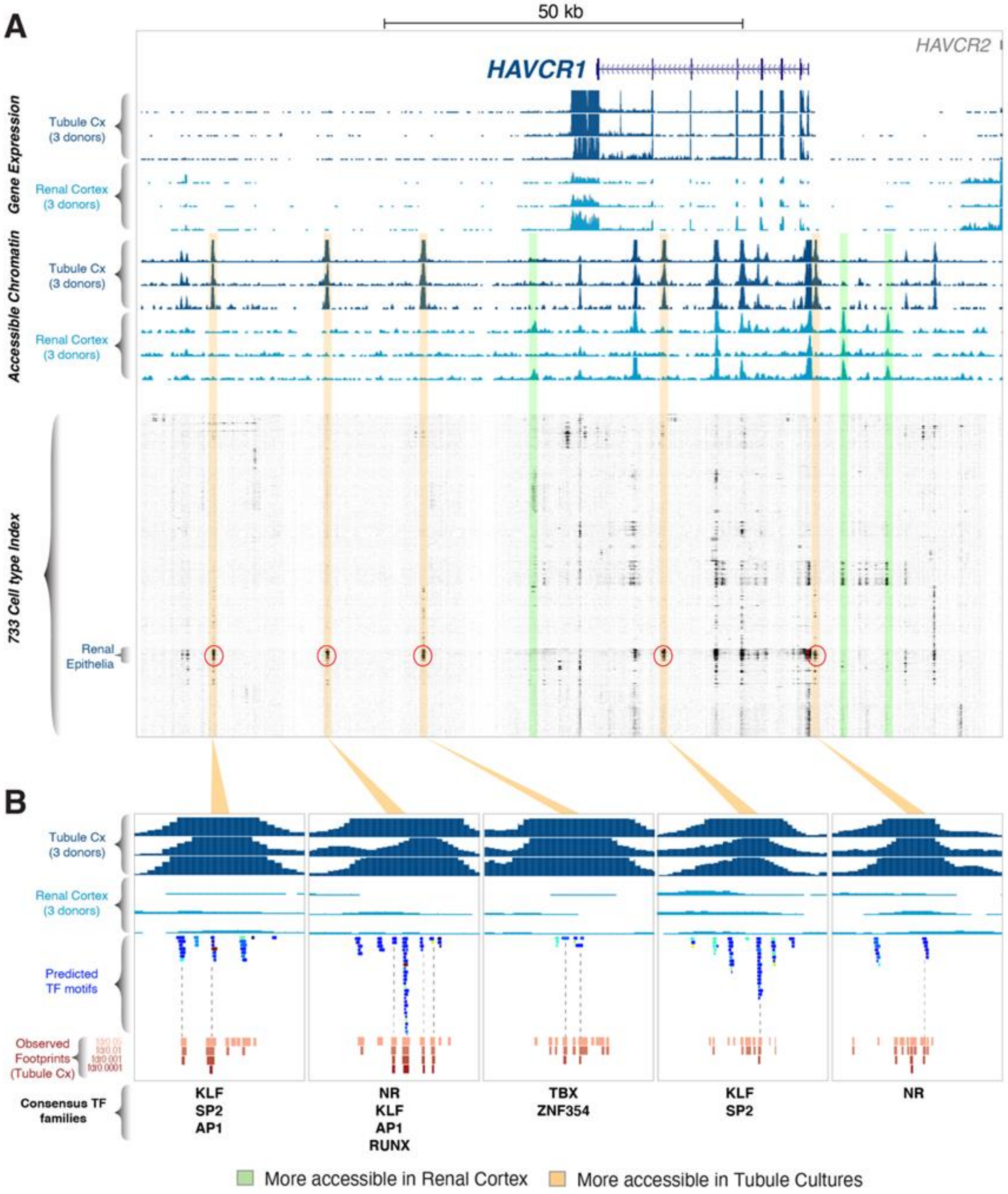

Figure 3.5. Integrative analysis reveals unique regulatory circuitry of *HAVCR1*. Overview of the A) HAVCR1 gene locus with gene expression (top) and accessible chromatin (middle) tracks for cultured tubules and intact renal cortex (3 donors each). The HAVCR1 gene is expressed at higher levels in tubules cultured in 10% FBS. Green vertical bars indicate regulatory elements with greater accessibility in intact cortex, while orange vertical bars indicate regulatory elements with greater accessibility in cultured tubules. Lower panel shows the activity of the same loci in the 733-cell ENCODE regulatory index with elements showing kidney-selective activity highlighted. B) Comparison of the predicted transcription factor motif archetypes to actual footprints (FDR≤0.001) in tubule DNase-seq data reveals overlap of predicted motifs for AP1 and NR families in kidney-selective regulatory elements identified in panels A.

3.4.4 Human serum- but not albumin-exposed PT-MPS develop a pro-inflammatory phenotype

We next asked whether the serum-induced tubular injury signatures we had defined were driven by albumin, the primary protein component of serum and were persistent (i.e., longer than 48 hours). To characterize the changes induced by serum or albumin exposure, we extracted RNA from multiple replicates of PT-MPS treated with control, albumin (720 µg/mL), or 2% human serum for 7 days and measured gene expression by RNAseq. Exposure of PT-MPS to 2% human serum, but not albumin alone, induced expression of genes related to cellular proliferation, extracellular matrix reorganization, and inflammatory cytokine secretion with concomitant downregulation of genes related to metabolism and solute transport (Figure 3.6).

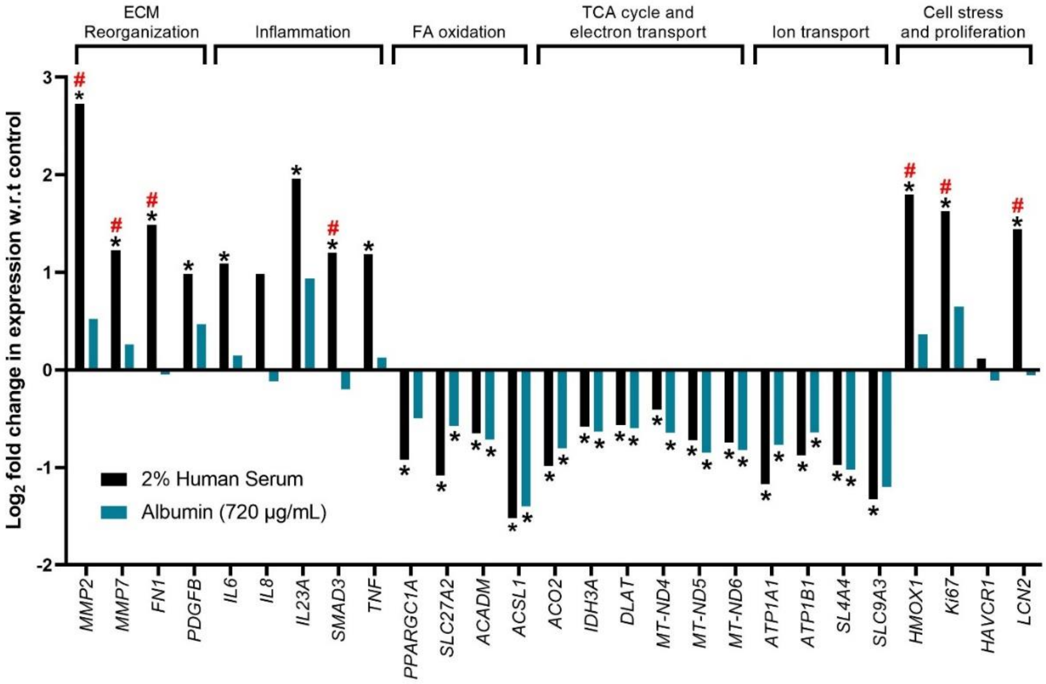

* Significant compared to respective control

Difference between 2% serum and albumin is also significant

Figure 3.6. Pro-inflammatory transcriptional response of PT-MPS to 2% human serum is independent of albumin. PT-MPS were treated for 7 days with either 2% human serum or an equivalent concentration (720µg/ml) of albumin then harvested for RNA-seq. A selected panel of genes and the $\log_2$ fold change in transcript expression relative to control are shown. * indicates the expression of the indicated gene (serum or albumin-treated) is significantly different from the control sample. # indicates the difference between serum and albumin is statistically significant.

To confirm the canonical stress response of tubular epithelial cells predicted from our transcriptomic and epigenomic studies, we next measured protein levels of pro-inflammatory cytokines (IL6 and CXCL8), matrix remodeling enzymes (MMP1 and MMP7) and shed HAVCR1 in control, albumin (720 µg/mL), and 2% human serum exposed PT-MPS effluents by ELISA. We collected effluents from early (8 hours) to later timepoints (7 days) and also exposed a parallel set of PT-MPS from the same donors to purified human albumin at concentrations equivalent to 2% human serum (720 µg/ml). For the majority of conditions, serum treatment rapidly and significantly increased secretion of these analytes relative to control, confirming the predictions from our multi-omic studies (Figure 3.7A). In contrast, albumin treatment induced only modest secretion of KIM-1 or MMP7 in 1 or 2 donors (Figure 3.7A).

Lastly, we asked if the pattern of a pro-inflammatory transcriptional signature induced in PT-MPS in response to 2% human serum, but not albumin, was conserved in patients with different forms of proteinuria. Patients with minimal change disease (MCD) experience heavy proteinuria with selective spillage of albumin but no other higher molecular weight serum proteins into the urine.[260] By contrast, patients with focal and segmental glomerulosclerosis (FSGS) experience non-selective proteinuria with spillage of albumin and other serum proteins into the urine.[261, 262] MCD has a favorable prognosis with little residual kidney injury or fibrosis. By contrast patients with FSGS often experience progressive kidney dysfunction, scarring and chronic kidney disease. We rationalized that the pro-inflammatory tubular injury response to serum but not albumin that we had discovered may underlie this difference in prognosis. To test this, we examined gene expression profiles of microdissected tubules from MCD and FSGS patients in the NEPTUNE cohort.[263] Correlating with the findings from the 3D PT-MPS and 10% FBS cultured tubular epithelial cells, we found that mRNA levels of *IL6*, *CXCL8*, *MMP1*, *MMP7* and *HAVCR1* were all increased in the tubulointerstitium of FSGS patients compared to MCD patients

(Figure 3.7B). These results orthogonally validated our multi-omic findings and demonstrated the power of the PT-MPS for dissection of tubular injury responses to defined stimuli.

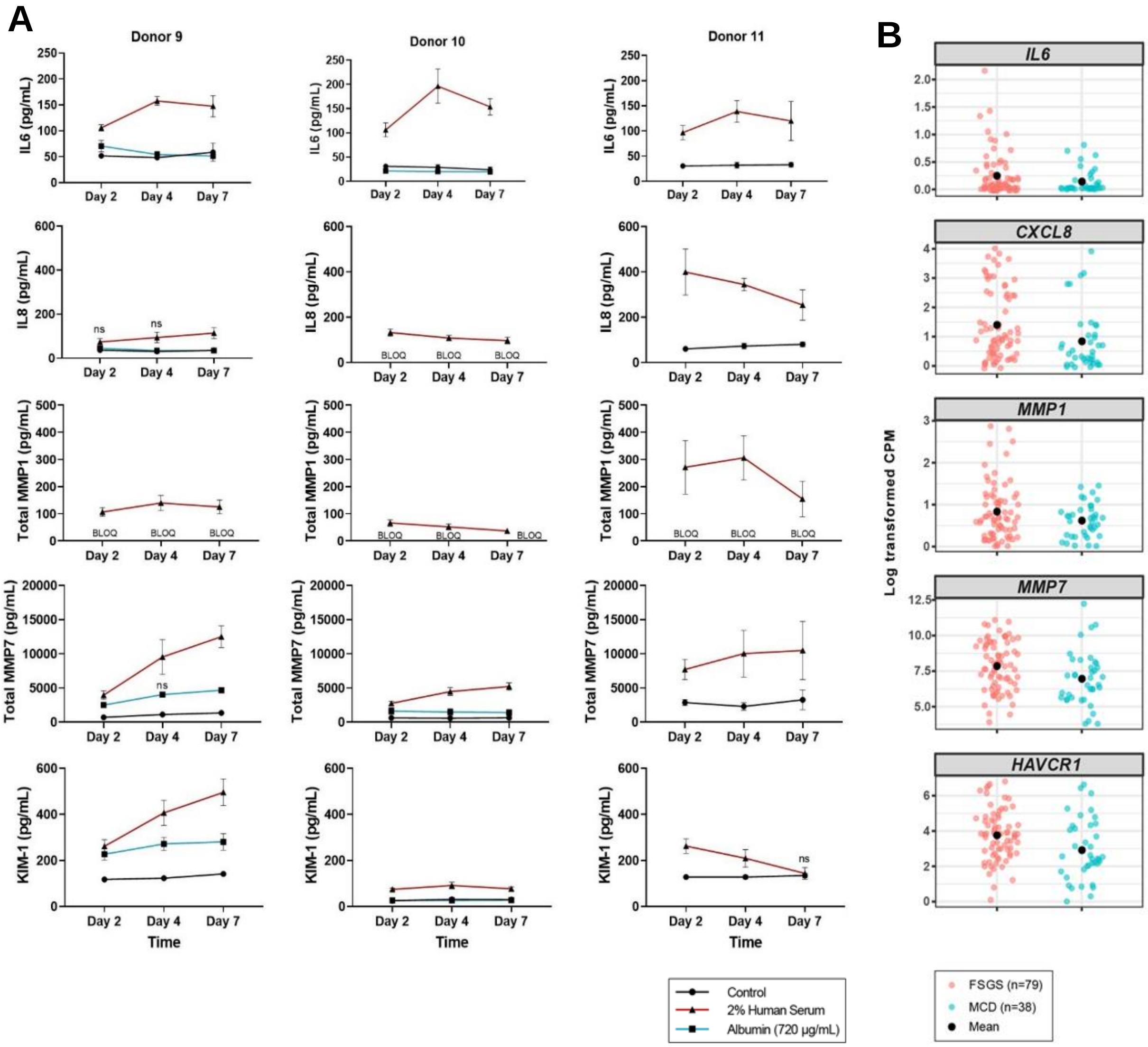

Figure 3.7. Serum exposure induces secretion of cytokines, matrix metalloproteinases and shedding of HAVCR1 in PT-MPS. A) Effluents from serum- and albumin-treated PT-MPS from 3 donors were assayed for IL6, IL8, MMP1, MMP7, and KIM-1 proteins by ELISA. All comparisons included at least 4 replicates for each timepoint and treatment, except for Donor 9, for which only 1 replicate was available for the day 2 and day 4 timepoints. Except where indicated as not significant (ns), all comparisons between serum and control samples were significant at an adjusted p-value < 0.05 using an unpaired t-test with Sidak-Holm correction for multiple comparisons. All comparisons between albumin and control were not significant, except for MMP7 for donor's 9 and 10 and for KIM-1 for donor 9, which were significant at all timepoints at an adjusted p-value <0.05 using an unpaired t-test with Sidak-Holm correction for multiple comparisons. B) Log transformed CPM expression levels of selected genes in the microdissected tubulointerstitium of FSGS (n=79) and MCD (n=38) patients from the NEPTUNE consortium. All p<0.05 by 1-tailed t-test. BLOQ, below limit of quantification.

3.5 Discussion

Here we demonstrate that exposure of human kidney tubular epithelial cells to serum but not albumin induces proliferation and upregulation of TNF-signaling associated cytokine and ECM remodeling genes with concomitant downregulation of transporters, channels and metabolic and biosynthetic programs. We propose that this represents a maladaptive response that can lead to progressive kidney damage and fibrosis (Figure 3.7). One of the central mediators, TNFα is produced by tubular epithelial cells[264] and its levels are increased during injury due to active rejection[265], cisplatin[264, 266] or unilateral ureteral obstruction.[267] After serum exposure, we were able to detect IL6 and CXCL8 in PT-MPS effluents which appears to mimic the increased levels of those same cytokines in urine from patients with ischemic injured allograft kidneys.[268] The perturbed pathways we have described do share many commonalities with other insults/disease states but, there are also distinctions compared to other nephrotoxins. While serum exposure represses the cholesterol biosynthetic pathway, we have previously shown that this same pathway can be dramatically upregulated in response to polymyxin B.[86] For the first time, we describe the epigenomic regulation of *HAVCR1*, a key kidney injury biomarker gene. *HAVCR1* is also upregulated in FSGS patients versus MCD patients and this correlates with increased shedding of HAVCR1 protein into the urine of these patients[269] and in our PT-MPS exposed to serum. We also detected secreted MMP7 and MMP1 within PT-MPS effluents following injury. Urinary MMP7 has recently been described as an adverse prognostic biomarker of AKI.[270, 271] MMP7 degrades E-cadherin and can release b-catenin[272] which in turn can reinforce MMP7 expression.[273] MMP7 is also induced in folic acid nephropathy and UUO animal models.[274] Besides being a biomarker, MMP7 may in fact be a pathogenic driver of kidney fibrosis.[270] Diabetic kidney disease is the most common etiology for proteinuria and in proteinuric diabetic patients, elevated urinary MMP7 levels are associated with progressive kidney disease and increased mortality.[275] In contrast, relatively little is known about the role of MMP1 in AKI. Therefore, further investigation of MMP1 and MMP7 as possible targets to treat AKI and subsequent remodeling of the tubulointerstitium is warranted.

The exact concentration of albumin that is physiologically present in the proximal tubule is a matter of continuing debate. It is thought to vary from ~30 µg/ml (glomerular sieving coefficient for albumin, GSC_A ~ 0.00062) determined from early micropuncture studies in the rat [276-279] to almost 40-50x higher, ~1.2 mg/ml (GSC_A ~ 0.025) using more recent two photon microscopy based approaches.[251, 252] The concentration of albumin used in our study (720 µg/ml) falls between the rat renal micropuncture and two photon microscopy estimates. If delivered to the final urine without reabsorption, 720 µg/mL albumin would result in albumin excretion of >1g/24 hrs and would represent clinically significant proteinuria. Our studies demonstrate that normal purified albumin alone does not induce a pro-inflammatory secretory phenotype for which other components of the serum appear necessary. Instead, we propose that non-selective proteinuria with albumin and other serum proteins being delivered to the tubules is responsible for the progressive tubulointerstitial injury and fibrosis seen with diseases such as FSGS and diabetic nephropathy[261, 262] (Figure 3.7). This would explain the favorable prognosis of MCD, which is associated with selective proteinuria (albuminuria), and recovery without kidney scarring. In contrast FSGS, which presents with non-selective proteinuria, often progresses to end-stage kidney disease. Of course, albumin can bind to numerous molecules whose composition and abundance in the serum can vary between healthy and disease states. Albumin is also subject to various modifications[280] that can alter its biodistribution and pharmacodynamics as was recently demonstrated for carbamylated albumin.[281] In future studies, multi-omic characterization of PT-MPS exposed to patient derived albumin (e.g. glycated forms)[282] or albumin ± other serum components will prove useful to dissect tubular injury mechanisms.

Our epigenomic findings complement and extend two recent single nucleus and single cell-based profiling studies of human and mouse kidney. Muto and colleagues integrated single nucleus RNA-seq and ATAC-seq to identify cell-type heterogeneity within the human kidney.[283] Park and colleagues used single cell RNA-seq and ATAC-seq as well as bulk RNA-seq to characterize cell-specific changes in human and mouse kidney during disease states.[284] Overall, our data presented here is in good agreement with their findings – namely that the activity of stress-associated transcription factors such as

NF-κB and AP-1 are enriched in PTEC subpopulations during injury, which may play a role in acquisition of a proinflammatory gene signature. Indeed, NF-κB has previously been implicated in driving the inflammatory response of PTECs to high molecular weight protein challenge, and its inhibition has been shown to mitigate pro-inflammatory cytokine production and prevent renal fibrosis in animal models of kidney disease.[112, 285, 286]

One limitation of our study is the limited number of samples, which was somewhat mitigated by consistent trends across biological replicates and cross-validation of key findings in patients with proteinuric kidney disease. A major advantage is our use of primary human kidney cells and tissues and orthogonal validation in the PT-MPS. In summary, the coordinated injury response that we described was consistent across both 2D and 3D model systems and was similar to pathways that were activated in the murine unilateral ureteral obstruction model of kidney fibrosis.[257] High-resolution epigenomic analyses identified kidney-selective open chromatin regions encoding features of stress-activated transcription factors in the AP-1 and NF-κB families. We confirmed our findings by demonstrating secretion of cytokines (IL-6, CXCL8) and matrix remodeling enzymes (MMP1, MMP7) in effluents of PT-MPS exposed to serum. Similar changes in expression of *IL6*, *CXCL8*, *MMP1*, *MMP7*, and *HAVCR1* (KIM-1) were seen in patients with FSGS, but not MCD, further supporting the notion that proteinuria, but not albuminuria, is directly causal to progressive kidney injury and fibrosis.

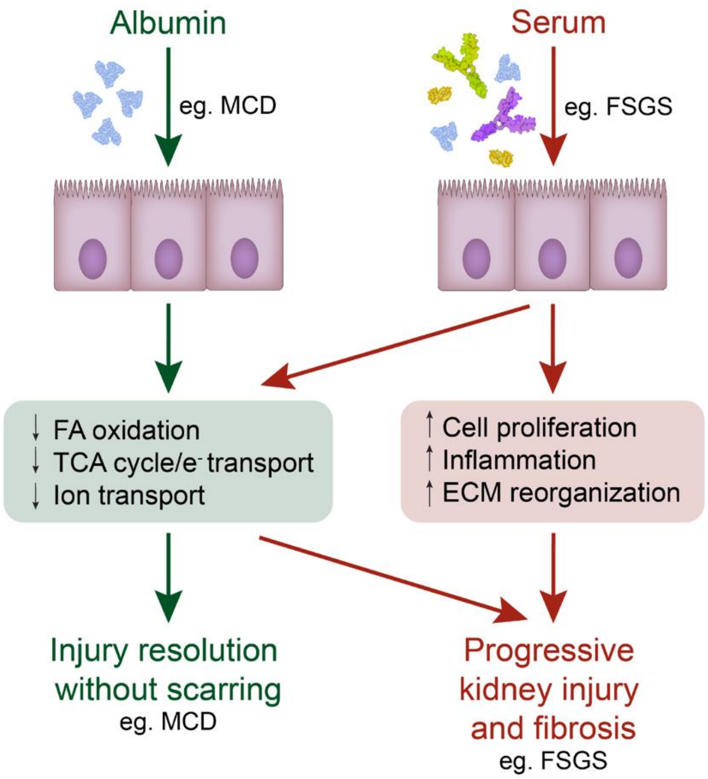

Figure 3.8. Serum but not albumin exposure induces a pro-inflammatory response that pre-disposes to progressive kidney injury and fibrosis.

Supplemental Materials

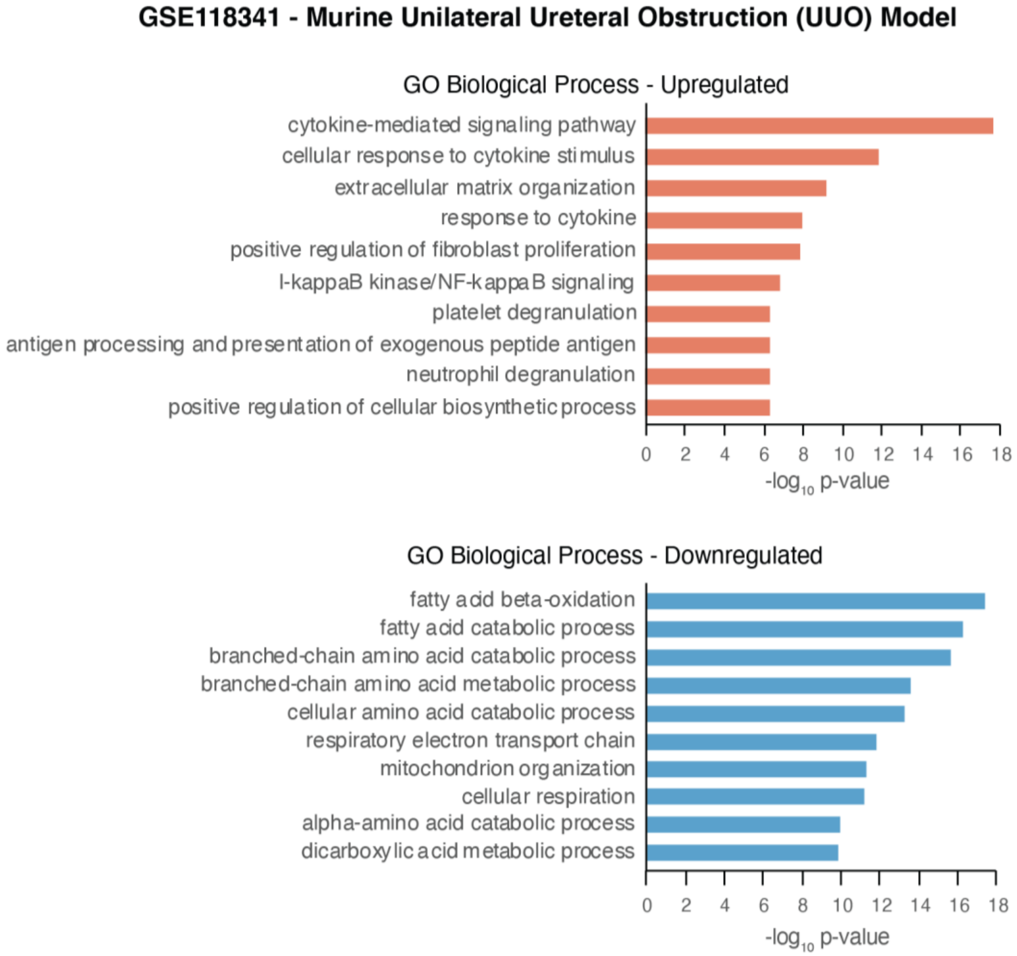

Supplemental Figure 3.1. Gene ontology molecular function enrichments for differentially expressed genes in the murine unilateral ureteral obstruction model of tubular injury and fibrosis. From GSE118341. Compare to Figure 3.2B.

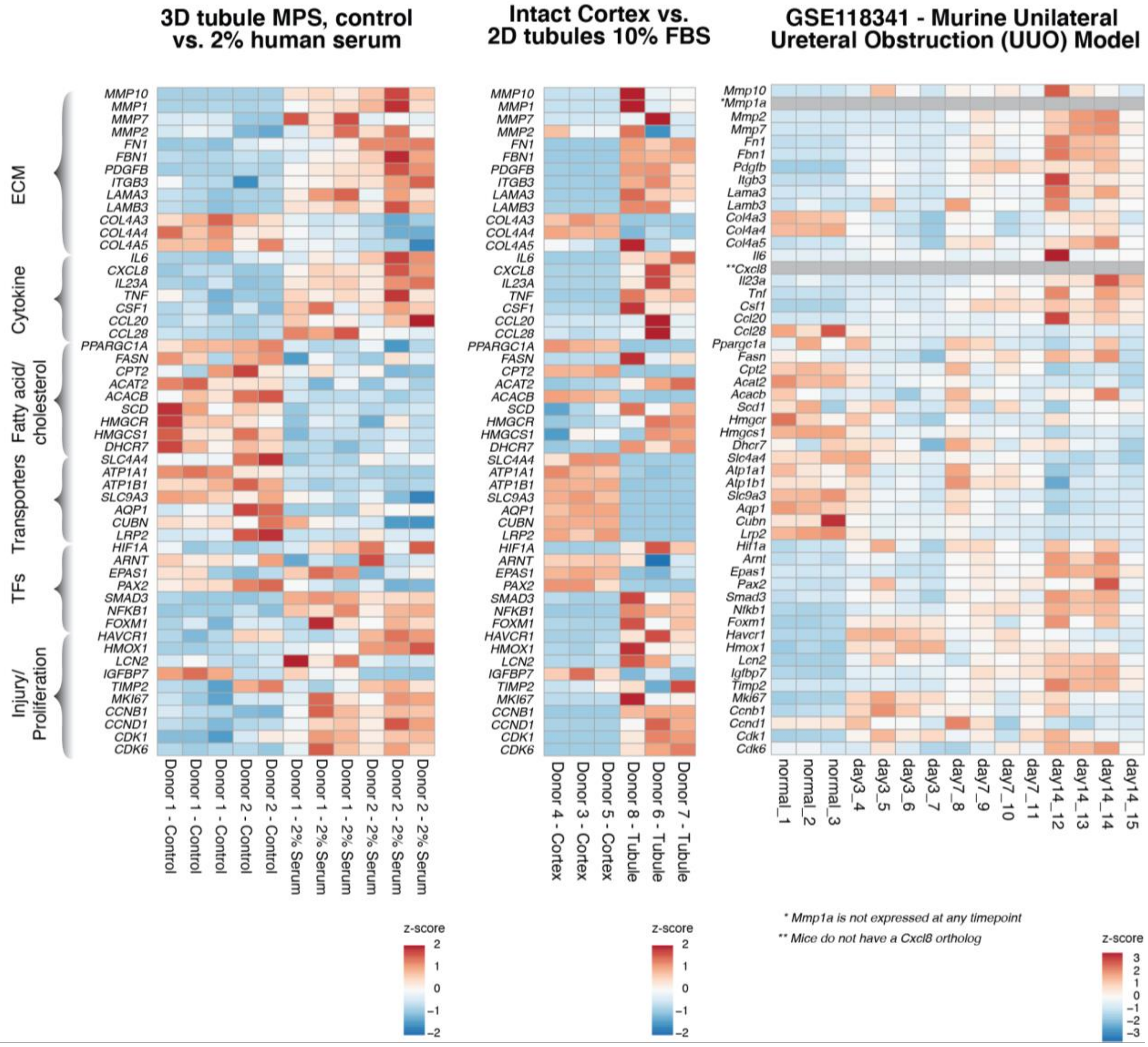

Supplemental Figure 3.2. Gene expression patterns of key genes associated with tubular injury phenotypes. Row normalized gene expression values for indicated genes are shown for the two model systems in this study and the murine unilateral ureteral obstruction model (right heatmap).

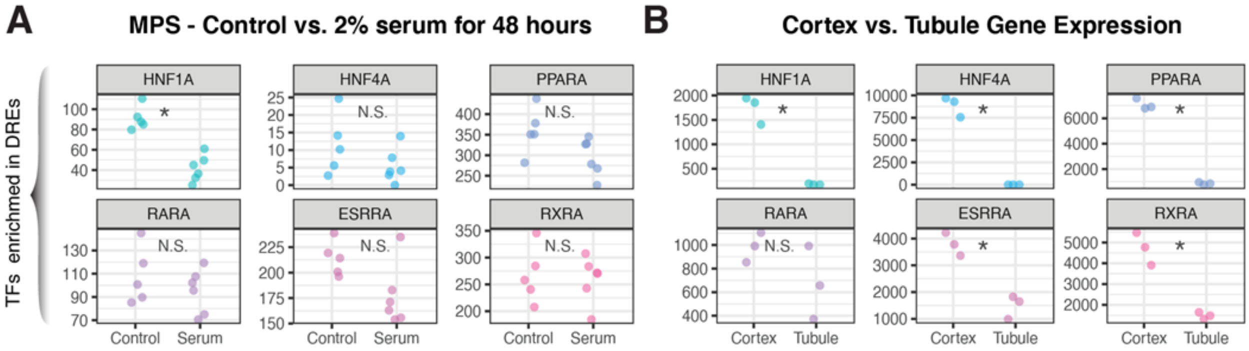

Supplemental Figure 3.3. Expression of transcription factors associated with significant motif enrichments in intact renal cortex. Expression of selected transcription factors is shown in A) serum-treated tubule MPS and B) tubules cultured in 10% FBS.

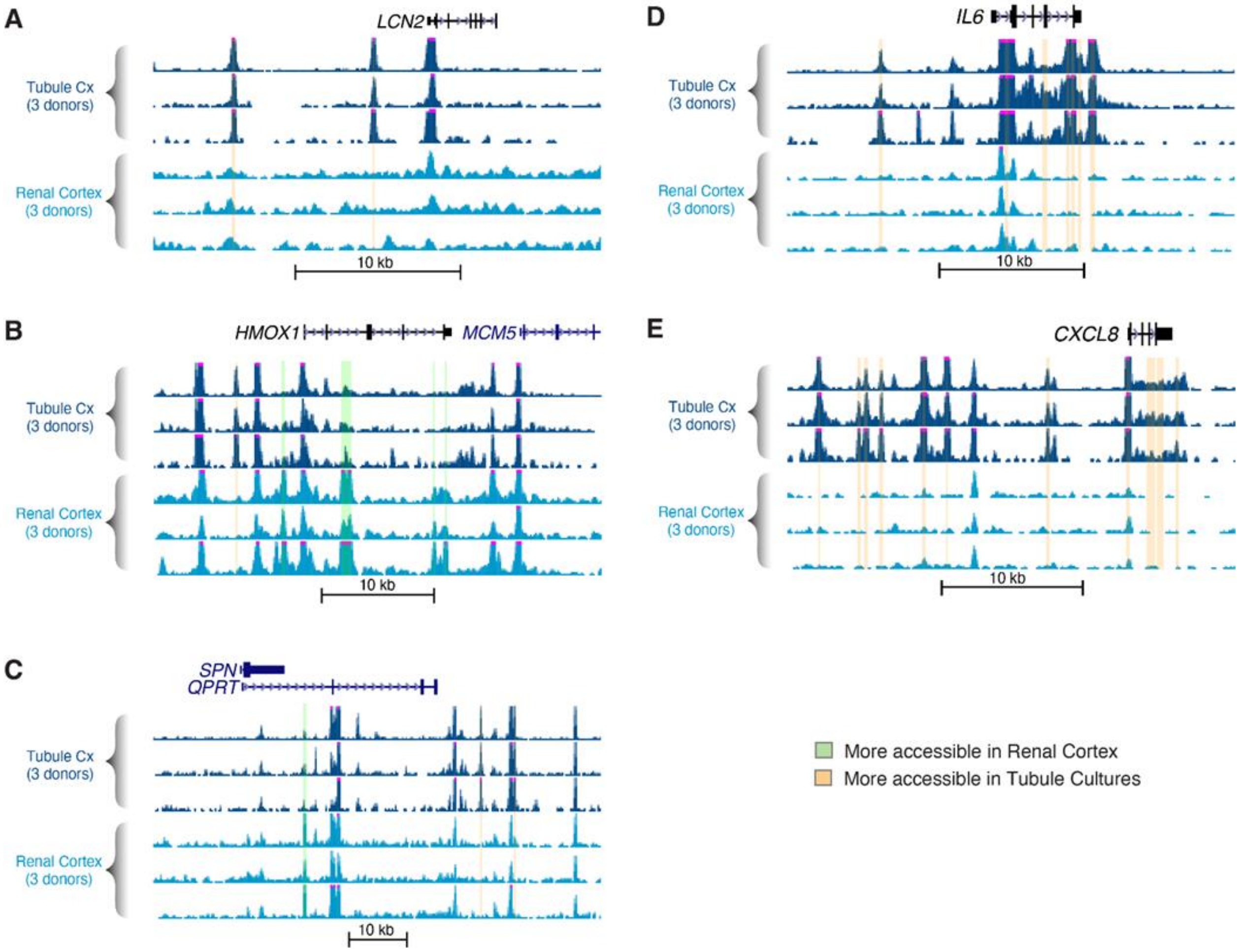

Supplemental Figure 3.4. Regulatory landscape of kidney injury biomarker and pro-inflammatory cytokine genes. Overview of the indicated loci with gene expression (top) and accessible chromatin (bottom) tracks for cultured tubules and intact renal cortex (3 donors each). For kidney injury biomarkers, *LCN2* and *HMOX1* are expressed at higher levels in tubules cultured in 10% FBS compared to intact renal cortex whereas *QPRT* shows the opposite pattern of expression. As secreted pro-inflammatory cytokines, *IL6* and *CXCL8* are expressed at higher levels in tubules cultured in 10% FBS compared to intact renal cortex whereas Green vertical bars indicate regulatory elements with greater accessibility in intact cortex, while orange vertical bars indicate regulatory elements with greater accessibility in cultured tubules.

Donor	Figures	Age	Sex	Ethnicity	Pre-existing conditions	Renal pathology
1	Fig. 1B-C, Fig. 2, Fig. 4A, sup Fig. 2-3	55	Male	White	Depression, OSA, reflux disease, T2D, vascular disease	ccRCC
2	Fig. 1B-C, Fig. 2, Fig. 4A, sup Fig. 2-3	63	Female	White	HTN, meningomyelocele, T2D	Chronic inflammation of kidney
3	Fig. 3, Fig. 4B-D, Fig. 5, sup Fig. 2-4	56	Male	White	hx nephrolithiasis, Laryngeal cancer, Thyroid disorder, Hepatitis C, Cholelithiasis	Papillary RCC
4	Fig. 3, Fig. 4B-D, Fig. 5, sup Fig. 2-4	74	Male	White	BPH, HTN, prediabetes, TURP	ccRCC
5	Fig. 3, Fig. 4B-D, Fig. 5, sup Fig. 2-4	67	Male	White	Arthritis, chronic lymphocytic leukemia, Disorder of muscle, ligament, and fascia	ccRCC
6	Fig. 3, Fig. 4B-D, Fig. 5, sup Fig. 2-4	80	Female	White	HTN, osteoarthritis, scleroderma	ccRCC
7	Fig. 3, Fig. 4B-D, Fig. 5, sup Fig. 2-4	61	Male	White	HTN	RCC
8	Fig. 3, Fig. 4B-D, Fig. 5, sup Fig. 2-4	62	Male	Hispanic	None	Renal mass
9	Fig. 6 and Fig. 7B	51	Female	White	Chronic fatigue, fibromyalgia, IBS, migraines	ccRCC
10	Fig. 6 and Fig. 7B	64	Male	Black	Fibrillary glomerulonephritis, hepatitis C	Renal papillary adenoma
11	Fig. 6 and Fig. 7B	45	Male	White	Angioneurotic edema, anxiety, hematuria, HTN, hypersomnia, morbid obesity, T2D, sleep apnea	ccRCC

Supplemental Table 3.1. Demographics of donors from which cells or tissue were isolated. Abbreviations: BPH, benign prostatic hyperplasia; ccRCC, clear cell renal cell carcinoma; IBS, irritable bowel syndrome; hx, history of; HTN, hypertension OSA, obstructive sleep apnea; T2D, Type 2 diabetes; TURP, transurethral resection of the prostate.

4. Impact of microgravity on human tubular epithelial cell response to serum and vitamin D

4.1 Abstract

Decreased production of 1α,25-dihydroxy vitamin D_3 (1α,25$(OH)_2D_3$), the active form of vitamin D_3, by the kidney may contribute to bone loss in astronauts in microgravity. As the kidney bioactivates 1α,25$(OH)_2D_3$ through hydroxylation of 25-hydroxy vitamin D_3 (25$(OH)_2D_3$) via cytochrome P450 27B1 (CYP27B1) as well as inactivates 25$(OH)_2D_3$ via cytochrome P450 24A1 (CYP24A1) and cytochrome p450 3A5 (CYP3A5), a change in the expression or activity of these enzymes could reduce plasma levels of 1α,25$(OH)_2D_3$. The primary mechanism of entry of 25$(OH)_2D_3$ into proximal tubule epithelial cells (PTECs) is through endocytosis of 25$(OH)D_3$ bound to vitamin D binding protein (DBP) via the megalin and cubilin receptor complex. Altered megalin/cubilin activity could therefore also result in lower production of 1α,25$(OH)_2D_3$. As megalin and cubilin modulate the response of the proximal tubule to proteinuria induced injury in animal models, the response of PTECs to serum challenge may be a surrogate indicator of megalin and cubilin activity. To test whether microgravity affects the transcript expression or activity of CYP27B1, CYP24A1, and CYP3A5, we treated proximal tubule epithelial cells (PTECs) cultured in a microphysiological device with 25$(OH)D_3$ and monitored metabolite formation as well as conducted global transcriptomics via RNAseq. To probe whether megalin and cubilin activity or localization is impacted by microgravity, PTECs were challenged with serum treatment. PTECs treated with 25$(OH)_2D_3$ formed equivalent levels of the metabolites of CYP24A1, CYP27B1, and CYP3A5 in microgravity compared to normogravity. Transcript expression of *CYP24A1*, *CYP27B1*, and *CYP3A5* was also unchanged by microgravity. Furthermore, microgravity did not significantly alter nor induce a unique response of PTECs to serum. In both terrestrial and microgravity conditions, serum treatment induced genes associated with proliferation, inflammation, and reorganization of the extracellular matrix environment, with a concomitant downregulation of metabolic and biosynthetic pathways. In conclusion, microgravity does not alter the intrinsic ability of PTECs to regulate the levels of 1α,25$(OH)_2D_3$. The impact of other factors such parathyroid hormone and hypercalciuria on PTEC metabolism of 25$(OH)_2D_3$ should be investigated in future studies.

4.2 Introduction

The International Space Station (ISS) is a modular spacecraft replete with stressors that challenge the bounds of human physiology. Astronauts aboard the ISS live in a tight-quarter, enclosed, near-weightless environment that orbits the Earth. Astronauts face superterrestrial levels of ionizing radiation, disruption of circadian rhythms, and encephalic fluid redistribution.[133, 134] For example, during a 340 day spaceflight on the ISS, astronaut Scott Kelly encountered an effective radiation dose equivalent to 54 years of background exposure on Earth.[135] Ionizing radiation promotes cellular and genetic damage, generation of reactive oxygen species, alters antioxidant-oxidant balance, and activates various stress responses.[136] Because of ionizing radiation and microgravity-induced physiological changes, astronauts commonly exhibit muscle atrophy, ophthalmic disorders, serum chemistry alterations, and bone demineralization.[137-140] Many of these physiological changes mirror what happens in disease states on Earth, such as age-related changes in telomere maintenance and hormonal perturbations.[141, 142] As such, the microgravity environment has been proposed to be a unique stressor that can be used to understand the underlying cellular and molecular drivers of pathological changes observed in astronauts with the goal of developing strategies to enable long-term spaceflight and better treat disease on Earth.[143]

We hypothesize that the kidney may play an important role in bone loss in microgravity through altered metabolism of 25-hydroxy vitamin D_3 ($25(OH)D_3$) to its most biologically active form, $1\alpha,25$-dihydroxy vitamin D_3 ($1\alpha,25(OH)_2D_3$). $1\alpha,25(OH)D_3$ is important for bone homeostasis, primarily through regulation of uptake of calcium in the intestine and modulation of osteoclast number and activity.[47] Despite dietary supplementation of vitamin D_3 and plasma levels of $25(OH)D_3$ remaining constant, plasma levels of $1\alpha,25(OH)_2D_3$ in astronauts in flight decrease over time.[144, 287] At the same time, absorption of calcium in the intestine is impaired.[144] The kidney is the primary site for bioactivation of $25(OH)D_3$ to $1\alpha,25(OH)_2D_3$, via cytochrome P450 27B1 (CYP27B1). The kidney can metabolize $25(OH)D_3$ via CYP3A5 and cytochrome P450 24A1 (CYP24A1) can metabolize $25(OH)D_3$ and $1\alpha,25(OH)_2D_3$ to inactive products.[47] In addition, the kidney maintains the levels of $1\alpha,25(OH)_2D_3$

through an autocrine mechanism, whereby $1\alpha,25(OH)_2D_3$ activates the vitamin D receptor (VDR) leading to induction of *CYP24A1*. Thus, microgravity could decrease plasma levels of $1\alpha,25(OH)_2D_3$ by 1) decreasing renal CYP27B1 activity, 2) increasing renal CYP24A1 activity, or 3) increasing renal CYP3A5 activity.

An alternative explanation for the reduced renal formation of $1\alpha,25(OH)_2D_3$ is altered protein handling or delivery. $25(OH)_2D_3$ is highly protein bound in plasma (~99.9%), almost exclusively to vitamin D binding protein (DBP).[47] After filtration in the glomerulus of the kidney, DBP is taken up by PTECs via megalin-cubilin endocytosis.[145] If megalin-cubilin localization or activity are impaired by microgravity it could reduce formation of $1\alpha,25(OH)_2D_3$. Data concerning renal handling of filtered protein such as albumin in astronauts in flight is conflicting. While it was initially reported that urinary excretion of albumin was increased in astronauts in flight, follow up studies showed decreased urinary excretion of albumin.[288-290]

To test whether microgravity affects the transcript expression or activity of CYP27B1, CYP24A1, or CYP3A5, we treated proximal tubule epithelial cells (PTECs) cultured in a microphysiological device with $25(OH)D_3$ and monitored metabolite formation and conducted global transcriptomics via RNAseq on cells undergoing flight (microgravity) and their control (ground). As megalin and cubilin have been shown to modulate proteinuria induced tubular injury in animal models, an altered response of PTECs to serum challenge could implicate differential activity or localization of megalin/cubilin in microgravity.[125, 126] To probe whether megalin and cubilin activity was impacted by microgravity, PTECs were challenged with serum treatment as a model of tubular injury (see Chapter 3 for proteinuria-induced tubular injury).

4.3 Materials and methods

4.3.1 Cell culture

Human cortical kidney samples were collected in deidentified fashion through the Northwest Biotrust at the University of Washington Medical Center with local IRB approval (Study 1297). Primary human proximal tubule epithelial cells were isolated by mechanical and enzymatic dissociation and cultured as previously described.[88, 255] Serum-free tubular cell cultures were maintained in PTEC maintenance media consisting of DMEM/F12 (Gibco, 11330-032) supplemented with 1x insulin-transferrin-selenium-sodium pyruvate (ITS-A, Gibco, 51300044), 50 nM hydrocortisone (Sigma, H6909), and 1x Antibiotic-Antimycotic (Gibco, 15240062). Upon reaching 70-80% confluence, PTECs were passaged by enzymatic digestion with 0.05% trypsin EDTA (Gibco, 25200056) and manual cell scraping to obtain a single-cell suspension that was subsequently neutralized with defined trypsin inhibitor (Gibco, R007100). Cells were pelleted by centrifugation at 200 x g for 6 minutes, resuspended in maintenance media, and plated in cell culture-treated flasks at >30% confluency. PTECs were passage number 2-3 from all donors in these experiments.

4.3.2 Microphysiological devices

Triplex microfluidic devices were purchased from Nortis, Inc (Woodinville, WA) and prepared as previously described in Chapter 3.3.2. Triplex microfluidic devices contain three fluidic circuits, which enables generation of three PTEC tubules on a single device that can be continuously perfused with media.

4.3.3. Maintenance, treatment, and fixation of devices in BioServe perfusion platform

The Bioserve perfusion platform was developed to house three Triplex devices in a self-contained, hermetically sealed system to meet the levels of containment required by NASA and reduce the space required to perfuse the Triplex devices. A flow rate of 0.5 µL/min was used for cell maintenance and treatment. The treatments were control, vitamin D, or 2% human serum. Control treatment was PTEC maintenance media (see cell culture). To prepare 2% human serum treatment media, normal human serum (Valley Biomedical, HS1021) was diluted in PTEC maintenance media to a final concentration of 2%. Vitamin D treatment media consisted of PTEC maintenance media supplemented with 1.5 µM 25(OH)D_3 (Toronto Research Chemicals, C125700) and 3 µM DBP (Athens Research, 16-16-070307). To prepare vitamin D treatment media, stock 25(OH)D_3 was solubilized with molecular biology grade ethanol to 5 mM, with 10 minutes of gentle agitation at room temperature. DBP was reconstituted to 3 µM in PTEC maintenance medium in 50 mL conical tubes to create PTEC-DBP medium. 25(OH)D_3 was then diluted into PTEC-DBP medium to 1.5 µM and the 50 mL conical tubes were allowed to equilibrate at room temperature for 30 minutes prior to filling the treatment cassette to ensure binding of 25(OH)D_3 to DBP. The final concentration of ethanol in the vitamin D treatment media was 0.02%. In order to preserve the tubules at the end of treatment for analyses, the devices were fixed for 2 hours with either 10% neutral buffered formalin (Thermo, 5725) or RNALater (ThermoFisher, AM7024) at a flow rate of 10 µL/min.

4.3.4 RNA isolation, sequencing, and analysis

RNA was isolated from devices fixed with RNALater by injecting 100 µL of RLT lysis buffer (Qiagen, 79216) into the injection port using a 1 mL slip-tip syringe (BD, 309659) outfitted with a 22-gauge needle (BD, 305142). The cell lysate was collected at the outlet into a clean microcentrifuge tube. An additional 400 µL of RLT lysis buffer was added to each tube and the samples were stored at -80°C until extraction. RNA was extracted using the RNeasy Micro Kit (Qiagen, 74004) and converted to cDNA with the SMART-Seq v4 Ultra Low Input RNA Kit (Takara, 634891). Sequencing libraries were constructed using the SMARTer ThruPlex DNA-Seq Kit (Takara, R400676) and sequenced on a NovaSeq 6000 instrument (Illumina, San Diego, CA). Sequencing reads were aligned to GRCh38.p12 with reference transcriptome GENCODE human release 30 (with additional ERCC spike-in sequences) using STAR (v2.6.1d).

Prior to fitting any model, we excluded genes that are expressed at consistently low levels across all samples.[221] Prior to filtering we had data for 58870 genes and after filtering we had data for 14094 genes. The trimmed mean of M-values (TMM) normalization method was conducted.[220] We used the voom method from the Bioconductor limma package, which estimates the mean-variance relationship of the log-counts per million (logCPM), and generates a precision weight for each observation and enters these into the limma analysis pipeline.[291] A small positive value was added to each raw count to avoid taking the logarithm of zero, and logCPM can be interpreted as a normalized count data by the corresponding total sample counts (in millions). We used the linear mixed model approach, fitting the condition_treatment as the fixed effect and the donor as the random effect by estimating the within-donor correlation.[292] We then fit a linear model with condition_treatment and incorporated the within-donor correlation (corr = 0.3). Since not all donors received all the treatments under each condition, the mixed model approach provides more statistical power for the unbalanced design. Both observation level and sample-specific weights were used, which enabled up or down-weighting of individual samples. This allowed us to keep all samples in the analysis and minimized the need to make decisions about removing possible outlier samples from consideration. The approach of using observation level and sample-specific weights has been shown to increase power in both real and simulated studies.[293]

We selected genes based on a 1.1-fold or greater difference in expression, and a false discovery rate (FDR) of 5%. Rather than using a post-hoc fold-change filtering criterion, we used the TREAT function from limma, which incorporates the fold-change into the statistic, meaning that instead of testing for genes which have fold-changes different from zero ($H0:\beta=0$ versus $HA:\beta\neq0$), we tested whether the fold-change was greater than 1.1-fold in absolute value ($H0:|\beta|<=1.1$ versus $HA:|\beta|>1.1$).[222]

4.3.5 Gene ontology and iPathwayGuide

Advaita iPathwayGuide scores pathways using the Impact Analysis method which considers two types of evidence 1) over-representation of DE genes in a given pathway relative to random chance (pORA) and 2) the perturbation of the pathway computed by taking into account factors such as the magnitude of each gene's expression change, position within the pathway, and gene interactions (pAcc). In gene ontology (GO) analysis, the number of DE genes annotated to a term was compared with the number of DE genes expected by chance. Pathways and GO terms were determined to be significant at a false-discovery rate < 0.05.

4.3.6 Quantification of IL-6, IL-8, KIM-1, MMP1, and MMP7 by ELISA

The DuoSet® line of ELISAs from R&D Systems (Minneapolis, MN) were used to quantify the protein levels of IL-6, IL-8, KIM-1 (HAVCR1), total MMP1, and total MMP7 from device effluents according to the manufacturer's instructions. For quantification of MMP7, all samples were diluted 1:12 in reagent diluent (R&D systems, DY995). The levels of IL-6, IL-8, KIM-1, MMP1, and MMP7 in 2% human serum were below the limit of detection. Samples were assayed in technical duplicates.

4.3.7 Standard preparation and extraction of vitamin D analytes

Stock solutions of 1α,25$(OH)_2D_3$ (20 ng/mL; Cerilliant, H-089), 25$(OH)D_3$ (10 µg/mL; Cerilliant, H-083), and a mixture of 4β,25$(OH)_2D_3$ (8 ng/mL; TRC, D455015) and 24R,25$(OH)_2D_3$ (150 ng/mL; TRC, S211500) were all prepared in methanol. 10 standard curve points of each standard stock were prepared in methanol by serial 2x dilutions. A stock solution containing internal standards was prepared in methanol [1α,25$(OH)_2D_3$-d_6 (Cerilliant, H-089), 24R,25$(OH)_2D_3$-d_6 (TRC, S211502), 25$(OH)D_3$-d_6 (Cerilliant, H-074); 60, 250, and 500 ng/mL respectively]. PTEC maintenance media containing 3 µM DBP (PTEC-DBP media) was used as the blank matrix. Quality control samples were prepared by diluting 1α,25$(OH)_2D_3$, 4β,25$(OH)_2D_3$, 24R,25$(OH)_2D_3$, and 25$(OH)D_3$ into PTEC-DBP media to a final concentration of 0.02, 0.02, 0.2, and 200 ng/mL, respectively. QC samples and standard stocks were stored at -80°C. Effluent from the 48-hour 25$(OH)D_3$ treatment was collected and stored at -80°C aboard the ISS U.S. National Laboratory. All treated samples remained frozen throughout the return trip to Earth and shipment to the University of Washington where they were stored at -80°C until extraction.

Because vitamin D and its metabolites are light sensitive, all steps were performed under low light. QC and treatment samples were thawed, vortexed, then 500 µL was transferred to 2 mL screw cap plastic microcentrifuge tubes (Fisher 02-681-344). If the treatment sample volume was less than 500 µL, it was brought up to 500 µL with PTEC-DBP media. A 10-point standard curve was made by adding 10 µL of $1\alpha,25(OH)_2D_3$ and 25 µL of $4\beta,25(OH)_2D_3$, $24R,25(OH)_2D_3$, and $25(OH)D_3$ from each level of standard stock into PTEC-DBP media. 20 µL of internal standard was spiked into the standard, QC, and treatment samples and the tubes were capped, vortexed, and equilibrated for 20 min at room temperature. Proteins were precipitated by adding 1 mL of 1:1 isopropanol:methanol, vortexing, then incubating at room temperature for 10 minutes, followed by centrifugation at 16,100 x *g* for 10 minutes. The supernatant was decanted into silanized 16x100mm tubes (Fisher, 12100387) before liquid-liquid extraction by adding 3 mL of 60:40 hexane:methylene chloride. The tubes were capped, shaken on a horizontal shaker for 15 minutes, then centrifuged for 10 minutes at 16,100 x g in a swinging bucket rotor. The resultant upper solvent layer was transferred to clean silanized 16x100mm glass tubes using a plastic transfer pipet. The liquid-liquid extraction procedure was repeated two more times, with the resultant upper solvent layer combined into a single tube for each sample each time. After complete evaporation of the solvent under a nitrogen stream at 40°C the residue was derivatized with 4-(4-(Dimethylamino)phenyl)-3H-1,2,4-triazole-3,5(4H)-dione (DAPTAD). To generate the derivatizing reagent DAPTAD, 6 mg diacetoxyiodo benzene (Sigma, 178721), 4 mg 4-(4'-dimethylaminophenyl)-1,2,4-triazolidine-3,5-dione (Santa Cruz, SC-206796), and 4 mL ethyl acetate were added into a 20 mL glass vial and stirred at room temperature for 3 hours. The resultant DAPTAD was stored at -20°C until use (either same day or overnight). DAPTAD was diluted 1:1 in acetonitrile and 200 uL was added to the residue, vortexed, and incubated at room temperature for 45 minutes with vortex-mixing every 15 minutes. At the end of the incubation, the samples were dried down under a nitrogen stream at 40°C (Organomation Associates, 8105), resuspended in 52 µL methanol, and vortexed. 23 uL deionized water was added to the samples before vortexing, and reconstituted samples were transferred to 0.5 mL snap cap microcentrifuge tubes (Fisher, 02-681-273), and centrifuged for 15 minutes at 16,100 x g to remove excess DAPTAD and solid precipitate. The supernatant was transferred to amber liquid chromatography vials containing silanized glass inserts. The vials were capped with slitted snap caps and stored at -80°C until LC/MS/MS analysis the following day.

4.3.8 Vitamin D chromatography and mass spectrometry

Chromatographic separation was performed using an RP-Amide (2.1 x 150mm, 2.7 µm) column (Supelco 2-0943) at room temperature on a Shimadzu Nexera UPLC using water (A, 0.1% formic acid) and methanol (B, 0.1% formic acid) as the mobile phases. Analytes were separated using the following gradient: solvent B starting at 55% for the first minute, increasing linearly to 65% from 1-6 minutes, held at 65% until 8 minutes, increasing linearly to 75% from 8-15 minutes, held at 75% until 15.5 minutes, increasing linearly until 90% from 15.5-17 minutes, held at 90% until 23 minutes, then returning to 55% from 23-23.5 minutes. The injection volumes were 0.3 µL for analysis of $25(OH)D_3$ while a 10 uL was used for all other analytes. Analytes were detected using a positive ionization method on an AB Sciex 6500 QTRAP mass spectrometer (SCIEX, Framingham, MA). The parent and daughter ions were detected using multiple reaction monitoring with channels of m/z set to detect $25(OH)D_3$ ($619.2 \rightarrow 601.1$), $25(OH)D_3$-d_6 ($625.4 \rightarrow 341.1$), $24R,25(OH)_2D_3$ ($635.2 \rightarrow 341.1$), $24R,25(OH)_2D_3$-d_6 ($641.2 \rightarrow 341.1$), $4\beta,25(OH)D_3$ ($635.2 \rightarrow 357.1$), $1\alpha,25(OH)D_3$ ($635.2 \rightarrow 357.1$), $1\alpha,25(OH)D_3$-d_6 ($641.2 \rightarrow 357.1$). The retention times for the analytes were as follows: $25(OH)D_3$, 18.16 min; $25(OH)D_3$-d_6, 18.13 min; $24R,25(OH)_2D_3$, 13.4 min; $24R,25(OH)_2D_3$-d_6, 13.34 min; $4\beta,25(OH)D_3$, 15.06 min; $1\alpha,25(OH)D_3$, 15.3; and $1\alpha,25(OH)D_3$-d_6, 15.2 min.

4.3.9 Treatment of PT-MPS with fenofibric acid

PT-MPS were seeded and allowed to culture for 11 days before treatment with either vehicle control (0.1% DMSO in PTEC maintenance media), 2% normal human serum with 0.1% DMSO, or 2% normal human serum with 5 µM fenofibric acid. To prepare fenofibric acid treatment media, powder fenofibric acid was solubilized in DMSO to 5 mM then diluted into PTEC maintenance media containing 2% normal human serum. The final concentration of DMSO in the vehicle control and 2% human serum treatment media was 0.1%. The PT-MPS were treated for 7 days with effluent collected on days 2, 4, and 7. Fresh treatment media was added on day 4.

4.3.10 Treatment of PT-MPS with tocilizumab, ruxolitinib, and albumin

To prepare tocilizumab treatment media, stock tocilizumab (20 mg/mL, Genentech, South San Francisco, CA) was diluted to 10 µg/mL in PTEC maintenance media containing 2% normal human serum. To prepare ruxolitinib treatment media, powder ruxolitinib (Selleckchem, S1378) was solubilized in DMSO to 100 mM then diluted to 100 nM in PTEC maintenance media containing 2% normal human serum. To prepare human serum albumin treatment media, powder albumin (GeminiBio, 800-126P) was solubilized in PTEC maintenance medium to 720 µg/mL. Control was serum-free maintenance PTEC media. PT-MPS were allowed to culture for 7 days prior to treatment with control (maintenance media), 2% normal human serum, 2% normal human serum with tocilizumab (10 µg/mL), 2% normal human serum with ruxolitinib (100 nM), or human serum albumin (720 µg/mL) for 7 days. Treatment media was collected at 8hrs and on day 2, day 4, and day 7. Fresh treatment media was added on day 4.

4.4 Results

4.4.1 Reduction of PT-MPS perfusion footprint

Nortis microfluidic chips are molded from polydimethylsiloxane, a semi-transparent, flexible, generally bio-compatible, and gas-permeable silicone polymer. Because of the ease of molding polydimethylsiloxane, three fluidic circuits can be created in close proximity to each other, enabling generation of three tubules on a single Nortis Triplex chip (Figure 1A, flow paths in blue). While the footprint of the Nortis Triplex chip is relatively small, the equipment required for perfusion including chip platform, shelves, docking station, and pneumatic pump are relatively large (Figure 1B and C). In fact, the volume occupied by 48 Triplex chips during perfusion with the pneumatic platform is 30-fold larger than the space allocated to our group on the ISS U.S. National laboratory (1350L vs 45L). In order to reduce the footprint of the Triplex chip during perfusion and meet the levels of containment required by the National Aeronautics and Space Administration (NASA) for personnel safety, we partnered with BioServe Space Technologies to design, machine, and fabricate a novel perfusion platform. Briefly, the Triplex chips were arranged in a stacked formation within a housing unit (Figure 1D). Prior to sealing the housing unit with an adapter unit, sterile gauze was wetted with deionized water then placed into the housing unit to humidify the air and prevent the chips from drying out during the experiment. The housing unit fitted with the adapter unit was then attached to a media cassette (Figure 1D). The media cassette contained nine channels, each corresponding to an input on the three Triplex chips, as well as nine collection chambers that receive the outflow from each channel. Each pump held two housing-media cassette units and contained heating elements that contacted the top and bottom of the housing unit to ensure the internal temperature of the housing unit was maintained at 37°C. Each pump had a programmable motor that pushed a set of pistons into the bottom of the media cassette to drive perfusion of the devices. In all, it was a single-pass perfusion system that maintained the chips at 37°C within a humidified environment. The novel perfusion system drastically reduced the space required to perfuse six Triplex chips and was small enough that astronauts could perform all necessary tasks, such as swapping media cassettes, within the limited space of the Life Sciences Glovebox aboard the ISS U.S. National Lab (Figure 1E).

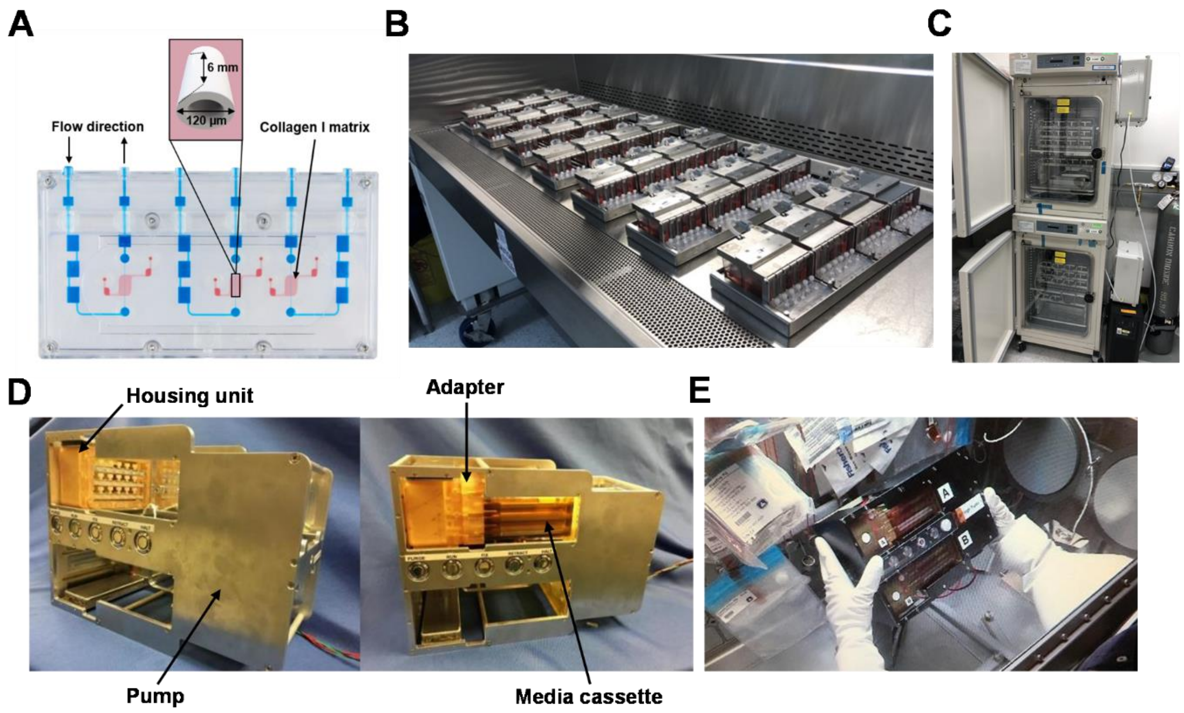

Figure 4.1. Design of a novel single-pass perfusion platform for Nortis Triplex chips. A) Schematic depicting three fluidic circuits within a single Nortis Triplex chip. B) Image demonstrating the amount of laboratory space 28 Triplex chips occupy when attached to platforms and shelves in a six foot biosafety cabinet. C) Image depicting the amount of space 30 Triplex chips occupy when the platforms and shelving is placed with the docking stations within tissue culture incubators, with the pneumatic pumps mounted on the right side of each incubator. D) Image of the novel programmable perfusion platform designed by BioServe Space Technologies showing three Triplex chips situated within a housing unit before (left side) and after (right side) being hooked up to the adapter unit and media cassette. E) The small footprint of BioServe perfusion platform enables astronauts to work within the limited space of the Life Sciences Glovebox.

4.4.2 Experimental design and loss of devices to mold contamination

A general overview of the experimental scheme is provided in Figure 4.2. A schematic of the experimental design including the treatment and fixative each chip received is depicted in Supplemental Figure 4.1. During dismantling of the chips from the housing unit, mold was observed on the outside of several chips near the matrix port, cell seeding port, and edges (Figure 4.3). Mold was also observed within the flow path of some devices (not shown). Media leakage from the injection port was noted from 9.7% (14/144) of the channels before integration into the BioServe perfusion platform and may have contributed to the contamination. Consequently, channels that had mold that was visible by eye, issues with RLT perfusion during RNA isolation, or notably discolored effluents were excluded from the analyses. In total, 65.3% (47/72) and 66.7% (48/72) of the ground and flight samples were included for effluent analyses, respectively. 72.2% (39/54) and 61.1% (33/54) of the ground and flight samples were analyzed by RNAseq, respectively. 94.4% (17/18) and 55.6% (10/18) of the ground and flight samples were used for the analysis of vitamin D metabolites, respectively. The number of usable samples for each donor separated by treatment and condition (ground vs flight) is summarized in Tables 4.1 and 4.2.

Figure 4.2. General experimental scheme. All 48 Triplex chips were seeded on ground at the Kennedy Space Station Processing Facility. The chips were maintained for 15 days via perfusion with the Nortis pneumatic perfusion system within cell culture incubators maintained at 5% CO_2 and 37°C. On day 15, all chips were transferred to BioServe’s perfusion platform and half the chips were loaded onto a SpaceX Falcon 9 rocket for Commercial Resupply Services mission 17 (CRS-17) to the ISS while the other half served as ground controls. After docking to the ISS and unloading, the used media cassettes were swapped out with fresh maintenance media cassettes. The chips were perfused for 6 days to allow for acclimation to the microgravity environment. After 6 days of acclimation, the maintenance media cassettes were switched to treatment media cassettes containing either maintenance media, 2% human serum, or 3 µM vitamin D binding protein (DBP) + 1.5 µM vitamin D ($25(OH)D_3$) and treated for 2 days before fixation with either RNAlater for RNAseq or formalin for immunocytochemsitry. The time it took the astronauts to perform every step on the flight chips was recorded and replicated with the corresponding ground controls.

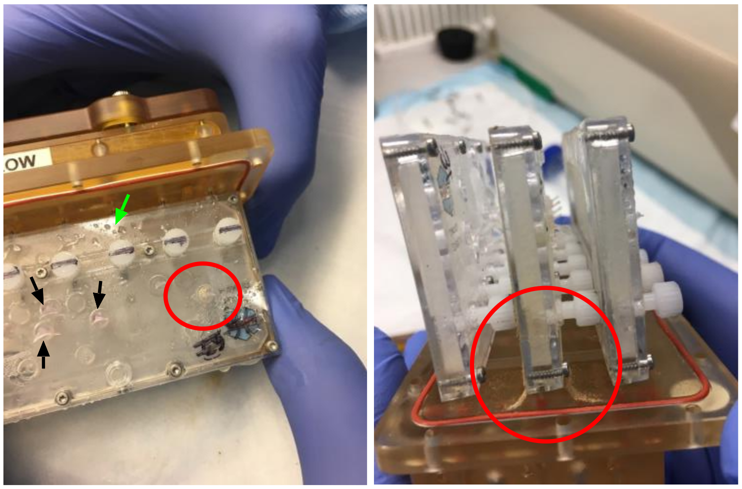

Figure 4.3. Observation of mold on chip exterior. Photos taken immediately after dismantling of the chips from the housing unit show mold was visibly present on the exterior of certain chips (red circles). The mold was present on the matrix port plug and injection port. Excess collagen I from filling the chamber was visibly present on several plugs (black arrows). Water droplets were present on the chip exterior, consistent with a high humidity environment within the sealed housing unit (green arrow).

Table 4.1. Number of samples usable for effluent analysis.

	Donor			
	M1	M2	F1	F2
Ground				
Media	2/9	0/9	5/12	6/6
Vitamin D	5/6	3/3	6/6	3/3
2% Human serum	5/6	3/3	6/6	3/3
Flight				
Media	6/9	7/9	10/12	0/6
Vitamin D	5/6	0/3	3/6	2/3
2% Human serum	5/6	2/3	6/6	2/3

Table 4.2. Number of samples usable for RNAseq.

	Donor			
	M1	M2	F1	F2
Ground				
Media	2/6	0/3	3/6	3/3
Vitamin D	5/6	3/3	6/6	2/3
2% Human serum	5/6	2/3	6/6	2/3
Flight				
Media	3/6	3/3	4/6	0/3
Vitamin D	4/6	0/3	2/6	2/3
2% Human serum	6/6	2/3	5/6	2/3

Tables 4.1 and 4.2. The fractions represent the number of samples included in each analysis over the total number of samples at the beginning of the experiment.

4.4.3 Transcriptional response of PTECs to 2% human serum in ground and flight conditions

To characterize the changes induced by serum exposure and identify condition-dependent responses, RNA from multiple replicates of control- or serum-treated PT-MPS was isolated and transcriptomic profiles were measured by RNA-seq. Exposure of PT-MPS to 2% normal human serum resulted in differential expression of 2,389 and 2,220 genes compared to control in the ground and flight conditions, respectively, based on a fold change of at least 1.1 at an adjusted p-value threshold of 0.05. In the ground condition, 1,144 and 1,245 genes were up- and down-regulated, respectively, whereas in the flight condition 1,108 and 1,112 genes were up- and down-regulated, respectively. Comparing the differentially expressed (DE) genes in the ground and flight conditions revealed that 1,122 genes were unique to ground and 953 genes were unique to flight with 1,267 genes differentially expressed in both conditions (Figure 4.4A). No genes were differentially expressed between 1) ground media vs. flight media, 2) ground serum vs. flight serum, or 3) (ground serum vs. ground media) vs. (flight serum vs. flight media), indicating that 1) flight alone did not impact PTEC gene expression, 2) the relative expression level for a given gene between the ground and flight serum-treated samples was similar, and 3) the flight condition did not affect the magnitude of change in expression of a gene between control treatment and serum treatments (i.e., the difference in differences).

To elucidate the functional networks regulated by serum exposure in PTECs, we performed Advaita gene ontology analyses and iPathwayGuide analyses on the genes differentially expressed between serum and control treatments in the ground and flight conditions. Gene ontology enrichment analysis showed over-representation of the set of DE genes in cellular component terms, such as mitochondrion (GO:0005739), plasma membrane (GO:0005886), extracellular space (GO:0005615), and condensed chromosome (GO:0000793) (Figure 4.4B). While the false discovery rate (FDR) adjusted p-value calculated for each cellular component term was different between ground and flight (Figure 4.4.B, top axis), the number of DE genes within a given term was comparable suggesting the overall response to serum between ground and flight chips was similar (Figure 4.4B, bottom axis). Advaita Pathway analysis revealed that several cellular pathways were significantly affected by serum treatment in both the ground and flight conditions including cell cycle (ground: $p=3.19\times10^{-6}$ and flight: $p=7.7\times10^{-6}$), cytokine-cytokine receptor interaction (ground: $p=6.93\times10^{-6}$ and flight: $p=1.12\times10^{-8}$), chemokine signaling (ground: p=0.0337 and flight: p=0.0039), peroxisome proliferator-activated receptor (PPAR) signaling (ground: $p=1.49\times10^{-4}$ and flight: $p=2.54\times10^{-5}$), and metabolic pathways (ground: $p=3.96\times10^{-17}$ and flight: 8.16×10^{-15}) (Figure 4C and 4D). Most of the genes within the cell cycle, cytokine-cytokine receptor interaction and chemokine signaling pathways were upregulated. Examination of the cell cycle pathway showed upregulation of genes that promote progression through the G1, S, G2, and M stages of the cell cycle (Supplemental Figures 4.2 and 4.3). Several members of the CC chemokine, CXC chemokine, and interleukin families were upregulated in the chemokine signaling and cytokine-cytokine receptor interaction pathways (Supplemental Table 4.1). On the other hand, the PPAR signaling (Supplemental Table 4.1) and metabolic pathways were downregulated. More specifically, genes within fatty acid metabolism (ground: $p=7.39\times10^{-6}$ and flight: $p=3.79\times10^{-7}$), tricarboxylic acid cycle (ground: $p=4.05\times10^{-3}$ and flight: $p=4.09\times10^{-7}$), and steroid biosynthesis (ground: $p=3.3\times10^{-5}$ and flight: $p=1.9\times10^{-5}$) pathways were downregulated (Supplemental Table 4.1). Non-alcoholic fatty liver disease, Alzheimer disease, and Huntington disease pathways were affected only in the ground condition. Inspection of the DE genes within those pathways indicated that the statistical significance was largely driven by a group of mitochondrial genes associated with oxidative phosphorylation (Figure 4C and 4D). Consistent with this observation, the oxidative phosphorylation pathway was far more impacted by 2% human serum treatment in the ground condition ($p=1.87\times10^{-24}$, 63 DE genes) than in the flight condition ($p=2.5\times10^{-6}$, 33 DE genes) (Figure 4.4C and 4.4D). Overall, these data suggest that serum exposure caused PTECs to activate a proliferative program, shift cellular bioenergetics, and promote a pro-inflammatory extracellular environment.

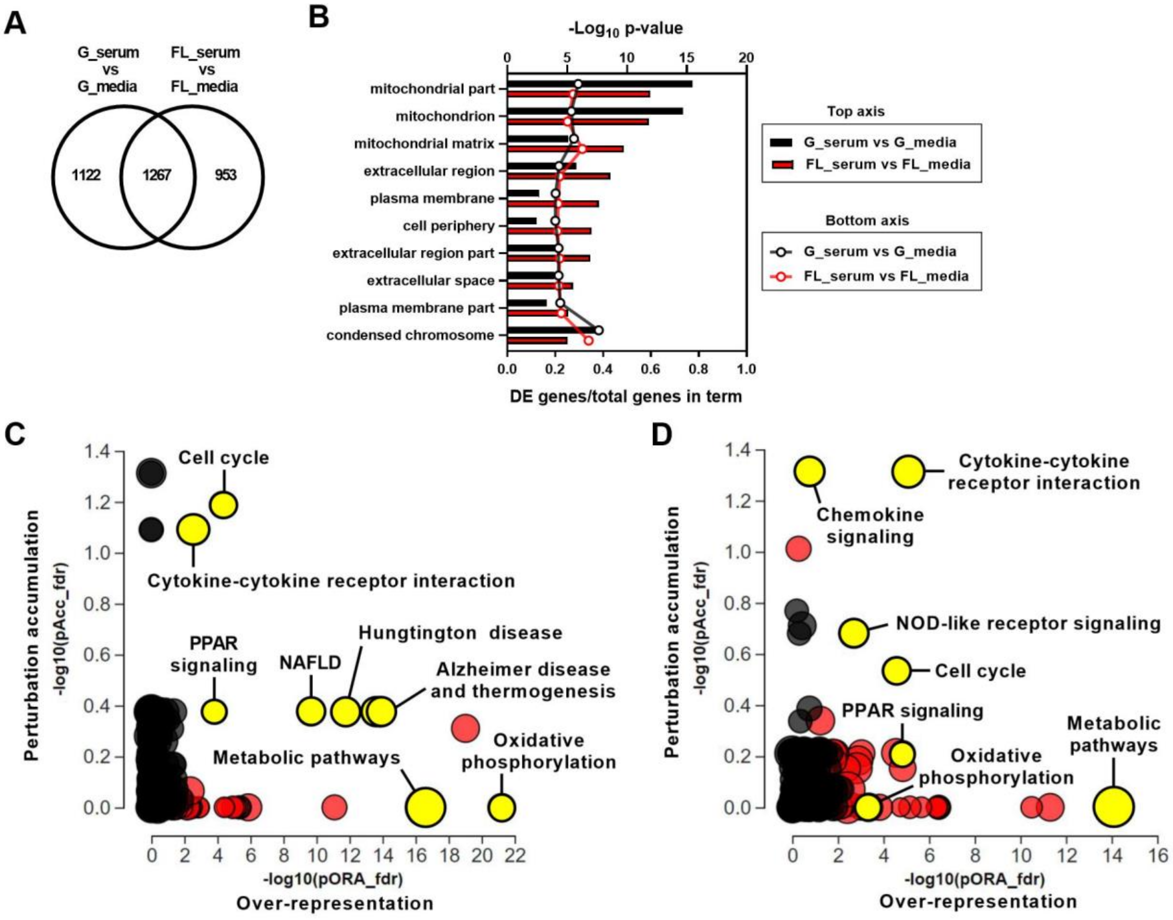

Figure 4.4. Serum promotes PTEC proliferation, alters cellular energetics, and modifies the disposition of the extracellular environment. A) Venn diagram depicting the number of DE genes between serum and control treatments in the ground and flight conditions. B) Gene ontology analysis of the set of DE genes showing enrichment in cellular component terms associated with mitochondria, extracellular space, and nucleus. Top axis displays FDR adjusted p-value for the cellular component term while the bottom axis displays the ratio of DE genes over the total number of genes within that specific term. C) and D) iPathwayGuide analysis plots of the FDR adjusted impact analysis p-value (pAcc) on the y-axis and over-representation p-value (pORA) on the x-axis for pathways identified as affected by serum treatment in ground (C) and flight (D) conditions. Black circles represent non-significant pathways while red circles indicate significant pathways and yellow circles indicate significant pathways of interest. The size of the circle corresponds to the number of genes within the pathway.

Next, we focused on gene-level changes to help delineate the biological consequence of exposure of PT-MPS to serum. First, we looked at metabolic reprogramming as it included the largest set of genes and was the most significantly impacted by serum treatment. Adenosine triphosphate (ATP) is a molecule that plays an important role in signal transduction (via being a substrate for kinases) and provides energy to drive a variety of cellular processes including transport of ions and solutes via ATP-binding cassette transporters such as the sodium-potassium-ATPase. PTECs generate the bulk of ATP through mitochondrial oxidative phosphorylation, wherein the transfer of electrons from nicotinamide adenine dinucleotide hydride (NADH) and dihydroflavin adenine dinucleotide ($FADH_2$) to molecular oxygen (O_2) through a series of protein complexes (complexes I-IV) in the mitochondrial inner membrane results in pumping of protons across the inner mitochondrial matrix membrane and creation of a transmembrane pH gradient that is subsequently utilized by complex V (or ATP synthase) to create ATP from adenosine diphosphate (ADP) and phosphate (P_i).[294] The DE genes within the oxidative phosphorylation pathway were found to be involved in the mitochondrial electron transport chain, with representation of all five of the major respiratory chain protein complexes (Figure 4.5A). A greater number of genes were identified in the ground condition compared to flight condition (58 vs 27, respectively), though all DE genes in both conditions were downregulated by similar magnitudes suggesting that both ground and flight conditions had reduced mitochondrial respiration following serum treatment. The mitochondrion has its own genome which encodes thirteen proteins that participate in the electron transport chain.[294, 295] Thirteen of those mitochondrial encoded genes were downregulated in the ground condition, but not the flight condition (Figure 4.5B). The expression of four key factors that control mitochondrial gene transcription including RNA polymerase mitochondrial (*POLRMT*), transcription factor A mitochondrial (*TFAM*), transcription factor B2 mitochondrial (*TFB2M*), and transcription elongation factor mitochondrial (*TEFM*), were unchanged with serum treatment in both the flight and ground conditions (adj. p-value=1).

To fuel the mitochondrial electron transport chain and oxidative phosphorylation, a steady source of reducing equivalents of NADH and $FADH_2$ are required.[294] β-oxidation of fatty acids and intermediary metabolism in the tricarboxylic acid (TCA) cycle, each of which occur in mitochondria, are the primary processes that generate $FADH_2$ and NADH.[294] β-oxidation is the stepwise enzymatic process that shortens fatty acid chains by two carbon atoms, producing acetyl coenzyme A (acetyl-CoA), NADH, and $FADH_2$.[296] Acetyl-CoA can subsequently be utilized in the TCA cycle, a series of chemical reactions that oxidize acetate (derived from acetyl-CoA) to ultimately produce GTP, NADH, and $FADH_2$, and carbon dioxide.[294]

Serum treatment of the PT-MPS significantly reduced the expression of a set of genes that function in β-oxidation, catabolism, and synthesis of fatty acids including carnitine palmitoyltransferase 1 (*CPT1A*), a transporter that is rate-limiting in fatty acid β-oxidation, and acetyl-CoA carboxylase alpha (*ACACA*) and fatty acid synthase (*FASN*), the rate-limiting enzymes in fatty acid biosynthesis (Figure 4.5C). In addition, serum caused a modest, but broad downregulation of genes within the TCA cycle and solute carrier 25 (SLC25) family, that are mitochondrial membrane transporters for a variety of ions and metabolic intermediates (Supplemental Table 4.2). Expression of the lipogenic enzymes (*GPAT3, GPAT4, AGPAT1-5, DGAT1,* and *DGAT2*) were unchanged (data not shown) whereas only lipin 1 (*LPIN1)* was significantly reduced (Supplemental Table 4.2). The expression of genes that are targets of the sterol-regulatory element binding transcription factor 2 (*SREBF2*) were considerably repressed (Supplemental Table 4.2). Because SREBF2 activity is inhibited in the presence of high cellular cholesterol levels, repression of SREBF2 target genes indicated that serum treatment increased cytosolic cholesterol levels. The transcriptional repression of genes involved in fatty acid metabolism, cholesterol metabolism, and intermediary metabolism (TCA cycle) strongly indicated that serum treatment caused metabolic reprograming in PTECs.

Next, we evaluated genes which could be potential maladaptive effectors in the tubular response to protein challenge. Serum treatment induced the expression of genes that function in the extracellular space and are associated with tissue remodeling. This group of genes included extracellular matrix proteins (e.g., fibronectin 1 (*FN1*) and transforming growth factor beta induced (*TGFBI*)), growth factors (e.g., platelet derived growth factor beta (*PDGFB*)), transcription factors (e.g., mothers against decapentaplegic homolog 3 (*SMAD3*)), and extracellular matrix modifying enzymes (e.g., matrix metallopeptidase 7 (*MMP7*), lysyl oxidase like 2 (*LOXL2*), transglutaminase 2 (*TGM2*)) (Figure 4.5D). It also induced pro-inflammatory molecules including chemokines (e.g., chemokine c-x-c motif chemokine ligand 5 (*CXCL5*)), cytokines (e.g., interleukin 8 (*IL8*), interleukin 23a (*IL23A*), tumor necrosis factor

(*TNF*)), transcription factors (e.g., interferon regulatory factor 1 (*IRF1*)), and the lipocalin neutrophil gelatinase-associated lipocalin (*NGAL* or *LCN2*) (Figure 4.5D). *IRF1*, *LCN2* (*NGAL*), *PLAUR*, *LOXL2*, *TGFBI*, and *SMAD3* are among the top 20 most significantly upregulated genes in PTECs following 2% human serum treatment (Supplemental Tables 4.3 and 4.4).

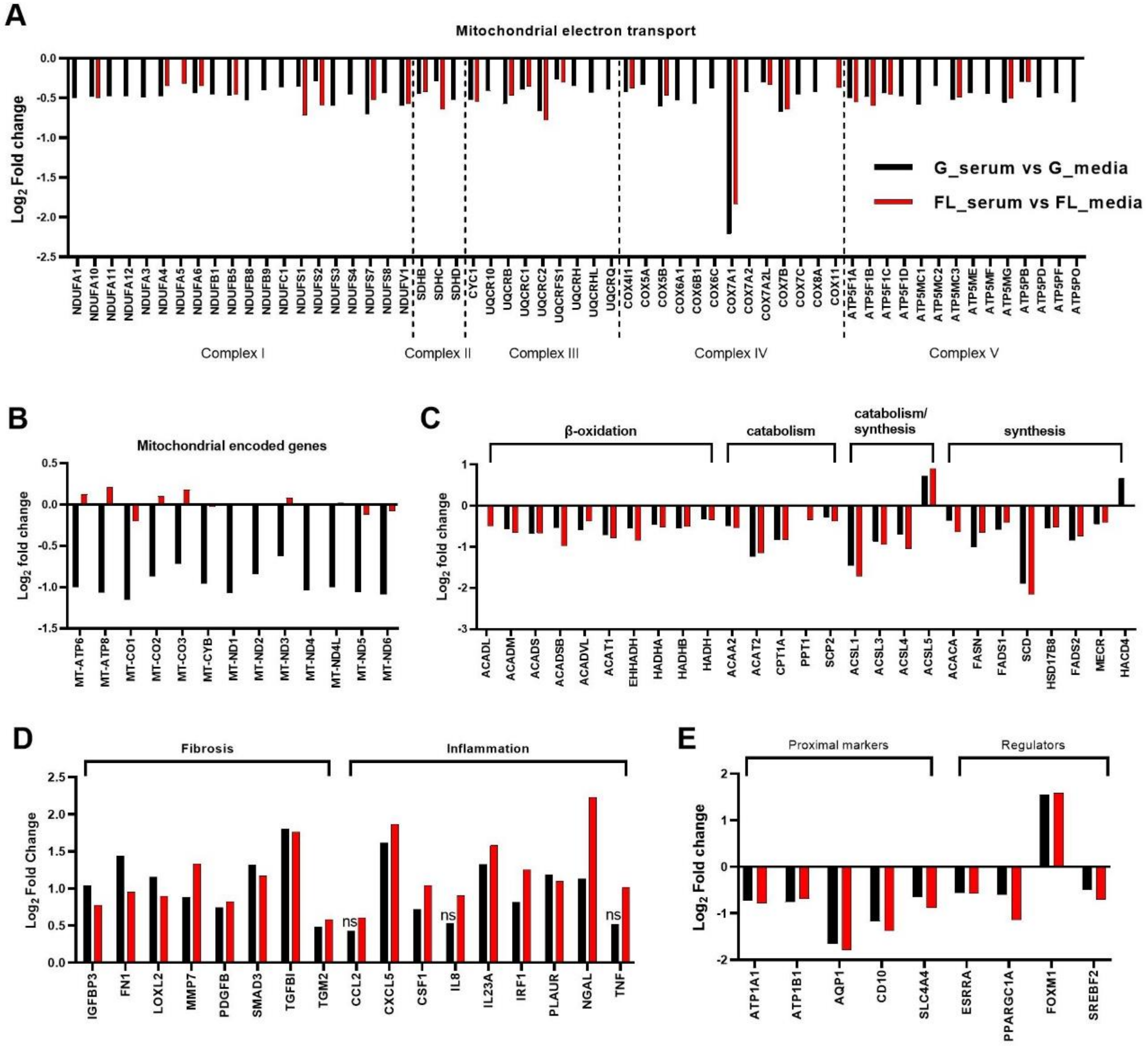

Figure 4.5 Serum induces metabolic reprogramming and a tissue remodeling gene signature in PTECs. Select genes that were differentially expressed after 48-hour 2% human serum in PTECs which function in A) mitochondrial electron transport chain, B) mitochondrial-encoded electron transport chain, C) fatty acid metabolism, D) fibrosis and inflammation, and E) proximal tubule makers and transcriptional regulators. Data are presented as the $\log_2$ fold change in gene expression of serum samples relative to control samples in the ground condition (black bars) and the flight condition (red bars). Genes that were not statistically significant are noted by “ns”. Abbreviations: G_serum = ground serum; G_media = ground control; FL_serum = flight serum; FL_media = flight control.

Because the loss of metabolic capacity and gain of pro-inflammatory and pro-fibrotic attributes could be detrimental to PTEC function, we next looked at whether the expression of proximal marker genes changed. Serum treatment caused a downregulation of several genes selectively expressed by PTECs *in vivo* including the water channel aquaporin 1 (*AQP1*) and the sodium potassium-transporting ATPase subunits alpha and beta (*ATP1B1* and *ATP1A1*) (Figure 4.5E). Concomitantly, there was downregulation of three key transcriptional regulators: peroxisome proliferator-activated receptor gamma coactivator 1-alpha (*PPARGC1A*), estrogen related receptor alpha (*ESRRA*), and *SREBF2*, while forkhead box M1 (*FOXM1*) was induced (Figure 4.5E). *ATP1B1* and *PPARGC1A* were among the top 20 downregulated genes in the flight condition (Supplemental Table 4.4). Advaita upstream regulator analysis identified both TNF (ground: $p=9.0x10^{-3}$ and flight: $p=2.4x10^{-2}$) and FOXM1 (ground: $p=2.71x10^{-9}$ and flight: $p=1.31x10^{-8}$) as transcription factors likely to have been activated by serum treatment based on the number of consistently observed DE genes and gene interactions (Table 4.3). Conversely, SREBF2 (ground: $p=5.86x10^{-9}$ and flight: $p=8.31x10^{-9}$) and PPARGC1A (ground: $p=1.2x10^{-1}$ and flight: $p=1.75x10^{-2}$) were predicted to have been inhibited by serum treatment (Table 4.3). The target genes of PPARGC1A include genes involved in mitochondrial oxidative phosphorylation (e.g., *CPT1A* and *EHHADHA*) as well as genes with regulatory roles (e.g., *ESRRA* and *SIRT3*), while those of FOXM1 tend to be related to cell proliferation (e.g., *CCNA1* and *CCNB1*) and DNA damage response (e.g., *RAD51* and *RAD54*).

		Ground serum vs Ground media			Flight serum vs Flight media		
Upstream regulator	Directional change	DE targets (+/-) / DE targets	p.value	FDR p.value	DE targets (+/-) / DE targets	p.value	FDR p.value
TNF	activated	32/45	6.15E-04	9.00E-03	31/42	1.00E-03	2.40E-02
FOXM1	activated	18/18	1.27E-10	2.71E-09	18/19	5.45E-10	1.31E-08
SREBF2	inhibited	15/15	2.99E-12	5.86E-09	15/15	3.76E-12	8.31E-09
PPARGC1A	inhibited	7/8	1.00E-03	1.20E-01	8/9	1.75E-04	1.40E-02
PPARA	inhibited	12/16	8.00E-03	4.94E-01	16/20	6.50E-05	8.00E-03
RXRA	inhibited	10/12	5.00E-03	3.57E-01	16/20	5.26E-06	1.00E-03

Table 4.3. Upstream regulators of the transcriptional response of PTECs to 2% human serum. Proteins predicted to have been inhibited or activated by 2% human serum treatment in PTECs in ground and flight conditions based on Advaita upstream regulator analysis. For each upstream regulator, the predicted directional change in activity (activation or inhibition) with 2% human serum treatment is shown. The DE targets (+/-) / DE targets column depicts the number of target genes with a directional change in expression consistent with the predicted change in upstream regulator activity over the total number of differentially expressed target genes for that upstream regulator. The unadjusted p-value and FDR adjusted p-value is presented for each upstream regulator. Upstream regulators with non-significant p-values are noted by red text.

To validate the transcriptional observations that 2% human serum appeared to promote cellular proliferation and induce proinflammatory genes, we quantified KIM-1 and IL-6 from device effluents. The magnitude of 2% human serum-induced secretion of KIM-1 and IL-6 varied by donor but was consistently increased relative to media control (Figure 4.6A and B). Serum treatment significantly increased KIM-1 secretion relative to media control for both ground (20.9-fold, $p<0.0001$) and flight conditions (14.5-fold, $p<0.0001$) (Figure 4.6C). There was no difference in serum-induced secretion of KIM-1 between ground and flight. IL-6 secretion was significantly increased by serum treatment relative to media control in both ground (3.3-fold, $p=0.0004$) and flight conditions (5.2-fold, $p<0.0001$) (Figure 4.6D). The difference in IL-6 change from media control to serum between the flight and ground condition was not statistically different ($p=0.073$, linear mixed effects model) suggesting that there was no interaction between microgravity and serum exposure on IL-6 secretion.

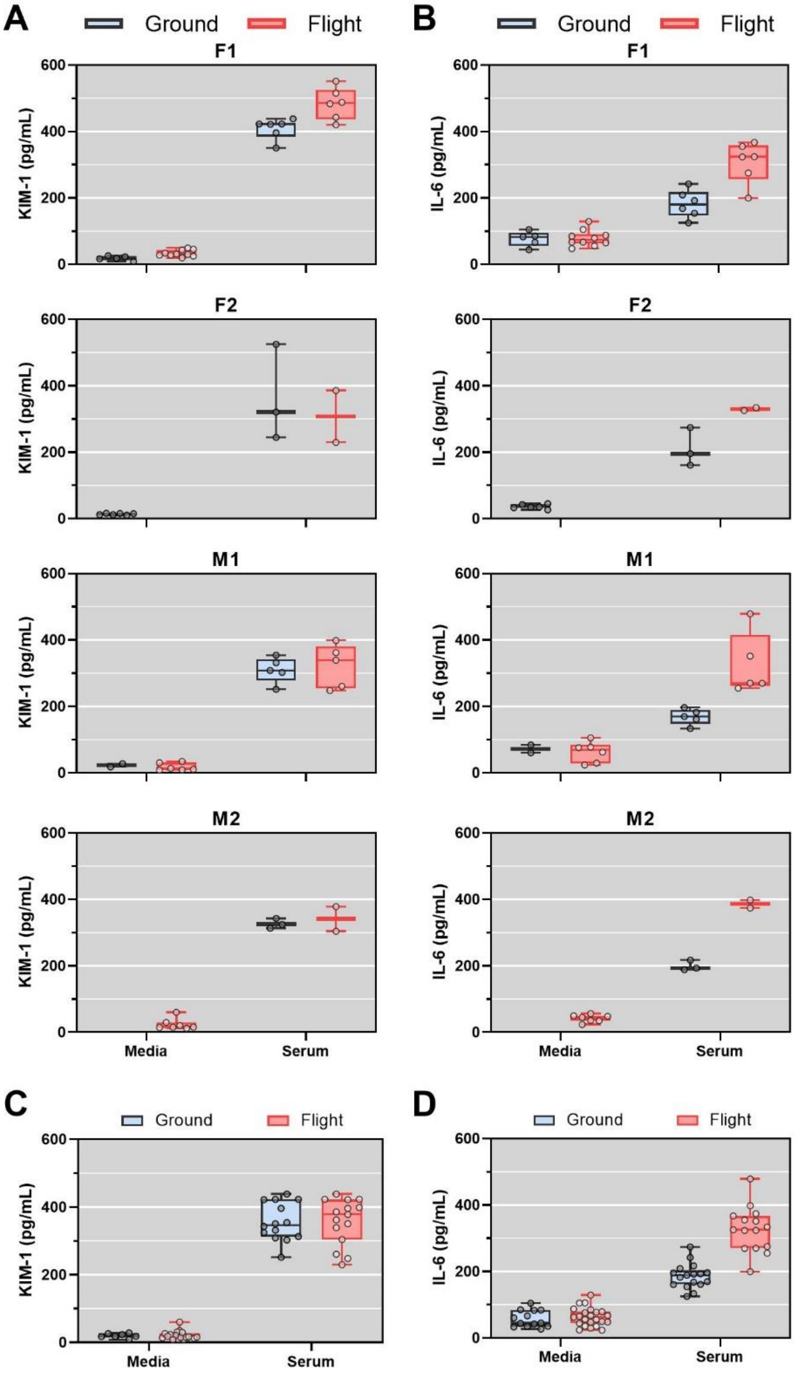

Figure 4.6. Serum-induced secretion of KIM-1 and IL-6. A and B) Quantification of KIM-1 (A) or IL-6 (B) levels in PT-MPS effluents after 48 hours of treatment with media control or 2% human serum in ground (black) and flight conditions (red) from two female donors (F1 and F2) and two male donors (M1 and M2). C) KIM-1 levels of all four donors in each treatment and condition. KIM-1 secretion was significantly increased by treatment with serum ($p<0.0001$; one way ANOVA). D) IL-6 levels of all four donors in each treatment and condition. IL-6 secretion was significantly increased by serum treatment in ground ($p=0.0004$; one-way ANOVA) and flight ($p<0.0001$; one-way ANOVA).

4.4.4 Transcriptional response of PTECs to vitamin D

To characterize the changes induced by vitamin D exposure and identify condition-dependent responses, RNA from multiple replicates of control- or 25(OH)D_3-treated PT-MPS was isolated and transcriptomic profiles were measured by RNA-seq. Vitamin D treatment significantly affected the expression of 1,019 and 408 genes in the ground and flight conditions, respectively. In each condition roughly half the genes were upregulated, and half were downregulated. Comparing the differentially expressed (DE) genes in the ground and flight groups revealed 807 were unique to ground and 196 were unique to flight with 212 genes DE in both conditions (Figure 4.7A). Gene ontology enrichment analysis revealed over-representation of the set of DE genes in cellular component terms such as mitochondrion (GO:0005739) and mitochondrial respiratory chain (GO:0005746) (Figure 4.7B). The number of DE genes within each term varied by condition, with the ground condition having a greater number DE in each term (Figure 4.7B, bottom axis). Advaita iPathwayGuide analysis showed the pathways most affected by vitamin D treatment were metabolic pathways, oxidative phosphorylation, and cytokine-cytokine receptor interaction (Figure 4.7C). Oxidative phosphorylation was more affected by vitamin D treatment on ground ($p=1.43\times10^{-19}$, 42 DE genes) than in flight ($p=1.22\times10^{-8}$, 19 DE genes). Consistent with this observation, more genes within the electron transport chain were downregulated in ground than in flight (Figure 4.7D). Vitamin D treatment induced several members of the c-x-c motif ligand family in both conditions including *CXCL1*, *CXCL2*, *CXCL3* and *CXCL6*, while the cytokine interleukin 6 (*IL6*) was only induced with 25(OH)D_3 treatment for the ground condition (Figure 4.7E). The proliferation associated genes *FOXM1* and marker of proliferation Ki67 (*Ki67*) were only significantly upregulated in the ground condition (Figure 4.7E).

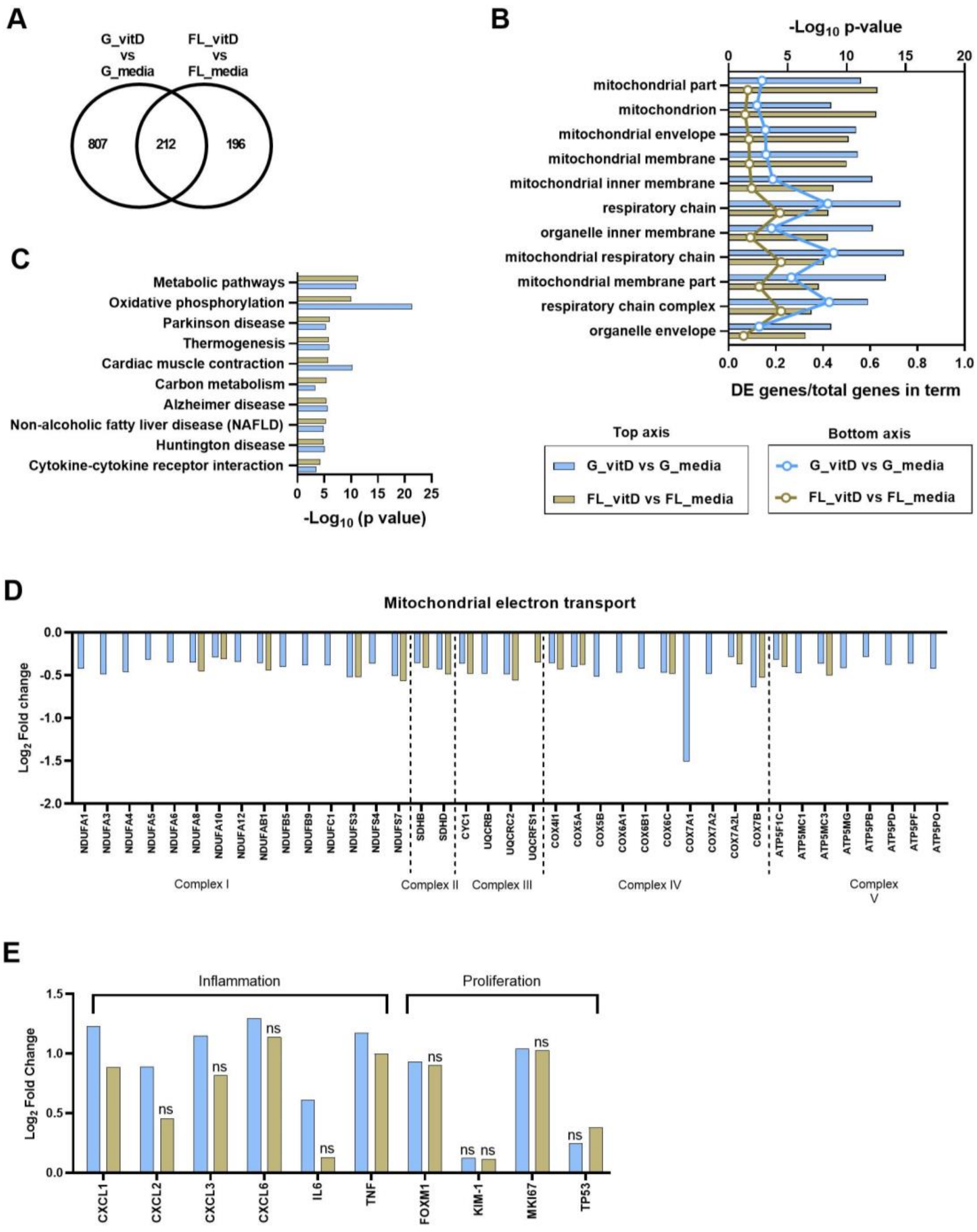

Figure 4.7. Vitamin D represses mitochondrial gene expression and induces chemokines in PTECs. A) Venn diagram depicting the number of DE genes between 25(OH)D_3 and control treatments in the ground and flight conditions. B) Gene ontology analysis of the set of DE genes showing enrichment of mitochondrial terms. Top axis displays FDR adjusted p-value for the cellular component term while the bottom axis displays the ratio of DE genes over the total number of genes within that specific term. C) iPathwayGuide analysis of the pathways significantly impacted by 25(OH)D_3 treatment in ground and flight conditions. D) Plot of genes differentially expressed in mitochondrial electron transport. E) Selected genes involved in inflammation and cellular proliferation. The bars represent the comparison of vitamin D (25(OH)D_3) and control (media) treated PT-MPS for the ground condition (blue bars) and the flight condition (gold bars). Genes that were not statistically significant are noted by "ns".

4.4.5 Impact of microgravity on PTEC metabolism of vitamin D

To evaluate the impact of microgravity on PTEC metabolism of vitamin D, we quantified vitamin D and its primary metabolites 1α,25-dihydroxy vitamin D3 (1α,25$(OH)_2D_3$), 4β,25-dihydroxy vitamin D3 (4β,25$(OH)_2D_3$), and 24R,25-dihydroxy vitamin D3 (24R,25$(OH)_2D_3$) in the device effluents. Expression of *CYP3A5*, *CYP24A1*, and *CYP27B1* was detected in all samples (Figure 4.8B). Formation of 1α,25$(OH)_2D_3$ and 4β,25$(OH)_2D_3$ was consistent across donors, whereas formation of 24R,25$(OH)_2D_3$ varied by donor (Figure 4.8C). Formation of 1α,25$(OH)_2D_3$ (p=0.1036), 4β,25$(OH)_2D_3$ (p=0.4451), and 24R,25$(OH)_2D_3$ (p=0.2228) did not differ between ground and flight (Figure 4.8D). Consistent with formation of 1α,25$(OH)_2D_3$ and agonism of the VDR, the expression of *CYP24A1* but not *CYP3A5* or *CYP27B1* was significantly higher in vitamin D treated samples than media controls for both ground and flight conditions (Figure 4.8E). Expression of *CYP24A1* was correlated with formation of 24R,25$(OH)_2D_3$ in ground samples (r=0.77, p=0.008) but not flight samples (r=0.17, p=0.715).

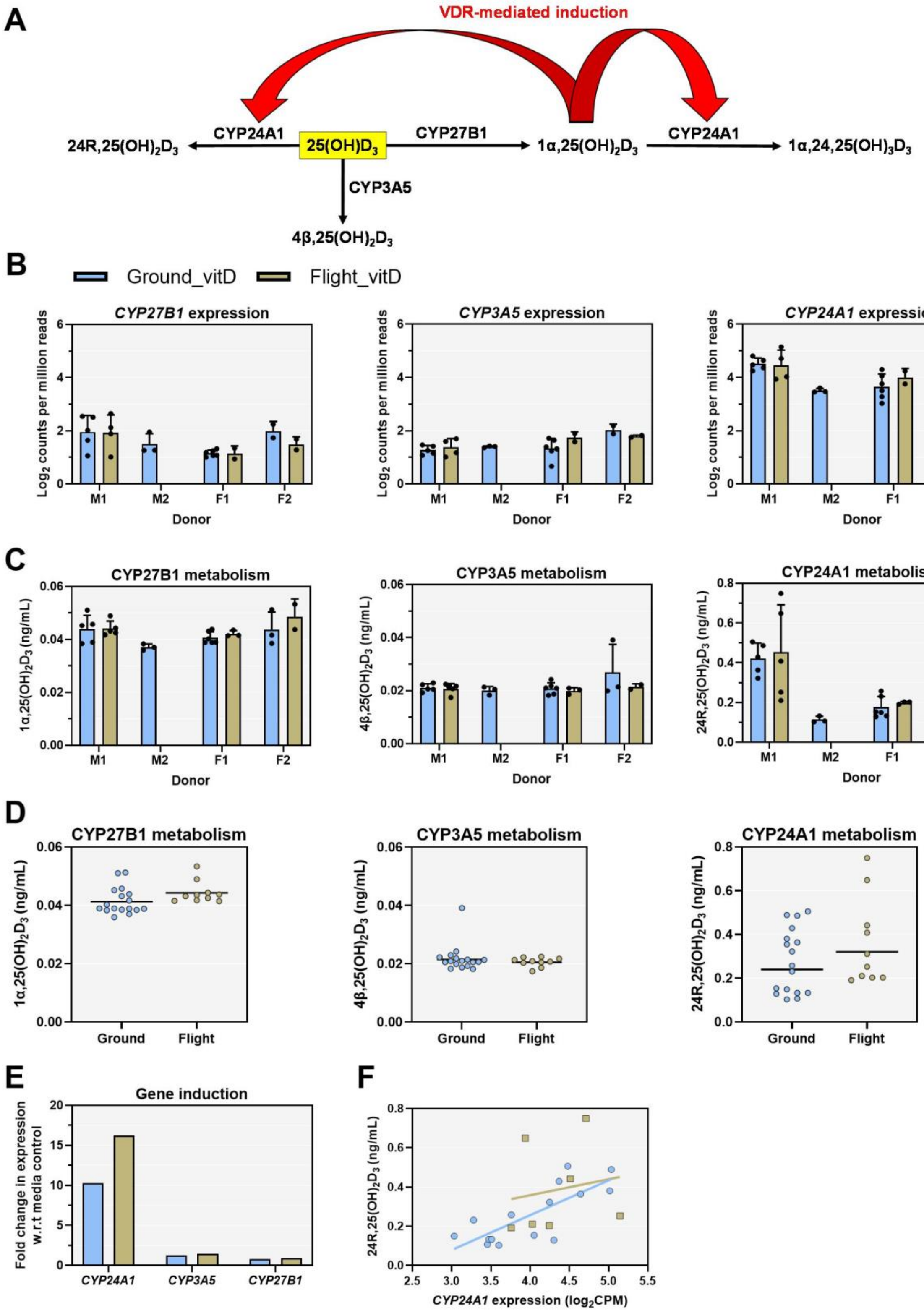

Figure 4.8. Microgravity does not alter metabolism of vitamin D or transcriptional regulation of *CYP24A1*. A) Scheme of vitamin D metabolism and feedback regulation of *CYP24A1* via the VDR in

PTECs. 25(OH)D_3 undergoes multiple metabolic reactions within PTECs including bioactivation to 1α,25$(OH)_2D_3$ via CYP27B1 as well as inactivation through CYP24A1 mediated conversion to 24R,25$(OH)_2D_3$ and CYP3A5 mediated conversion to 4β,25$(OH)_2D_3$. 1α,25$(OH)_2D_3$ undergoes sequential metabolism by CYP24A1 to 1α,24R,25$(OH)_3D_3$, however, this analyte was not quantified in this assay. 1α,25$(OH)_2D_3$ agonizes the VDR leading to induction of *CYP24A1*. B) Plots of $\log_2$ counts per million reads of vitamin D metabolizing cytochrome P450 enzymes. Data are presented as mean±s.d. C) Levels of vitamin D metabolites in device effluents formed from each P450 pathway separated by donor and condition. Data are presented as mean±s.d. D) Average metabolite concentrations of 1α,25$(OH)_2D_3$, 4β,25$(OH)_2D_3$, and 24R,25$(OH)_2D_3$ in ground and flight. E) Fold-change in *CYP24A1*, *CYP3A5*, and *CYP27B1* expression after 48-hour vitamin D treatment relative to media controls in ground and flight conditions. F) Plot of 24R,25$(OH)_2D_3$ effluent levels compared to the corresponding expression of *CYP24A1* in that sample. *CYP24A1* expression was correlated with levels of 24R,25$(OH)_2D_3$ in ground samples (r=0.77, p=0.0008) but not flight samples (r=0.17, p=0.71). Ground condition samples are represented by blue bars/symbols while flight condition samples are represented by gold bars/symbols.

4.5 Discussion

To explain the observation that plasma levels of 1α,25$(OH)_2D_3$ decline in astronauts in flight (microgravity), we explored the effects of a microgravity environment on PTEC metabolism of exogenous vitamin D. In both the ground condition and flight condition, PTECs treated with 25(OH)D_3 generated 1α,25$(OH)_2D_3$, 4β,25$(OH)_2D_3$, and 24R,25$(OH)_2D_3$, the primary metabolites of CYP27B1, CYP3A5, and CYP24A1, respectively (Figure 4.8). The levels of these metabolites did not differ between ground and flight conditions. Induction of *CYP24A1*, a canonical target gene of the VDR, was robust indicating that the feedback mechanism within PTECs was intact and did not differ between ground and flight conditions (Figure 4.8). We conclude that microgravity did not alter the metabolic activity of CYP27B1, CYP24A1, or CYP3A5, nor did it significantly alter the inducibility of *CYP24A1*, a feedback mechanism which helps to tightly regulate plasma levels of 1α,25$(OH)_2D_3$.

There are a couple of reasons why plasma levels of 1α,25$(OH)_2D_3$ decrease over time in astronauts independent of a direct change in the intrinsic activity of renal CYP27B1, CYP3A5, or CYP24A1. First, in microgravity, changes in hydrostatic pressure drive a movement of water and protein from the intravascular space to intracellular and interstitial compartments resulting in a decrease in plasma volume, total circulating albumin, and total circulating protein.[297] As 25(OH)D_3 is delivered to the proximal tubule bound to its carrier protein (DBP), a redistribution of this protein out of the central compartment to interstitial spaces could reduce delivery of $25(OH)D_3$ to the proximal tubule and result in reduced formation of $1\alpha,25(OH)_2D_3$.

Second, a variety of adaptive endocrine and sympathetic nervous system responses attempt to account for the effective decrease in plasma volume including through activation of the renin-angiotensin-aldosterone system and release of vasopressin (antidiuretic hormone) that alters vascular tone and promotes sodium retention.[298] Vasopressin, which is considerably elevated in microgravity, acts to increase trafficking of the water channel aquaporin 2 (AQP2) from intracellular vesicles to the plasma membrane in collecting-duct cells, and promotes *AQP2* expression if vasopressin levels remain high.[299] Normally, increased sodium retention would be followed by increased water reabsorption. However, in microgravity, these processes are potentially disconnected because of hypercalciuria secondary to bone mineral loss.[299] Indeed, high luminal calcium antagonizes vasopressin-mediated trafficking of AQP2 through activation of the calcium sensing receptor (CaSR) and a subsequent reduction in cyclic adenosine monophosphate, micro-RNA targeting of *AQP2* RNA, and proteasomal degradation of AQP2.[300, 301] Moreover, urinary excretion of AQP2 is higher in microgravity than normogravity.[302, 303] A similar, counter-productive hormonal feedback response to high serum calcium may occur in the regulation of vitamin D. Parathyroid hormone (PTH), released from the parathyroid gland when serum calcium levels are low, acts on the parathyroid hormone 1 receptor on PTECs to induce *CYP27B1*.[47, 304] As astronauts present with elevated serum calcium and tend to have lower plasma PTH levels compared to pre-flight, decreased PTH production may be a mechanism by which *CYP27B1* expression and thus formation of $1\alpha,25(OH)_2D_3$ is reduced in microgravity.[144, 287] Furthermore, high extracellular calcium can directly modulate PTEC regulation of vitamin D homeostasis, possibly via the CaSR.[305, 306] Future studies should include PTH and/or different levels of calcium in $25(OH)D_3$ treatment media to better emulate the renal microenvironment of astronauts and determine the impact of PTH and calcium on regulation of vitamin D metabolism in PTECs.

The metabolite 1α,24R,25-trihydroxy vitamin D_3 ($1\alpha,24R,25\ (OH)_3D_3$), which is generated by CYP27B1-mediated metabolism of $1\alpha,25(OH)_2D_3$, was not measured in our assay. Therefore, it is unclear whether the reason for the low levels of $1\alpha,25(OH)_2D_3$ was poor formation from $25(OH)D_3$ or rapid elimination to $1\alpha,24R,25(OH)_3D_3$. The levels of $25(OH)D_3$ (~750 ng/mL) used in our study were supraphysiological and far exceeded those of $1\alpha,25(OH)_2D_3$ (~0.04 ng/mL). The average ratio of $25(OH)D_3$:$1\alpha,25(OH)_2D_3$ in human plasma is ~500, whereas in this study it was ~18,750.[307] While $1\alpha,25(OH)_2D_3$ is the most potent vitamin D metabolite binding to the VDR, $25(OH)D_3$ can compete with $1\alpha,25(OH)_2D_3$ for binding of intestinal chromatin homogenates when administered at concentrations 150-fold higher than that of $1\alpha,25(OH)_2D_3$.[308] Similarly, $25(OH)D_3$ stimulates calcium transport, a marker of VDR activity, in perfused intestine when administered at levels 200-times that of $1\alpha,25(OH)_2D_3$.[308] *In vitro*, there is strong evidence that $25(OH)D_3$ can activate the VDR.[309, 310] Thus, both $25(OH)D_3$ and $1\alpha,25(OH)_2D_3$ can elicit VDR responses if the ratio of $25(OH)D_3$:$1\alpha,25(OH)_2D_3$ is greater than 200. Consequently, as the actual intracellular levels of $1\alpha,25(OH)_2D_3$ were unknown in this study, it is unclear whether activation of the VDR and induction of *CYP24A1* was triggered by $25(OH)D_3$ or $1\alpha,25(OH)_2D_3$. Nevertheless, we can conclude that microgravity did not appear to affect metabolism of $25(OH)D_3$ via CYP27B1, CYP3A5, or CYP24A1.

A final mechanism by which microgravity could alter renal metabolism of vitamin D is through a change in megalin localization or activity and reduced uptake of $25(OH)D_3$-bound DBP. Megalin is the entry receptor for $25(OH)D_3$-bound DBP. As megalin plays a major role in the response of PTECs to proteinuria [125, 126], we tested whether megalin activity was altered in flight compared to ground condition by treating the PTECs with 2% normal human serum. In both ground and flight conditions, pathway analysis revealed serum treatment induced genes associated with proliferation, inflammation, and reorganization of the extracellular matrix environment, with a concomitant downregulation of metabolic and biosynthetic pathways (Figure 4.4). Upstream regulator analysis predicted the transcriptional changes were driven by upstream regulators associated with inflammation (TNF), proliferation (FOXM1), and metabolism (SREBF2, PPARGC1A, PPARA)(Table 4.3). A serum-induced switch to a proliferative, secretory phenotype was confirmed by increased secretion of KIM-1 and IL-6 in device effluents, respectively (Figure 4.6). The transcriptional and protein-level response of PTECs to 2%

normal human serum did not differ between ground and flight conditions, suggesting that PTEC megalin activity was unchanged by microgravity. While there was no condition-dependent response of PTECs to 2% human serum treatment, the observed transcriptional responses suggest PTECs have the potential to promote renal inflammation and fibrosis during proteinuria.

The most noticeable effect of serum on the PTEC transcriptome was alteration of mitochondrial energetics through repression of electron transport chain, fatty acid catabolism and synthesis, tricarboxylic acid, and mitochondrial transporter genes (Figures 4.4 and 4.5). Disruption of fatty acid metabolism and oxidative phosphorylation is particularly important because they are key characteristics of fibrotic renal tissue. Genome-wide transcriptomic analysis comparing fibrotic and normal human renal tissue identified inflammation and metabolism as the top dysregulated pathways.[129] More specifically, genes involved in fatty acid metabolism and transcriptional regulators of fatty acid metabolism and oxidative phosphorylation such as *PPARGC1A* and *PPARA* were decreased.[129] In mouse and rat models of fibrosis, treatment with the PPARA agonists, fenofibrate or MHY2013, restored fatty acid oxidation enzyme expression and ameliorated disease severity.[129, 311-313] Agonism of PPARA with fenofibrate lowered the rate of eGFR decline and reduced the incidence of microalbuminuria and macroalbuminuria in patients with type 2 diabetes, suggesting that PPARA is a potential target to treat progressive renal disease in humans.[314] Moreover, separate from its action as a transcriptional activator of mitochondrial biogenesis and fatty acid oxidation, PPARA has been shown to interact directly with NF-κB and AP-1 subunits, inhibiting their transactivation in human aortic smooth muscle cells.[315] However, co-treatment of PTECs with fenofibric acid did not prevent or significantly alter serum induced secretion of KIM-1, IL-6, IL-8, MMP1, or MMP7 (Supplemental Figure 4.3). Future studies will be needed to evaluate the degree of agonism of PPARA by 5μM fenofibric acid in the PT-MPS.

IL-6 is a pleiotropic cytokine that plays important roles in acute-phase response, B-cell and T-cell differentiation and growth, hematopoiesis, and metabolism in non-immune cells such as myocytes.[316, 317]. The breadth of effects of IL-6 stems, in part, from its ability to elicit cell signaling through two distinct mechanisms. The first mechanism is termed canonical IL-6 signaling wherein IL-6 binds to the

IL-6 receptor (IL-6R) followed by binding of the IL-6/IL-6R complex to the transmembrane protein, glycoprotein 130 (gp130) which leads to gp130 dimerization and initiation of intracellular signaling.[318] The second mechanism is termed IL-6 trans-signaling which occurs when IL-6 binds a soluble version of the IL-6R (sIL-6R), formed either from alternative splicing of the *IL-6R* transcript or proteolytic cleavage of the extracellular portion of the IL-6R. The IL-6/sIL-6R complex binds to gp130 leading to its homodimerization and initiation of intracellular signaling.[318] In both signaling mechanisms, IL-6 classic and trans-signaling augment janus kinase (JAK) and signal transducers and activators of transcription (STAT) and mitogen activated protein kinase (MAPK) pathways.[316, 318] Importantly, while IL-6R expression is primarily limited to immune cells, hepatocytes, and podocytes, virtually all cells express gp130 and can therefore be subject to IL-6 trans-signaling effects.[316] IL-6, sIL-6R, and a soluble form of gp130, which acts as a negative regulator of IL-6 trans-signaling by binding the IL-6/sIL-6R complex, are detectable in serum, while sIL-6R is also present in urine.[319, 320] In cells that express IL-6R, the initiation of classic or trans-signaling mechanism depends on the availability of IL-6, membrane bound IL-6R, sIL-6R, and gp130.[321] The result of the IL-6 signaling, either pro- or anti-inflammatory, depends on the particular target cell. For example, IL-6 classic signaling can direct CD4$^+$ T-cells to differentiate into pro-inflammatory T$_h$17 cells while maintenance of T$_h$17 status and inhibition of differentiation of CD4$^+$ T-cells into anti-inflammatory T$_{REG}$ cells occurs through IL-6 trans-signaling.[322, 323] Because IL-6 is increased in the proximal tubules of patients with IgA nephropathy and its expression correlated with disease severity [324], and as tubular epithelial cells stimulated with albumin *in vitro* secrete IL-6 [325], we investigated whether serum treatment promoted an IL-6 response.[324, 325] Serum treatment induced IL-6 secretion (Figure 4.6) but not *IL-6* expression, suggesting a post-transcriptional mechanism may drive tubular secretion of IL-6 in proteinuric states. Aside from transcriptional control, regulation of IL-6 expression occurs through a variety of post-transcriptional mechanisms including stabilization of mRNA via p38 MAPK and AT-rich interaction domain 5A (ARID5A), or promotion of mRNA degradation by the RNA-binding proteins, tristetraprolin and butyrate response factor 1, or the nuclease regnase-1.[316] While *IL-6* transcription was not induced, its gene contains elements that are regulated by stress-associated factors such as NF-κB and AP-1 that have previously been implicated in controlling tubular response to proteinuria.[120, 316] In a follow up study on ground, co-treatment with tocilizumab, a monoclonal antibody that binds both IL-6R and sIL-6R, or ruxolitinib, a JAK1/2 inhibitor, did not affect serum-induced secretion of IL-6 or KIM-1 (Supplemental Figure 4.4). Future experiments will need to validate that the concentration of tocilizumab and ruxolitinib used were sufficient to prevent IL-6 signaling through the JAK/STAT pathway. Furthermore, soluble gp130 should be included as a control to delineate IL-6 classic from IL-6 trans-signaling.

KIM-1 is a transmembrane glycoprotein absent from healthy tubule cells but is the most highly induced transcript following AKI in rat.[104] The ectodomain undergoes matrix metalloproteinase-dependent proteolytic cleavage resulting in a soluble form that is readily detectable in urine.[326] KIM-1 is validated as a preclinical biomarker of AKI, showing better sensitivity and specificity than traditional renal injury markers such as blood urea nitrogen and serum creatinine.[327] KIM-1 conveys phagocytic function to the epithelial cells as a receptor for phosphatidylserine and oxidized lipoproteins, a function that is protective early after injury by modulating innate immune responses.[328, 329] However, constitutive or prolonged expression of KIM-1 in human kidney tissue is associated with renal fibrosis and inflammation, regardless of disease (i.e., IgA nephropathy, diabetic nephropathy, membranous glomerulonephritis).[330] Moreover, proximal tubule cells that express KIM-1 also express various dedifferentiation markers such as Ki67 and vimentin as well as CD133 and CD24 which are associated with cells with progenitor-like features.[128, 283, 331] A portion of KIM-1^+ PTECs exhibit a pro-inflammatory gene signature that was predicted to be driven via NF-κB.[283] We observed that serum induce a marked increase in KIM-1 secretion in device effluents in both flight and ground conditions (Figure 4.6). This was most likely the result of dedifferentiation and activation of a cellular proliferation program, as the increase in KIM-1 secretion after serum treatment in our follow-up study on ground (supplementary figure 4.6) was gradual rather than sudden, which is more consistent with a change in cell number. A change in cell number is supported by the observation of a broad and robust induction of cell cycle genes (Supplemental Figures 4.1 and 4.2). However, a significant increase in KIM-1 was observed as soon as 8 hours, indicating that serum may have also caused an acute stress response that resulted in activation of metalloproteinases and proteolytic cleavage of the ectodomain.

One mechanism by which PTECs acquire a proinflammatory phenotype is through cell cycle arrest at either the G1/S or G2/M phases of the cell cycle. While there are no definitive transcriptional markers of cell cycle arrest, we observed induction of genes involved in cell cycle arrest. For example, SMAD3 was the first and second most significantly induced gene by serum treatment in ground and flight, respectively (Supplemental Tables 4.3 and 4.4). SMAD3 is strongly associated with renal fibrosis as SMAD3 knockout prevents fibrosis in mouse models of UUO, diabetic nephropathy, hypertensive nephropathy, and chronic aristolochic acid nephropathy.[332-335] A potential mechanism by which SMAD3 contributes to renal fibrosis is promotion of cell cycle arrest. For example, SMAD3 contributes to c reactive protein mediated G1/S cell cycle arrest in a mouse model of IRI and in human kidney 2 (HK-2) cells.[336] Arrest of proximal tubule cells in the G2/M phase has also been implicated in acquisition of a proinflammatory secretory phenotype in IRI, UUO, and aristolochic acid nephropathy mouse models of AKI.[130] Arrest in the G2/M phase would be expected to be associated with higher levels of DNA damage response transcripts. In our data, we observed that several DNA damage response transcripts were induced including *RAD51*, *RAD54*, and *BRCA1*. However, *RAD51*, *RAD54*, and *BRCA1* have also been shown to be downstream targets of FOXM1 during epithelial repair after IRI.[128] Whether serum treatment increases the proportion of PTECs arrested at either the G1/S or G2/M stages should be investigated in future studies.

In summary, we demonstrated that microgravity did not alter PTEC metabolism of vitamin D nor did it induce a unique response of PTECs to human serum. The decline in the plasma levels of $1\alpha,25(OH)_2D_3$ in astronauts in flight appears to be independent of a change in renal expression of vitamin D metabolizing enzymes. Future efforts should focus on delineating the role of PTH and serum calcium on PTEC metabolism of vitamin D. The overall response of PTECs to serum challenge is congruent with the maladaptive repair response *in vivo* in which a failure of PTECs to re-differentiate after tubular injury is associated with tissue inflammation and fibrosis. The factors regulating PTEC differentiation status during proteinuric and disease states should further be elucidated and their potential as novel therapeutic targets for treating and preventing renal inflammation and fibrosis should be investigated.

Supplemental Figure 4.1. Serum induces cell cycle genes in ground condition

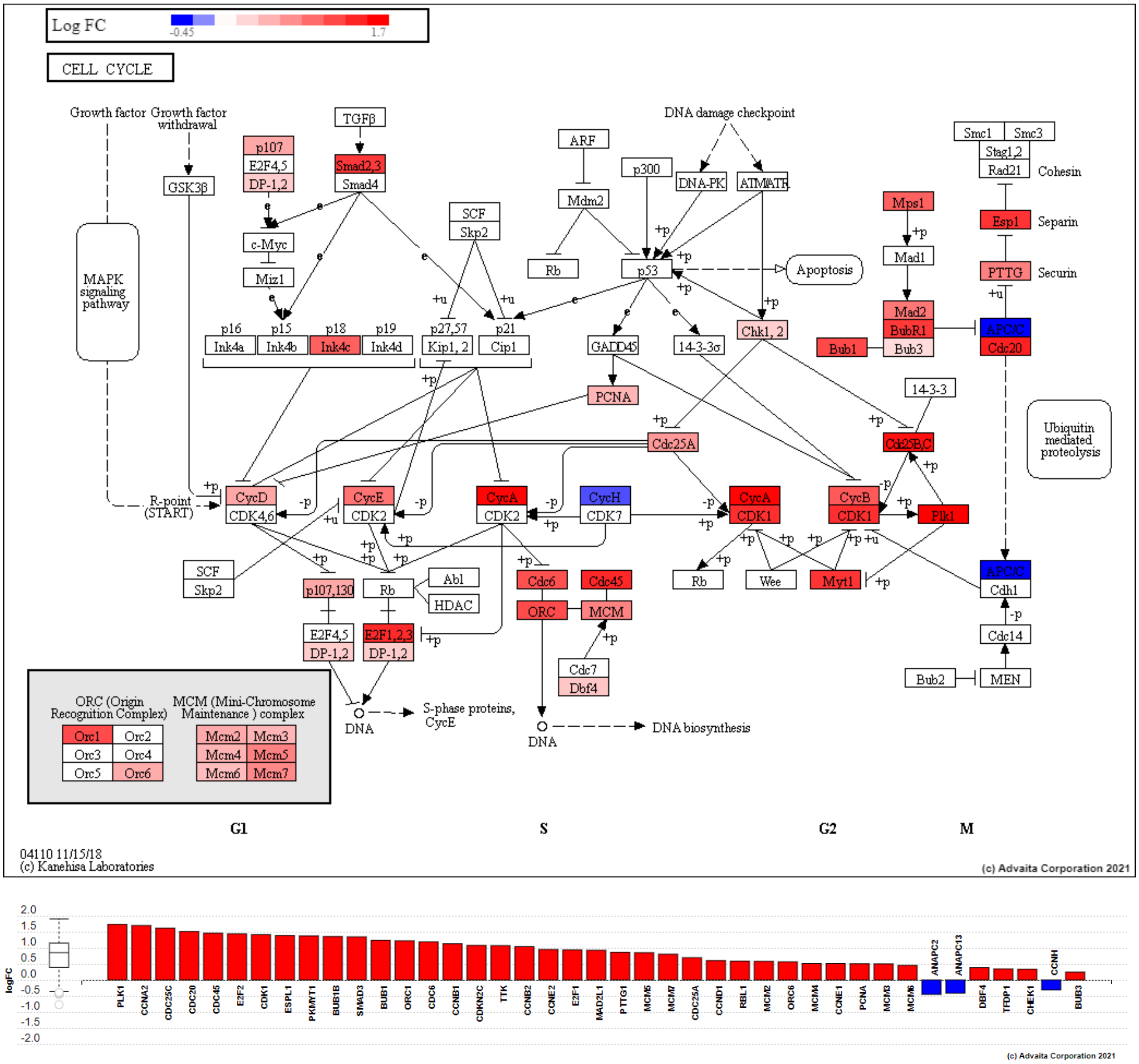

Treatment of PT-MPS with 2% normal human serum in the ground condition for 48-hours induces cell cycle genes. Top panel: the position of gene within the cell cycle (i.e., G1, S, G2, M) and their interaction (inhibtion or activation) with other cell cycle associated genes is shown. Bottom panel: The $\log_2$ fold change in gene expression in the serum-treated samples relative to media control samples is displayed.

Supplemental Figure 4.2. Serum induces cell cycle genes in flight condition.

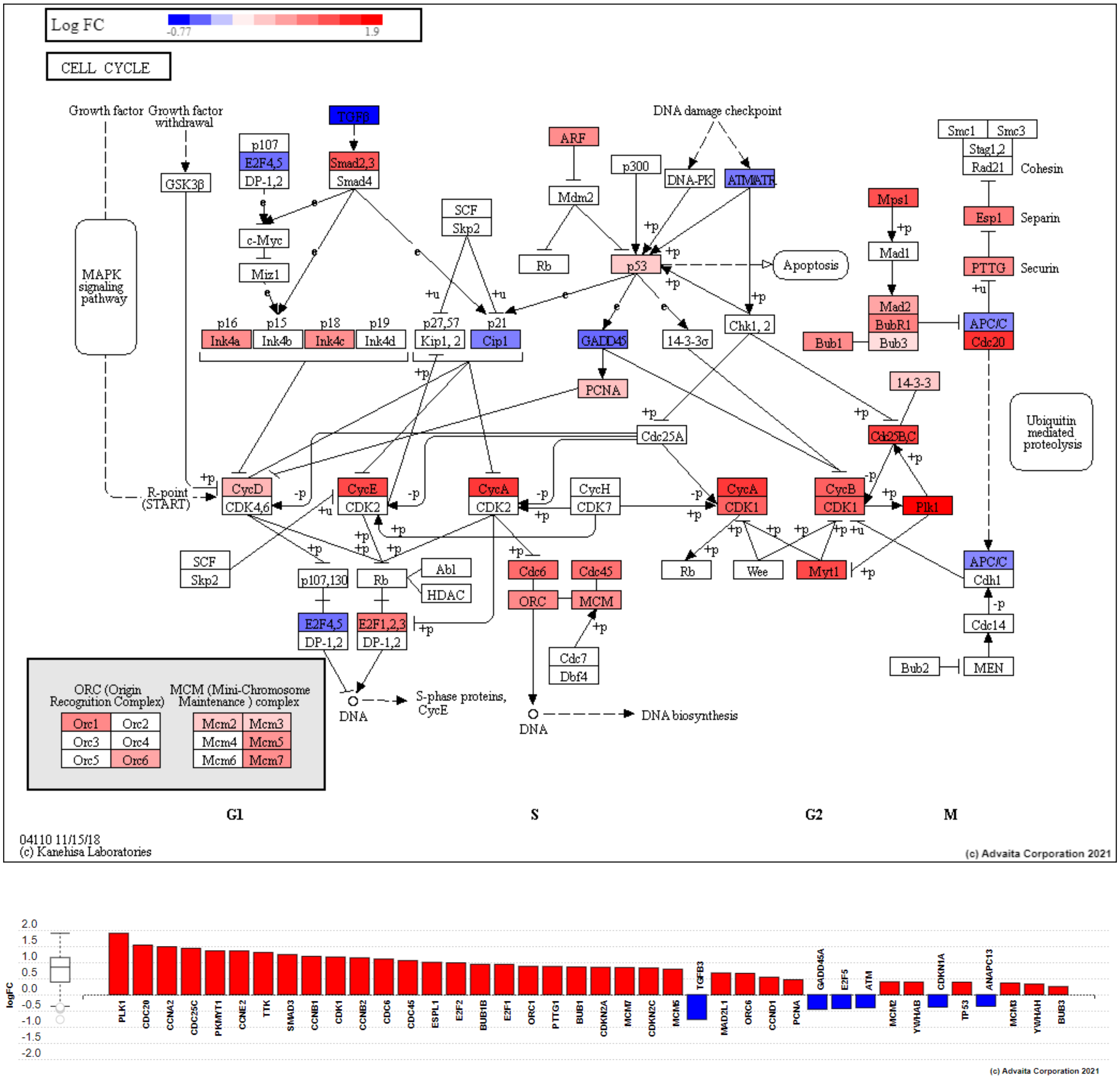

Treatment of PT-MPS with 2% normal human serum in the flight condition for 48-hours induces cell cycle genes. Top panel: the position of gene within the cell cycle (i.e., G1, S, G2, M) and their interaction (inhibtion or activation) with other cell cycle associated genes is shown. Bottom panel: The $\log_2$ fold change in gene expression in the serum-treated samples relative to media control samples is displayed.

Supplemental Figure 4.3. Fenofibric acid does not prevent a serum-induced secretory phenotype in PTECs.

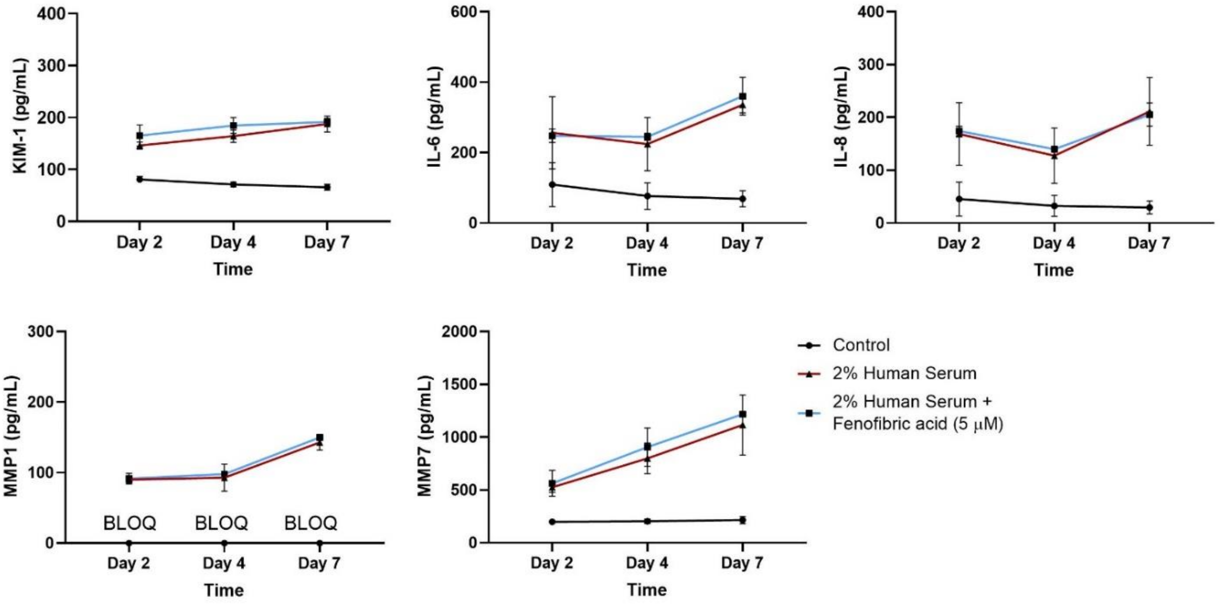

PT-MPS were treated for 7 days at a flow rate of 1 µL/min with media control (n=3, black line), 2% normal human serum (n=2, red line), or 2% normal human serum + 5 µM fenofibric acid (n=2, blue line). Effluent was collected at day 2, 4, and 7, and assayed by ELISA for quantification of KIM-1, IL-6, IL-8, total MMP1, and total MMP7. Levels of MMP1 for the media control were below the limit of quantification of the assay and are noted by "BLOQ".

Supplemental Figure 4.4. Serum induced secretion of KIM-1 and IL-6 secretion may be independent of JAK1/2 pathway.

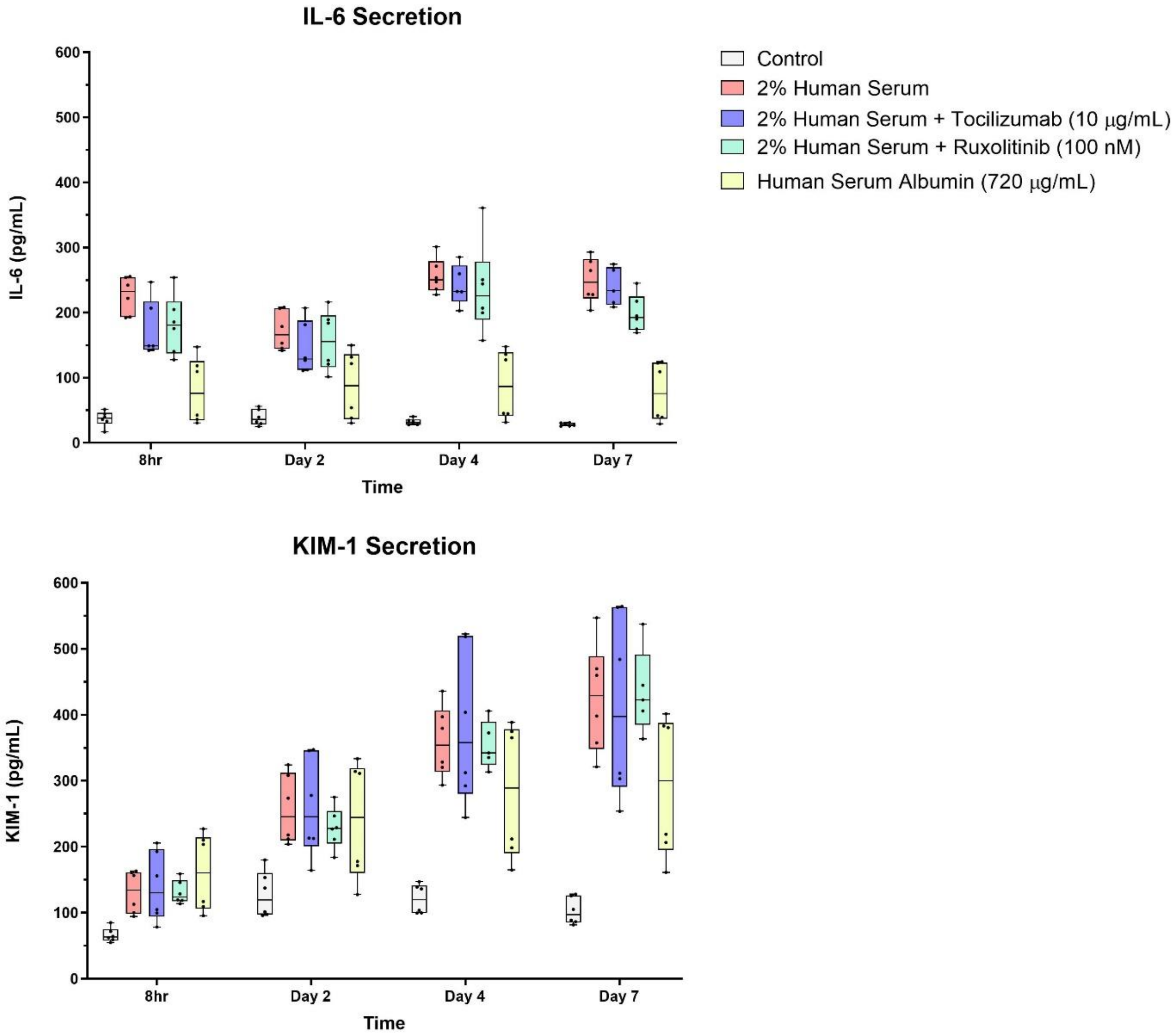

PT-MPS were treated for 7 days at a flow rate of 1 µL/min with media control (n=6, white box), 2% normal human serum (n=6, red box), 2% normal human serum + tocilizumab (n=5-6, 10 µg/mL) (purple box), 2% normal human serum + ruxolitinib (n=6, 100 nM) (green box), or an equivalent concentration of human serum albumin present in 2% human serum treatment media (n=6, 720 µg/mL) (yellow box). Effluent was collected at 8 hours and day 2, day 4, and day 7, and assayed by ELISA for quantification of KIM-1 and IL-6.

Supplemental Table 4.1. Genes differentially expressed in PTECs by 2% human serum treatment in selected pathways in the ground and flight conditions.

		Ground serum vs Ground media	**Flight serum vs Flight media**
Pathway	**Direction**	**Gene**	**Gene**
Cytokine-cytokine receptor interaction	Upregulated	*BMP2, BMPR1A, CCL20, CCL28, CD40, CD70, CSF1, CXCL1, CXCL16, CXCL3, CXCL5, CXCL6, EDA2R, EDAR, FAS, IL18R1, IL1RL1, IL23A, IL32, IL6ST, LIF, LTB, RELT, TGFBR2, TNFRSF11A, TNFRSF11B, TNFSF10*	*CCL2, CCL20, CCL28, CD40, CD70, CLCF1, CSF1, CXCL1, CXCL16, CXCL2, CXCL3, CXCL5, CXCL6, CXCL8, EDAR, IL15RA, IL18R1, IL23A, IL32, INHBB, LIF, LTB, PF4V1, TNF, TNFRSF11A, TNFRSF11B, TNFSF10, TNFSF15*
	Downregulated	*GDF15, IL13RA2, IL17RB, POR, TNFRSF14*	*CTF1, GDF15, GDF7, IL13RA2, IL17RB, IL1RL2, LEPR, LIFR, TGFB3*
Chemokine signaling	Upregulated	*ADCY3, ADCY7, CCL20, CCL28, CXCL1, CXCL16, CXCL3, CXCL5, CXCL6, DOCK2, MAP2K1, NFKB1, PXN, SHC4, VAV1*	*CCL2, CCL20, CCL28, CDC42, CXCL1, CXCL16, CXCL2, CXCL3, CXCL5, CXCL6, CXCL8, DOCK2, HRAS, NFKBIA, PF4V1, PXN, RAC1, SHC4*
	Downregulated	*MAPK3*	*ADCY9, GNAI1, GRK2, MAPK3, SOS1, SOS2*
PPAR signaling	Upregulated	*ACSL5, FABP5, SORBS1*	*ACSL5, FABP5, SORBS1*
	Downregulated	*ACADM, ACSL1, ACSL3, ACSL4, ANGPTL4, CPT1A, DBI, EHHADH, FABP3, FADS2, GK* *NR1H3, SCD, SCP2, SLC27A2, SLC27A5*	*ACADL, ACADM, ACSL1, ACSL3, ACSL4, ANGPTL4, CPT1A, EHHADH, FABP3, FADS2, GK, ME1, NR1H3, PLIN2, SCD, SCP2, SLC27A2*
Fatty acid metabolism	Upregulated	*ACSL5, HACD4*	*ACSL5*
	Downregulated	*ACAA2, ACACA, ACADM, ACADS, ACADSB, ACADVL, ACAT1, ACAT2, ACSL1, ACSL3, ACSL4, CPT1A, EHHADH, FADS1, FADS2, FASN, HADH, HADHA, HADHB, HSD17B8, MECR, SCD, SCP2*	*ACAA2, ACACA, ACADL, ACADM, ACADS, ACADSB, ACADVL, ACAT1, ACAT2, ACSL1, ACSL3, ACSL4* *CPT1A, EHHADH, FADS1, FADS2, FASN, HADH, HADHA, HADHB, HSD17B8, MECR, PPT1* *SCD, SCP2*
TCA cycle	Downregulated	*ACO2, CS, IDH2, IDH3G, MDH1, MDH2, OGDHL, PDHA1, SDHB, SDHC, SDHD, SUCLG1, SUCLG2*	*ACO2, CS, DLAT, DLD, FH, IDH1, IDH2, IDH3A, MDH1, MDH2, OGDH, OGDHL, PDHA1, SDHB, SDHD, SUCLA2, SUCLG1, SUCLG2*
Steroid biosynthesis	Upregulated	*CYP24A1*	*CYP24A1*
	Downregulated	*CYP51A1, DHCR7, EBP, FDFT1, HSD17B7, LSS, MSMO1, NSDHL, SC5D, SQLE, TM7SF2*	*CYP51A1, DHCR7, EBP, FDFT1, HSD17B7, LSS, MSMO1, NSDHL, SC5D, SQLE, TM7SF2*

Table displays genes differentially expressed by 48-hour 2% normal human serum treatment relative to control for various pathways in the ground (middle column) and flight conditions (far right column).

Supplemental Table 4.2. Fatty acid, intermediary, and cholesterol metabolism genes.

		Ground serum vs Ground media		Flight serum vs Flight media	
Role	**Gene**	**Log$_2$FC**	**Adj. p-value**	**Log$_2$FC**	**Adj. p-value**
Formation of diacylglycerol, lipogenesis	*LPIN1*	-0.40	8.61E-03	-0.49	1.74E-03
FA binding	*FABP3*	-1.55	4.94E-14	-1.38	3.06E-10
FA acyl-CoA ligase activity	*SLC27A3*	-1.17	4.72E-13	-1.21	7.32E-12
Mitochondrial membrane transporters	*SLC25A1*	-0.62	1.02E-09	-0.5	5.43E-06
	SLC25A3	-0.31	7.43E-03	-0.29	3.37E-02
	SLC25A4	-0.65	4.22E-08	-0.73	8.89E-09
	SLC25A5	-0.63	1.17E-09	-0.64	6.33E-09
	SLC25A6	-0.64	2.54E-09	-0.66	8.20E-09
	SLC25A11	-0.45	7.53E-06	-0.46	1.80E-05
	SLC25A16	-0.42	1.02E-03	-0.39	1.39E-02
	SLC25A23	-0.38	2.59E-04	-0.39	5.53E-04
	SLC25A30	-0.71	5.70E-06	-0.98	4.50E-08
Tricarboxylic acid cycle (TCA)	*ACO2*	-0.64	3.87E-07	-0.81	1.17E-09
	CS	-0.34	3.56E-03	-0.48	9.12E-06
	DLAT	-0.27	2.28E-01	-0.60	4.10E-05
	DLD	-0.18	6.49E-01	-0.40	1.73E-02
	IDH2	-0.55	9.06E-06	-0.58	1.14E-05
	IDH3A	-0.27	2.40E-01	-0.42	2.42E-02
	MDH1	-0.45	1.89E-06	-0.52	9.71E-08
	MDH2	-0.37	1.12E-04	-0.39	3.12E-04
	OGDH	-0.23	3.00E-01	-0.54	1.22E-05
	OGDHL	-0.93	1.85E-08	-0.81	6.66E-06
	PDHA1	-0.37	1.12E-04	-0.35	1.14E-03
	SDHB	-0.44	1.04E-05	-0.42	1.33E-04
	SDHC	-0.28	2.11E-02	-0.24	1.46E-01
	SDHD	-0.52	1.61E-06	-0.64	1.00E-06
	SUCLA2	-0.21	4.77E-01	-0.39	1.34E-02
	SUCLG1	-0.49	1.46E-05	-0.59	6.65E-07
	SUCLG2	-0.37	6.92E-03	-0.45	8.14E-04
SREBF2 target genes	*CYP51A1*	-0.86	1.36E-06	-1.00	2.32E-07
	DHCR7	-1.44	3.89E-20	-1.35	4.11E-17
	FDFT1	-0.87	8.11E-16	-0.82	4.89E-13
	FDPS	-0.73	1.97E-09	-0.48	8.03E-04
	HMGCR	-0.43	2.88E-02	-0.68	1.98E-04
	HMGCS1	-0.77	6.14E-03	-1.19	5.94E-05
	IDI1	-1.32	1.42E-14	-1.31	4.89E-13
	LDLR	-1.08	1.43E-11	-1.11	7.25E-11
	LSS	-0.98	6.64E-12	-0.93	5.50E-10
	MVD	-0.74	1.66E-10	-0.55	1.18E-05
	NPC1L1	-0.94	2.31E-04	-1.20	5.52E-05
	PCSK9	-1.25	1.03E-10	-1.46	2.27E-11
	SC5D	-0.65	1.54E-05	-0.73	6.81E-06
	SQLE	-0.82	2.59E-11	-0.73	2.10E-08
	TM7SF2	-0.66	5.23E-09	-0.49	1.34E-04

Genes differentially expressed in PT-MPS after 48-hour 2% normal human serum treatment relative to media control in the flight and ground condition. Numbers highlighted in red are not statistically significant at an adjusted p-value of 0.05. Adj. p-value, adjusted p-value, FA, fatty acid; Log$_2$FC, Log$_2$ fold change.

Supplemental Table 4.3. Top 20 genes up- and down-regulated by serum on ground

Ground serum vs Ground media					
Upregulated			**Downregulated**		
Gene	**Log$_2$FC**	**Adj. p-value**	**Gene**	**Log$_2$FC**	**Adj. p-value**
SMAD3	1.35	1.50E-21	*DHCR7*	-1.44	3.89E-20
NCEH1	1.21	4.80E-16	*ACAT2*	-1.24	9.99E-17
FAM149A	1.91	1.83E-13	*FDFT1*	-0.87	8.11E-16
IRF1	0.81	2.29E-13	*MVK*	-1.17	5.61E-15
DHRS3	3.52	1.77E-12	*IDI1*	-1.32	1.42E-14
TGFBI	1.91	2.67E-12	*MMAB*	-0.89	1.88E-14
HMGA1	1.07	3.43E-12	*FABP3*	-1.55	4.94E-14
VSIR	1.97	4.52E-12	*GCAT*	-1.00	2.49E-13
DEPP1	1.08	1.62E-11	*ACADVL*	-0.60	3.47E-13
LINC00511	0.94	1.76E-11	*SCD*	-1.90	3.80E-13
ELK3	0.98	2.74E-11	*SLC27A3*	-1.17	4.72E-13
LAMC2	1.25	2.75E-11	*NSUN5P1*	-1.01	4.91E-13
APOBEC3B	1.48	3.01E-11	*SLC16A7*	-1.54	2.81E-12
LOXL2	1.19	8.55E-11	*HPN*	-1.19	3.12E-12
EPHB2	0.78	1.43E-10	*ACSS2*	-0.87	3.38E-12
PLAUR	1.18	1.49E-10	*EBP*	-1.03	3.82E-12
TPX2	1.31	1.49E-10	*RDH11*	-0.61	3.92E-12
RACGAP1	0.95	4.21E-10	*LSS*	-0.98	6.64E-12
GPRC5A	1.11	4.21E-10	*LDLR*	-1.08	1.43E-11
TFPI2	1.77	5.37E-10	*HAGHL*	-1.00	1.89E-11

Top-20 genes most significantly differentially expressed after 48-hour 2% normal human serum treatment relative to media control in PT-MPS in the ground condition. Abbreviations: Log$_2$FC, Log$_2$ fold change; Adj p.value, adjusted p.value.

Supplemental Table 4.4 Top 20 genes up- and down-regulated by serum in flight

Flight serum vs Flight media					
Upregulated			**Downregulated**		
Gene	**Log_2FC**	**Adj. p-value**	**Gene**	**Log_2FC**	**Adj. p-value**
IRF1	1.25	8.80E-20	*DHCR7*	-1.35	4.11E-17
SMAD3	1.24	1.02E-17	*SCD*	-2.16	9.62E-14
TAGLN2	0.85	3.79E-13	*ACAT2*	-1.15	3.07E-13
PLAU	1.01	1.08E-12	*IDI1*	-1.31	4.89E-13
TNFSF10	1.39	1.95E-12	*FDFT1*	-0.82	4.89E-13
SAT1	0.69	3.19E-12	*SLC16A7*	-1.75	9.83E-13
ELF3	0.74	2.27E-11	*ACSS2*	-0.97	9.83E-13
LINC00511	1.07	2.27E-11	*ACSL1*	-1.71	1.11E-12
APOBEC3B	1.78	3.52E-11	*PLA2G4F*	-1.50	2.72E-12
EPHB2	0.88	3.80E-11	*SLC27A3*	-1.21	7.32E-12
HMGA1	1.07	3.80E-11	*PAIP2B*	-1.38	1.06E-11
DEPP1	1.20	1.15E-10	*PCSK9*	-1.46	2.27E-11
CPM	0.87	1.46E-10	*PPARGC1A*	-1.14	2.27E-11
LGALS9	2.05	1.50E-10	*PANK1*	-1.14	2.66E-11
KPNA2	0.72	1.83E-10	*MSMO1*	-1.26	2.78E-11
TGFBI	1.80	3.06E-10	*UQCRC2*	-0.78	3.87E-11
DHRS3	3.63	3.12E-10	*LDLR*	-1.11	7.25E-11
LCN2	2.09	3.52E-10	*OSBPL1A*	-0.89	9.61E-11
TBXAS1	0.97	5.50E-10	*ATP1B1*	-0.78	9.75E-11
PLAUR	1.23	5.63E-10	*RAP1GAP*	-1.20	1.12E-10

Top-20 genes most significantly differentially expressed after 48-hour 2% normal human serum treatment relative to media control in PT-MPS in the flight condition. Abbreviations: Log_2FC, Log_2 fold change; Adj p.value, adjusted p.value.

5. Conclusions

Evaluation of the properties of novel therapeutic molecular entities entails a broad repertoire of testing that occurs across *in silico*, *in vitro*, and *in vivo* experiments. While the current drug development paradigm has identified and validated safe and efficacious drugs, there is room for improvement. In particular, the *in vitro* to *in vivo* extrapolation accuracy of conventional cell culture methods or cell lines to renal tubular cells is poor and these *in vitro* methods often fail to recapitulate the tubular phenotype *in vivo*.[65] Consequently, investigators have started to move toward utilizing more complex microenvironments called microphysiological systems or “organs-on-chips” as a means to improve *in vitro* renal cell phenotype. One that was under development and characterization when I joined the lab of Dr. Edward J. Kelly in the spring of 2015 was the proximal tubule microphysiological system or PT-MPS. The PT-MPS utilized primary renal tubular epithelial cells and a commercial microfluidic device. With the help of several former pioneering graduate students, the functionality of the ‘kidney-on-a-chip’ was described and later independently validated, including its homeostatic regulation of vitamin D metabolism and injury response to nephrotoxicants.[84, 200] The goal of my research in this dissertation was to take this emerging technology and apply it in the context of drug safety assessment and disease modeling.

In chapter 2 I characterized the safety of antisense oligonucleotides (ASOs) with two different backbone chemistries and discussed a novel mechanism by which CYP3A5 pre-mRNA is regulated. Characterization of the safety of ASOs remains a challenge in drug development, in part because ASO safety is modulated by both chemistry and sequence. Current *in vitro* models, including monolayer PTECs, are insensitive to ASO-induced toxicity and even when a positive signal is detected it is at supraphysiological drug concentrations and requires a treatment duration of at least six days.[100] Furthermore, the levels of KIM-1, which is a commonly used preclinical biomarker of AKI, do not correlate with ASO toxicity in PTEC cultures.[100] Therefore, I sought to evaluate whether the PT-MPS could successfully detect ASO toxicity at physiologically relevant concentrations and identify novel biomarkers of ASO toxicity. Two ASO chemistries were used: one a 2’-OMe-phosphorothioate (2’-OMe-

PSO) and a phosphorodiamidate morpholino oligonucleotide (PMO). The 2'-OMe-PSO used in this study caused tubular dysfunction in clinical trials, whereas PMOs have long been regarded for their safety and lack of off-target effects. When dosed at or near the maximal plasma concentration (1 μM), neither the 2'-OMe-PSO or PMO increased heme oxygenase 1 (HO-1) expression or KIM-1 secretion, markers of cellular stress and injury, respectively. Similarly, when a 2'-OMe-PSO and PMO were dosed at 10 μM, KIM-1 secretion was unaffected, consistent with it being a poor biomarker of ASO toxicity *in vitro*. However, RNAseq revealed that the 2'-OMe-PSO significantly affected the expression of ribosomal and RNA binding proteins (e.g. RNA5S9, SNORD3A, SNORD3B-1, SNORD3C, SNORD3D) which may point to the 2'-OMe-PSO causing non-specific off-target modulation of RNA binding protein activity. In addition, the 2'-OMe-PSO but not the PMO increased the secretion of microRNA 30e-5p (miR-30e-5). Secretion of miR-30e-5p could be evaluated in future studies as a potential biomarker for ASO-induced toxicity. In addition, a novel mechanism regulating the splicing of *CYP3A5*3* transcripts was described and the potential of CYP3A5 as a mediator of hypertension was discussed. Because oligonucleotides preferentially accumulate in proximal tubule cells and target RNA, ASOs targeting *CYP3A5* transcripts may be a novel strategy to treat hypertension. Our data suggest that PMOs are an optimal chemistry for treating a chronic condition such as hypertension given their excellent safety profile.

In Chapter 3, the ability of the PT-MPS to model a renal disease state and tubular injury response was evaluated. Proteinuria, the spillage of serum proteins into the urine, occurs in a variety of disease states and may contribute to disease progression and the development of renal fibrosis. However, it remains controversial as to whether specific components such as albumin can directly injure tubular cells. Because specific serum components cannot be delivered to tubular cells in animal models, we tested the effects of 2% normal human serum protein exposure or an equivalent concentration of albumin (720 μg/mL) in the PT-MPS. Cellular injury and secretion of pro-inflammatory cytokines were induced by serum, but not albumin. Both serum and albumin caused downregulation of transporters, channels, and metabolic and biosynthetic programs. The transcriptional changes induced by serum treatment mirrored those observed in a murine unilateral obstruction model of kidney fibrosis. Epigenomic analysis indicated these transcriptional changes were driven by stress-associated transcription factors (e.g., NF-κB and AP-1) along with a repression of transcription factors associated with a differentiated proximal tubule state (e.g., HNF4A and HNF1A). We propose that proteinuria, but not albuminuria, is directly causal in kidney injury and fibrosis through activation of a maladaptive phenotype characterized by secretion of pro-inflammatory cytokines and extracellular matrix-modifying enzymes. The PT-MPS was useful in allowing exploration of tubular injury responses to defined stimuli. Future studies could evaluate the effect of different forms of albumin (e.g., carbamylated albumin, highly glycosylated albumin) which can occur in disease states (e.g., diabetes, inflammation, chronic kidney disease) and determine whether these forms of albumin are more injurious to tubular epithelial cells.

The focus of the last section of my dissertation was evaluation of the effect of microgravity on tubular response to serum and vitamin D. In Chapter 4, I described the experiment to send the PT-MPS to the International Space Station U.S. National Laboratory. Astronauts experience accelerated bone loss in microgravity despite preventative measures such as regimented exercise and dietary supplementation of vitamin D_3.[144, 287] As the kidney is the primary site for the bioactivation of $25(OH)D_3$ to $1\alpha,25(OH)_2D_3$ and because plasma levels of $1\alpha,25(OH)_2D_3$ decrease in microgravity [287], impaired renal vitamin D metabolism may contribute to bone loss in astronauts. We investigated whether microgravity affected vitamin D metabolism by treating the PT-MPS with $25(OH)D_3$ and monitored metabolite formation in device effluents by LC/MS/MS and global transcriptomics with RNAseq. In addition, since megalin and cubilin are responsible for $25(OH)D_3$ uptake into PTECs and modulate proteinuria-induced tubular injury in animal models, we challenged the PT-MPS with serum exposure. If megalin/cubilin localization or activity was impaired by microgravity, we hypothesized the response of PTECs to serum exposure would be blunted. We showed that microgravity did not impact the activity or expression of the key enzymes (e.g., CYP27B1, CYP24A1, and CYP3A5) involved in PTEC metabolism of $25(OH)D_3$. Similarly, microgravity did not alter the response of PTECs to serum suggesting that megalin/cubilin activity was not affected. The metabolism of vitamin D by PTECs in microgravity in this study may not have been affected because the devices were only in microgravity for a total of eight days and this may not be a long enough period of exposure to ionizing radiation to cause a cellular stress response. Also, other factors such as parathyroid hormone or hypercalciuria that change in astronauts were not included in our study but may significantly affect the activity or expression of vitamin D metabolizing machinery in PTECs.[144, 287, 304] Future studies could strive for a longer maintenance period of devices in microgravity before treatment and include co-incubation of $25(OH)D_3$ with other treatments such as parathyroid hormone or calcium.

The response of PTECs to serum in Chapter 4 was remarkably similar to what was observed in Chapter 3. The pro-inflammatory effects of serum were marked along with strong downregulation of mitochondrial and fatty acid metabolism genes. Loss of fatty acid metabolism and oxidative phosphorylation in PTECs *in vivo* is associated with dedifferentiation and renal fibrosis.[313] A portion of dedifferentiated PTECs display a pro-inflammatory gene signature.[337] Therefore, a key driver of renal inflammation and fibrosis in chronic renal diseases may be an increase in the percentage of dedifferentiated PTECs. While PTECs are capable of producing numerous pro-inflammatory and pro-fibrotic molecules (e.g., IL-6, IL-8, CXCL5, PDGFB, FN1, LOXL2), the relative importance of each of those particular molecules in promoting renal fibrosis may vary by disease state and from patient-to-patient. Therefore, rather than targeting those specific pro-inflammatory or pro-fibrotic molecules, a more effective strategy may be to promote PTEC differentiation. With the availability of an increasing number of single-cell RNAseq datasets, the transcription factors controlling PTEC differentiation status may be uncovered and represent novel therapeutic targets (e.g., agonism of PPARA). As transcription factors tend to be expressed in numerous cell types, selective targeting transcription factors in proximal tubule cells may be achieved simply by using antisense oligonucleotides. Future studies could evaluate the ability of antisense oligonucleotides to modulate transcription factor activity and the resultant effect on PTEC differentiation.

In summary, the data described in this dissertation provide proof of concept that organs-on-chips have utility in drug safety and disease modeling contexts. In particular, the PT-MPS could prove useful to identification of novel biomarkers of drug induced nephrotoxicity given its better sensitivity and functionality than conventional monolayer cultures. In addition, the PT-MPS exhibited a reproducible and robust inflammatory response to serum exposure in the proteinuria model. Future efforts could focus on incorporating additional factors to better emulate the renal microenviroment. For example, embedding fibroblasts or CD4$^+$ T-cells into the collagen I matrix would enable evaluation of the effect of serum-induced PTEC-derived factors on fibroblast activation or T-cell differentiation (i.e., into pro-inflammatory T_h17 vs anti-inflammatory T_{reg}). A multi-cellular PT-MPS could be used to identify human-relevant drug targets and better evaluate the efficacy of potential therapeutics.

6. References

1. Marx, U., et al., *Biology-inspired microphysiological system approaches to solve the prediction dilemma of substance testing.* ALTEX, 2016. **33**(3): p. 272-321.
2. Harrison, R.K., *Phase II and phase III failures: 2013-2015.* Nat Rev Drug Discov, 2016. **15**(12): p. 817-818.
3. Hartung, T., *Per aspirin ad astra.* Altern Lab Anim, 2009. **37 Suppl 2**: p. 45-7.
4. Hackam, D.G. and D.A. Redelmeier, *Translation of research evidence from animals to humans.* JAMA, 2006. **296**(14): p. 1731-2.
5. Seok, J., et al., *Genomic responses in mouse models poorly mimic human inflammatory diseases.* Proc Natl Acad Sci U S A, 2013. **110**(9): p. 3507-12.
6. Leenaars, C.H.C., et al., *Animal to human translation: a systematic scoping review of reported concordance rates.* J Transl Med, 2019. **17**(1): p. 223.
7. Perel, P., et al., *Comparison of treatment effects between animal experiments and clinical trials: systematic review.* BMJ, 2007. **334**(7586): p. 197.
8. Mak, I.W., N. Evaniew, and M. Ghert, *Lost in translation: animal models and clinical trials in cancer treatment.* Am J Transl Res, 2014. **6**(2): p. 114-8.
9. Clark, M. and T. Steger-Hartmann, *A big data approach to the concordance of the toxicity of pharmaceuticals in animals and humans.* Regul Toxicol Pharmacol, 2018. **96**: p. 94-105.
10. Martic-Kehl, M.I., R. Schibli, and P.A. Schubiger, *Can animal data predict human outcome? Problems and pitfalls of translational animal research.* Eur J Nucl Med Mol Imaging, 2012. **39**(9): p. 1492-6.
11. Baillie, T.A. and A.E. Rettie, *Role of biotransformation in drug-induced toxicity: influence of intra- and inter-species differences in drug metabolism.* Drug Metab Pharmacokinet, 2011. **26**(1): p. 15-29.
12. Sena, E.S., et al., *Publication bias in reports of animal stroke studies leads to major overstatement of efficacy.* PLoS Biol, 2010. **8**(3): p. e1000344.
13. Haley, P.J., *Species differences in the structure and function of the immune system.* Toxicology, 2003. **188**(1): p. 49-71.
14. Suntharalingam, G., et al., *Cytokine storm in a phase 1 trial of the anti-CD28 monoclonal antibody TGN1412.* N Engl J Med, 2006. **355**(10): p. 1018-28.
15. Smith-Garvin, J.E., G.A. Koretzky, and M.S. Jordan, *T cell activation.* Annu Rev Immunol, 2009. **27**: p. 591-619.
16. Schwartz, R.H., *T cell anergy.* Annu Rev Immunol, 2003. **21**: p. 305-34.
17. Riley, J.L., et al., *Modulation of TCR-induced transcriptional profiles by ligation of CD28, ICOS, and CTLA-4 receptors.* Proc Natl Acad Sci U S A, 2002. **99**(18): p. 11790-5.
18. Marinari, B., et al., *CD28 delivers a unique signal leading to the selective recruitment of RelA and p52 NF-kappaB subunits on IL-8 and Bcl-xL gene promoters.* Proc Natl Acad Sci U S A, 2004. **101**(16): p. 6098-103.
19. Tacke, M., et al., *CD28-mediated induction of proliferation in resting T cells in vitro and in vivo without engagement of the T cell receptor: evidence for functionally distinct forms of CD28.* Eur J Immunol, 1997. **27**(1): p. 239-47.
20. Luhder, F., et al., *Topological requirements and signaling properties of T cell-activating, anti-CD28 antibody superagonists.* J Exp Med, 2003. **197**(8): p. 955-66.
21. Margulies, D.H., *CD28, costimulator or agonist receptor?* J Exp Med, 2003. **197**(8): p. 949-53.

22. Stebbings, R., et al., *"Cytokine storm" in the phase I trial of monoclonal antibody TGN1412: better understanding the causes to improve preclinical testing of immunotherapeutics.* J Immunol, 2007. **179**(5): p. 3325-31.
23. Romer, P.S., et al., *Preculture of PBMCs at high cell density increases sensitivity of T-cell responses, revealing cytokine release by CD28 superagonist TGN1412.* Blood, 2011. **118**(26): p. 6772-82.
24. Lin, C.H. and T. Hunig, *Efficient expansion of regulatory T cells in vitro and in vivo with a CD28 superagonist.* Eur J Immunol, 2003. **33**(3): p. 626-38.
25. Beyersdorf, N., et al., *Selective targeting of regulatory T cells with CD28 superagonists allows effective therapy of experimental autoimmune encephalomyelitis.* J Exp Med, 2005. **202**(3): p. 445-55.
26. Beyersdorf, N., et al., *CD28 superagonists put a break on autoimmunity by preferentially activating CD4+CD25+ regulatory T cells.* Autoimmun Rev, 2006. **5**(1): p. 40-5.
27. Gogishvili, T., et al., *Rapid regulatory T-cell response prevents cytokine storm in CD28 superagonist treated mice.* PLoS One, 2009. **4**(2): p. e4643.
28. Saule, P., et al., *Accumulation of memory T cells from childhood to old age: central and effector memory cells in CD4(+) versus effector memory and terminally differentiated memory cells in CD8(+) compartment.* Mech Ageing Dev, 2006. **127**(3): p. 274-81.
29. Weissmuller, S., et al., *TGN1412 Induces Lymphopenia and Human Cytokine Release in a Humanized Mouse Model.* PLoS One, 2016. **11**(3): p. e0149093.
30. Hanke, T., *Lessons from TGN1412.* Lancet, 2006. **368**(9547): p. 1569-70; author reply 1570.
31. Eastwood, D., et al., *Monoclonal antibody TGN1412 trial failure explained by species differences in CD28 expression on CD4+ effector memory T-cells.* Br J Pharmacol, 2010. **161**(3): p. 512-26.
32. Waibler, Z., et al., *Toward experimental assessment of receptor occupancy: TGN1412 revisited.* J Allergy Clin Immunol, 2008. **122**(5): p. 890-2.
33. Tabares, P., et al., *Human regulatory T cells are selectively activated by low-dose application of the CD28 superagonist TGN1412/TAB08.* Eur J Immunol, 2014. **44**(4): p. 1225-36.
34. Diamond, S., et al., *Species-specific metabolism of SGX523 by aldehyde oxidase and the toxicological implications.* Drug Metab Dispos, 2010. **38**(8): p. 1277-85.
35. Infante, J.R., et al., *Unexpected renal toxicity associated with SGX523, a small molecule inhibitor of MET.* Invest New Drugs, 2013. **31**(2): p. 363-9.
36. Lolkema, M.P., et al., *The c-Met Tyrosine Kinase Inhibitor JNJ-38877605 Causes Renal Toxicity through Species-Specific Insoluble Metabolite Formation.* Clin Cancer Res, 2015. **21**(10): p. 2297-2304.
37. Mutlib, A.E., et al., *The species-dependent metabolism of efavirenz produces a nephrotoxic glutathione conjugate in rats.* Toxicol Appl Pharmacol, 2000. **169**(1): p. 102-13.
38. Monticello, T.M., et al., *Current nonclinical testing paradigm enables safe entry to First-In-Human clinical trials: The IQ consortium nonclinical to clinical translational database.* Toxicol Appl Pharmacol, 2017. **334**: p. 100-109.
39. Sutherland, M.L., K.M. Fabre, and D.A. Tagle, *The National Institutes of Health Microphysiological Systems Program focuses on a critical challenge in the drug discovery pipeline.* Stem Cell Res Ther, 2013. **4 Suppl 1**: p. I1.
40. Low, L.A., et al., *Organs-on-chips: into the next decade.* Nat Rev Drug Discov, 2020.
41. Hamm, L.L., N. Nakhoul, and K.S. Hering-Smith, *Acid-Base Homeostasis.* Clin J Am Soc Nephrol, 2015. **10**(12): p. 2232-42.
42. Zhuo, J.L. and X.C. Li, *Proximal nephron.* Compr Physiol, 2013. **3**(3): p. 1079-123.
43. Pollak, M.R., et al., *The glomerulus: the sphere of influence.* Clin J Am Soc Nephrol, 2014. **9**(8): p. 1461-9.

44. Chen, L., et al., *Renal-Tubule Epithelial Cell Nomenclature for Single-Cell RNA-Sequencing Studies.* J Am Soc Nephrol, 2019. **30**(8): p. 1358-1364.
45. Curthoys, N.P. and O.W. Moe, *Proximal tubule function and response to acidosis.* Clin J Am Soc Nephrol, 2014. **9**(9): p. 1627-38.
46. Meyer, C., J.M. Dostou, and J.E. Gerich, *Role of the human kidney in glucose counterregulation.* Diabetes, 1999. **48**(5): p. 943-8.
47. Dusso, A.S., A.J. Brown, and E. Slatopolsky, *Vitamin D.* Am J Physiol Renal Physiol, 2005. **289**(1): p. F8-28.
48. Zheng, S., et al., *CYP3A5 gene variation influences cyclosporine A metabolite formation and renal cyclosporine disposition.* Transplantation, 2013. **95**(6): p. 821-7.
49. Morrissey, K.M., et al., *Renal transporters in drug development.* Annu Rev Pharmacol Toxicol, 2013. **53**: p. 503-29.
50. Nigam, S.K., et al., *Handling of Drugs, Metabolites, and Uremic Toxins by Kidney Proximal Tubule Drug Transporters.* Clin J Am Soc Nephrol, 2015. **10**(11): p. 2039-49.
51. Kohler, J.J., et al., *Tenofovir renal proximal tubular toxicity is regulated by OAT1 and MRP4 transporters.* Lab Invest, 2011. **91**(6): p. 852-8.
52. Wagner, D.J., T. Hu, and J. Wang, *Polyspecific organic cation transporters and their impact on drug intracellular levels and pharmacodynamics.* Pharmacol Res, 2016. **111**: p. 237-246.
53. Filipski, K.K., et al., *Contribution of organic cation transporter 2 (OCT2) to cisplatin-induced nephrotoxicity.* Clin Pharmacol Ther, 2009. **86**(4): p. 396-402.
54. Gibaldi, M. and M.A. Schwartz, *Apparent effect of probenecid on the distribution of penicillins in man.* Clin Pharmacol Ther, 1968. **9**(3): p. 345-9.
55. Thyss, A., et al., *Clinical and pharmacokinetic evidence of a life-threatening interaction between methotrexate and ketoprofen.* Lancet, 1986. **1**(8475): p. 256-8.
56. Tracy, T.S., et al., *The effects of a salicylate, ibuprofen, and naproxen on the disposition of methotrexate in patients with rheumatoid arthritis.* Eur J Clin Pharmacol, 1992. **42**(2): p. 121-5.
57. Nakamura, T., et al., *Disruption of multidrug and toxin extrusion MATE1 potentiates cisplatin-induced nephrotoxicity.* Biochem Pharmacol, 2010. **80**(11): p. 1762-7.
58. Sandri, A.M., et al., *Population pharmacokinetics of intravenous polymyxin B in critically ill patients: implications for selection of dosage regimens.* Clin Infect Dis, 2013. **57**(4): p. 524-31.
59. Cunningham, R.F., Z.H. Israili, and P.G. Dayton, *Clinical pharmacokinetics of probenecid.* Clin Pharmacokinet, 1981. **6**(2): p. 135-51.
60. Motohashi, H. and K. Inui, *Organic cation transporter OCTs (SLC22) and MATEs (SLC47) in the human kidney.* AAPS J, 2013. **15**(2): p. 581-8.
61. Jonker, J.W., et al., *Deficiency in the organic cation transporters 1 and 2 (Oct1/Oct2 [Slc22a1/Slc22a2]) in mice abolishes renal secretion of organic cations.* Mol Cell Biol, 2003. **23**(21): p. 7902-8.
62. Tahara, H., et al., *A species difference in the transport activities of H2 receptor antagonists by rat and human renal organic anion and cation transporters.* J Pharmacol Exp Ther, 2005. **315**(1): p. 337-45.
63. Paine, S.W., et al., *Prediction of human renal clearance from preclinical species for a diverse set of drugs that exhibit both active secretion and net reabsorption.* Drug Metab Dispos, 2011. **39**(6): p. 1008-13.
64. Johnson, B.M., et al., *Characterization of transport protein expression in multidrug resistance-associated protein (Mrp) 2-deficient rats.* Drug Metab Dispos, 2006. **34**(4): p. 556-62.
65. Khundmiri, S.J., et al., *Transcriptomes of Major Proximal Tubule Cell Culture Models.* J Am Soc Nephrol, 2021. **32**(1): p. 86-97.

66. Brown, C.D., et al., *Characterisation of human tubular cell monolayers as a model of proximal tubular xenobiotic handling.* Toxicol Appl Pharmacol, 2008. **233**(3): p. 428-38.
67. Gozalpour, E. and K.S. Fenner, *Current State of In vitro Cell-Based Renal Models.* Curr Drug Metab, 2018. **19**(4): p. 310-326.
68. Orosz, D.E., et al., *Growth, immortalization, and differentiation potential of normal adult human proximal tubule cells.* In Vitro Cell Dev Biol Anim, 2004. **40**(1-2): p. 22-34.
69. Brezis, M., et al., *Renal ischemia: a new perspective.* Kidney Int, 1984. **26**(4): p. 375-83.
70. Palm, F. and L. Nordquist, *Renal tubulointerstitial hypoxia: cause and consequence of kidney dysfunction.* Clin Exp Pharmacol Physiol, 2011. **38**(7): p. 474-80.
71. Gai, Z., et al., *The Role of Mitochondria in Drug-Induced Kidney Injury.* Front Physiol, 2020. **11**: p. 1079.
72. Christensen, E.I. and H. Birn, *Megalin and cubilin: multifunctional endocytic receptors.* Nat Rev Mol Cell Biol, 2002. **3**(4): p. 256-66.
73. Yu, H., et al., *Alpha-1-microglobulin: an indicator protein for renal tubular function.* J Clin Pathol, 1983. **36**(3): p. 253-9.
74. Zeng, X., et al., *Urinary beta2-Microglobulin Is a Good Indicator of Proximal Tubule Injury: A Correlative Study with Renal Biopsies.* J Biomark, 2014. **2014**: p. 492838.
75. Kapalczynska, M., et al., *2D and 3D cell cultures - a comparison of different types of cancer cell cultures.* Arch Med Sci, 2018. **14**(4): p. 910-919.
76. Kusaba, T., et al., *Differentiated kidney epithelial cells repair injured proximal tubule.* Proc Natl Acad Sci U S A, 2014. **111**(4): p. 1527-32.
77. Chang-Panesso, M. and B.D. Humphreys, *Cellular plasticity in kidney injury and repair.* Nat Rev Nephrol, 2017. **13**(1): p. 39-46.
78. Chen, Y., et al., *Mature hepatocytes exhibit unexpected plasticity by direct dedifferentiation into liver progenitor cells in culture.* Hepatology, 2012. **55**(2): p. 563-74.
79. Wang, W.E., et al., *Dedifferentiation, Proliferation, and Redifferentiation of Adult Mammalian Cardiomyocytes After Ischemic Injury.* Circulation, 2017. **136**(9): p. 834-848.
80. de Carvalho Ribeiro, P., et al., *Differentiating Induced Pluripotent Stem Cells into Renal Cells: A New Approach to Treat Kidney Diseases.* Stem Cells Int, 2020. **2020**: p. 8894590.
81. Lam, A.Q., B.S. Freedman, and J.V. Bonventre, *Directed differentiation of pluripotent stem cells to kidney cells.* Semin Nephrol, 2014. **34**(4): p. 445-61.
82. Trzpis, M., et al., *Expression of EpCAM is up-regulated during regeneration of renal epithelia.* J Pathol, 2008. **216**(2): p. 201-8.
83. He, Q., et al., *Single-cell RNA sequencing analysis of human kidney reveals the presence of ACE2 receptor: A potential pathway of COVID-19 infection.* Mol Genet Genomic Med, 2020. **8**(10): p. e1442.
84. Weber, E.J., et al., *Development of a microphysiological model of human kidney proximal tubule function.* Kidney Int, 2016. **90**(3): p. 627-37.
85. Chang, S.Y., et al., *Human liver-kidney model elucidates the mechanisms of aristolochic acid nephrotoxicity.* JCI Insight, 2017. **2**(22).
86. Weber, E.J., et al., *Human kidney on a chip assessment of polymyxin antibiotic nephrotoxicity.* JCI Insight, 2018. **3**(24).
87. Imaoka, T., et al., *Microphysiological system modeling of ochratoxin A-associated nephrotoxicity.* Toxicology, 2020. **444**: p. 152582.
88. Chapron, B.D., et al., *Reevaluating the role of megalin in renal vitamin D homeostasis using a human cell-derived microphysiological system.* ALTEX, 2018. **35**(4): p. 504-515.
89. Bennett, C.F., et al., *Pharmacology of Antisense Drugs.* Annu Rev Pharmacol Toxicol, 2017. **57**: p. 81-105.

90. Rinaldi, C. and M.J.A. Wood, *Antisense oligonucleotides: the next frontier for treatment of neurological disorders.* Nat Rev Neurol, 2018. **14**(1): p. 9-21.
91. Eckstein, F., *Phosphorothioates, essential components of therapeutic oligonucleotides.* Nucleic Acid Ther, 2014. **24**(6): p. 374-87.
92. Stein, D., et al., *A specificity comparison of four antisense types: morpholino, 2'-O-methyl RNA, DNA, and phosphorothioate DNA.* Antisense Nucleic Acid Drug Dev, 1997. **7**(3): p. 151-7.
93. Geary, R.S., *Antisense oligonucleotide pharmacokinetics and metabolism.* Expert Opin Drug Metab Toxicol, 2009. **5**(4): p. 381-91.
94. Amantana, A. and P.L. Iversen, *Pharmacokinetics and biodistribution of phosphorodiamidate morpholino antisense oligomers.* Curr Opin Pharmacol, 2005. **5**(5): p. 550-5.
95. Flierl, U., et al., *Phosphorothioate backbone modifications of nucleotide-based drugs are potent platelet activators.* J Exp Med, 2015. **212**(2): p. 129-37.
96. Henry, S.P., et al., *Mechanism of alternative complement pathway dysregulation by a phosphorothioate oligonucleotide in monkey and human serum.* Nucleic Acid Ther, 2014. **24**(5): p. 326-35.
97. van Meer, L., et al., *Renal Effects of Antisense-Mediated Inhibition of SGLT2.* J Pharmacol Exp Ther, 2016. **359**(2): p. 280-289.
98. Swayze, E.E., et al., *Antisense oligonucleotides containing locked nucleic acid improve potency but cause significant hepatotoxicity in animals.* Nucleic Acids Res, 2007. **35**(2): p. 687-700.
99. Burel, S.A., et al., *Hepatotoxicity of high affinity gapmer antisense oligonucleotides is mediated by RNase H1 dependent promiscuous reduction of very long pre-mRNA transcripts.* Nucleic Acids Res, 2016. **44**(5): p. 2093-109.
100. Moisan, A., et al., *Inhibition of EGF Uptake by Nephrotoxic Antisense Drugs In Vitro and Implications for Preclinical Safety Profiling.* Mol Ther Nucleic Acids, 2017. **6**: p. 89-105.
101. van Poelgeest, E.P., et al., *Acute kidney injury during therapy with an antisense oligonucleotide directed against PCSK9.* Am J Kidney Dis, 2013. **62**(4): p. 796-800.
102. Goemans, N.M., et al., *Systemic administration of PRO051 in Duchenne's muscular dystrophy.* N Engl J Med, 2011. **364**(16): p. 1513-22.
103. Goemans, N., et al., *A randomized placebo-controlled phase 3 trial of an antisense oligonucleotide, drisapersen, in Duchenne muscular dystrophy.* Neuromuscul Disord, 2018. **28**(1): p. 4-15.
104. Han, W.K., et al., *Kidney Injury Molecule-1 (KIM-1): a novel biomarker for human renal proximal tubule injury.* Kidney Int, 2002. **62**(1): p. 237-44.
105. Bailly, V., et al., *Shedding of kidney injury molecule-1, a putative adhesion protein involved in renal regeneration.* J Biol Chem, 2002. **277**(42): p. 39739-48.
106. Carver, M.P., et al., *Toxicological Characterization of Exon Skipping Phosphorodiamidate Morpholino Oligomers (PMOs) in Non-human Primates.* J Neuromuscul Dis, 2016. **3**(3): p. 381-393.
107. Aartsma-Rus, A. and A.M. Krieg, *FDA Approves Eteplirsen for Duchenne Muscular Dystrophy: The Next Chapter in the Eteplirsen Saga.* Nucleic Acid Ther, 2017. **27**(1): p. 1-3.
108. Mujais, S.K., et al., *Health-related quality of life in CKD Patients: correlates and evolution over time.* Clin J Am Soc Nephrol, 2009. **4**(8): p. 1293-301.
109. Tonelli, M., et al., *Chronic kidney disease and mortality risk: a systematic review.* J Am Soc Nephrol, 2006. **17**(7): p. 2034-47.
110. System, U.S.R.D., *2019 USRDS annual data report: epidemiology of kidney disease in the United States.* 2019.
111. Chawla, L.S. and P.L. Kimmel, *Acute kidney injury and chronic kidney disease: an integrated clinical syndrome.* Kidney Int, 2012. **82**(5): p. 516-24.

112. Abbate, M., C. Zoja, and G. Remuzzi, *How does proteinuria cause progressive renal damage?* J Am Soc Nephrol, 2006. **17**(11): p. 2974-84.
113. Inker, L.A., et al., *Early change in proteinuria as a surrogate end point for kidney disease progression: an individual patient meta-analysis.* Am J Kidney Dis, 2014. **64**(1): p. 74-85.
114. Thompson, A., et al., *Proteinuria Reduction as a Surrogate End Point in Trials of IgA Nephropathy.* Clin J Am Soc Nephrol, 2019. **14**(3): p. 469-481.
115. Troost, J.P., et al., *Proteinuria Reduction and Kidney Survival in Focal Segmental Glomerulosclerosis.* Am J Kidney Dis, 2020.
116. Thomas, M.E., et al., *Proteinuria induces tubular cell turnover: A potential mechanism for tubular atrophy.* Kidney Int, 1999. **55**(3): p. 890-8.
117. Hill, G.S., et al., *Proteinuria and tubulointerstitial lesions in lupus nephritis.* Kidney Int, 2001. **60**(5): p. 1893-903.
118. Benigni, A., et al., *Angiotensin-converting enzyme inhibition prevents glomerular-tubule disconnection and atrophy in passive Heymann nephritis, an effect not observed with a calcium antagonist.* Am J Pathol, 2001. **159**(5): p. 1743-50.
119. Wang, Y., et al., *Induction of monocyte chemoattractant protein-1 by albumin is mediated by nuclear factor kappaB in proximal tubule cells.* J Am Soc Nephrol, 1999. **10**(6): p. 1204-13.
120. Baines, R.J. and N.J. Brunskill, *Tubular toxicity of proteinuria.* Nat Rev Nephrol, 2011. **7**(3): p. 177-80.
121. Yard, B.A., et al., *Regulation of endothelin-1 and transforming growth factor-beta1 production in cultured proximal tubular cells by albumin and heparan sulphate glycosaminoglycans.* Nephrol Dial Transplant, 2001. **16**(9): p. 1769-75.
122. Tang, S., et al., *Albumin stimulates interleukin-8 expression in proximal tubular epithelial cells in vitro and in vivo.* J Clin Invest, 2003. **111**(4): p. 515-27.
123. Yung, S., et al., *Effect of human anti-DNA antibodies on proximal renal tubular epithelial cell cytokine expression: implications on tubulointerstitial inflammation in lupus nephritis.* J Am Soc Nephrol, 2005. **16**(11): p. 3281-94.
124. Mezzano, S.A., et al., *Tubular NF-kappaB and AP-1 activation in human proteinuric renal disease.* Kidney Int, 2001. **60**(4): p. 1366-77.
125. Motoyoshi, Y., et al., *Megalin contributes to the early injury of proximal tubule cells during nonselective proteinuria.* Kidney Int, 2008. **74**(10): p. 1262-9.
126. Liu, D., et al., *Megalin/Cubulin-Lysosome-mediated Albumin Reabsorption Is Involved in the Tubular Cell Activation of NLRP3 Inflammasome and Tubulointerstitial Inflammation.* J Biol Chem, 2015. **290**(29): p. 18018-28.
127. Humphreys, B.D., et al., *Repair of injured proximal tubule does not involve specialized progenitors.* Proc Natl Acad Sci U S A, 2011. **108**(22): p. 9226-31.
128. Chang-Panesso, M., et al., *FOXM1 drives proximal tubule proliferation during repair from acute ischemic kidney injury.* J Clin Invest, 2019. **129**(12): p. 5501-5517.
129. Kang, H.M., et al., *Defective fatty acid oxidation in renal tubular epithelial cells has a key role in kidney fibrosis development.* Nat Med, 2015. **21**(1): p. 37-46.
130. Yang, L., et al., *Epithelial cell cycle arrest in G2/M mediates kidney fibrosis after injury.* Nat Med, 2010. **16**(5): p. 535-43, 1p following 143.
131. Wu, H., et al., *Proximal Tubule Translational Profiling during Kidney Fibrosis Reveals Proinflammatory and Long Noncoding RNA Expression Patterns with Sexual Dimorphism.* J Am Soc Nephrol, 2020. **31**(1): p. 23-38.
132. Grgic, I., et al., *Targeted proximal tubule injury triggers interstitial fibrosis and glomerulosclerosis.* Kidney Int, 2012. **82**(2): p. 172-83.
133. Lobrich, M. and P.A. Jeggo, *Hazards of human spaceflight.* Science, 2019. **364**(6436): p. 127-128.

134. Law, J., et al., *Relationship between carbon dioxide levels and reported headaches on the international space station.* J Occup Environ Med, 2014. **56**(5): p. 477-83.
135. Purvis, J., *The Final Frontier.* Ulster Med J, 2020. **89**(1): p. 1-2.
136. Pavlakou, P., et al., *Oxidative Stress and the Kidney in the Space Environment.* Int J Mol Sci, 2018. **19**(10).
137. di Prampero, P.E. and M.V. Narici, *Muscles in microgravity: from fibres to human motion.* J Biomech, 2003. **36**(3): p. 403-12.
138. Smith, S.M., et al., *The nutritional status of astronauts is altered after long-term space flight aboard the International Space Station.* J Nutr, 2005. **135**(3): p. 437-43.
139. Nelson, E.S., L. Mulugeta, and J.G. Myers, *Microgravity-induced fluid shift and ophthalmic changes.* Life (Basel), 2014. **4**(4): p. 621-65.
140. Nagaraja, M.P. and D. Risin, *The current state of bone loss research: data from spaceflight and microgravity simulators.* J Cell Biochem, 2013. **114**(5): p. 1001-8.
141. Biolo, G., et al., *Microgravity as a model of ageing.* Curr Opin Clin Nutr Metab Care, 2003. **6**(1): p. 31-40.
142. Luxton, J.J., et al., *Telomere Length Dynamics and DNA Damage Responses Associated with Long-Duration Spaceflight.* Cell Rep, 2020. **33**(10): p. 108457.
143. Low, L.A. and M.A. Giulianotti, *Tissue Chips in Space: Modeling Human Diseases in Microgravity.* Pharm Res, 2019. **37**(1): p. 8.
144. Zittermann, A., et al., *Microgravity inhibits intestinal calcium absorption as shown by a stable strontium test.* Eur J Clin Invest, 2000. **30**(12): p. 1036-43.
145. Kaseda, R., et al., *Role of megalin and cubilin in the metabolism of vitamin D(3).* Ther Apher Dial, 2011. **15 Suppl 1**: p. 14-7.
146. Conney, A.H., *Pharmacological implications of microsomal enzyme induction.* Pharmacol Rev, 1967. **19**(3): p. 317-66.
147. Aoyama, T., et al., *Cytochrome P-450 hPCN3, a novel cytochrome P-450 IIIA gene product that is differentially expressed in adult human liver. cDNA and deduced amino acid sequence and distinct specificities of cDNA-expressed hPCN1 and hPCN3 for the metabolism of steroid hormones and cyclosporine.* J Biol Chem, 1989. **264**(18): p. 10388-95.
148. Koch, I., et al., *Interindividual variability and tissue-specificity in the expression of cytochrome P450 3A mRNA.* Drug Metab Dispos, 2002. **30**(10): p. 1108-14.
149. Bolbrinker, J., et al., *CYP3A5 genotype-phenotype analysis in the human kidney reveals a strong site-specific expression of CYP3A5 in the proximal tubule in carriers of the CYP3A5*1 allele.* Drug Metab Dispos, 2012. **40**(4): p. 639-41.
150. Lamba, J.K., et al., *Genetic contribution to variable human CYP3A-mediated metabolism.* Adv Drug Deliv Rev, 2002. **54**(10): p. 1271-94.
151. Kuehl, P., et al., *Sequence diversity in CYP3A promoters and characterization of the genetic basis of polymorphic CYP3A5 expression.* Nat Genet, 2001. **27**(4): p. 383-91.
152. Watlington, C.O., et al., *Corticosterone 6 beta-hydroxylation correlates with blood pressure in spontaneously hypertensive rats.* Am J Physiol, 1992. **262**(6 Pt 2): p. F927-31.
153. Ghosh, S.S., et al., *Renal and hepatic family 3A cytochromes P450 (CYP3A) in spontaneously hypertensive rats.* Biochem Pharmacol, 1995. **50**(1): p. 49-54.
154. Zhang, Y.P., et al., *CYP3A5 polymorphism, amlodipine and hypertension.* J Hum Hypertens, 2014. **28**(3): p. 145-9.
155. Lustig, S., et al., *Effect of cyclosporin on blood pressure and renin-aldosterone axis in rats.* Am J Physiol, 1987. **253**(6 Pt 2): p. H1596-600.
156. Basu, A.K., et al., *Augmented arterial pressure responses to cyclosporine in spontaneously hypertensive rats. Role of cytochrome P-450 3A.* Hypertension, 1994. **24**(4): p. 480-5.

157. Sacerdoti, D., et al., *Treatment with tin prevents the development of hypertension in spontaneously hypertensive rats.* Science, 1989. **243**(4889): p. 388-90.
158. Ho, H., et al., *Association between the CYP3A5 genotype and blood pressure.* Hypertension, 2005. **45**(2): p. 294-8.
159. Bochud, M., et al., *Association of CYP3A5 genotypes with blood pressure and renal function in African families.* J Hypertens, 2006. **24**(5): p. 923-9.
160. Givens, R.C., et al., *CYP3A5 genotype predicts renal CYP3A activity and blood pressure in healthy adults.* J Appl Physiol (1985), 2003. **95**(3): p. 1297-300.
161. Fromm, M.F., et al., *CYP3A5 genotype is associated with elevated blood pressure.* Pharmacogenet Genomics, 2005. **15**(10): p. 737-41.
162. Xi, B., et al., *Association of the CYP3A5 polymorphism (6986G>A) with blood pressure and hypertension.* Hypertens Res, 2011. **34**(11): p. 1216-20.
163. Fisher, D.L., et al., *CYP3A5 as a candidate gene for hypertension: no support from an unselected indigenous West African population.* J Hum Hypertens, 2016. **30**(12): p. 778-782.
164. Lin, Y.S., et al., *Co-regulation of CYP3A4 and CYP3A5 and contribution to hepatic and intestinal midazolam metabolism.* Mol Pharmacol, 2002. **62**(1): p. 162-72.
165. Merkin, J., et al., *Evolutionary dynamics of gene and isoform regulation in Mammalian tissues.* Science, 2012. **338**(6114): p. 1593-9.
166. Lee, Y. and D.C. Rio, *Mechanisms and Regulation of Alternative Pre-mRNA Splicing.* Annu Rev Biochem, 2015. **84**: p. 291-323.
167. Annalora, A.J., C.B. Marcus, and P.L. Iversen, *Alternative Splicing in the Cytochrome P450 Superfamily Expands Protein Diversity to Augment Gene Function and Redirect Human Drug Metabolism.* Drug Metab Dispos, 2017. **45**(4): p. 375-389.
168. Xiao, X., et al., *Splice site strength-dependent activity and genetic buffering by poly-G runs.* Nat Struct Mol Biol, 2009. **16**(10): p. 1094-100.
169. Ribeiro, M.M., et al., *G-quadruplex formation enhances splicing efficiency of PAX9 intron 1.* Hum Genet, 2015. **134**(1): p. 37-44.
170. Marcel, V., et al., *G-quadruplex structures in TP53 intron 3: role in alternative splicing and in production of p53 mRNA isoforms.* Carcinogenesis, 2011. **32**(3): p. 271-8.
171. Sirand-Pugnet, P., et al., *An intronic (A/U)GGG repeat enhances the splicing of an alternative intron of the chicken beta-tropomyosin pre-mRNA.* Nucleic Acids Res, 1995. **23**(17): p. 3501-7.
172. Munroe, S.H., et al., *Evolution of the Antisense Overlap between Genes for Thyroid Hormone Receptor and Rev-erbalpha and Characterization of an Exonic G-Rich Element That Regulates Splicing of TRalpha2 mRNA.* PLoS One, 2015. **10**(9): p. e0137893.
173. Kralovicova, J., et al., *Optimal antisense target reducing INS intron 1 retention is adjacent to a parallel G quadruplex.* Nucleic Acids Res, 2014. **42**(12): p. 8161-73.
174. Didiot, M.C., et al., *The G-quartet containing FMRP binding site in FMR1 mRNA is a potent exonic splicing enhancer.* Nucleic Acids Res, 2008. **36**(15): p. 4902-12.
175. Fisette, J.F., et al., *A G-rich element forms a G-quadruplex and regulates BACE1 mRNA alternative splicing.* J Neurochem, 2012. **121**(5): p. 763-73.
176. Keniry, M.A., *Quadruplex structures in nucleic acids.* Biopolymers, 2000. **56**(3): p. 123-46.
177. Lodish, H.F., *Molecular cell biology*. Eighth edition. ed. 2016, New York: W.H. Freeman-Macmillan Learning. xl, 1170 pages.
178. Williamson, J.R., M.K. Raghuraman, and T.R. Cech, *Monovalent cation-induced structure of telomeric DNA: the G-quartet model.* Cell, 1989. **59**(5): p. 871-80.
179. Neidle, S., *The structures of quadruplex nucleic acids and their drug complexes.* Curr Opin Struct Biol, 2009. **19**(3): p. 239-50.

180. Kosuge, K., et al., *Discovery of osmosensitive transcriptional regulation of human cytochrome P450 3As by the tonicity-responsive enhancer binding protein (nuclear factor of activated T cells 5).* Mol Pharmacol, 2007. **72**(4): p. 826-37.
181. Thummel, K.E. and G.R. Wilkinson, *In vitro and in vivo drug interactions involving human CYP3A.* Annu Rev Pharmacol Toxicol, 1998. **38**: p. 389-430.
182. Yu, J., et al., *Risk of Clinically Relevant Pharmacokinetic-Based Drug-Drug Interactions with Drugs Approved by the U.S. Food and Drug Administration Between 2013 and 2016.* Drug Metab Dispos, 2018. **46**(6): p. 835-845.
183. Havens, M.A. and M.L. Hastings, *Splice-switching antisense oligonucleotides as therapeutic drugs.* Nucleic Acids Res, 2016. **44**(14): p. 6549-63.
184. Henry, S.P., et al., *Renal uptake and tolerability of a 2'-O-methoxyethyl modified antisense oligonucleotide (ISIS 113715) in monkey.* Toxicology, 2012. **301**(1-3): p. 13-20.
185. Sazani, P., et al., *Repeat-dose toxicology evaluation in cynomolgus monkeys of AVI-4658, a phosphorodiamidate morpholino oligomer (PMO) drug for the treatment of duchenne muscular dystrophy.* Int J Toxicol, 2011. **30**(3): p. 313-21.
186. Komaki, H., et al., *Systemic administration of the antisense oligonucleotide NS-065/NCNP-01 for skipping of exon 53 in patients with Duchenne muscular dystrophy.* Sci Transl Med, 2018. **10**(437).
187. *Spinraza (nusinersen) [package insert]*, I. Pharmaceuticals, Editor. 2016: Carlsbad, CA.
188. Mendell, J.R., et al., *Longitudinal effect of eteplirsen versus historical control on ambulation in Duchenne muscular dystrophy.* Ann Neurol, 2016. **79**(2): p. 257-71.
189. Vyondys 53 (golodirsen) [package insert]. Cambridge, M.S.T.
190. Janssen, M.J., et al., *Therapy with 2'-O-Me Phosphorothioate Antisense Oligonucleotides Causes Reversible Proteinuria by Inhibiting Renal Protein Reabsorption.* Mol Ther Nucleic Acids, 2019. **18**: p. 298-307.
191. Iversen, P.L., *Structure activity study of clinically observed adverse events and oligomer chemistry.* J Drug Discov Develop and Deliv, 2016. **3**: p. 1022.
192. Crooke, S.T., et al., *The Effects of 2'-O-Methoxyethyl Oligonucleotides on Renal Function in Humans.* Nucleic Acid Ther, 2018. **28**(1): p. 10-22.
193. Hagedorn, P.H., et al., *Managing the sequence-specificity of antisense oligonucleotides in drug discovery.* Nucleic Acids Res, 2017. **45**(5): p. 2262-2282.
194. Scharner, J., et al., *Hybridization-mediated off-target effects of splice-switching antisense oligonucleotides.* Nucleic Acids Res, 2020. **48**(2): p. 802-816.
195. van Meer, L., et al., *Novel SGLT2 inhibitor: first-in-man studies of antisense compound is associated with unexpected renal effects.* Pharmacol Res Perspect, 2017. **5**(1): p. e00292.
196. Herrington, W.G., et al., *Association of long-term administration of the survivin mRNA-targeted antisense oligonucleotide LY2181308 with reversible kidney injury in a patient with metastatic melanoma.* Am J Kidney Dis, 2011. **57**(2): p. 300-3.
197. Chapron, A., et al., *An Improved Vascularized, Dual-Channel Microphysiological System Facilitates Modeling of Proximal Tubular Solute Secretion.* ACS Pharmacology & Translational Science, 2020.
198. Adler, M., et al., *A Quantitative Approach to Screen for Nephrotoxic Compounds In Vitro.* J Am Soc Nephrol, 2016. **27**(4): p. 1015-28.
199. Homan, K.A., et al., *Bioprinting of 3D Convoluted Renal Proximal Tubules on Perfusable Chips.* Sci Rep, 2016. **6**: p. 34845.
200. Sakolish, C., et al., *Technology Transfer of the Microphysiological Systems: A Case Study of the Human Proximal Tubule Tissue Chip.* Sci Rep, 2018. **8**(1): p. 14882.

201. Lin, N.Y.C., et al., *Renal reabsorption in 3D vascularized proximal tubule models.* Proc Natl Acad Sci U S A, 2019. **116**(12): p. 5399-5404.

202. Jang, K.J., et al., *Human kidney proximal tubule-on-a-chip for drug transport and nephrotoxicity assessment.* Integr Biol (Camb), 2013. **5**(9): p. 1119-29.

203. Vaidya, V.S., et al., *Kidney injury molecule-1 outperforms traditional biomarkers of kidney injury in preclinical biomarker qualification studies.* Nat Biotechnol, 2010. **28**(5): p. 478-85.

204. Jenkins, R.H., et al., *miR-192 induces G2/M growth arrest in aristolochic acid nephropathy.* Am J Pathol, 2014. **184**(4): p. 996-1009.

205. Cardenas-Gonzalez, M., et al., *Identification, Confirmation, and Replication of Novel Urinary MicroRNA Biomarkers in Lupus Nephritis and Diabetic Nephropathy.* Clin Chem, 2017. **63**(9): p. 1515-1526.

206. Hudziak, R.M., et al., *Antiproliferative effects of steric blocking phosphorodiamidate morpholino antisense agents directed against c-myc.* Antisense Nucleic Acid Drug Dev, 2000. **10**(3): p. 163-76.

207. McClorey, G., et al., *Induced dystrophin exon skipping in human muscle explants.* Neuromuscul Disord, 2006. **16**(9-10): p. 583-90.

208. Fall, A.M., et al., *Induction of revertant fibres in the mdx mouse using antisense oligonucleotides.* Genet Vaccines Ther, 2006. **4**: p. 3.

209. Fletcher, S., et al., *Morpholino oligomer-mediated exon skipping averts the onset of dystrophic pathology in the mdx mouse.* Mol Ther, 2007. **15**(9): p. 1587-92.

210. Mitrpant, C., et al., *By-passing the nonsense mutation in the 4 CV mouse model of muscular dystrophy by induced exon skipping.* J Gene Med, 2009. **11**(1): p. 46-56.

211. Mourich, D.V., et al., *Alternative splice forms of CTLA-4 induced by antisense mediated splice-switching influences autoimmune diabetes susceptibility in NOD mice.* Nucleic Acid Ther, 2014. **24**(2): p. 114-26.

212. Panchal, R.G., et al., *Induced IL-10 splice altering approach to antiviral drug discovery.* Nucleic Acid Ther, 2014. **24**(3): p. 179-85.

213. Nambiar, M., et al., *G-quadruplex structures formed at the HOX11 breakpoint region contribute to its fragility during t(10;14) translocation in T-cell leukemia.* Mol Cell Biol, 2013. **33**(21): p. 4266-81.

214. Livak, K.J. and T.D. Schmittgen, *Analysis of relative gene expression data using real-time quantitative PCR and the 2(-Delta Delta C(T)) Method.* Methods, 2001. **25**(4): p. 402-8.

215. Kumarakulasingham, M., et al., *Cytochrome p450 profile of colorectal cancer: identification of markers of prognosis.* Clin Cancer Res, 2005. **11**(10): p. 3758-65.

216. Stepankova, M., et al., *Optical isomers of dihydropyridine calcium channel blockers display enantiospecific effects on the expression and enzyme activities of human xenobiotics-metabolizing cytochromes P450.* Toxicol Lett, 2016. **262**: p. 173-186.

217. Stresser, D.M., et al., *Substrate-dependent modulation of CYP3A4 catalytic activity: analysis of 27 test compounds with four fluorometric substrates.* Drug Metab Dispos, 2000. **28**(12): p. 1440-8.

218. Donato, M.T., et al., *Fluorescence-based assays for screening nine cytochrome P450 (P450) activities in intact cells expressing individual human P450 enzymes.* Drug Metab Dispos, 2004. **32**(7): p. 699-706.

219. Chapron, B., et al., *Reversible, time-dependent inhibition of CYP3A-mediated metabolism of midazolam and tacrolimus by telaprevir in human liver microsomes.* J Pharm Pharm Sci, 2015. **18**(1): p. 101-11.

220. Robinson, M.D. and A. Oshlack, *A scaling normalization method for differential expression analysis of RNA-seq data.* Genome Biol, 2010. **11**(3): p. R25.

221. Lun, A.T., Y. Chen, and G.K. Smyth, *It's DE-licious: A Recipe for Differential Expression Analyses of RNA-seq Experiments Using Quasi-Likelihood Methods in edgeR.* Methods Mol Biol, 2016. **1418**: p. 391-416.
222. McCarthy, D.J. and G.K. Smyth, *Testing significance relative to a fold-change threshold is a TREAT.* Bioinformatics, 2009. **25**(6): p. 765-71.
223. Frees, S., et al., *QGRS-Conserve: a computational method for discovering evolutionarily conserved G-quadruplex motifs.* Hum Genomics, 2014. **8**: p. 8.
224. Chang, Y.F., J.S. Imam, and M.F. Wilkinson, *The nonsense-mediated decay RNA surveillance pathway.* Annu Rev Biochem, 2007. **76**: p. 51-74.
225. Sauliere, J., et al., *CLIP-seq of eIF4AIII reveals transcriptome-wide mapping of the human exon junction complex.* Nat Struct Mol Biol, 2012. **19**(11): p. 1124-31.
226. Moes, D.J., et al., *Effect of CYP3A4*22, CYP3A5*3, and CYP3A Combined Genotypes on Cyclosporine, Everolimus, and Tacrolimus Pharmacokinetics in Renal Transplantation.* CPT Pharmacometrics Syst Pharmacol, 2014. **3**: p. e100.
227. Dai, Y., et al., *In vitro metabolism of cyclosporine A by human kidney CYP3A5.* Biochem Pharmacol, 2004. **68**(9): p. 1889-902.
228. Peltz, S.W., et al., *Ataluren as an agent for therapeutic nonsense suppression.* Annu Rev Med, 2013. **64**: p. 407-25.
229. Basu, S. and E. Wickstrom, *Temperature and salt dependence of higher order structure formation by antisense c-myc and c-myb phosphorothioate oligodeoxyribonucleotides containing tetraguanylate tracts.* Nucleic Acids Res, 1997. **25**(7): p. 1327-32.
230. Noer, S.L., et al., *Folding dynamics and conformational heterogeneity of human telomeric G-quadruplex structures in Na+ solutions by single molecule FRET microscopy.* Nucleic Acids Res, 2016. **44**(1): p. 464-71.
231. Schuetz, J.D., et al., *Identification of a novel dexamethasone responsive enhancer in the human CYP3A5 gene and its activation in human and rat liver cells.* Mol Pharmacol, 1996. **49**(1): p. 63-72.
232. Krishna, G.G. and S.C. Kapoor, *Potassium depletion exacerbates essential hypertension.* Ann Intern Med, 1991. **115**(2): p. 77-83.
233. Appel, L.J., et al., *Dietary approaches to prevent and treat hypertension: a scientific statement from the American Heart Association.* Hypertension, 2006. **47**(2): p. 296-308.
234. Thompson, E.E., et al., *CYP3A variation and the evolution of salt-sensitivity variants.* Am J Hum Genet, 2004. **75**(6): p. 1059-69.
235. Suarez-Kurtz, G., et al., *Global pharmacogenomics: distribution of CYP3A5 polymorphisms and phenotypes in the Brazilian population.* PLoS One, 2014. **9**(1): p. e83472.
236. Shen, W., X.H. Liang, and S.T. Crooke, *Phosphorothioate oligonucleotides can displace NEAT1 RNA and form nuclear paraspeckle-like structures.* Nucleic Acids Res, 2014. **42**(13): p. 8648-62.
237. Lorenz, P., et al., *Phosphorothioate antisense oligonucleotides induce the formation of nuclear bodies.* Mol Biol Cell, 1998. **9**(5): p. 1007-23.
238. Wang, Y., et al., *Phosphorothioate Antisense Oligonucleotides Bind P-Body Proteins and Mediate P-Body Assembly.* Nucleic Acid Ther, 2019. **29**(6): p. 343-358.
239. Liang, X.H., et al., *Identification and characterization of intracellular proteins that bind oligonucleotides with phosphorothioate linkages.* Nucleic Acids Res, 2015. **43**(5): p. 2927-45.
240. Weidner, D.A., et al., *Phosphorothioate oligonucleotides bind in a non sequence-specific manner to the nucleolar protein C23/nucleolin.* FEBS Lett, 1995. **366**(2-3): p. 146-50.
241. Ginisty, H., F. Amalric, and P. Bouvet, *Nucleolin functions in the first step of ribosomal RNA processing.* EMBO J, 1998. **17**(5): p. 1476-86.

242. Nachmani, D., et al., *Germline NPM1 mutations lead to altered rRNA 2'-O-methylation and cause dyskeratosis congenita.* Nat Genet, 2019. **51**(10): p. 1518-1529.
243. Turner, A.J., et al., *A novel small-subunit processome assembly intermediate that contains the U3 snoRNP, nucleolin, RRP5, and DBP4.* Mol Cell Biol, 2009. **29**(11): p. 3007-17.
244. Shen, W., et al., *Chemical modification of PS-ASO therapeutics reduces cellular protein-binding and improves the therapeutic index.* Nat Biotechnol, 2019. **37**(6): p. 640-650.
245. Hudziak, R.M., et al., *Resistance of morpholino phosphorodiamidate oligomers to enzymatic degradation.* Antisense Nucleic Acid Drug Dev, 1996. **6**(4): p. 267-72.
246. United States Renal Data System, N.I.o.H., National Institute of Diabetes and Digestive and Kidney Diseases., *2020 USRDS annual data report: epidemiology of kidney disease in the United States.* 2020.
247. Hannedouche, T., et al., *Randomised controlled trial of enalapril and beta blockers in non-diabetic chronic renal failure.* BMJ, 1994. **309**(6958): p. 833-7.
248. Group, M.o.D.i.R.D.S., *Effects of dietary protein restriction on the progression of moderate renal disease in the Modification of Diet in Renal Disease Study.* J Am Soc Nephrol, 1996. **7**(12): p. 2616-26.
249. Jafar, T.H., et al., *Proteinuria as a modifiable risk factor for the progression of non-diabetic renal disease.* Kidney Int, 2001. **60**(3): p. 1131-40.
250. Bakris, G.L., *Slowing nephropathy progression: focus on proteinuria reduction.* Clin J Am Soc Nephrol, 2008. **3 Suppl 1**: p. S3-10.
251. Russo, L.M., et al., *Impaired Tubular Uptake Explains Albuminuria in Early Diabetic Nephropathy.* 2009. **20**(3): p. 489-494.
252. Russo, L.M., et al., *The normal kidney filters nephrotic levels of albumin retrieved by proximal tubule cells: Retrieval is disrupted in nephrotic states.* Kidney International, 2007. **71**(6): p. 504-513.
253. Khundmiri, S.J., et al., *Transcriptomes of Major Proximal Tubule Cell Culture Models.* Journal of the American Society of Nephrology, 2021. **32**(1): p. 86-97.
254. Sieber, K.B., et al., *Integrated Functional Genomic Analysis Enables Annotation of Kidney Genome-Wide Association Study Loci.* J Am Soc Nephrol, 2019.
255. Van Ness, K.P., et al., *Microphysiological Systems to Assess Nonclinical Toxicity.* Curr Protoc Toxicol, 2017. **73**: p. 14 18 1-14 18 28.
256. Lawrence, M., et al., *Software for computing and annotating genomic ranges.* PLoS Comput Biol, 2013. **9**(8): p. e1003118.
257. Pavkovic, M., et al., *Multi omics analysis of fibrotic kidneys in two mouse models.* Sci Data, 2019. **6**(1): p. 92.
258. Meuleman, W., et al., *Index and biological spectrum of human DNase I hypersensitive sites.* Nature, 2020. **584**(7820): p. 244-251.
259. Vierstra, J., et al., *Global reference mapping of human transcription factor footprints.* Nature, 2020. **583**(7818): p. 729-736.
260. Joachim, G.R., et al., *Selectivity of Protein Excretion in Patients with the Nephrotic Syndrome.* J Clin Invest, 1964. **43**: p. 2332-46.
261. Friedman, S., et al., *Mechanisms of proteinuria in diabetic nephropathy. II. A study of the size-selective glomerular filtration barrier.* Diabetes, 1983. **32 Suppl 2**: p. 40-6.
262. Carrie, B.J. and B.D. Myers, *Proteinuria and functional characteristics of the glomerular barrier in diabetic nephropathy.* Kidney Int, 1980. **17**(5): p. 669-76.
263. Gadegbeku, C.A., et al., *Design of the Nephrotic Syndrome Study Network (NEPTUNE) to evaluate primary glomerular nephropathy by a multidisciplinary approach.* Kidney Int, 2013. **83**(4): p. 749-56.

264. Zhang, B., et al., *Cisplatin-induced nephrotoxicity is mediated by tumor necrosis factor-alpha produced by renal parenchymal cells.* Kidney Int, 2007. **72**(1): p. 37-44.

265. Wiggins, M.C., et al., *Tumour necrosis factor levels during acute rejection and acute tubular necrosis in renal transplant recipients.* Transpl Immunol, 2000. **8**(3): p. 211-5.

266. Ramesh, G. and W.B. Reeves, *TNF-alpha mediates chemokine and cytokine expression and renal injury in cisplatin nephrotoxicity.* J Clin Invest, 2002. **110**(6): p. 835-42.

267. Guo, G., et al., *Role of TNFR1 and TNFR2 receptors in tubulointerstitial fibrosis of obstructive nephropathy.* Am J Physiol, 1999. **277**(5): p. F766-72.

268. Kwon, O., et al., *Urinary actin, interleukin-6, and interleukin-8 may predict sustained ARF after ischemic injury in renal allografts.* Am J Kidney Dis, 2003. **41**(5): p. 1074-87.

269. Wu, Q., et al., *Kidney Injury Molecule-1 and Periostin Urinary Excretion and Tissue Expression Levels and Association with Glomerular Disease Outcomes.* Glomerular Diseases, 2021: p. 1-15.

270. Zhou, D., et al., *Matrix Metalloproteinase-7 Is a Urinary Biomarker and Pathogenic Mediator of Kidney Fibrosis.* J Am Soc Nephrol, 2017. **28**(2): p. 598-611.

271. Yang, X., et al., *Urinary Matrix Metalloproteinase-7 Predicts Severe AKI and Poor Outcomes after Cardiac Surgery.* J Am Soc Nephrol, 2017. **28**(11): p. 3373-3382.

272. Fu, H., et al., *Matrix metalloproteinase-7 protects against acute kidney injury by priming renal tubules for survival and regeneration.* Kidney Int, 2019. **95**(5): p. 1167-1180.

273. He, W., et al., *Matrix metalloproteinase-7 as a surrogate marker predicts renal Wnt/beta-catenin activity in CKD.* J Am Soc Nephrol, 2012. **23**(2): p. 294-304.

274. Surendran, K., et al., *Matrilysin (MMP-7) expression in renal tubular damage: association with Wnt4.* Kidney Int, 2004. **65**(6): p. 2212-22.

275. Afkarian, M., et al., *Urine matrix metalloproteinase-7 and risk of kidney disease progression and mortality in type 2 diabetes.* J Diabetes Complications, 2015. **29**(8): p. 1024-31.

276. Oken, D.E. and W. Flamenbaum, *Micropuncture studies of proximal tubule albumin concentrations in normal and nephrotic rats.* Journal of Clinical Investigation, 1971. **50**(7): p. 1498-1505.

277. Stolte, H., H.J. Schurek, and J.M. Alt, *Glomerular albumin filtration: a comparison of micropuncture studies in the isolated perfused rat kidney with in vivo experimental conditions.* Kidney Int, 1979. **16**(3): p. 377-84.

278. Van Liew, J., et al., *Protein excretion: micropuncture study of rat capsular and proximal tubule fluid.* American Journal of Physiology-Legacy Content, 1970. **219**(2): p. 299-305.

279. Tojo, A. and H. Endou, *Intrarenal handling of proteins in rats using fractional micropuncture technique.* Am J Physiol, 1992. **263**(4 Pt 2): p. F601-6.

280. Lee, P. and X. Wu, *Review: modifications of human serum albumin and their binding effect.* Curr Pharm Des, 2015. **21**(14): p. 1862-5.

281. Yadav, S.P.S., et al., *Mechanism of how carbamylation reduces albumin binding to FcRn contributing to increased vascular clearance.* Am J Physiol Renal Physiol, 2021. **320**(1): p. F114-F129.

282. Raghav, A. and J. Ahmad, *Glycated albumin in chronic kidney disease: Pathophysiologic connections.* Diabetes Metab Syndr, 2018. **12**(3): p. 463-468.

283. Muto, Y., et al., *Single cell transcriptional and chromatin accessibility profiling redefine cellular heterogeneity in the adult human kidney.* Nat Commun, 2021. **12**(1): p. 2190.

284. Park, J., et al., *Renal proximal tubule cell state and metabolism are coupled by nuclear receptors.* bioRxiv, 2020: p. 2020.09.21.307231.

285. Chade, A.R., et al., *Molecular targeting of renal inflammation using drug delivery technology to inhibit NF-kappaB improves renal recovery in chronic kidney disease.* Am J Physiol Renal Physiol, 2020. **319**(1): p. F139-F148.

286. Rangan, G.K., et al., *Inhibition of nuclear factor-kappaB activation reduces cortical tubulointerstitial injury in proteinuric rats.* Kidney Int, 1999. **56**(1): p. 118-34.

287. Smith, S.M., et al., *Benefits for bone from resistance exercise and nutrition in long-duration spaceflight: Evidence from biochemistry and densitometry.* J Bone Miner Res, 2012. **27**(9): p. 1896-906.

288. Grigoriev, A.I., B.V. Morukov, and D.V. Vorobiev, *Water and electrolyte studies during long-term missions onboard the space stations SALYUT and MIR.* Clin Investig, 1994. **72**(3): p. 169-89.

289. Cirillo, M., et al., *Urinary albumin in space missions.* J Gravit Physiol, 2002. **9**(1): p. P193-4.

290. Cirillo, M., et al., *Low urinary albumin excretion in astronauts during space missions.* Nephron Physiol, 2003. **93**(4): p. p102-5.

291. Ritchie, M.E., et al., *limma powers differential expression analyses for RNA-sequencing and microarray studies.* Nucleic Acids Res, 2015. **43**(7): p. e47.

292. Smyth, G.K., J. Michaud, and H.S. Scott, *Use of within-array replicate spots for assessing differential expression in microarray experiments.* Bioinformatics, 2005. **21**(9): p. 2067-75.

293. Liu, R., et al., *Why weight? Modelling sample and observational level variability improves power in RNA-seq analyses.* Nucleic Acids Res, 2015. **43**(15): p. e97.

294. Nolfi-Donegan, D., A. Braganza, and S. Shiva, *Mitochondrial electron transport chain: Oxidative phosphorylation, oxidant production, and methods of measurement.* Redox Biol, 2020. **37**: p. 101674.

295. Taanman, J.W., *The mitochondrial genome: structure, transcription, translation and replication.* Biochim Biophys Acta, 1999. **1410**(2): p. 103-23.

296. Schulz, H., *Beta oxidation of fatty acids.* Biochim Biophys Acta, 1991. **1081**(2): p. 109-20.

297. Leach, C.S., et al., *Regulation of body fluid compartments during short-term spaceflight.* J Appl Physiol (1985), 1996. **81**(1): p. 105-16.

298. Bankir, L., et al., *Vasopressin-V2 receptor stimulation reduces sodium excretion in healthy humans.* J Am Soc Nephrol, 2005. **16**(7): p. 1920-8.

299. Drummer, C., et al., *Vasopressin, hypercalciuria and aquaporin--the key elements for impaired renal water handling in astronauts?* Nephron, 2002. **92**(3): p. 503-14.

300. Ranieri, M., et al., *Calcium sensing receptor exerts a negative regulatory action toward vasopressin-induced aquaporin-2 expression and trafficking in renal collecting duct.* Vitam Horm, 2020. **112**: p. 289-310.

301. Khositseth, S., et al., *Hypercalcemia induces targeted autophagic degradation of aquaporin-2 at the onset of nephrogenic diabetes insipidus.* Kidney Int, 2017. **91**(5): p. 1070-1087.

302. Pastushkova, L., et al., *Detection of renal tissue and urinary tract proteins in the human urine after space flight.* PLoS One, 2013. **8**(8): p. e71652.

303. Garrett-Bakelman, F.E., et al., *The NASA Twins Study: A multidimensional analysis of a year-long human spaceflight.* Science, 2019. **364**(6436).

304. Brenza, H.L., et al., *Parathyroid hormone activation of the 25-hydroxyvitamin D3-1alpha-hydroxylase gene promoter.* Proc Natl Acad Sci U S A, 1998. **95**(4): p. 1387-91.

305. Bland, R., et al., *Constitutive expression of 25-hydroxyvitamin D3-1alpha-hydroxylase in a transformed human proximal tubule cell line: evidence for direct regulation of vitamin D metabolism by calcium.* Endocrinology, 1999. **140**(5): p. 2027-34.

306. Riccardi, D. and G. Valenti, *Localization and function of the renal calcium-sensing receptor.* Nat Rev Nephrol, 2016. **12**(7): p. 414-25.

307. Ahmed, L.H.M., et al., *Vitamin D3 metabolite ratio as an indicator of vitamin D status and its association with diabetes complications.* BMC Endocr Disord, 2020. **20**(1): p. 161.

308. Brumbaugh, P.F. and M.R. Haussler, *1 Alpha,25-dihydroxycholecalciferol receptors in intestine. I. Association of 1 alpha,25-dihydroxycholecalciferol with intestinal mucosa chromatin.* J Biol Chem, 1974. **249**(4): p. 1251-7.
309. Lou, Y.R., et al., *25-Hydroxyvitamin D(3) is an agonistic vitamin D receptor ligand.* J Steroid Biochem Mol Biol, 2010. **118**(3): p. 162-70.
310. Munetsuna, E., et al., *Anti-proliferative activity of 25-hydroxyvitamin D3 in human prostate cells.* Mol Cell Endocrinol, 2014. **382**(2): p. 960-70.
311. Jao, T.M., et al., *ATF6alpha downregulation of PPARalpha promotes lipotoxicity-induced tubulointerstitial fibrosis.* Kidney Int, 2019. **95**(3): p. 577-589.
312. Chung, K.W., et al., *PPARalpha/beta Activation Alleviates Age-Associated Renal Fibrosis in Sprague Dawley Rats.* J Gerontol A Biol Sci Med Sci, 2020. **75**(3): p. 452-458.
313. Dhillon, P., et al., *The Nuclear Receptor ESRRA Protects from Kidney Disease by Coupling Metabolism and Differentiation.* Cell Metab, 2021. **33**(2): p. 379-394 e8.
314. Frazier, R., et al., *Associations of Fenofibrate Therapy With Incidence and Progression of CKD in Patients With Type 2 Diabetes.* Kidney Int Rep, 2019. **4**(1): p. 94-102.
315. Delerive, P., et al., *Peroxisome proliferator-activated receptor alpha negatively regulates the vascular inflammatory gene response by negative cross-talk with transcription factors NF-kappaB and AP-1.* J Biol Chem, 1999. **274**(45): p. 32048-54.
316. Tanaka, T., M. Narazaki, and T. Kishimoto, *IL-6 in inflammation, immunity, and disease.* Cold Spring Harb Perspect Biol, 2014. **6**(10): p. a016295.
317. Glund, S. and A. Krook, *Role of interleukin-6 signalling in glucose and lipid metabolism.* Acta Physiol (Oxf), 2008. **192**(1): p. 37-48.
318. Rose-John, S., *IL-6 trans-signaling via the soluble IL-6 receptor: importance for the pro-inflammatory activities of IL-6.* Int J Biol Sci, 2012. **8**(9): p. 1237-47.
319. Gaillard, J., et al., *Interleukin-6 receptor signaling. II. Bio-availability of interleukin-6 in serum.* Eur Cytokine Netw, 1999. **10**(3): p. 337-44.
320. Novick, D., et al., *Soluble cytokine receptors are present in normal human urine.* J Exp Med, 1989. **170**(4): p. 1409-14.
321. Reeh, H., et al., *Response to IL-6 trans- and IL-6 classic signalling is determined by the ratio of the IL-6 receptor alpha to gp130 expression: fusing experimental insights and dynamic modelling.* Cell Commun Signal, 2019. **17**(1): p. 46.
322. Scheller, J., et al., *The pro- and anti-inflammatory properties of the cytokine interleukin-6.* Biochim Biophys Acta, 2011. **1813**(5): p. 878-88.
323. Jones, G.W., et al., *Loss of CD4+ T cell IL-6R expression during inflammation underlines a role for IL-6 trans signaling in the local maintenance of Th17 cells.* J Immunol, 2010. **184**(4): p. 2130-9.
324. Ranieri, E., et al., *Urinary IL-6/EGF ratio: a useful prognostic marker for the progression of renal damage in IgA nephropathy.* Kidney Int, 1996. **50**(6): p. 1990-2001.
325. Pearson, A.L., et al., *Albumin induces interleukin-6 release from primary human proximal tubule epithelial cells.* J Nephrol, 2008. **21**(6): p. 887-93.
326. Zhang, Z., B.D. Humphreys, and J.V. Bonventre, *Shedding of the urinary biomarker kidney injury molecule-1 (KIM-1) is regulated by MAP kinases and juxtamembrane region.* J Am Soc Nephrol, 2007. **18**(10): p. 2704-14.
327. Bonventre, J.V., *Kidney injury molecule-1: a translational journey.* Trans Am Clin Climatol Assoc, 2014. **125**: p. 293-9; discussion 299.
328. Ichimura, T., et al., *Kidney injury molecule-1 is a phosphatidylserine receptor that confers a phagocytic phenotype on epithelial cells.* J Clin Invest, 2008. **118**(5): p. 1657-68.
329. Yang, L., et al., *KIM-1-mediated phagocytosis reduces acute injury to the kidney.* J Clin Invest, 2015. **125**(4): p. 1620-36.

330. van Timmeren, M.M., et al., *Tubular kidney injury molecule-1 (KIM-1) in human renal disease.* J Pathol, 2007. **212**(2): p. 209-17.

331. Smeets, B., et al., *Proximal tubular cells contain a phenotypically distinct, scattered cell population involved in tubular regeneration.* J Pathol, 2013. **229**(5): p. 645-59.

332. Sato, M., et al., *Targeted disruption of TGF-beta1/Smad3 signaling protects against renal tubulointerstitial fibrosis induced by unilateral ureteral obstruction.* J Clin Invest, 2003. **112**(10): p. 1486-94.

333. Fujimoto, M., et al., *Mice lacking Smad3 are protected against streptozotocin-induced diabetic glomerulopathy.* Biochem Biophys Res Commun, 2003. **305**(4): p. 1002-7.

334. Liu, Z., X.R. Huang, and H.Y. Lan, *Smad3 mediates ANG II-induced hypertensive kidney disease in mice.* Am J Physiol Renal Physiol, 2012. **302**(8): p. F986-97.

335. Zhou, L., et al., *Mechanism of chronic aristolochic acid nephropathy: role of Smad3.* Am J Physiol Renal Physiol, 2010. **298**(4): p. F1006-17.

336. Lai, W., et al., *C-reactive protein promotes acute kidney injury via Smad3-dependent inhibition of CDK2/cyclin E.* Kidney Int, 2016. **90**(3): p. 610-26.

337. Kirita, Y., et al., *Cell profiling of mouse acute kidney injury reveals conserved cellular responses to injury.* Proc Natl Acad Sci U S A, 2020. **117**(27): p. 15874-15883.